ABSTRACT

Title of Dissertation: Development of a biogeochemical modeling system to estimate fluxes and controls of estuarine organic matter cycling

John Blake Clark, Doctor of Philosophy, 2019

Dissertation directed by: Professor Dr. Raleigh R. Hood, Department of Marine Estuarine Environmental Science

This dissertation is an analysis of organic matter cycling using a biogeochemical modeling system to estimate a comprehensive organic carbon budget in an estuary. New processes were built into the model, including sediment-water column dissolved organic matter (DOM) fluxes, wetland input of DOM, and a more sophisticated representation of DOM reactions in the water column. First, the Sediment Flux Model was updated to include DOM as a diagenesis intermediate in the breakdown of organic matter. Long term time series of sediment-water column nitrogen and oxygen fluxes constrained the updated sediment model. On average, subtidal sediment was a net source of 1.00 mol C m^{-2} yr^{-1} and 0.19 mol N m^{-2} yr^{-1}, substantially larger than previous estimates.

Wetland derived DOM undergoes transformations due to absorbing large quantities of UV-Visible light during estuarine transport. To account for this in the model, the light absorbed by DOM drives mechanistic photochemical degradation reactions in a new module in the organic carbon reaction suite. The reaction equations were parameterized and tested by recreating bench top photochemical degradation experiments using the model. Predicted organic carbon transformation rates ranged from 0.59 to 4.86 μmol C L^{-1} hr^{-1} and a test data set was recreated with 3.66% mean percent error.

The enhanced modeling system was implemented in the Rhode River, MD, USA, a well studied tributary of Chesapeake Bay. Coupled observations and 3-D modeling results at the outflow of the Kirkpatrick Marsh creek showed that wind variability was important in driving variations in salinity and was strongly correlated with fluorescent DOM. Finally, the fully coupled organic carbon cycle model was implemented and constrained by water column observations. Numerical experiments with and without the tidal wetland input showed that the marsh contributed 20.5% to the total DOC stock within the tributary and 20.7% to the total flux of DOC from the Rhode River to the Chesapeake Bay. A geographic relationship derived from the Rhode River predicts that tidal wetlands contribute 3.0% to the total DOC inputs in Chesapeake Bay and 13.4% to the total DOC stock.

Development of a biogeochemical modeling system to estimate fluxes and controls of estuarine organic matter cycling

by

John Blake Clark

Dissertation submitted to the Faculty of the Graduate School of the
University of Maryland, College Park, in partial fulfillment
of the requirements for the degree of
Doctor of Philosophy
2019

Advisory Committee:
Professor Raleigh R. Hood, Chair
Dr. Jeffrey Cornwell
Dr. Maria Tzortziou
Dr. Jeremy Testa
Dr. Wen Long

Foreword

Contained within this dissertation are four research chapters that were conducted in collaborative efforts with multiple scientists. Chapter 2 and Chapter 4 are works that were published in academic journals with myself as the primary author and major contributor with co-authors also contributing. Chapters 3 and 5 are also collaborative efforts where I am the first author and major contributor that are currently in review at academic journals. At the end of each chapter, I acknowledge my collaborators and co-authors.

Dedication

The last four and a half years have been some of the best, most rewarding of my life. Without the support of my partner, Rosie, I would never have been able to get to the moment of earning my PhD. From moving across the country, to building her own career, to always being supportive in the highs and the lows of the doctoral degree experience, she has always been there for me.

I would also like to dedicate this dissertation to my parents, John and Kelley Clark. I was extremely lucky to grow up in a supportive environment where my parents always encouraged me to follow my aspirations and helped me to achieve my goals. Not everybody is so privileged, and if I have learned anything over the last five years (beyond the carbon cycle…) it is that I am truly blessed to have them as parents.

Acknowledgements

First I would like to acknowledge my advisor, Dr. Raleigh Hood, and all the members of my advisory committee. Without your support, advice, and criticism this research would not have been possible.

Many institutions, people, and funding sources supported the research within this dissertation. First, thank you to the National Aeronautics and Space Administration for providing funding to support the first three years of my PhD under grant # NNH13ZDA001N-CARBON. Thank you to the Horn Point Laboratory for providing a Doctoral Fellowship to support the final two years of my PhD. Thank you to the Horn Point Laboratory Education committee and the Izaak Walton League of America, Easton Chapter for providing extra-curricular support for travel to academic meetings in addition to research funding. Thank you to the University of Maryland Department of Marine Estuarine and Environmental Science and the University of Maryland Graduate School for a Dean's Fellowship award that helped support my research and allowed travel to academic meetings.

I had the pleasure of working with many collaborators who contributed to aspects of each chapter, and they will be acknowledged in each chapter accordingly. In addition, sources of data and analytical tools will also be acknowledged within where appropriate. I would like to thank all of my collaborators for the invaluable opportunity to work together to produce some novel and (hopefully) impactful research.

Table of Contents

List of Tables

List of Figures

Figure 2.5 Station R-64 modeled and observed (a) sediment oxygen demand (SOD; left axis) and water column O_2 concentration (right axis), (b) NH_4^+ flux (JNH_4^+), and (c) NO_3^- flux (JNO_3^-). N fluxes are positive out of the sediment.

Figure 2.6 Modeled vs. observed sediment oxygen demand (SOD) for all three stations using (a) the Chesapeake Bay Program dissolved oxygen data or (b) the sediment oxygen and nutrient exchange (SONE; Boynton and Baily, 2008) incubation oxygen data for the overlying water column oxygen boundary forcing in SedDOM-SFM. SOD model skill is improved substantially by using the SONE data (r = 0.59, 100% improvement, MEF = 0.12, 121% improvement, RMSE = 12.15 mmol O_2 m^{-2} d^{-1}, 24.1% improvement)

Figure 2.7 11-year average climatology of dissolved organic carbon flux (JDOC) across the sediment layer 1 and overlying water column interface for (a) station R-64, (b) RGPT, and (c) PNPT. A positive flux is out of the sediment into the water column. DOC_1 is labile DOC, DOC_2 is semi-labile DOC, DOC_3 is refractory DOC and TDOC is the sum of all three reactivity classes. The shocks in each plot are due to discontinuities in the interpolated forcing.

Figure 2.8 11-year averaged climatology of the three reactivity classes of dissolved organic carbon (DOC; G1, G2, G3) and the total (TDOC) flux out of the sediment for (a) station R-64, (b) RGPT and (c) PNPT. The dates on the plot are when peak flux rates are observed for DOC_1 and DOC_2 and total DOC (TDOC).

Figure 2.9 11-year average climatology of the three reactivity classes of dissolved organic nitrogen (DON; G1, G2, G3) and the total (TDON) flux out of the sediments for station (a) R-64, (b) Ragged Point and (c) PNPT. The dates on the plot are when peak flux rates are observed for DON_1 and DON_2 and total DON (TDON).

Figure 2.10 Time series of dissolved organic carbon flux (JDOC) across the sediment water interface for (a) stations R-64 (b) RGPT, and (c) PNPT. The total flux (TDOC) is the sum of the labile (DOC_1), semi-labile (DOC_2) and inert (DOC_3) fractions. Note the scale on (b) is different than that on (a) and (c). The stars on panel (a) in 1991-1992 (Burdige and Homstead, 1994) and 1995-1996 (Burdige and Zheng, 1998) are measured fluxes from a similarly located mid-channel Chesapeake Bay station.

Figure 2.11 The forced modeled downward sinking particulate organic carbon (JPOC, left axis) for (a) station R-64, (b) RGPT, and (c) PNPT. The right axis is the fraction of JPOM (both organic carbon and nitrogen) that is either lost (positive) or gained (negative) out of the sediment as the dissolved organic matter flux (JDOM). Particulate organic nitrogen was forced with the same inter-annual variability as that of POC at a ratio of 6.6:1 POC:PON

Figure 2.12 Annual average climatology of the fraction of particulate organic matter flux (JPOM; both organic carbon and nitrogen) that is either lost (positive) or gained

(negative) out of the sediment as the dissolved organic matter flux (JDOM) for (a) station R-64, (b), RGPT and (c) PNPT.

Chapter 3

Figure 3.1 Chesapeake Bay (a-c) and mid-Atlantic Bight (d-f) absorption at 355 nm (a355), dissolved organic carbon concentration (DOC), and spectral absorption slope ratio (SR) used to parameterize the specific absorption for colored DOC_2 and colored DOC_3. SR is the ratio between the slope of the absorption spectra in the 275-295 nm region and the 350-400 nm region.

Figure 3.2 Colored dissolved organic carbon (CDOC) specific absorption spectra for the three photoreactivity classes in DOM-PD.

Figure 3.3 Spectral distribution of the irradiance used to force the numerical model of the test data set. The total irradiance used was 17.9 W m^{-2}

Figure 3.4 Dissolved organic carbon (DOC) as a function of absorbance at 355nm (a355) for (a) the GCREW marsh creek derived samples used to generate the colored DOC_3 specific absorption spectra (diamonds=2015, squares =2016, orange=June, blue=July, magenta=August.),(b) the mid-Chesapeake Bay NASA GEOCAPE cruise data used to generate the colored DOC_2 specific absorption spectra, and (c) the mid-Atlantic coastal ocean NASA CLiVEC cruise data used to generate the colored DOC_1 specific absorption spectra. Information on each data set can be found in Table 3.e.

Figure 3.5 Photobleaching of absorbance (a300) after filtered Xenon lamp exposure for filtrate from the marsh low tide sample (filled circles), marsh high tide samples, (x's) and Rhode River estuary sample (circles) as a function of total absorbed energy during the exposure. Variation in exposure and photobleaching results from the use of six long-pass cutoff filters and exposure durations of 12 and 24 h.

Figure 3.6 Predicted vs observed a300 (m^{-1}) for DOM-PD model fits to the (a) marsh low tide data and (b) Rhode River estuary samples. Open symbols are for 12 hour exposures, filled symbols 24 hour exposures to Xenon irradiance through the various long-pass filters (Table 3.2). The marsh low tide samples were used to estimate $AQY_{3,j}$ and the Rhode River estuary samples were used to estimate $AQY_{2,j}$.

Figure 3.7 The spectrally explicit apparent quantum yields (AQY) estimated from the Xenon lamp solar exposures for each pathway and a photochemical degradation conceptual diagram with the shading of each dissolved organic matter (DOM) pool representative of the fraction of the total absorbance in each pool after the seven day incubation experiments for an average marsh low tide condition. The width of the arrows are scaled to the magnitude of the apparent quantum yield (AQY) for each pathway (see scale key in lower right corner). There is no arrow from $CDOM_2$ to non-colored DOM/DIC because the AQY for that pathway is virtually 0.

Figure 3.8 (a) Seven day final predicted and observed absorbance at 300 nm (a300, m^{-1}) for all 15 Rhode River incubations in the test data set, with the numbers corresponding to the incubation data in Table 3.3. Blue numbers indicate marsh low tide incubations and orange numbers dock (estuary) water incubations. (b) predicted (dashed lines) and observed (diamonds) colored dissolved organic carbon (CDOC) absorbance at 300 nm (a300) for marsh low tide (LT) and marsh high tide (HT) samples from incubations 8 and 9. Time series of modeled CDOC concentration beginning with the (c) average dock initial concentration and (d) average marsh low tide initial concentration.

Figure 3.9 Rate of change of colored dissolved organic carbon (CDOC; dDOC dt^{-1}, µmol C L^{-1} hr^{-1}) over the course of the (a) average estuary incubation and (b) the average marsh low tide incubation. The total DOC (tDOC) is the sum of each pool and the negative rate of change is the loss of CDOC to non-colored DOC and dissolved inorganic carbon.

Chapter 4

Figure 4.1 (a) Chesapeake Bay with the (b) RhodeFVCOM model domain and (c) the Kirkpatrick Marsh area in the RhodeFVCOM model domain. Stars represent freshwater discharge points and the dot represents the marsh element used in marsh hydrology analysis. The Kirkpatrick Marsh is outlined in (c) and measurements were taken at the marsh creek and SERC, indicated by the arrows.

Figure 4.2 Low-pass cutoff filtered (36 hour frequency) salinity and DOM fluorescence (*fDOM)* observed at the Kirkpatrick Marsh creek in (a) spring, (b) summer and (c) fall in 2015. The stick plots are the observed hourly wind speed at Tolchester Beach, MD (NOAA Tides and Currents). Black dots indicate days when greater than 3 mm of rain fell at Annapolis, MD (weatherunderground.com)

Figure 4.3 Cross covariance of North-South (NS) winds, East-West (EW) winds and salinity with *fDOM* at the Kirkpatrick Marsh creek for the three time periods in Figure 4.2. Southerly wind (v) and westerly wind (u) are defined as positive. Lags at the maximum absolute covariances are given in Table 3

Figure 4.4 *fDOM* versus (a) observed sea surface height (SSH) and (b) salinity at the Kirkpatrick Marsh Creek for the three time series in Figure 4.2.

Figure 4.5 (a) Unfiltered *fDOM* and (b) depth for the entire sampling period in 2015. Gaps in the data indicate periods when the EXO-2 Sonde was not deployed.

Figure 4.6 Modeled and observed (a) salinity (r = 0.88, RMSE = 1.43) and (b) temperature (r = 0.98, RMSE =1.71 °C) at the SERC dock. Gaps in the observed data are periods when the sonde was removed for maintenance.

Figure 4.7 A hypsometric curve generated by RhodeFVCOM and calculated inundation area vs elevation from acoustic Doppler velocimetry (ADV) probe observations at the Kirkpatrick Marsh creek from June – December 2015. Inundation areas were calculated

as the flow rate at the marsh creek (m^3 s^{-1}) divided by the rate of tide stage change (m s^{-1}; Eq. 2). The modeled inundated area is the actual area of a sub-section of the marsh that RhodeFVCOM has predicted with a height above D_{min} (0.05 m) at each time step

Figure 4.8 (a) Modeled salinity in the Kirkpatrick marsh creek for the three numerical experiments and (b) interpolated river discharge forcing from the Muddy Creek watershed. Test SW is forced with wind from the south during storms, and test NW is forced with wind from the north during storms.

Figure 4.9 (a) Modeled low-pass cutoff filtered (36 hr frequency) marsh creek velocity and (b) sea surface height (SSH) gradient from Kirkpatrick Marsh creek to the opposite side of the Rhode River in spring and early summer. Positive velocity is marsh water efflux and a positive gradient indicates the water surface is sloping away from the marsh towards the mouth of the river. The asterisks indicate when modeled storm winds were applied. Test SW is forced with wind from the south during storms; test NW is forced with wind from the north during storms.

Figure 4.10 Low-pass filtered flow (m^3 s^{-1}), deviation from mean water depth (m), and mean-normalized *fDOM* at the marsh creek. Negative flow is out of the marsh, positive is into the marsh.

Figure 4.11 Conceptual diagram of the estuarine surface gradient progression during a "typical" wind progression in the Rhode River, MD in the spring and fall. As southerly winds blow a barotropic surface pressure gradient sets up in the back of the Rhode River depicted by the H in (a) that forces water back towards the marsh, depressing flow out of the wetland depicted by the shaded region. As Northwesterly winds progress, local wind driven flow enhances flow out of the creek back towards the marsh, while local wind effects set up a low pressure in the back and mouth of the Rhode River, depicted by the L's (b).

Chapter 5

Figure 5.1 (a) RhodeFVM model domain extending from the William Preston Lane Memorial (Chesapeake Bay) Bridge in the north to Poplar Island in the south, (b) 3-dimensional bathymetric rendering of (a) showing three Chesapeake Bay Program (CBP) stations used for model tuning and validation and (c) the Rhode tributary with the Kirkpatrick Marsh at the head of the tributary and the eight watershed inflows depicted with X's. CBP stations XGE3275 and WT8.2 are shown which were used for modeling tuning and validation. Contours represent model depth. These figures were generated using Tecplot 360 (C).

Figure 5.2 Model Conceptual Diagram with an emphasis placed on transformations related to colored and non-colored dissolved organic matter (CDOM and NCDOM; both C and N). The potential coagulation pathway and hydrolytic pathway between DOM and particulate organic matter (POM) is highlighted by a red arrow, and the photochemical reaction pathway is highlighted by a violet arrow. All reaction terms and parameters are defined in the Appendices.

Figure 5.3 Specific absorption spectra for (a) colored dissolved organic carbon (CDOC) 1-3 and (b) water, particles, and chl *a*. Curves in (b) were taken from Rose et al. (2018) and interpolated to the 1 nm interval.

Figure 5.4 Linear regression of fraction of forest cover with the dissolved organic carbon to dissolved organic nitrogen ratio (C:N) from Lu et al., 2014; Final equation is C:N = 4.78 x %Forest + 11.27 where x is the fraction of forest in the watershed

Figure 5.5 The spectral distribution of light at 100 W m^{-2} of incident irradiation.

Figure 5.6 Model-observation comparisons for station WT8.2 (a,b) and station XGE3275 (c,d). Contours represent model output for dissolved organic carbon (DOC) in time, while each dot represents an observation.

Figure 5.7 Model-observation comparison along the transect in Figure 1c for (a) dissolved organic carbon (DOC) and (b) colored dissolved organic matter (CDOM) absorbance at 440 nm (a440). Observations were collected at various times during ebb tide phase and averaged. The model output is at an hourly interval for July 2005 when the change in tidal elevation, dz dt^{-1}, was less than the median change in tidal elevation for all ebb tides (dz dt^{-1} < -2.16 cm hr^{-1}; n=153). Collection methods and analytical techniques can be found in Tzortziou et al. (2011) and Logozzo (2017). Modeled a440 is the product of the specific absorption of each colored DOC class (1-3) at 440 nm (m^2 g C^{-1}) and colored DOC concentration (g C m^{-3}).

Figure 5.8 Model (contours) and Chesapeake Bay Program observations (circles) for stations WT8.2 (upper) and XGE3275 (lower) for dissolved organic nitrogen (a,b)(g N m^{-3}), dissolved oxygen (c,d) (g O_2 m^{-3}), chlorophyll *a* (e,f)(mg chl *a* m^{-3}), NH_4^+ (g,h)(g N m^{-3}), NO_3^- (i,j)(g N m^{-3}) and particulate organic carbon (POC)(k,i)(g C m^{-3}). Observed POC is estimated from measured values of particulate organic nitrogen and converted to carbon units using a ratio of 5.67 g C g N^{-1}.

Figure 5.9 Average marsh-estuary (a) dissolved organic carbon flux (JDOC) and particulate organic carbon flux (JPOC). A positive flux is out of the marsh, negative flux into the marsh. The orange line represents the low pass frequency filtered flux using a period of 14 days as the filter cutoff frequency. The grey line is the instantaneous average flux taken at an hourly interval.

Figure 5.10 The complete dissolved organic carbon (DOC) budget for the Rhode River tributary (Figure 1c). Each bar represents the cumulative DOC sources (positive) or sinks (negative) for DOC from the Rhode River over April 1 – November 30, 2005. The total is the sum of the three reactivity classes. From left to right, the terms are defined as the marsh sediment-water column DOC flux (marsh JDOC), estuarine sediment-water column DOC flux (estuary JDOC), planktonic algal derived DOC from both exudation and predation, hydrolysis of particulate organic carbon to DOC, denitrification loss of DOC, heterotrophic remineralization of DOC, abiotic photochemical remineralization of

DOC, riverine inputs from the watershed of DOC, photochemical transformation of DOC between colored and non-colored pools and reactivity classes, photochemical loss of DOC (inverse of production), the change in DOC concentration over the model time period (ΔDOC) and flux between the Rhode River and the main stem of the model domain (MainStem).

Figure 5.11 Difference network between the model scenarios with (+M) and without (-M) marsh dissolved organic matter (DOM) inputs and marsh NH_4^+ uptake. The dashed lines represent processes that are unchanged, orange arrows represent processes that decreased under the –M scenario, black arrows represent processes that increased under the –M scenario. The width of the arrow represents the total difference (Tons C) over the 242 day model time period.

Figure 5.12 (a) Transect moving out of the Kirkpatrick Marsh through the Rhode River into the Chesapeake Bay displaying the concentration gradient of colored and non-colored dissolved organic carbon (CDOC and NCDOC) in the model runs with (+M) and without (-M) the marsh input and the difference (Diff.) between the +M and –M scenario for (b) $CDOC_1$, (c) $CDOC_2$, (d) $CDOC_3$, (e) total DOC, (f) $NCDOC_1$, (g) $NCDOC_2$, and (h) $NCDOC_3$. The dashed line represents the cutoff for the section of the Rhode River used in the budget analysis.

Figure 5.13 Absolute difference in nitrogen budgets for runs with (+M) and without (-M) the marsh for (a) ammonium (NH_4^+), (b) nitrate (NO_3^-) and (c) dissolved organic nitrogen (DON) for the Rhode River integrated from April 1st – November 30th, 2005. Terms in regular print are sources while terms in bold are sinks.

Figure 5.14 The average difference between runs with and without the marsh for mid-water column (+M minus –M) (a) ammonium (NH_4^+), (b) nitrate (NO_3^-), (c) net primary production (NPP) and (d) photosynthetically active radiation (PAR).

Figure 5.15 Percent dissolved organic carbon (DOC) contribution from the marsh to the gross DOC production and estuarine DOC stock within the Rhode River modeled as a function of Estuary volume to marsh area (EV:MA) ratio. The model function was derived using a generalized logarithmic linear model predicted by the five segments from the Rhode River and extrapolated to estimate the marsh DOC contribution based on the EV:MA for the entire Chesapeake Bay (59.6 m, dashed line). Diamonds indicate model extracted values for each segment. (p value for % GDP = 0.002, p value for stock = 0.001)

Introduction

1.1 Overview

We are in an era of change, with anthropogenic greenhouse gas emissions since the industrial revolution driving rapid and widespread shifts in Earth's climate. In order to understand and predict the effects of anthropogenically driven climate change, quantifying the drivers and understanding the processes that contribute to the past and current climate state is key. One of the main components of the regulation of Earth's climate is carbon, and in particular carbon dioxide and methane and the cycles that govern their distribution. Quantifying the carbon cycle as a whole is paramount to predicting the future state of the Earth and how each component of the highly complex and always changing carbon cycle contributes to the changing climate.

One large and relatively uncharacterized pool of carbon is aquatic and marine organic carbon that has two main forms: dissolved and particulate organic carbon (DOC and POC). DOC is comprised of a highly complex heterogeneous pool of tens of thousands of compounds (Gonsior et al., 2017; Hawkes et al., 2016; Hernes, 2003; Medeiros et al., 2016) with many sources to the marine environment. In the open ocean, the primary source is from phytoplankton primary production (Carlson et al., 1994; Carlson et al., 2010; Romera-Castillo et al., 2016) whereby much of the DOC produced by phytoplankton is subsequently remineralized in the epipelagic and mesopelagic waters. The oceanic DOC concentration of 667 Pg of carbon is on the same order of magnitude as the recent atmospheric concentration of CO_2 (Hedges et al., 1997) and small changes in the oceanic pool of DOC can alter the atmospheric concentration; DOC

that is remineralized into CO_2 in the ocean will eventually enter the atmosphere and potentially contribute to further warming. The standing concentration of DOC in the ocean is driven by the balance of inputs (e.g., oceanic production and terrestrial runoff) and outputs (e.g., remineralization to CO_2 and degassing) therefore constraining these flux terms is key to understanding the past, current, and future state of the DOC stock of the ocean.

Sources of DOC in coastal waters include riverine input (Fichot and Benner, 2014; Hedges et al., 1997; Raymond and Spencer, 2015) much of which is chemically distinct from compounds that are produced within the water column from phytoplankton production (Mannino and Harvey, 2000; Medeiros et al., 2016). Globally, the riverine export of DOC to the coastal ocean is estimated at 250 Tg C yr^{-1}, with 36.1% originating from the world's 30 largest rivers (Raymond & Spencer 2015). The remaining 63.9 % comes from smaller rivers and streams, many of which drain into estuarine systems where much of the DOC can undergo further transformation and processing before reaching the continental shelf and open ocean. In addition to rivers, wetlands and vegetated systems also contribute large quantities of DOC to coastal waters. Estimates of tidal wetland (both tropical mangroves and temperate marshes) DOC export range from 50-150 Tg C yr^{-1} (Raymond & Spencer 2015) to 174-400 Tg C yr^{-1} (Cai, 2011), extremely large ranges with significant uncertainty associated with each estimate. Indeed, it is widely considered that tidal wetlands export DOC on the same order of magnitude as rivers, although the molecular composition is likely distinct from riverine inputs.

Knowing the contemporary state of these systems is key to making future predictions about how changes in land use and watershed inputs, loss of coastal

ecosystems such as wetlands due to sea level rise and other forms of anthropogenically driven change will alter the input and role of terrestrial derived DOC in the global carbon cycle. My dissertation specifically focuses on organic carbon biogeochemical cycling in estuaries. Estuarine ecosystems are undergoing rapid change, are often influenced directly by anthropogenic pressures, and are particularly challenging to study due to varying inputs and substantial physical and biogeochemical gradients. Challenges aside, the majority of terrestrial derived compounds pass through some type of estuarine system on the way to the coastal and open ocean. Therefore, understanding the processing of organic carbon within estuaries is key to quantifying the linkage of the land-ocean organic carbon cycle. The scientific community has recently composed a well-informed estimate of the flux of carbon between estuaries and the coastal ocean (Windham-Myers et al., 2018), but the original source of the DOC that is being advected from estuaries to the coastal ocean is less clear. This is due to varying levels of reactivity of DOC that depends on many factors that will be discussed below; not all DOC is created equal which has important implications on how long it remains in the organic form in the water column.

1.2 Sources of dissolved organic matter to estuarine waters

In this section, I provide an overview of the various sources of dissolved organic matter (DOM) to estuarine waters, touching on the chemical composition and the processes that contribute to the cycling of the DOM from each source. DOM includes not only carbon but all other elements contained within the thousands of formulae of dissolved organic molecules. This research primarily focuses on DOC, although dissolved organic nitrogen (DON) is also considered; carbon makes up the majority of the total chemical

composition of most DOM. Figure 1.1 details a conceptual model of the coastal carbon cycle with dominant sources and processes included (Bauer et al., 2013). This introduction focuses on DOM as the primary form of organic matter of interest while particulate organic matter (POM) will also be considered as an important pool of organic carbon where appropriate.

1.2.1 Riverine inflow

Rivers provide substantial input of both organic and inorganic matter to estuarine waters. Land use within a watershed can influence the age of the DOM influx, with anthropogenically-disturbed watersheds exporting older DOM on average (Butman et al., 2012; Lu et al., 2013). Vascular plant derived organic compounds such as lignin make up a large portion of riverine DOM and have been used as a biomarker for tracing terrestrially derived DOM in marine systems (Benner and Opsahl, 2001; Hernes, 2003; Opsahl and Benner, 1997). Microbial reactivity of riverine DOM is somewhat determined by the composition of the DOM pool, in addition to environmental factors and the microbial community that is utilizing DOM as a substrate for growth and respiration (Raymond & Spencer, 2015). Aromatic compounds and lignin are susceptible to photochemical degradation and alteration, especially as riverine water is transported into less turbid coastal regions where more light penetrates into the water column (Bélanger et al., 2006; Cao et al., 2016; Smith and Benner, 2005). A large portion of riverine water contains colored DOM (CDOM) (Spencer et al., 2013; Spencer et al., 2012) that absorbs light at exponentially increasing amounts as wavelength decreases. As DOM in river water flows into estuarine and coastal waters, it is photochemically degraded by ultra-violet (UV) light, transforming high molecular weight compounds into low molecular

weight compounds (Figure 1.2) (Helms et al., 2008; McKay et al., 2016). Photochemical degradation tends to increase the bioavailability of riverine DOM (Lu et al., 2013; Moran et al., 2000; Reader and Miller, 2014; Smith and Benner, 2005), although the precise mechanisms and drivers of the enhanced biological reactivity are less clear. The chemical complexity of the DOM composition in riverine waters makes a quantitative assessment of the varying processes that govern the distribution in time and space difficult as it is transported through estuarine and coastal waters. There remains a lot of uncertainty surrounding the ultimate fate of terrestrial derived DOM in estuaries and the coastal ocean.

1.2.2 Wetland export

Wetlands export large quantities of optically and chemically distinct DOM (Tzortziou et al., 2008), potentially contributing substantially to the DOM pool within estuarine waters. Wetland derived DOM has a very high CDOM content with DOC specific absorption (the amount of light absorbed per unit carbon; m^{-1} g C^{-1} m^{-3} or m^2 g C^{-1}) in a Chesapeake Bay sub-estuary decreasing non-conservatively with distance away from the wetland source (Tzortziou et al., 2011). This indicates that the estuary acts as a net sink of colored dissolved organic matter (CDOM) and biogeochemical processes beyond physically-driven conservative mixing are leading to the loss of CDOM. The composition of wetland derived DOM varies, from highly aromatic, high molecular weight humic compounds to low molecular weight aliphatic compounds (Helms et al., 2008; Medeiros et al., 2015; Osburn et al., 2015). Wetland DOM can be both biologically available and highly photolabile, with photochemical degradation enhancing biological reactivity during estuarine transport (Miller et al., 2002; Vähätalo and Wetzel, 2004;

Vähätalo and Wetzel, 2008). In general, the main source of DOM from wetlands is the sediment pore water (Qualls & Richardson, 2003)**,** although controls on the timing of fluxes and the direct contribution of recently fixed carbon in the form of plant biomass are unclear (Schiebel et al., 2018; Wang et al., 2014).

Wetlands are large sources of DOM to the adjacent tidal waters, but unlike rivers, they can be a source (Childers 1993; Ganju et al., 2013; Odum, 2000) or a sink (Jordan and Correll, 1991) of particulate organic matter, depending on various factors including wetland hydrology and tidal inundation (Fagherazzi et al., 2013; Friedrichs & Aubrey, 1988). Wetlands in temperate regions such as the Mid-Atlantic and Chesapeake Bay experience large seasonal variation in both plant biomass and nutrient fluxes (Rasse et al., 2005). Undoubtedly, a large amount of organic matter that is fixed by wetland plants contributes to the DOM that is lost, although the time scales and processes that lead to the loss of the highly colored, humic compounds from wetland sediment are less clear. What we do know is that wetland DOM is potentially biologically available, highly photoreactive, and can be a large flux to the adjacent estuaries.

1.2.3 Sub-tidal sediments

Relatively sparse observations of sediment-water column DOM fluxes show a potentially substantial albeit poorly quantified contribution to the overlying water column (Burdige and Homstead, 1994; Burdige and Zheng, 1998). With the high organic matter flux across the sediment water interface and generally shallow water in estuaries, sediment DOM may be important in the overall budget of organic matter. Fluxes of both DOC and DON across the sediment water interface have been shown to make up ~10 % of the total sinking POM flux, based on estimates from sediment core incubations

(Burdige and Homstead, 1994; Burdige and Zheng, 1998) and sediment trap data from main stem Chesapeake Bay (Roden et al., 1995). Although relatively small when compared to the downward organic matter flux, the composition and reactivity of sediment derived DOM efflux is less clear. In addition, the paucity of measurements within the bay makes a thorough quantitative analysis of sediment DOM flux difficult, with some incubations indicating a flux of DON into the sediments (Cowan & Boynton 1996), rather than out (Burdige & Zheng 1998). Our understanding is particularly lacking with regard to the temporal and spatial variability of DOM efflux and the reactivity of sediment porewater DOM.

1.2.4 Autochthonous algal production

Inland waters with high residence times and large allocthonous nutrient inputs tend to exhibit high primary production. Some of this fixed carbon is lost as DOC from algal exudation (Baines and Pace, 1991; Lignell, 1990) and when zooplankton graze on phytoplankton in a process called sloppy feeding (Møller, 2007). The chemical composition and reactivity of algal produced DOM is generally thought to be relatively labile supporting up to 50% of the marine heterotrophic microbial community (Thornton, 2014). The non-conservative loss of CDOM away from terrestrial and wetland sources indicates that algal derived DOM is optically and chemically distinct from both wetland and riverine derived DOM, with less light absorption per unit carbon. Phytoplankton produced CDOM is more protein-like relative to wetland or terrestrial derived DOM, as indicated by fluorescence excitation-emission matrices and absorption spectra (Romera-Castillo et al., 2010). Even though phytoplankton can contribute significant amounts of DOM to estuarine waters, the relative contribution of phytoplankton derived DOM to the

standing stock within an estuary is unclear; a relationship between phytoplankton and DOC concentration is not always apparent. For example, long-term data sets of main-stem Chesapeake Bay DON and DOC show a lack of distinct seasonality (Figure 1.3), contrary to the strong seasonality in algal biomass and primary production (Adolf et al., 2006; Cerco and Noel 2004; Gallegos et al., 1997). The lack of any discernible relationship between estuarine DOC or DON and chl *a* biomass over a 10 year period (Figure 1.3c, d) supports the idea that allocthonous DOM is potentially subsidizing the standing stocks in Chesapeake Bay waters.

1.3 Important biogeochemical pathways that alter dissolved organic matter (DOM) distribution

1.3.1 Physics

Longer residence time allows more thorough processing of DOM as it moves away from terrestrial and wetland sources towards the coast. Physical forcing determines the fate of a mass of water and therefore has a strong influence of the material within it. For example, the two-layer circulation (Pritchard, 1952) and strong seasonal stratification of Chesapeake Bay, in addition to wind driven circulation (Wang, 1979b) can exert profound influence over the larger scale biogeochemical processes such as dissolved oxygen dynamics (Scully 2010). Tidal exchange and wetland inundation is important in governing the exchange of solutes between a wetland and the estuary (Correll, 1991) but advective processes on longer time scales are less clear. A water mass that is enriched with DOM during tidal inundation over a marsh becomes diluted due to advection and diffusion as it is flushed out towards the mouth of an estuary, the rate of which is controlled by mixing and flow velocity. In addition, flow can modulate wetland stability

and sedimentation processes (Friedrichs and Aubrey, 1988; Ganju et al., 2013). Understanding flow variability with as high as resolution as possible is foremost to quantifying the biogeochemical controls on marsh-estuary solute exchange.

1.3.2 Heterotrophic microbial degradation

Heterotrophic microbial breakdown of organic matter is the primary process through which organic matter gets decomposed into inorganic components. In estuaries, large inputs of organic matter that are subsequently remineralized creates a large input of CO_2 to the water column (Wang & Cai, 2004; Cai, 2011), making most estuaries on the east coast of the United States net heterotrophic, i.e., the rates of organic matter remineralization are greater than primary production (Herrmann et al., 2014). Chesapeake Bay, however, has a net neutral metabolism due to the large amount of algal production in the water column (Herrmann et al., 2014). Cai (2011) shows that much of the organic matter that is remineralized to CO_2 in estuaries comes from tidal wetland sources, and that a large amount of the organic matter that is exported to the shelf is potentially of wetland origin. The high molecular weight (HMW) DOC that is typically exported from terrestrial systems (Helms et al., 2008) is initially resistant to biological break down (Moran & Hodson, 1990; Moran et al., 2000), potentially increasing the distance it can be transported from its source towards the ocean. In the estuarine environment, many factors can influence biological reactivity and heterotrophic remineralization rates of organic matter. The interactions between molecular composition, UV-Visible light absorption, photochemical degradation, and biological availability should be considered when attempting to quantify the cycling of DOM in estuarine waters.

1.3.3 Photochemical processing of colored dissolved organic matter (CDOM) from tidal wetlands

Wetlands in Georgia and Chesapeake Bay have been shown to produce optically active DOM, with photochemical degradation enhancing microbial activity in samples that are experimentally exposed to UV irradiation (Logozzo, 2017; Miller et al., 2002; Moran et al., 2000). For example, in incubations where DOM was exposed to UV radiation, Moran et al. (2000) saw a ~4 fold increase in the amount of O_2 drawdown (and thus DOC loss). UV absorption by HMW "humic" compounds that are exported from wetlands, and the subsequent photochemical breakdown of these compounds, leads to lower molecular weight compounds on average (Figure 1.2) (Helms et al., 2008). There is a direct causal link between spectral absorbance characteristics of DOM and the average molecular weight of the DOM, with HMW DOM absorbing more strongly across all UV-Visible wavelengths.

The spectral absorption characteristics of CDOM such as the slope ratio (SR) can inform the source and biogeochemical history of the DOM in a parcel of water (Helms et al., 2008). SR, one of many useful absorption spectra metrics (Hu et al., 2002), is defined as the ratio of the exponential slope of the CDOM absorption spectra between 275-295 nm and 350-400 nm. The shallower the slope, the lower the slope ratio, and the less photodegraded a water parcel is; SR is used as a proxy of light exposure history and DOM photoreactivity. Different biogeochemical processes can have opposing effects on DOM optical properties, which can confound the interpretation of source and history by optical properties alone (Hansen et al., 2016). Nonetheless, optical methods and bioassays can offer snapshots of the in-situ conditions. Wetland, terrestrial and algal

produced DOM all undergo different processing due to biological and photochemical production and degradation. Understanding the combined effects of spectrally dependent light absorption, light energy reaction efficiency (known as the apparent quantum yield or AQY), and photochemical-biological degradation is necessary to thoroughly capture the source-sink dynamics of DOM in an estuarine ecosystem.

1.4 Organic carbon budgets of estuarine systems

All of the above sources and associated processes contribute to the total organic carbon budget of estuarine waters, yet teasing apart the relative contribution of each to the total organic carbon stock and flux at any given time or place is very difficult. Recent comprehensive analyses of the wetlands and estuaries of the East Coast of the United States provides estimates of organic carbon budgets across systems (Najjar et al., 2018; Herrmann et al., 2014). These estimates are based on empirical relationships that are used to estimate estuarine organic carbon production and they utilize relatively sparse measurements of inputs to extrapolate to a regional budget. In addition, important aspects of the budgets are often estimated by difference, e.g., what is left over after summing the estimated quantities. Some processes are well constrained (e.g., net tidal wetland carbon uptake measured by eddy covariance) (Forbrich & Giblin, 2015) while others are relatively uncertain (e.g., marsh-estuary DOC fluxes during tidal inundation) (Herrmann et al., 2014). Using a difference method (Inputs - Losses = Net flux out), Cai (2011) estimated that 5.5 Tg C yr^{-1} was exported out of US South Atlantic Bight salt marshes to the downstream estuaries. This leads to an areal flux of 1100.0 g C m^{-2} yr^{-1} that, when extrapolated out to the global wetland area of 3.8×10^{11} m^2, gives the large estimate of 174-400 Tg C yr^{-1}. This estimate also makes the assumption that in-estuary processing is

insignificant and the vast majority of marsh derived DOC is exported to the shelf. This assumption may be valid in energetic systems with a short residence times, but in large estuaries with small tides, such as Chesapeake Bay, in-estuary processing of allocthonous DOC is likely important. Even with the associated caveats, this initial estimate by Cai (2011) of organic carbon fluxes on a large scale shows the potential importance of marshes to the global organic carbon budget, contributing ~half of the total organic carbon flux from terrestrial to marine ecosystems.

Following Cai (2011), Herrmann et al. (2014) compiled estimates of the lateral flux of organic carbon between tidal marshes and estuaries on the East Coast of the United States, with values averaging 184.8 ± 123.0 g C m^{-2} yr^{-1}. Looking at Table 1 from Herrmann et al. (2014), organic carbon flux estimates range from 48 g C m^{-2} $yr^{—1}$ (Jordan and Correll, 1991) to 456 g C m^{-2} yr^{-1} (Dame, 1995). Locations of the measured fluxes span from Georgia (264 g C m^{-2} yr^{-1}) to New York (324 g C m^{-2} yr^{-1}) with no clear geographic pattern to explain differences. Herrmann (2014) predicts the average DOC flux across the East Coast of the US is ~20% that of Cai's (2011) estimate. Having a robust flux estimate that is as tightly constrained as possible is key to producing a reliable budget. Depending on whether Herrmann's (2014) estimate or Cai's (2011) estimate is used will give very different answers on the relative importance of tidal wetlands in the global carbon budget when extrapolating to the global wetland area. Having a large range of DOC estimates is helpful when considering carbon budgets on multiple scales, but understanding why the flux estimates vary is paramount to extrapolating relatively sparse direct measurements of DOC flux to large areas from representative marshes.

The large range of flux estimates beg some important questions: why do marshes behave differently in terms of the total carbon flux, where does all of the organic carbon go once it enters the water column, and what processes govern its fate? Ranging back to the 1960s when marsh-estuary biogeochemical measurement techniques were pioneered, field and experimental studies can offer windows into important processes in estuarine and coastal ocean carbon cycling. This falls short, however, when attempting to do a high spatial and temporal resolution comprehensive budget analysis of all of the important processes affecting organic matter cycling. Building tools such as sophisticated biogeochemical models that can be used to narrow the uncertainty around these estimates is important to further constrain marsh-estuary-ocean carbon cycling.

1.5 Aims and Objectives

As discussed above, quantifying the flux of DOM into and out of estuaries and towards the coastal and open ocean is a high priority to narrow uncertainty associated with some aspects of the carbon cycle. The complex processing along the environmental gradients from land to sea makes this task difficult in practice when relying on observational methods alone. This study aims to incorporate new biogeochemical components into a mechanistic carbon cycle and water quality model, ICM, to directly estimate the role of each process on the transport and transformation of organic matter in estuarine waters. The new model, hereinafter ICM-DOM-PD (Integrated Compartment Model-Dissolved Organic Matter-Photochemical Degradation) was implemented in a tributary of Chesapeake Bay to estimate processes that were previously unrepresented in modeling systems.

Two new modules were built into ICM to model the sediment-water column exchange of DOM and the mechanistic photochemical degradation of DOM in the water column. The Sediment Flux Model (Brady et al., 2013; Di Toro and Fitzpatrick, 1993) was altered to include DOM as an intermediate state variable in the breakdown of POM to inorganic carbon and nutrients. This was done to provide one of the first long-term estimates of DOM fluxes between subtidal sediment and the overlying estuarine water in a shallow ecosystem, and to provide a mechanism to load DOM into the sediments at locations specifically designated as intertidal wetland in the 3-D model domain. The photochemical degradation model achieves two main goals: first, the mechanistic representation of photochemical degradation allows an estimate of the flux of CDOM through the photochemical pathways and the potential to alter the biological reactivity of CDOM. The photochemical degradation model can calculate the impact of marsh derived CDOM on the underwater UV-Visible light field which is important to provide a more realistic simulation of light attenuation. The updated SFM and the photochemical degradation model were tested in stand alone frameworks and compared to experimental data to estimate key fluxes and properties of both carbon cycle pathways. This methodology allowed for a robust parameterization, with the experimental data providing the bounds on the new components of the model before implementation into the three-dimensional biogeochemical modeling system.

To better understand physical drivers of material transport in an estuarine environment, the 3-D hydrodynamic model FVCOM (Chen et al., 2003) was built to represent the Rhode River, MD, USA, a well studied tributary of Chesapeake Bay. The hydrodynamic model was used to simulate the physical properties of water such as water

transport, salinity and temperature. In addition, the drivers of the variability of water flow and transport between a tidal wetland and the Rhode River were explored. High resolution observations at the marsh creek were used to contextualize organic matter fluxes at the outflow of the marsh. It was found the variability of organic matter and salinity was correlated with variations in wind velocity, and the modeling system was used to explore mechanisms on how wind affects flow at the marsh creek.

To explore marsh-estuary organic carbon cycling and fluxes, the FVCOM hydrodynamic model was coupled to the updated organic carbon cycle model, ICM-DOM-PD, with the enhancements described above for the Rhode River. The modeling system was used to carry out one of the first comprehensive organic carbon and nitrogen budgets in a fully coupled marsh-estuary ecosystem model. In addition, model scenarios with and without the marsh DOM input and the photochemical degradation of DOM were used to understand the role of each process on the direct cycling of organic matter and indirectly on other biogeochemical cycles such as nitrogen cycling. The export of DOC from the marsh to the tributary and from the tributary to the mainstem of the Chesapeake Bay was quantified on time scales that can capture seasonality in environmental conditions. From this representative estuarine ecosystem, estimates of the wetland contribution to total DOC inputs and DOC stock within Chesapeake Bay were derived.

Each chapter of this research builds on the previous, with the methods and modules developed in the first three chapters built into the full model system in the final chapter. The modeling system is a tool that can be used in ecosystems where the cycling of organic matter across the terrestrial-marine continuum is important. The model will be

open source with all inputs, pre and post processing scripts, and source code publicly available in an online repository. Figure 1.4 displays the work flow for this dissertation.

Figures Chapter 1

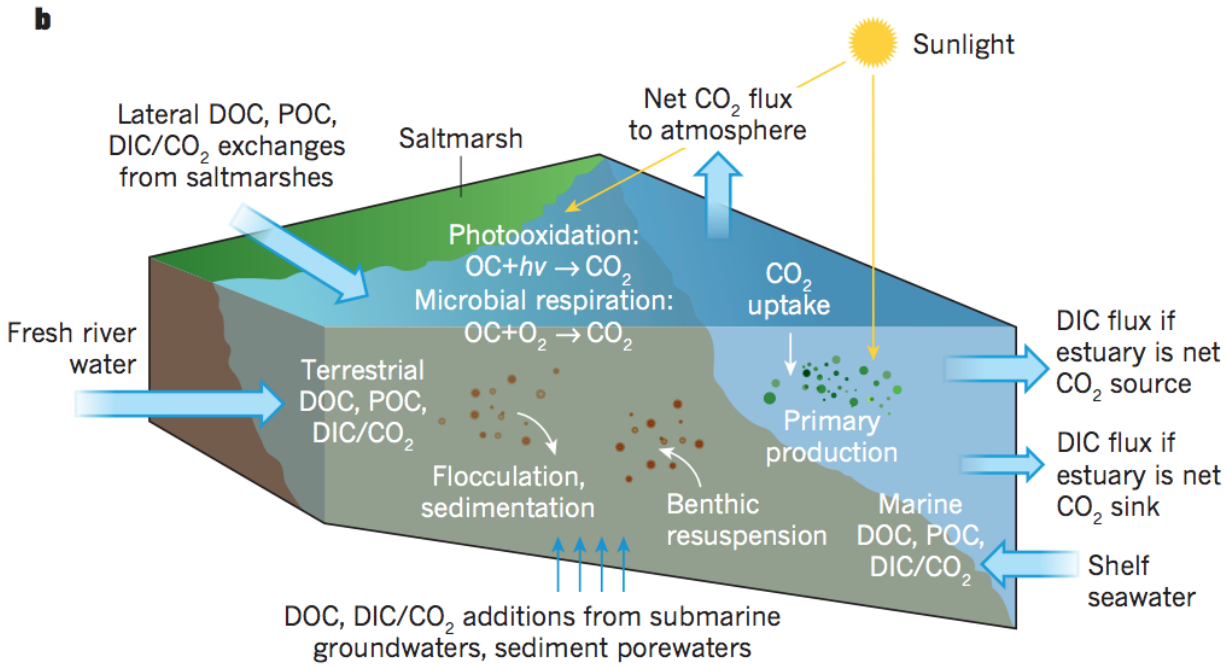

Figure 1.1 From Bauer et al. (2013) the coastal carbon cycle with all-important processes related to the cycling of organic carbon displayed.

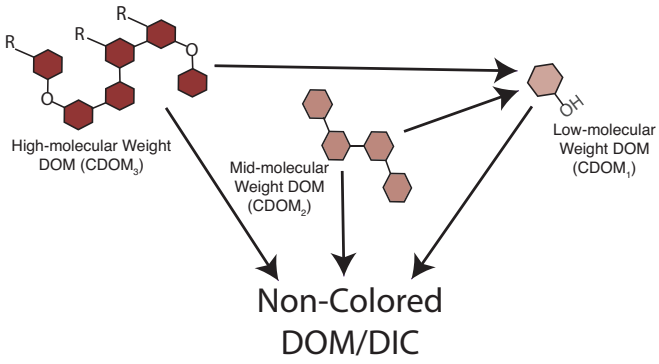

Figure 1.2 Conceptual model showing the breakdown of high- and mid-molecular weight compounds during the photochemical degradation process. The shading of each idealized compound is also indicative of the relative color of each pool, with darker compounds

absorbing more light per unit carbon. The general concepts for this model were adapted from Helms et al., 2008 and are detailed in Chapter 3.

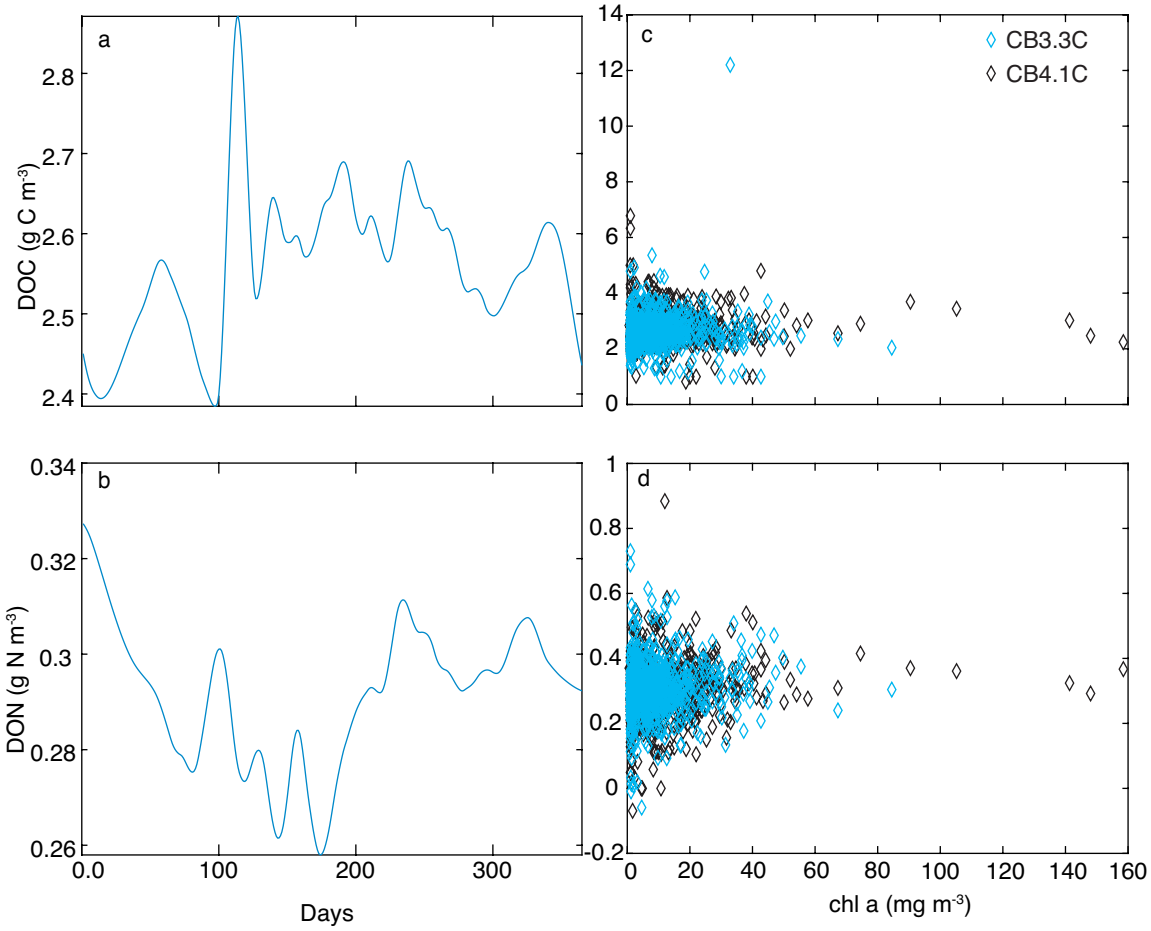

Figure 1.3 Annual climatology of (a) dissolved organic carbon (DOC) and (b) dissolved organic nitrogen at mainstem Chesapeake Bay Program (CBP) water quality monitoring station 4.1C and (c) DOC and (d) DON plotted as a function of chlorophyll *a* at mainstem CBP stations 3.3C and 4.1C. The DOC data was collected from 1985 to 1995 while the DON data was collected from 1985 to 2005. Periodograms and cross covariance analysis revealed no significant seasonality in the full time series.

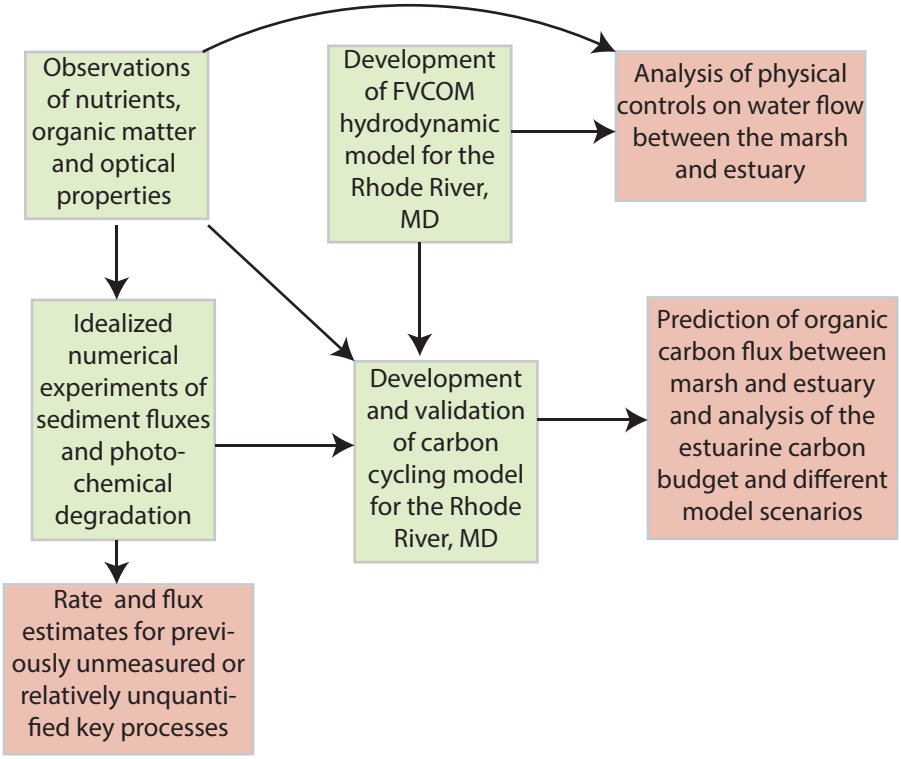

Figure 1.4 Workflow of the research process in this dissertation. Green boxes indicate method development and implementation while red boxes indicate outcomes of each methodology.

Estuarine sediment dissolved organic matter dynamics in an enhanced sediment flux model

2.1 Abstract

Sediment derived dissolved organic matter (DOM) can comprise a substantial portion of the organic carbon budget in coastal bottom waters, yet it is often neglected in coastal carbon cycle models. In most modern sediment-water column flux models, biologically mediated reactions that remineralize particulate organic matter (POM) into inorganic compounds are simplified. In reality, organic matter remineralization is a complex suite of reactions that include DOM intermediate compounds. To better represent the sequential breakdown of POM and remineralization of DOM, a DOM state variable was built into a widely used sediment flux model. In the model, DOM is created in the sediment by hydrolysis of POM, and all organic matter passes through the DOM pool before remineralization. The model was run for 11 years and tuned to reproduce observed sediment flux data collected in Chesapeake Bay and then used to assess the role of DOM in sediment organic matter dynamics. Sediment-water column fluxes of DOM are highly variable both on seasonal and inter-annual scales, with substantial variability among stations in both magnitude and flux direction. Across all stations, semi-labile and inert DOM is lost and labile DOM is taken up into the reactive first layer of the modeled sediment, with the net flux a balance of the two processes. The improved sediment flux model can be utilized to better understand the role of sediment biogeochemistry in the estuarine and coastal carbon cycle, and shed light on difficult to measure processes involving DOM intermediate compounds.

2.2 Introduction

Although estimates of sediment-derived dissolved organic matter (DOM) contribution to coastal organic matter cycling are potentially significant (Burdige et al., 1992; Vlahos et al., 2002), few studies assess the quantity, quality, and variability of sediment DOM exchange. In Chesapeake Bay, limited observations of sediment porewater DOM concentration show DOM accumulates and eventually approaches a constant value with depth (Burdige and Homstead, 1994; Burdige and Zheng, 1998), indicating that there is an internal source of DOM in the sediment. In addition, sediment-water column DOM flux data show that, in general, estuarine and coastal ocean sediment acts as a source of DOM to the overlying water column (Alperin et al., 1994; Burdige et al., 1992; Burdige and Homstead, 1994; Burdige and Zheng, 1998). To account for the depth distribution in sediment of DOM concentration, particulate organic matter (POM) that settles to the sediment from the overlying water column must pass through DOM intermediate compounds in the process of organic matter remineralization (Burdige and Gardner, 1998; Weston and Joye, 2005). Even though DOM plays an important role in early diagenesis and carbon preservation, the seasonal and inter-annual variability of estuarine sediment DOM dynamics and reactivity remains poorly quantified.

The paucity of measurements of Chesapeake Bay sediment DOM fluxes and concentrations makes a quantitative analysis of the role of DOM in the local and regional organic matter cycle difficult. Limited observations of dissolved organic carbon (DOC) and dissolved organic nitrogen (DON) fluxes reveal that both exhibit potentially substantial inter-annual variability (Burdige and Homstead, 1994; Burdige and Zheng, 1998). In addition, there is disagreement in the direction of fluxes in measurements of

DON in a mid-channel Chesapeake Bay, seasonally anoxic station, with both a DON efflux (Burdige and Zheng, 1998) and influx (Cowan and Boynton, 1996) being observed. In general and across systems, it does appear that estuarine and coastal ocean sediment is a source of DOM to the overlying water column. However, the variability in measured downward sinking flux of POM makes an analysis of the net flux, the fraction of the sinking POM that is lost from the sediment through the diffusion of DOM, elusive. Coupled water-column sediment biogeochemical models, however, can help address some of these shortcomings in our current observational and experimental understanding if DOM can be incorporated into them.

Coupled sediment-water column models range from simple no flux boundaries to complex multilayer depth explicit models (Soetaert et al., 2000). Burdige and Gardner (1998) first proposed the Pore Water Size Reactivity (PWSR) model to describe the size distribution and reactivity of DOM with depth in coastal sediment. Recently, an updated version of the PWSR model gives a realistic representation of porewater DOM depth profiles in coastal California sediment (Komada et al., 2013; Burdige et al., 2016). A similar, albeit depth integrated, model is the Sediment Flux Model (SFM), which is used in applications in estuarine and coastal waters to simulate sediment fluxes (Di Toro and Fitzpatrick, 1993; Brady et al., 2013; Testa et al., 2013). Unlike the PWSR model, in SFM diagenesis of organic matter is simplified into a one-step temperature dependent degradation coefficient where POM is converted directly to inorganic forms. Modeled and observed NH_4^+,and NO_3^- fluxes (JNH_4^+ and JNO_3^-) and sediment oxygen demand (SOD) comparisons show that SFM performs well in estuarine waters of Chesapeake Bay (Testa et al., 2013; Brady et al., 2013), reproducing observed fluxes at long-term

observational and experimental stations (Boynton and Bailey, 2008). However, the two-layer depth-integrated SFM does not include DOM as an intermediate compound in the diagenetic reactions, a potentially important omission especially in terms of organic matter budgeting. The lack of a porewater DOM state variable in SFM (and most other models) prevents a quantitative assessment of the role of DOM in bulk organic matter retention, reactivity and storage.

To analyze the role of DOM in estuarine sediment, DOM was incorporated as an intermediate diagenesis compound into SFM (hereinafter SedDOM-SFM). SedDOM-SFM was set up to analyze the reactivity and fate of DOM in three seasonally hypoxic Chesapeake Bay stations by tuning the model to 11-year observed time series of water column - sediment nutrient and oxygen fluxes (SONE) (Boynton and Bailey, 2008). The flux comparison model validation strategy is based on the principle that sediment-water column inorganic nitrogen and O_2 fluxes are primarily driven by the microbial breakdown of organic matter: to capture the sediment fluxes the remineralization of organic matter must be simulated reasonably well. It is shown that model skill is moderately improved with the inclusion of DOM as a diagenesis intermediate. In addition, the model indicates that DOM fluxes are highly seasonal in magnitude, reactivity, and nitrogen content, and can vary in direction across seasons, stations and years. SedDOM-SFM also allows a more complete mechanistic representation and analysis of early diagenesis of organic matter in estuarine sediment.

2.3 Methods

The model formulations of SFM have been discussed at length in recent publications (Brady et al., 2013; Testa et al., 2013), therefore a detailed description of the

model formulations is not included here. SFM is a two layer, depth integrated, biogeochemical sediment flux model that predicts sediment-water column diffusive fluxes based on concentration gradients of solutes and settling fluxes of particulates across the sediment water interface, as well as exchange between the two sediment layers (Di Toro and Fitzpatrick, 1993). Anoxic remineralization occurs in a finite depth layer and the thickness of the surface aerobic layer is adjusted based on overlying water column oxygen concentrations and model calculated SOD. The model assumes that the aerobic first layer is much thinner than the anoxic second layer (e.g. 1-2 mm vs. 10 cm), therefore all particulate organic matter hydrolysis occurs in the second layer. In this section, focus is placed on the new DOM state variables and the model tests that were conducted to assess how the inclusion of DOM into SFM affects organic matter cycling and thus nutrient flux variability.

DOM is modeled with the same strategy as other dissolved solutes, having a mass transfer between the aerobic layer 1 and anaerobic layer 2 that is temperature dependent, and a surface diffusivity approximation that is based on SOD and overlying water column O_2 concentration (Figure 2.1; following Di Toro, 2001). This treatment ensures that all porewater solutes are diffusing with the same mass transfer velocity. DOM is remineralized into both inorganic carbon (untracked in the model) and NH_4^+, which can diffuse with the overlying water column. The following section details the new model equations conceptualized in Figure 2.1.

2.3.1 New model formulations

Equation 2.1 is the mechanistic representation of sediment porewater compound x (carbon or nitrogen) and reactivity i (1-3) DOM in the aerobic sediment layer 1. DOM

reactivity is based on the 3-G model (Jorgensen, 1978; Westrich and Berner, 1984), with DOM_1 and DOM_2 representing labile and semi-labile fractions, and DOM_3 representing an inert fraction. From left to right, the first term is the terminal remineralization of DOM to inorganic forms via the first order temperature dependent remineralization rate $kD_{x,i}$, followed by two porewater diffusion terms based on Fick's law of diffusion. The first is calculated from the sediment layer 1 and layer 2 DOM ($DOM^1_{x,i}$, and $DOM^2_{x,i}$) concentration gradient using a temperature dependent mass transfer velocity KL_{12} (Table 2.1) over the depth of the sediment H_2 (~10 cm). The second term is the diffusion of DOM across the sediment layer 1-water column DOM ($DOM^0_{x,i}$) concentration gradient from the middle of the overlying water column (1m) and the middle of layer 1 (H_1) by surface mass transfer velocity KL_{01}. KL_{01} is approximated at each time step of the model by taking the ratio between SOD and the overlying water column dissolved O_2 concentration.

$$\frac{dDOM^1_{x,i}}{dt} = -kD_{x,i}DOM^1_{x,i} + \frac{KL_{12}}{H_2}\left[DOM^2_{x,i} - DOM^1_{x,i}\right] - \frac{KL_{01}}{H_1}\left[DOM^1_{x,i} - DOM^0_{x,i}\right] \qquad (2.1)$$

Anaerobic sediment layer 2 DOM ($DOM^2_{x,i}$), represented by Equation 2.2, is modeled similarly to layer 1 DOM but with one key difference: POM that is deposited in layer 2 ($POM_{x,i}$) by settling from the overlying water column is hydrolyzed via a first order temperature dependent reaction rate ($kP_{x,i}$) into DOM. This is the primary source of DOM into sediment layer 2, and is the primary mechanism beyond diffusion that DOM is added into the sediment. The fourth term is the sediment accretion velocity ω to account for the burial and loss of organic matter from the finite depth being modeled as sediment is deposited over time. All other terms are defined as in layer 1.

$$\frac{dDOM^{2}_{x,i}}{dt} = kP_{x,i}POM_{x,i} - kD_{x,i}DOM^{2}_{x,i} - \frac{KL_{12}}{H_2}\left[DOM^{2}_{x,i} - DOM^{1}_{x,i}\right] - \frac{\omega}{H_2}DOM^{2}_{x,i} \quad (2.2)$$

Temperature dependency is important in marine sediment diagenesis (Weston and Joye, 2005) and therefore was included explicitly in the model. Temperature dependency is modeled as an Arrhenius relationship with a basal value either increasing or decreasing around temperatures of 20° C. The temperature control function is shown in Equation 2.3 where M is either kP, kD or KL, $kb_{x,i}$ is the reference rate for each compound x (C or N) and reactivity i (1-3), θ_i is the temperature control parameter and T is the sediment temperature (°C). θ_i varies for each reactivity class of organic matter, while diffusion temperature control (θ_D) is the same for all three DOM reactivity classes (Table 2.1). Diffusion temperature control was included to account for the abiotic increase in diffusion with temperature. POM_3 reactivity is set to 5.0×10^{-6} rather than the literature value of 0.0 to account for the slow accumulation of DOM_3 with depth. DOM reaction rates were tuned manually to achieve an optimal model fit to observational data and subsequently fixed for model analysis.

$$M_{x,i} = kb_{x,i} * \theta_i^{T-20} \quad (2.3)$$

2.3.2 Model environment and implementation

SedDOM-SFM was implemented at main channel Chesapeake Bay stations R-64 (38.559 N, -76.426 W), and Point No Point (PNPT; 38.133 N, -76.252 W), in addition to Ragged Point (RGPT; 38.162 N, -76.589 W) in the Potomac River, a large tributary of Chesapeake Bay. Long-term sediment biogeochemical measurements were taken from 1985 through the summer of 1996 at all three stations, which are all seasonally hypoxic (Boynton and Baily, 2008). Observed seasonal time-series of JNH_4^+ and JNO_3^- as well as

SOD were used for model validation beginning May 6,1986 after a one year model spin-up, following Brady et al. (. Organic nitrogen reactivity provided one of the best constraints on model DOM remineralization parameterization because the relative rates of PON hydrolysis and DON remineralization are key to an accurate simulation of JNH_4^+. The sediment surface boundary was forced with time series of observed overlying water column concentrations collected by the Chesapeake Bay Program (CBP; http://www.chesapeakebay.net/data/downloads) for all model constituents including DOC, DON, NH_4^+, NO_3^-, O_2 and temperature. CBP data were used rather than the overlying water column measurements from SONE because the goal was to model in-situ rather than experimental conditions. A shape preserving piecewise cubic Hermite interpolation scheme (PCHIP) was used to interpolate to a 6 hour time step for the model forcing from the approximately biweekly CBP observations.

Time-variable overlying water column DOM forcing interpolated from the relatively uneven and sparse CBP data lacked distinct seasonality and didn't exhibit trends (Figure 2.2). Station PNPT provided a nearly regularly sampled continuous data set for both DON and DOC, but the other two stations lacked a complete and regularly sampled time series for both variables. In order to avoid interpolation errors, at time points when the interpolated data set exceeded the minimum or maximum of the observed data, the interpolated values were set to the mean. CBP data doesn't distinguish between reactivity classes as in SedDOM-SFM, therefore the data was partitioned into 20 % G-1 (labile), 30 % G-2 (semi-labile) and 50 % G-3 (inert), following a water column DOM modeling study in Chesapeake Bay (Keller and Hood, 2011). For reference, a cross aquatic system analysis (Søndergaard and Middelboe, 1995) found that ~17% of DOC

was utilized quickly during incubations, and up to 30 % of riverine derived DOC was utilized within estuaries in the southeastern United States (Moran et al., 2000). Two model runs were conducted to examine different timescales of interest. First, model runs with the time varying DOM forcing were used to see how overlying water column DOM concentration affected the model performance and sediment-water column flux predictions. Second, time-averaged overlying water column DOM forcing was used to look at differences on seasonal and inter-annual time scales that, due to the lack of seasonality and trend in the DOM observations, I hypothesized would be relatively unaffected by removing the time-variance.

SedDOM-SFM is parameterized as in Brady et al. (2013) and Testa et al. (2013) and forced with the same yearly average downward POM flux (JPOM), which is optimized in their modeling studies to achieve the best model fit to observed JNH_4^+. The semilabile POM reactivity was reduced to 1.8×10^{-4} in the model run with DOM turned on, which appropriately scaled the DOM fluxes and pore water concentration to the correct order of magnitude that has been measured while improving model skill. At steady state, the POM hydrolysis and the DOM remineralization must be equivalent, and the ratio of the POM hydrolysis rate and the DOM remineralization rate is proportional to the concentrations of each state variable. Sediment observations of POC and DOC in Chesapeake Bay show that POC is ~2–3 orders of magnitude greater than DOC (Burdige and Homstead, 1994; Burdige and Zheng, 1998); therefore, the reactivity of POC should be 2–3 orders of magnitude less than DOC if steady state is assumed. An updated JPOM optimization was not conducted for SedDOM-SFM because a direct comparison between the model with DOM and SFM was desired, and a new optimization would make such a

comparison ambiguous. Due to the lack of measured porewater DOM remineralization rates in the literature, it was necessary to use an inverse modeling technique to back out the DOM reactions rates, similar to Burdige et al. (2016). The comprehensive time series of flux data added confidence to the estimated DOM remineralization rates.

Model skill was characterized by model-data sediment flux comparisons using three metrics; coefficient of covariance (r), root mean square error (RMSE), and model efficiency (MEF). The coefficient of covariance is a measure of how well the model simulates the data variability, RMSE is an indicator of how accurate the model prediction is and MEF is an indication of the model's predictive capacity relative to the mean (Stow et al., 2009). A MEF > 0 indicates that the model gives a better estimate of observations than the observed mean at any given time, while a value < 0 indicates the model is not better than the mean at representing any one data point. Comparisons of these skill metrics between models with and without the DOM intermediate were conducted to determine how the inclusion of DOM affected JNH_4^+, JNO_3^- and SOD. The statistics presented are the combined mean values of all three stations unless otherwise noted.

2.4 Results and Discussion

2.4.1 Model validation and skill analysis

Model-data comparisons of inorganic nitrogen and O_2 fluxes show that SedDOM-SFM reasonably simulated the early diagenesis of organic matter in Chesapeake Bay (Figures 2.3-2.5). Although the skill of the SOD model solution is relatively low (Table 2 and Figure 2.6), overall SedDOM-SFM captured much of the dynamic seasonal and inter-annual variation in SOD and compares well with previously reported values of model skill in Chesapeake Bay (Brady et al., 2013; Di Toro, 2001). SOD is strongly driven by

both the seasonal variation in temperature-controlled microbial activity and the overlying water column O_2 concentration (Figure 2.3a). During summer, when there were re-aeration events of hypoxic bottom water that increase bottom water O_2 (e.g., in 1989 and 1995) there were large spikes in SOD. Small variations in bottom water O_2 concentration can lead to significant variation in modeled SOD because sediment microbial respiration consumes oxygen rapidly when it is available (Boynton and Kemp, 1985). For comparison, when the oxygen concentrations that were observed during the SONE core incubations were used as the boundary forcing, instead of the CBP data, all SOD skill metrics improved dramatically (Figure 2.6 and Table 2.3). This occurred because small deviations in model forcing from the true oxygen concentration that were observed during flux incubations can cause significant model errors. The CBP database was used for boundary forcing nonetheless because the goal was to model in-situ rather than experimental conditions.

The model sometimes under-predicted anoxic events, also likely due to the small variation in overlying water column dissolved oxygen forcing. There was also large variation in the model skill for each station, further emphasizing the importance of the overlying water conditions in determining the model's ability to predict SOD. Lastly, the model results suggest that the intra-seasonal variability in SOD was largely missed by the observational data, especially decreases in SOD during winter months that occurred at low temperatures. Statistical analysis with and without time varying overlying water column DOM forcing showed no difference for all three variables used for the model skill assessment, indicating short term variation in the DOM flux does not impact the seasonal variation of the inorganic nitrogen and O_2 flux.

Seasonal and inter-annual variability of JNH_4^+ was modeled very well (Table 2.2), with the model capturing the summer peak in all years, while also showing a marked shutdown in JNH_4^+ in the winter months. Variability in JNO_3^- was also captured quite well in SedDOM-SFM (Table 2.2), which is indicative of the ability of the model to simulate nitrification and denitrification. When compared with SFM, SedDOM-SFM performs better for MEF and RMSE for both JNH_4^+ and SOD, while differences in r-value performance were negligibly changed (Table 2.2). JNO_3^- model skill was not substantially improved by the inclusion of the DOM intermediate, supporting the idea that the overlying water column NO_3^- concentration largely drives JNO_3^- in Chesapeake Bay sediment (Testa et al., 2013).

From these comparisons between SFM and SedDOM-SFM, it appears that including a DOM diagenesis intermediate resulted in a more skillful model, with a particularly strong model performance and high MEF in JNH_4^+. JNH_4^+ is largely controlled by organic N remineralization (Cowan and Boynton, 1996; Kemp et al., 1990). Therefore, to capture JNH_4^+ organic N remineralization must be well represented by the model formulations, which adds confidence in our conclusion that the model's simulation of organic matter breakdown was improved by the addition of a DOM intermediate. The lack of improvement in the coefficient of covariance (r; Table 2.2) while the RMSE and MEF improved substantially indicates that both models exhibit similar ability to capture seasonal variations, but that SedDOM-SFM can potentially estimate SOD and JNH_4^+ for any given time point more accurately.

Model runs with constant DOM forcing and time variable DOM forcing resulted in no change in model skill metrics with respect to SOD, JNH_4^+, and JNO_3^-. This

indicates that although the DOM flux between the sediment and water column can be highly variable (see following sections), the short-term variability in the breakdown of DOM in the sediment doesn't have a large controlling influence over DIN fluxes and SOD. As in previous observational (Kemp et al., 1992) and modeling work (Brady et al., 2013), the seasonal variability in observations of sediment nutrient and oxygen fluxes is primarily driven by POM delivery to estuarine sediment and the variation in the overlying water column concentrations of DIN and O_2.

2.4.2 Sediment-Water column dissolved organic matter flux variability

The following sections detail different time scales of sediment-water column DOM flux variability for the three stations within the study. All fluxes are positive out of the sediment. Different controlling factors act on time scales spanning from days to multiple years. A comparison between the three stations demonstrates that sediment overlying water column POM delivery is an important controlling factor for DOM dynamics. Lastly, how the reactivity and partitioning of DOM within models can relate to conceptualizations and observations of organic matter cycling in shallow coastal sediment is discussed.

DOC flux short-term variability

Time-varying observed and interpolated DOM forcing was used to assess how the diffusive flux across the sediment water interface of DOC varies in response to changes in the overlying water column concentration. Figure 2.7 shows the 11-year averaged climatology for the three stations. The modeled DOC flux responded strongly to changes in overlying water column DOC concentration, represented by the short term pattern of

variation in each climatology. In general, the flux peaks in late summer and declines to around 0-1 mmol C $m^{-2}d^{-1}$ in the cooler months. The lack of overlying water column DOM concentration seasonality (Figure 2.2) but high frequency of variation suggest that the overlying water column doesn't exhibit a strong control on the seasonal variability of the sediment-water column DOC flux. The total flux is a balance between a net uptake of DOC_1 into the sediment and a net loss of DOC_2 and DOC_3 out of the sediment. Due to the temporal variability in the concentration gradient across the sediment-water interface, all stations can act as either a source or a sink for DOC. Station R-64 (Figure 2.7a) was a source in all seasons, on average, while station RGPT (Figure 2.7b) transitioned from a source to a DOC sink in the late summer, and station PNPT (Figure 2.7c) was generally a sink, although there were small-scale fluctuations when the sediment is periodically a source.

Fluctuations in the sediment layer 1 and overlying water column mass transfer velocity, KL_{01}, due to changes in the ratio between SOD and the overlying water column dissolved O_2 concentration also affect the diffusion across the sediment water interface. The variation in KL_{01} does not appear to drive much of the short-term variation in JDOC, although the seasonal JDOC cycle is largely determined by seasonal variation in KL_{01}. All three stations exhibited similar seasonal patterns of KL_{01} variance, with high KL_{01} in the summer, and varying by about an order of magnitude across seasons. This is due to a high oxygen demand but low oxygen concentration occurring at warmer temperatures (Brady et al., 2013). The non-linearity of the system is reflected in the rapidly changing flux, although the concentration in the modeled sediment layer 2 is relatively stable on short time scales (not shown). It is important to emphasize that in-station temporal

variance can offer a different interpretation of the *direction* of the flux, depending on when the station is sampled. The timing of sampling could potentially change the interpretation of the general sediment JDOC trend, which has implications for previous and future benthic DOC and DON flux measurements. The short-term dependency of the benthic flux on the overlying water column DOM concentration begs the question as to whether or not the relatively sparse flux measurements that have been made in Chesapeake Bay actually capture the behavior of the sediment fluxes.

DOC flux seasonality and annual averages

The measured and forced overlying water column DOM concentrations lacked any apparent seasonality or pattern of variability, allowing the mean value of DOM forcing for each station to be used. Removing all variance from the DOM forcing resulted in a smoother average DOC flux, although there was still strong seasonality for all three stations (Figure 2.8). This indicates that hydrolysis of POM and thus porewater DOM concentration, coupled with the seasonally varying mass transfer velocities between the 2 sediment layers and the water column, largely determined the seasonality of the modeled fluxes. In order to analyze the seasonal variability, each time series was decomposed into an 11-year climatology to get the mean conditions for our study period. The same general seasonal pattern as seen in the previous section is observed, indicating that processes within the sediment primarily governed the seasonal variation of DOC flux. SedDOM-SFM predicted that the sediment would actively take up and remineralize labile DOC from the water column while acting as a source of semi-labile and inert DOC. DOC_2 efflux peaked between Aug 17 and Aug 28, on average depending on the station, while

DOC_1 uptake by the sediment peaked from 25 August to 10 September. Station R-64 and RGPT had a positive average yearly integrated flux (Table 2.4), while PNPT was neutral. On average, DOC_3 contributed 34% and 38% to the total JDOC for stations R-64 and RGPT, and 45% at station PNPT. Across all three stations, inert DOC_3 contributed 41% to the net flux on average, similar albeit less when compared to results from Santa Barbara Channel anoxic sediment (53% of modeled total JDOC) (Burdige et al., 2016). DON flux exhibited similar seasonal patterns (Figure 2.9).

The JDOC:JDON ratio (C:N, Table 2.4) offers insight into how DON and DOC differentially behave across stations. On average, when compared to the Redfield ratio of 6.6 mols C mol N^{-1}, the sediment was a larger source of DON relative to DOC with a ratio of 4.75 mols C mol N^{-1}. In particular, station RGPT was a large source of DON relative to DOC, which appeared to be driven by the high C:N of the forced overlying water column DOM (Figure 2.2c). The three stations had an average water column DOC:DON ratio of 9.2 (Table 2.4). DOC and DON flux vary independently and are partly dependent on temperature due to the 1.14 times greater reaction rate of DON_1 and DON_2, in addition to the high overlying water column DON:DOC ratio. This suggests that sediment efflux of DOM in estuarine and coastal waters with a potentially high DOC:DON ratio in the water column may be a relative sink for nitrogen from the sediment. This can contribute to the increasing C:N that is observed in porewater profiles in Chesapeake Bay (Burdige and Zheng, 1998) and anoxic Santa Barbara Channel sediment (Burdige et al., 2016). For comparison, Burdige et al. (2016) predicted a DOC:DON sediment efflux of 2.98, while forcing their model with an overlying water column DON concentration assumed to be 0. The results across all stations suggest that

the sediment can act as a transformer of organic material: algal-derived POM that is hydrolyzed in even proportions into semi-labile and refractory DOC and DON, can diffuse back to the water column at different flux rates because the overlying water column has a high DOC:DON ratio. Estuarine and coastal ocean bottom water DOM often has a high C:N ratio relative to Redfield stoichiometry (Hopkinson et al., 2002), therefore this phenomenon of a low JDOC:JDON ratio may be more geographically widespread. This has implications for the net organic carbon and nitrogen flux across the sediment water interface.

The highly seasonal DOM flux is largely controlled by the production and accumulation of DOM by the temperature-controlled hydrolysis of POM. The rates of POM hydrolysis ($kP_{x,i}$) are an order of magnitude slower than DOM remineralization (Table 2.1). However, sediment POM concentration is much greater than DOM concentration in Chesapeake Bay (e.g. at the modeled sediment density of 360 g l^{-1}, ~1.1-2.31 mol C POC l^{-1} vs ~ 0.2-2 mmol C DOC l^{-1}) (Brady et al., 2013; Burdige and Zheng, 1998; Testa et al., 2013). Thus, POM hydrolysis and DOM remineralization generally are on the same order of magnitude. In addition, POM was sourced in the model with a yearly averaged constant overlying water column downward POM flux, allowing it to accumulate through winter before temperature ramps up. The seasonal cycle of DOM flux is indicative of the competing sources and sinks that lead to the makeup of the net concentration of DOM_1 and DOM_2. POM accumulated over fall and winter before hydrolysis ramped up as temperature increased in spring. As concentrations of DOM_1 and DOM_2 increased as the products of POM hydrolysis, DOM loss by remineralization and diffusion from layer 2 to layer 1 eventually out paced hydrolysis. This temperature driven

uncoupling of POM hydrolysis and DOM remineralization has been observed in experimental coastal ocean sediment slurries (Weston and Joye, 2005). The difference between stations, and whether a given location acts as a source or a sink of total DOC, is largely determined by the delivery of POM into the sediment on an inter-annual basis.

An important consideration is how much refractory POM is degraded into inert DOM (DOM_3) in the sediment. An order of magnitude increase in POM_3 reactivity substantially increased the modeled porewater DOM concentration and flux out of the sediment with the majority of the DOM efflux comprising DOM_3 (not shown). In order to keep the modeled DOM efflux within reasonable values compared to what has been observed in Chesapeake Bay, POM_3 must hydrolyze into DOM_3 slowly (5.0×10^{-6} d^{-1}) leading to DOM_3 making up a small portion of the total pool in both the porewater and efflux. The parameterization of POM_3 hydrolysis to DOM_3 will influence the conclusions drawn in terms of the relative contribution of each G-class and thus the bulk reactivity of DOM that leaves the sediment. It should be noted that if the modeled depth is increased to 20 cm (from 10 cm), DOM_3 made up a much greater portion of the total DOM pool. This is owed to the slow production of inert DOM from the breakdown of refractory POM. When the upper 10 cm is modeled, the loss of DOM_3 is roughly balanced by its hydrolytic production, although excess DOC_3 diffuses out of the sediment. However, if the depth is increased (and thus average age), the modeled sediment the inert DOM_3 can accumulate over time.

11-year time-series of DOM flux across three locations

For all three stations, there was strong inter-annual variability of the total DOC flux across the sediment water interface (Figure 2.10), although the general direction waslargely consistent with the climatologies presented in Figure 2.9. All stations exhibit a DOC efflux at the start of the time series, likely due to the initial condition over-estimating POC concentration in the sediment. After the first year, the time-series exhibits differential flux, with both the magnitude and direction varying. Across all years, all three stations were sinks for DOC_1 and sources of DOC_2 and DOC_3. Station RGPT exhibits the most inter-annual variability with three years acting as a source of DOC, six years as a sink, and two years with seasonally varying DOC flux direction.

The highly variable time series for the three stations indicate a variety of biogeochemical conditions were captured, adding confidence in the conclusions that can be drawn from the model results. The differential JPOM forcing at each station largely dictated the inter-annual variability of the DOC flux. Figure 2.11 depicts the JPOM for each station (left axis) and the net flux for both organic carbon and organic nitrogen (right axis). The net flux can also be thought of as the fraction of POM that is either lost (or gained) as DOM efflux (or uptake) across the sediment-water interface. A positive JDOM:JPOM indicates the sediment had a net loss of DOM, while a negative JDOM:JPOM indicates the sediment had a net gain of DOM which was subsequently remineralized. If the average of all three stations across all years is calculated, the sediment was a net source of DOC of 1.00 mol C m^{-2} yr^{-1} and a net source of DON of 190 mmol N m^{-2} yr^{-1} (Table 2.4). The modeled average DON flux was 9.5% of the measured NH_4^+ flux of 2.0 mol N m^{-2} yr^{-1} at similarly located stations (Cowan and Boynton, 1996). Looking specifically at station R-64, which is directly comparable to station M3, the

modeled estimate of the TDOC flux of 1.92 mol C m^{-2} yr^{-1} was 5.2 times greater than the measured DOC flux and 27% that of the observed benthic remineralization rate of organic carbon of 7.17 mol C m^{-2} yr^{-1} (Burdige and Zheng, 1998). It should also be noted that the calculated annual fluxes in Burdige and Zheng (1998) are relatively coarse estimates because of the lack of measurements in cold months, whereby SedDOM-SFM captured the full seasonal cycle in over many years with different biogeochemical conditions.

The variability across station and year for both DOC and DON can help explain some of the previous literature discrepancies in both magnitude and direction of DOC and DON fluxes. In general, Burdige and Homstead (1994) and Burdige and Zheng (1998) found that the sediment was a source for both DOC and DON to the water column. This contrasts with Cowan and Boynton (1996) who found the sediment was a sink for DON at a main-stem Chesapeake Bay station, while North Bay and South Bay stations were a source. To reconcile differences across observational and modeling studies, I propose that the key factor that drives DOM flux variability is the recent (2-3 year) POM flux history, and secondarily winter time temperature. A region with a high average POM flux will act as a DOM source, and the fraction of JPOM that is hydrolyzed into DOM and lost out of the sediment will be greater. A region with low POM flux will act as a DOM sink and the net flux will be greater into the sediment. Therefore, patchiness in how POM settles into the sediment could cause a station in a similar biogeochemical and redox environment, as the three stations in our study, to exhibit differences in both the DOM flux and the net organic matter flux.

2.4.3 Net organic matter flux and dissolved organic matter reactivity

The effects of the different remineralization rates of DOC and DON are realized in the yearly averaged fraction of JPOM that leaves the sediments as DOM, i.e., the net organic matter flux (Figure 2.11). The three stations exhibit differential net flux, which follows the general direction of the TDOC flux, although there was substantial inter-annual variability. On average, at R-64 23% of the PON flux (JPON) and 21% of the POC flux (JPOC) was lost as DOM at the summer peak (Figure 2.12). Integrating over the entire year, 7.8% and 10% of the organic carbon and nitrogen was lost as DOC and DON at R-64 (Table 2.5). Station RGPT (Figure 2.11b) exhibits substantial inter-annual variability, with some years exhibiting a decrease in net downward organic matter flux due to a large DOM efflux. In years following low JPOM into the sediment, the sediment acted as a sink and the net organic matter flux into the sediment is enhanced by labile DOM uptake. Station PNPT was consistent across all years, with the net organic matter flux into the sediment enhanced by labile DOM uptake.

The primary control on the net flux was the POM flux history of the sediment, and secondarily the concentration of overlying water column DOM. R-64 and RGPT both had a much higher average JPOC (15.6 and 13.7 mol C m^{-2} yr^{-1}) and JPON (2.4 and 2.07 mol N m^{-2} yr^{-1}) than station PNPT (8.65 mol C m^{-2} yr^{-1} and 1.3 mol N $^{-2}$ yr^{-1}). The years with higher average downward POM flux, and especially years with a relatively small flux that were preceded by a large flux (e.g. 1987 and 1989 at R-64 and 1987 at RGPT) exhibit a large net efflux of DOM. Station RGPT in year 1991 stands out as an outlier, where the DOM flux peaked out of the sediment in early summer and then was rapidly drawn down into the sediment. The bottom water temperature of the winter in 1990-1991

was ~1.5 °C warmer than the 11-year average. The high average temperature would have driven more POM_1 hydrolysis into DOM_1, and as temperature increased DOM_1 was rapidly drawn down due to the order of magnitude faster reactivity. This was a result of the very fast and highly temperature-responsive reaction rate of DOM_1 in SedDOM-SFM. This result implies that higher wintertime temperatures may cause more POM to be hydrolyzed and eventually remineralized into inorganic matter, reducing sediment organic matter retention and storage.

In order to fit the model to the observations DOM must be tuned to react an order of magnitude more rapidly than POM, in agreement with recent results from a similar modeling study in the Santa Barbara Channel, CA, USA (Burdige et al., 2016). In addition, DOC_2 reacted as fast as DON_2, rates that are partly constrained by the SOD solution and JNH_4^+. If $kD_{x,2}$ was slower, DON efflux became a sink for N that lead to an under prediction of JNH_4^+; if $kD_{x,2}$ is increased, JNH_4^+ was over predicted. Although the numerical model formulation and validation are different in this study from the modeling studies of Komada et al. (2013, 2016) and Burdige et al. (2016), the same general conclusions are drawn in terms of DOM reactivity. The sediment nutrient and oxygen flux data offered a robust test bed to tune and constrain SedDOM-SFM. Recent experimental work also shows that on short time scales much of sediment porewater DOM is turned over quickly (Arnosti and Holmer, 2003). The total DOM flux is relatively dependent on the labile DOM reaction rate, $kD_{x,1}$. If $kD_{x,1}$ is either increased or decreased, the direction of the flux can change because the DOM_1 flux and concentration gradient between layer 1 and the water column responds very strongly to changes in the DOM_1 concentration in layer 1.

Inert DOM (DOM_3) made up a small portion of the total pool in SedDOM-SFM, which was constrained by both the observed concentration and flux of DOM in Chesapeake Bay, but also importantly by JNH_4^+. If a large amount of organic nitrogen was sequestered from remineralization as inert DON, too much N was removed from the reactive pool as DON. This caused JNH_4^+ to be under predicted in addition to DON concentration and flux being unreasonably elevated. DON must turn over relatively quickly to achieve the observed JNH_4^+. Due to a lack of mechanistic understanding, pathways through which DOM_1 and DOM_2 transform to DOM_3 were also not built into the model, which contributed to the low background level of refractory DOM in the 10 cm deep model domain. The ability of the model to recreate JNH_4^+ and generate reasonable DOC and DON concentrations and fluxes indicates that the creation of inert DOM may not be an important process in diagenesis in shallow estuarine sediment. This leads me to conclude that the underlying processes that are being simulated in the model are likely well represented, and that the majority of porewater DOM in the upper 10 cm does, indeed, react rapidly.

2.4.4 Dissolved organic matter flux: controlling factors

Although the model-data comparisons of JNH_4^+, JNO_3^- and SOD show that SedDOM-SFM reasonably simulated the early diagenesis of organic matter in Chesapeake Bay, the sparseness of DOM measurements makes it difficult to quantitatively assess the accuracy of modeled DOM dynamics. What can be said is that the model DOM flux variability was highly dependent on the reaction rates chosen for DOM_1 and the overlying water column DOM_1 concentration. DOM_2 reactivity had a lesser effect due to the lower overall rate. Depending on how the model was forced and

parameterized with respect to DOM_1 the direction and magnitude of the total flux could be different. Inherent in the modeling exercise is the partitioning of the DOM forcing, which can potentially affect the result. SedDOM-SFM predicted that in regions with a greater concentration of water column labile DOM, the sediment would act as a sink, but would also be dependent on the delivery of POM into the sediment. This intriguing result begs the question of how the diffusion of a complex mixture of compounds can be reasonably modeled mechanistically. SedDOM-SFM uses the concentration gradient of labile, semi-labile and inert DOM to calculate the flux. Fick's Law of Diffusion, i.e. the governing diffusive term in Equations 2.1 and 2.2, is based on the diffusion of a single solute across a membrane; therefore, SedDOM-SFM represents what is in reality a complex mixture as one solute for each reactivity class. In order to reconcile the conceptualization of the model, the assumption must be made that each reactivity class is composed of very similar molecular formulae with a similar concentration in both the water column and porewater. I propose the thought experiment, whereby there is a high concentration of DOM compound X on one side of a membrane and a high concentration of DOM compound Y on the opposite side. If compound X and Y are DOM of different composition, for example a solution of amino acids and carbohydrates, they will diffuse down their concentration gradient in opposing directions. This is exactly what we see with the DOM_1 and DOM_2 in SedDOM-SFM. They conceptually must represent different compounds in order to diffuse in the opposite direction across the sediment water interface. This also implies that the sediment will act as a sink for certain classes of compounds that are in higher concentration in the water column, and a source of compounds that are in higher concentration in the sediment.

2.5 Conclusion

This study represents one of the first efforts to model the processes governing estuarine sediment porewater DOM fluxes, and examined the role of DOM in sediment organic matter breakdown and retention. The results suggest that the differential reactivity and response of POM and DOM were important in governing the temporal variability of the net sediment-water column organic matter flux. Stations with a high amount of POM settling into the sediment exhibit a larger DOM efflux, while stations with a low POM delivery acted as a DOM sink. DON and DOC had a similar seasonal response, although the flux of DOC between the sediment and water column was less than DON, relative to the Redfield ratio. There was substantial inter-annual variability of the net organic matter flux, with some years having large losses of organic matter out of the sediment as DOM efflux, relative to the sinking flux of POM. In addition, the order of magnitude higher reactivity of DOM made it more responsive to changes in temperature. Understanding the role of DOM in early diagenesis may be important for quantifying and modeling the response of sediment organic matter cycling to anthropogenically-driven warming in shallow, temperate estuaries. In order to better link DOM biogeochemical modeling efforts and observational work, future measurements and monitoring should focus on bottom water and pore water DOM chemical composition and reactivity.

In addition, the new model formulation in SedDOM-SFM now allows for modeling the dominant mechanism through which DOM is exchanged between tidal marshes and estuarine waters. Although highly simplified, SedDOM-SFM can now be used to model the marsh sediment boundary condition and the exchange of organic matter during tidal inundation and excursion in an estuarine ecosystem. Chapter 4 will

detail how marsh sediments are treated differently in terms of the loading of DOM into the sediment, but all subtidal and marsh sediments can now include DOM as a state variable to interact with the overlying water column.

2.6 Acknowledgements

I would like to acknowledge my co-authors who contributed to the published version of this manuscript in Journal of Geophysical Research: Biogeosciences, Wen Long and Raleigh R. Hood. In addition, I would like to acknowledge Walter Boynton for providing validation data and Jeremy Testa for providing model forcing and helpful discussions. To obtain the model forcing, output and source code, visit the repository at https://github.com/bclark805/SedDOM-SFM. This research was supported by National Aeronautics and Space Administration grant NNH13ZDA001N-CARBON. This is University of Maryland Center for Environmental Science contribution number 5409.

Figures Chapter 2

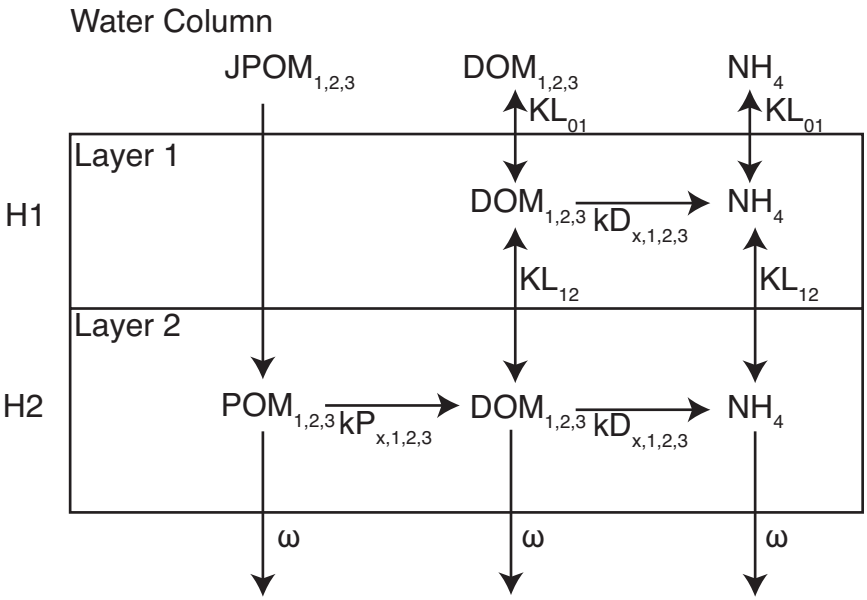

Figure 2.1 Conceptual diagram of the sediment flux model with a dissolved organic matter (DOM; SedDOM-SFM) diagenesis intermediate compound between the breakdown of particulate organic matter (POM) and NH_4^+. NH_4^+ is also oxidized to NO_3^- in layer 1 (not shown). All arrows represent fluxes between state variables. All parameters are defined in Table 1. POM and DOM can be either carbon or nitrogen, but only NH_4^+ is tracked as the pore water inorganic constituent product of organic nitrogen remineralization. Both carbon and nitrogen remineralization and NH_4^+ oxidation contribute to sediment oxygen demand.

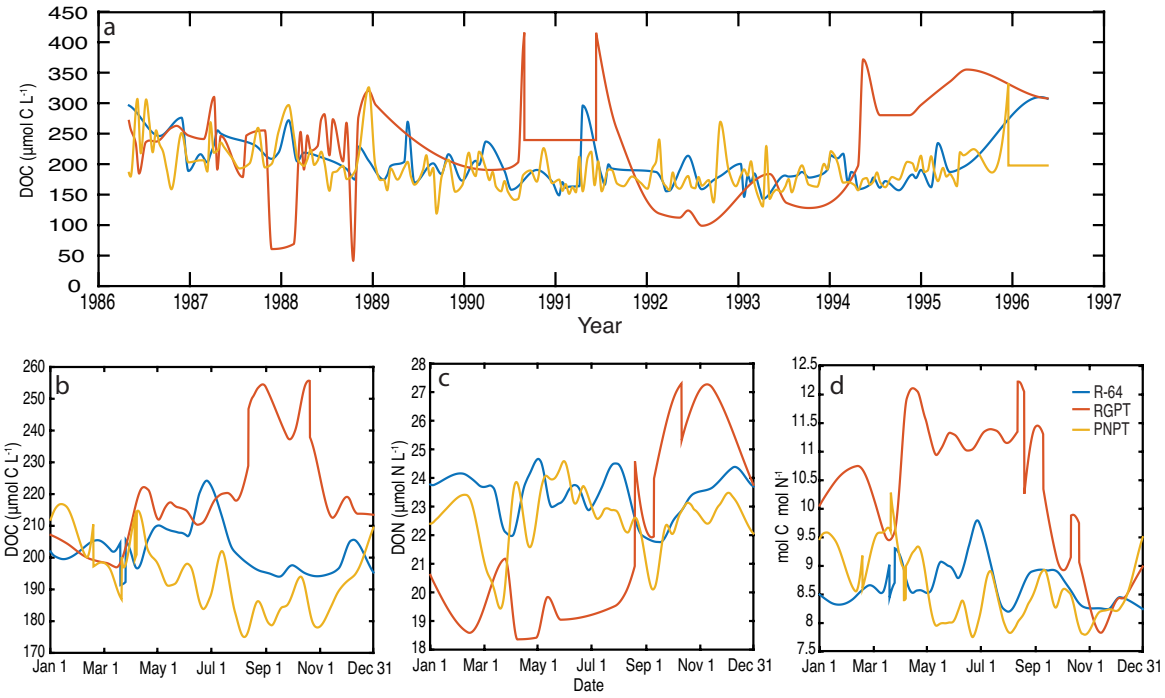

Figure 2.2 (a) Time variable overlying water column DOC forcing for all 3 stations in our modeling study, (b) 11-year climatology of DOC forcing and (c) DON forcing and (d) the DOC:DON ratio

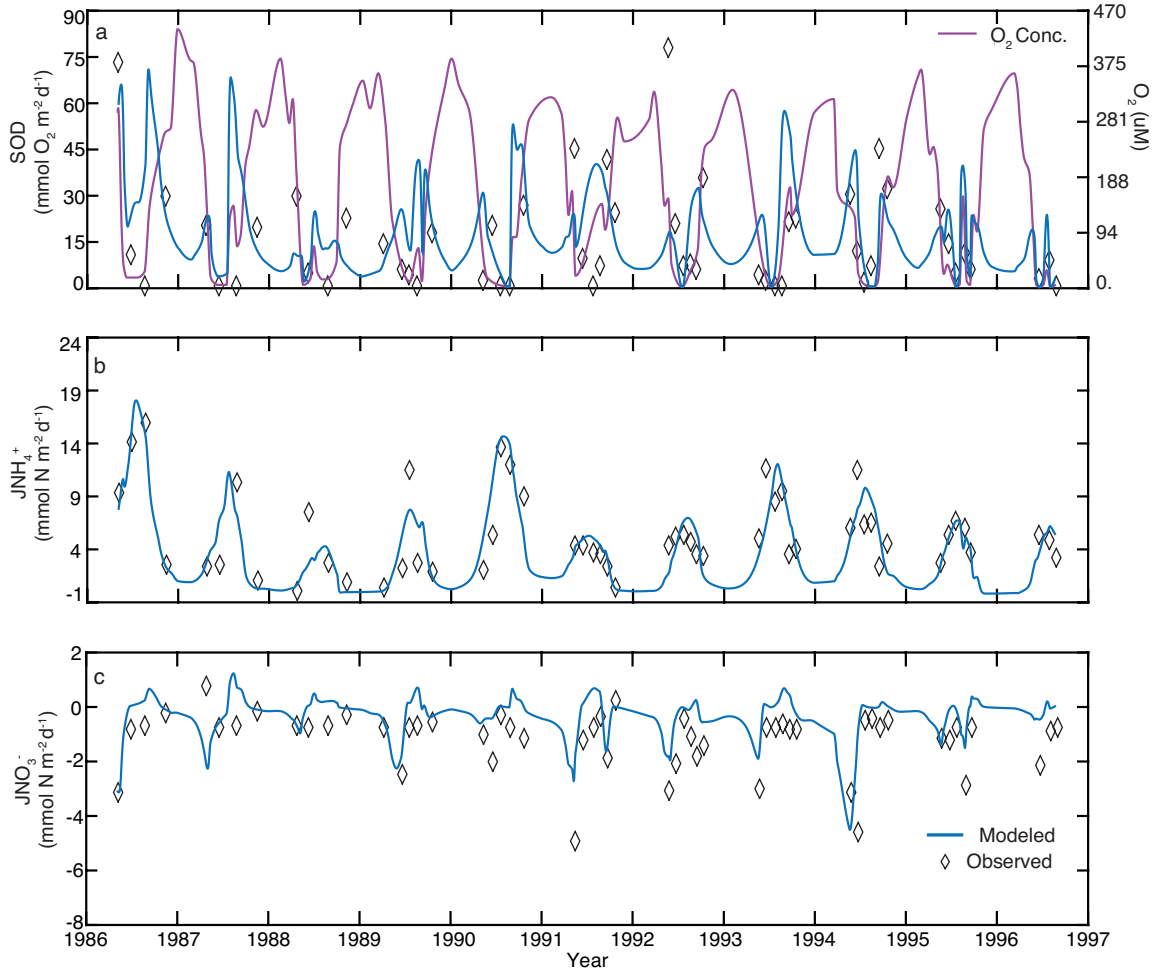

Figure 2.3 Station RGPT modeled and observed (a) sediment oxygen demand (SOD; left axis) and water column O_2 concentration (right axis), (b) NH_4^+ flux (JNH_4^+), and (c) NO_3^- flux (JNO_3^-). Nitrogen fluxes are positive out of the sediment.

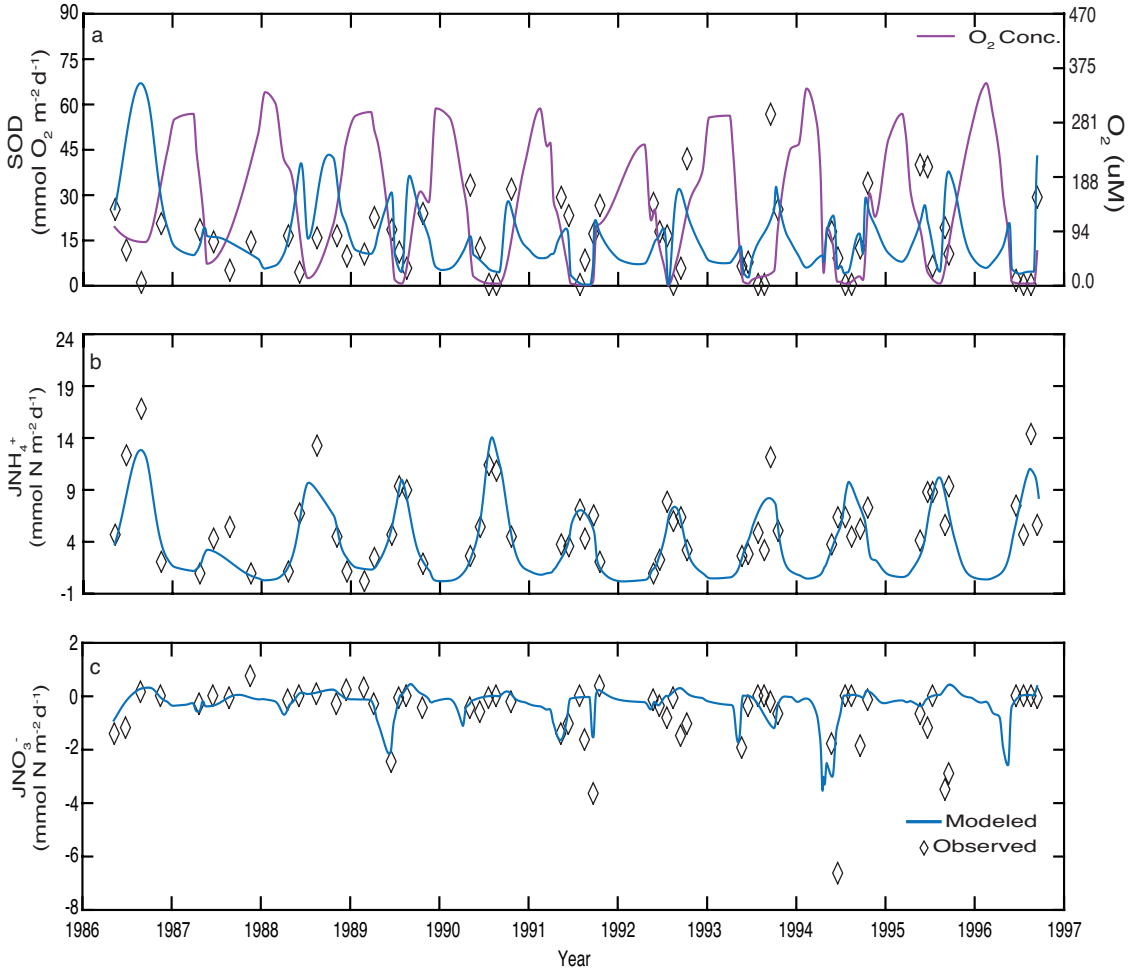

Figure 2.4 Station PNPT modeled and observed (a) sediment oxygen demand (SOD; left axis) and water column O_2 concentration (right axis), (b) NH_4^+ flux (JNH_4^+), and (c) NO_3^- flux (JNO_3^-). N fluxes are positive out of the sediment.

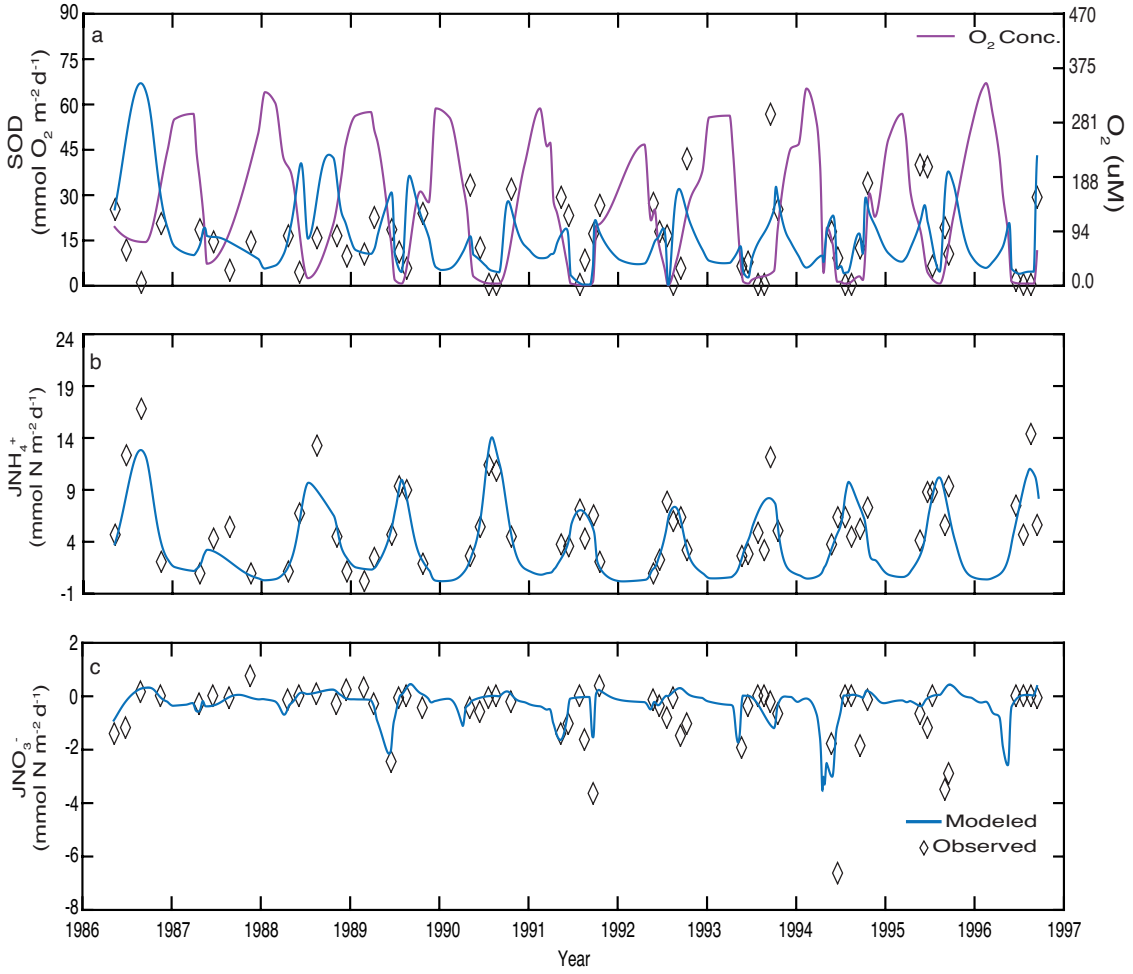

Figure 2.5 Station R-64 modeled and observed (a) sediment oxygen demand (SOD; left axis) and water column O_2 concentration (right axis), (b) NH_4^+ flux (JNH_4^+), and (c) NO_3^- flux (JNO_3^-). N fluxes are positive out of the sediment.

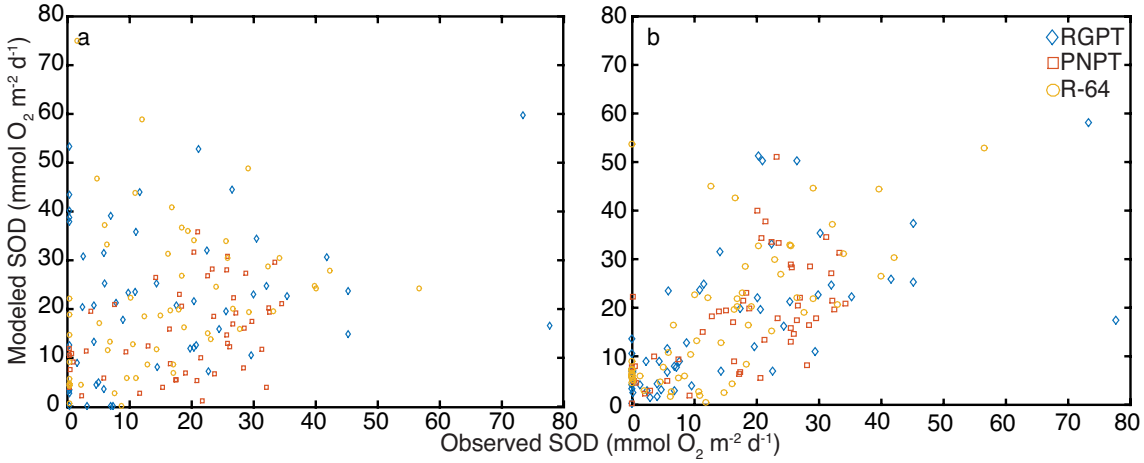

Figure 2.6 Modeled vs. observed sediment oxygen demand (SOD) for all three stations using (a) the Chesapeake Bay Program dissolved oxygen data or (b) the sediment oxygen and nutrient exchange (SONE; Boynton and Baily, 2008) incubation oxygen data for the overlying water column oxygen boundary forcing in SedDOM-SFM. SOD model skill is improved substantially by using the SONE data (r = 0.59, 100% improvement, MEF = 0.12, 121% improvement, RMSE = 12.15 mmol O_2 m^{-2} d^{-1}, 24.1% improvement)

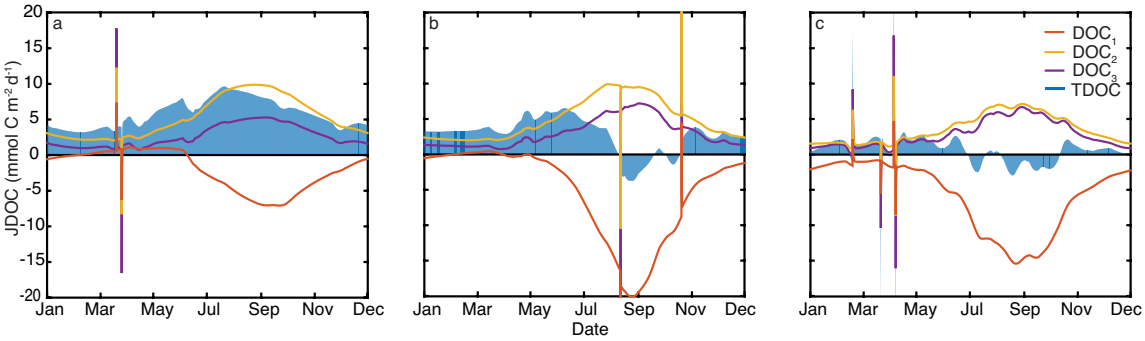

Figure 2.7 11-year average climatology dissolved organic carbon flux (JDOC) across the sediment layer 1 and overlying water column interface for (a) station R-64, (b) RGPT, and (c) PNPT. A positive flux is out of the sediment into the water column. DOC_1 is labile DOC, DOC_2 is semi-labile DOC, DOC_3 is refractory DOC and TDOC is the sum of all three reactivity classes. The shocks in each plot are due to discontinuities in the interpolated forcing.

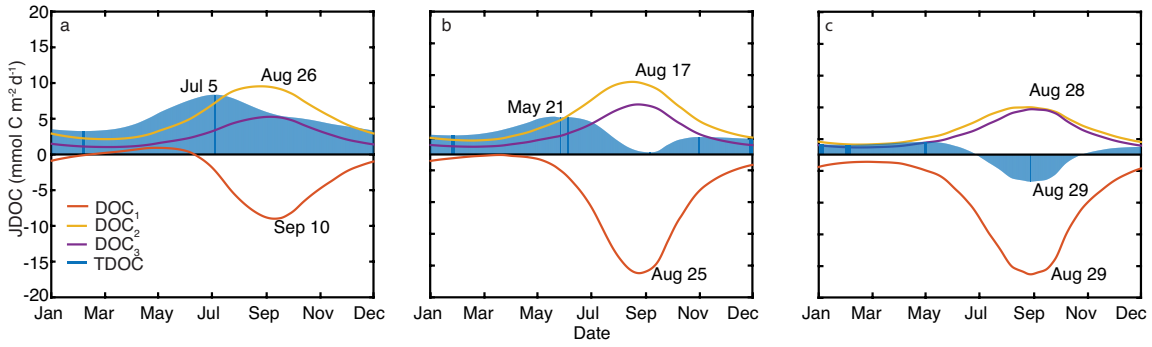

Figure 2.8 11-year averaged climatology of the three reactivity classes of dissolved organic carbon (DOC; G1, G2, G3) and the total (TDOC) flux out of the sediment for (a) station R-64, (b) RGPT and (c) PNPT. The dates on the plot are when peak flux rates are observed for DOC_1 and DOC_2 and total DOC (TDOC).

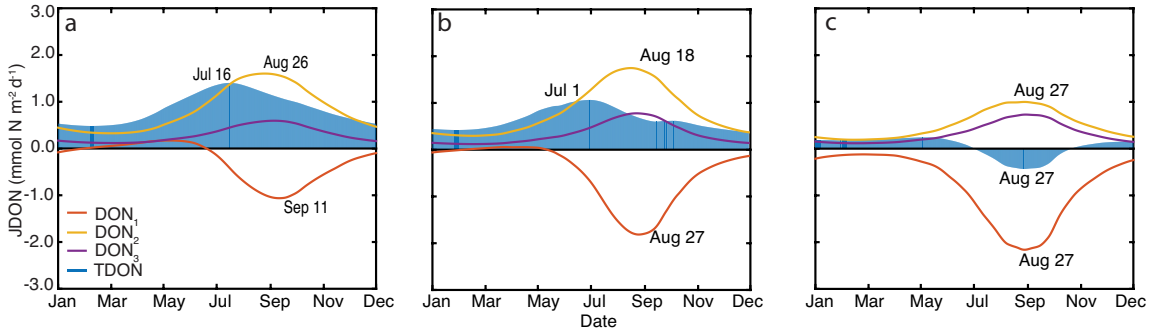

Figure 2.9 11-year average climatology of the three reactivity classes of dissolved organic nitrogen (DON; G1, G2, G3) and the total (TDON) flux out of the sediments for station (a) R-64, (b) Ragged Point and (c) PNPT. The dates on the plot are when peak flux rates are observed for DON_1 and DON_2 and total DON (TDON).

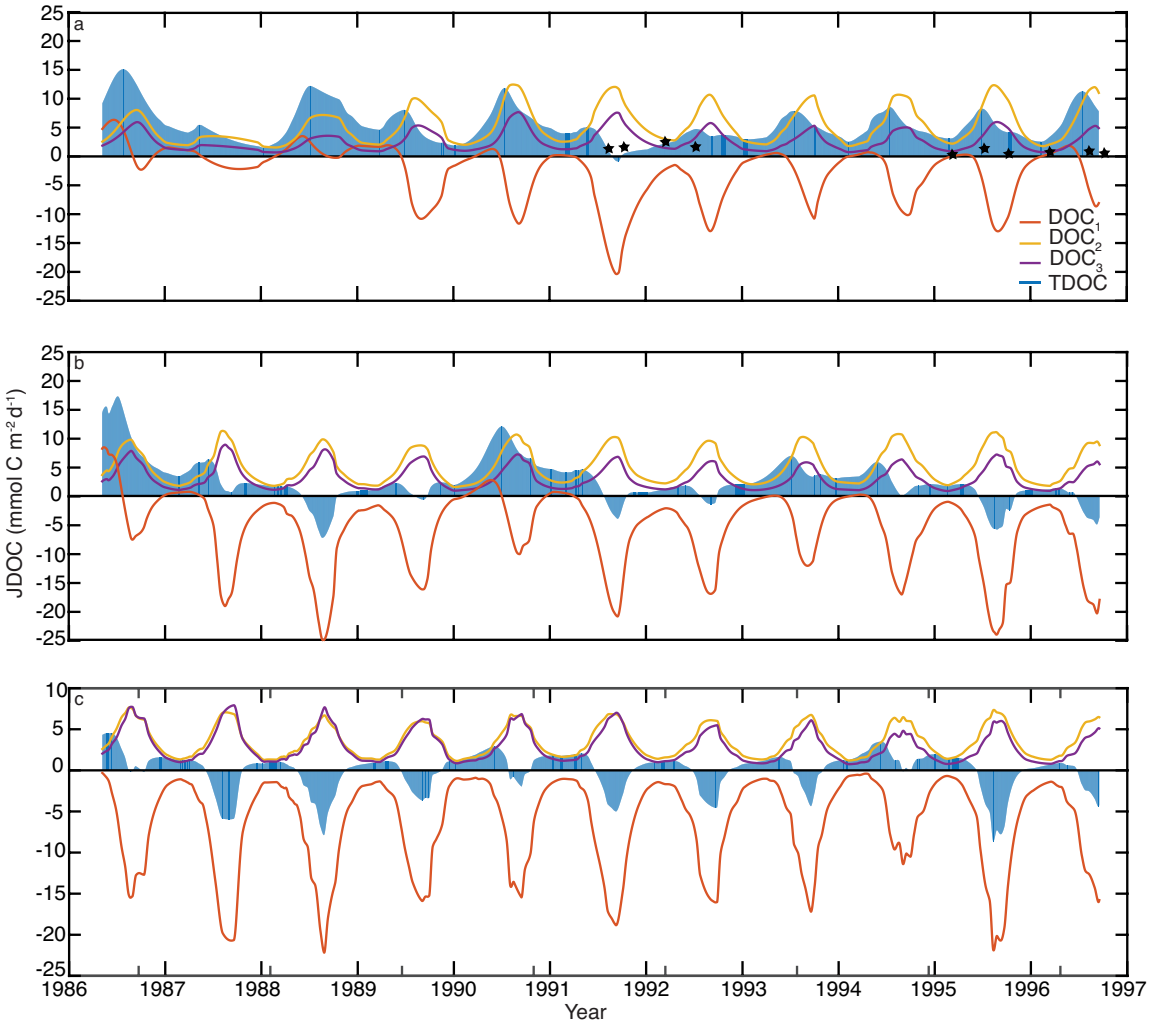

Figure 2.10 Time series of dissolved organic carbon flux (JDOC) across the sediment water interface for (a) stations R-64 (b) RGPT, and (c) PNPT. The total flux (TDOC) is the sum of the labile (DOC_1), semi-labile (DOC_2) and inert (DOC_3) fractions. Note the scale on (b) is different than that on (a) and (c). The stars on panel (a) in 1991-1992 (Burdige and Homstead, 1994) and 1995-1996 (Burdige and Zheng, 1998) are measured fluxes from a similarly located mid-channel Chesapeake Bay station.

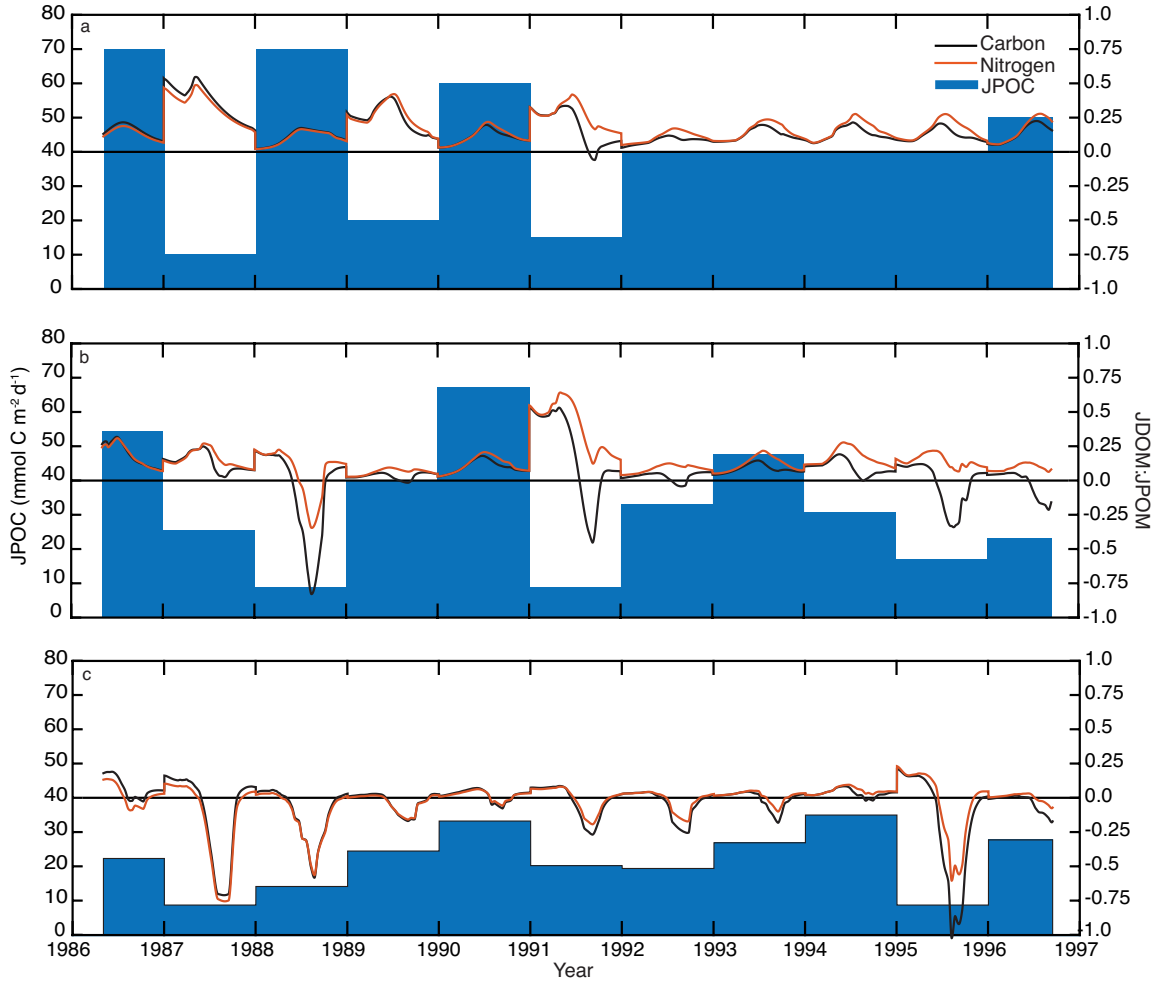

Figure 2.11 The forced modeled downward sinking particulate organic carbon (JPOC, left axis) for (a) station R-64, (b) RGPT, and (c) PNPT. The right axis is the fraction of JPOM (both organic carbon and nitrogen) that is either lost (positive) or gained (negative) out of the sediment as the dissolved organic matter flux (JDOM). Particulate organic nitrogen was forced with the same inter-annual variability as that of POC at a ratio of 6.6:1 POC:PON

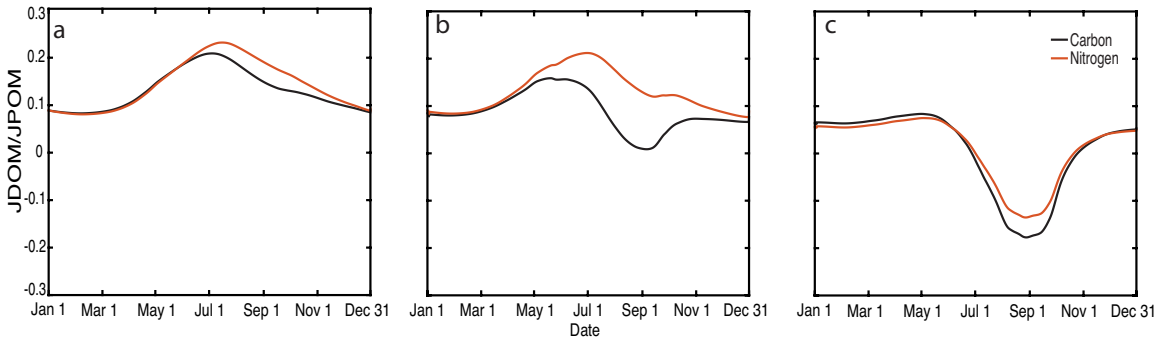

Figure 2.12 Annual average climatology of the fraction of particulate organic matter flux (JPOM; both organic carbon and nitrogen) that is either lost (positive) or gained (negative) out of the sediment as the dissolved organic matter flux (JDOM).

Tables Chapter 2

Table 2.1 Model parameters from Figure 2.1, and Equations 2.1 and 2.2

Parameter Description	Symbol	Value	units
$DOC_{1,2,3}$ Remineralization	$kD_{C,1,2,3}$ [c]	0.35, 0.030, 0.0	d^{-1}
$DON_{1,2,3}$ Remineralization	$kD_{N,1,2,3}$ [c]	0.4, 0.030, 0.0	d^{-1}
$POM_{1,2,3}$ Hydrolysis	$kP_{x,\ 1,2,3}$ [a,f]	0.01, $1.8x10^{-4}$, $5.0x10^{-6}$	d^{-1}
OM_1 temperature control	θ_1 [d,e]	1.10	unitless
OM_2 temperature control	θ_2 [d,e]	1.15	unitless
Diffusion temperature control	θ_D [d]	1.08	unitless
Sediment accretion velocity	ω [d,]	0.7	cm y^{-1}
Layer 1 and 2 diffusion coefficient	KL_{12} [a,b]	$5.0x10^{-4}$	$m^2\ d^{-1}$

a. Brady et al., 2013; Testa et al., 2013
b. 10x less for DOM, following Burdige et al., 2016
c. Parameters varied to find best model fit
d. Parameters fixed across all model runs
e. Same for both POM and DOM
f. Same for both PON and POC

Table 2.2 Model skill assessment metrics for SedDOM-SFM (DOM +) and SFM (DOM -) sediment oxygen demand (SOD), $NH\text{-}_4^+$ flux (JNH_4^+) and NO_3^- flux (JNO_3^-) when compared against SONE observations

DOM +	r [a,*]	MEF [c,*]	RMSE [c,*]
SOD	0.29	-0.55	16.77
JNH_4^+	0.77	0.47	2.09
JNO_3^-	0.58	0.28	0.88
DOM -			
SOD	0.32	-0.99	19.01
JNH_4^+	0.78	0.14	2.63
JNO_3^-	0.56	0.25	0.89
% Change			
SOD	-9.3	44.6	11.8
JNH_4^+	-0.86	244	20.6
JNO_3^-	2.96	13.5	1.12

a. coefficient of covariance
b. model efficiency
c. root mean square error
*Stow et al., 2009

Table 2.3 Model skill statistics for SedDOM-SFM with the overlying water column dissolved O_2 forcing obtained from the Sediment Oxygen and Nutrient Experiment (SONE) flux experiment data base and interpolated in time.

Station	Variable	r	MEF	RMSE (mmol N m^{-2} d^{-1})
R64	SOD	0.66	0.17	11.56
	NH4	0.79	0.57	2.35
	NO3	0.43	0.05	1.18
RGPT	SOD	0.52	0.06	16.66
	NH4	0.81	0.61	2.33
	NO3	0.72	0.52	0.84
PNPT	SOD	0.58	0.12	9.98
	NH4	0.70	0.21	1.63
	NO3	0.53	0.10	0.67
Mean value	SOD	0.59	0.12	12.73
	NH4	0.77	0.46	2.10
	NO3	0.56	0.22	0.90
Improvement SOD (%)		100.0	121.3	24.1

Table 2.4 Annual average benthic dissolved organic carbon (DOC) and dissolved organic nitrogen (DON) fluxes for the three stations with time variable overlying water column DOM forcing. The total (TDOC and TDON) is the sum of the three reactivity classes. All flux units are mol C or N m^{-2} yr^{-1}, and the TDOC:TDON ratio (C:N) is mol C mol N^{-1}. The forced Bottom water (BW) C:N ratio is also included.

	DOC_1	DOC_2	DOC_3	TDOC	DON_1	DON_2	DON_3	TDON	C:N	BW C:N
R-64	-0.94	1.89	0.97	1.92	-0.10	0.31	0.11	0.316	6.08	9.1
RGPT	-1.90	1.84	1.15	1.07	-0.19	0.30	0.13	0.24	4.46	9.7
PNPT	-2.30	1.27	1.06	0.03	-0.29	0.19	0.12	0.01	2.3	8.8
Mean	-1.71	1.67	1.05	1.00	-0.19	0.27	0.12	0.19	4.28	9.2

Table 2.5 Net fluxes for the three stations with time variable overlying water column DOM forcing; all fluxes are in mmol m^{-2} yr^{-1}. The % JDOC and % JDON is the 11-year averaged, time integrated net flux divided by the 11 year averaged, time integrated JPOM forcing.

Net Fluxes	JPOC	JPON	JDOC	JDON	% JDOC	% JDON
R-64	15.6	2.4	1.92	0.32	12.3	10.00
RGPT	13.74	2.07	1.07	0.24	7.79	6.28
PNPT	8.65	1.3	0.03	0.01	0.34	-6.92
mean	12.7	1.9	1.01	0.19	7.80	10.0

A mechanistic model of photochemical transformation and degradation of colored dissolved organic matter

3.1 Abstract

Photochemical degradation (PD) of colored dissolved organic matter (CDOM) is a key transformational process for both natural and anthropogenic DOM. A fully mechanistic model is presented that can simulate laboratory incubations of the controlled PD of marsh and estuarine derived CDOM. The model was designed and optimized to recreate the loss of absorbance for marsh low tide and estuarine samples, representing high molecular weight allochthonous and mid molecular weight estuarine CDOM. In the model, high specific absorbance fractions representative of marsh and estuarine CDOM are transformed into a low specific absorbance fraction representative of coastal ocean CDOM as well as non-colored fractions. The various transformations in the model have maximum apparent quantum yields (at 284 nm) that range from $3.22 \pm 1.75 \times 10^{-8}$ to 56.05 ± 21.5 (mmol C mol photons^{-1}), with non-colored DOM/ inorganic carbon production outpaced by inter-molecular organic carbon transformations. Model performance was tested using an independent incubation data set whereby experimental results of photobleaching of spectral absorbance at 300 nm were recreated with a Willmott model skill of 0.98 and mean percent error of -3.66%. The production of the low molecular weight photodegraded end member ranged from 0.59 to 4.86 μmol C L^{-1} hr^{-1}.

3.2 Introduction

Photochemical degradation of colored dissolved organic matter (CDOM) can affect the biological reactivity of dissolved organic carbon (DOC) (Aarnos et al., 2012; Miller et al., 2002; Moran et al., 2000; Reader and Miller. 2014; Smith and Benner, 2005), in addition to changing the optical properties and molecular composition of CDOM as it is transported away from its source (Helms et al., 2008; Tzortziou et al., 2011). In estuarine and coastal waters that are characterized by high amounts of strongly absorbing CDOM, photochemical alteration and degradation can substantially alter the distribution and ultimate fate of DOC. This is particularly the case for wetland derived CDOM which is both optically and chemically distinct and subject to significant alteration upon exposure to ultraviolet and visible light (Reader and Miller, 2014; Tzortziou et al., 2007, 2008, 2011). Up until now, however, few mechanistic estuarine and coastal carbon cycle models have accounted for the effects that photochemical alteration can have on the water column DOC pool. In addition, most models of the attenuation of light in estuarine and coastal waters account for CDOM absorbance based on a constant, decreasing exponential function whose spectral absorption shape does not change with increasing absorbed light energy (Del Vecchio and Blough, 2002; Gallegos et al., 1990; Gallegos et al., 2006; Rose et al. 2018; Twardowski et al., 2004). In reality, the shape and magnitude of absorption spectra of CDOM change as CDOM undergoes photochemical degradation during transport away from its source, primarily due to ultraviolet and visible light absorption (Helms et al., 2008). In regions where strong gradients of CDOM occur such as adjacent to tidal wetlands (Osburn et al., 2015; Tzortziou et al., 2011) and downstream of large rivers (Raymond and Spencer, 2015;

Spencer et al, 2013), an optical model that utilizes a constant CDOM spectral slope can't accurately capture the variations in absorption spectral shape and thus the transfer of absorbed light energy into changes in the DOC pool.

The lack of representation in current models is largely due to high levels of uncertainty regarding a key parameter, the apparent quantum yield (AQY), that relates the amount of light energy absorbed by DOC to its transformation into either dissolved inorganic carbon directly (Aarnos et al., 2012, 2018; Powers and Miller, 2015) or into DOC of a different biological reactivity (Aarnos et al., 2012; Miller et al., 2002; Reader and Miller, 2014). This uncertainty is likely a result of spatial heterogeneity in DOC composition and CDOM absorption in addition to complex mixing of different sources that contribute to the overall CDOM and DOC pool (Helms et al., 2008); attempting to encapsulate the spectral dependency of photochemical transformations for the thousands of compounds that compose CDOM into a single AQY is extremely challenging. Mechanistic modeling of CDOM and DOC and the biogeochemical processes that govern their distribution is thus a simplification, i.e., representative of the average of the total pool. Ambiguity and a lack of consistent spectral dependence across time and space limit the extrapolation of experimentally derived AQY's to systems outside of the geographic location and/or similar biogeochemical conditions.

This study presents a newly developed photochemical degradation model that simulates the transformation of CDOM due to the absorption of light in the UV-visible range (284-700 nm), simplifying a previously described conceptual model of the interactions of CDOM and biological reactivity of DOC (Reader and Miller, 2014). The model presented here is the first attempt at mechanistically representing photochemical

reactions in a way that can be incorporated into a full organic carbon cycle modeling system, the Integrated Compartment Model (ICM) (Cerco and Cole, 1993; Cerco and Noel, 2013). The absorption of light by CDOM results in changes in the overall DOC pool that correspond to hypothesized and observed changes in DOM molecular composition (Maizel and Remucal, 2017; Sharpless and Blough, 2014), absorption spectra, and biological reactivity. Experimental observations of CDOM and DOC photochemical degradation from a tidal marsh-estuary system in Chesapeake Bay, MD, USA inform the modeling effort and provide bounds for rates of transformations for the bulk CDOM and DOC pools (Logozzo, 2017). This allows the AQYs for CDOM to be estimated using an inverse modeling approach and also provides insight into the controlling factors when modeling the photochemical degradation of CDOM.

3.3 Methods

3.3.1 Photochemical degradation model

A new mathematical model was developed to mechanistically simulate the photochemical degradation of CDOM in an estuarine ecosystem, hereinafter DOM-PD. DOM-PD is included as a module in a full organic carbon-nutrient-phytoplankton water quality model originally developed to simulate Chesapeake Bay water quality and dissolved oxygen concentration, ICM (Integrated Compartment water quality Model, Cerco and Cole, 1993). In ICM, DOC is mainly loaded by marsh sediment-water column diffusion, riverine discharge, phytoplankton production, and subtidal sediment-water column diffusion. Non-colored DOC (DOC that doesn't absorb UV-Visible light) is not discussed in this research, as the DOM-PD is only constrained for the colored DOC dynamics in terms of photobleaching. In DOM-PD, colored dissolved organic carbon

(CDOC) pools are defined by optical properties related to the absorption of UV and visible light (Helms et al., 2008). A useful optical property is the absorption spectral slope ratio (SR) which is defined as the ratio of the slope of the log transformed spectral absorption between 275-295 nm and 350-400 nm (Helms et al., 2008). Increasing SR is indicative of a higher degree of photochemical degradation and a decrease in molecular weight (Helms et al., 2008).

Operationally, the model defines three types of CDOC. $CDOC_3$ represents marsh-derived compounds with a high DOC-specific absorption, or absorption per unit mass (m^2 mol C^{-1}), and primarily of a high molecular weight (HMW); this end-member was parameterized in our model using measurements at the outflow of the Global Change Research Wetland (GCREW) in the Rhode River, MD, USA. For the $CDOC_3$ pool, the SR is 0.845. $CDOC_2$ represents an estuarine fraction that has a lower specific absorption and higher SR (1.179; Figure 3.1a-c) compared to $CDOC_3$, and is assumed to primarily be composed of autochthonous-produced DOC and the photodegraded fraction of allochthonous DOC of a lower molecular weight compared to $CDOC_3$. $CDOC_1$ represents a low molecular weight (LMW) coastal ocean end member that has the lowest absorption and greatest SR (1.570; Figure 3.1d-f) and is also assumed to primarily be composed of autochthonous-produced DOC and some portion of the photodegraded fraction of allochthonous DOC. These pools are parameterized with absorption spectra that are derived from optical and chemical data collected across the wetland-estuarine-coastal ocean transition from the Chesapeake Bay to the mid-Atlantic continental shelf (Figure 3.1). This empirical approach limits our study to representing the CDOM absorption in Chesapeake Bay and the mid-Atlantic, but can be redefined to model other regions as

long as optical and DOC concentration data are available. The newly developed numerical modeling equations (Equations 3.1, 3.2 and 3.3) solve for the absorption of light at each wavelength by each CDOC pool and the conversion of absorbed light energy into CDOC transformations.

$$abs(\lambda)_i = CDOC_i \; a^{*}cdoc(\lambda)_i \tag{3.1}$$

Equation 3.1 specifies the spectral Naperian absorption coefficients, $abs(\lambda)_i$ (m^{-1}), associated with each CDOC pool (i=1-3) as equal to the product of the concentration of each $CDOC_i$ (mol C m^{-3}) and the spectral specific absorption $a^{*}cdoc(\lambda)_i$ (m^2 mol C^{-1}; Figure 3.2). $CDOC_i$ can't be directly measured in terms of its absolute concentration in mass per unit volume. Therefore, an estimate of the CDOC concentration for each pool is needed to estimate $a^{*}cdoc_i(\lambda)$. The results of the derivation of CDOC concentration and $a^{*}cdoc_i(\lambda)$ are in section 3.1. After Naperian absorption spectra are calculated using Equation 3.1 for each pool, they are passed to Equation 3.2 which defines $Iz_i(\lambda)$ (mols Photons m^{-2} s^{-1}), the total light energy absorbed across the UV-Visible wavelengths by each pool. $Iz_i(\lambda)$ is equal to the incident UV-Visible light energy, $Iz_0(\lambda)$ (mols Photons m^{-2} s^{-1}), scaled by the fraction of the total light energy that is absorbed by each CDOC pool which is equal to the Naperian absorption coefficient for each CDOC, $abs_i(\lambda)$, divided by the total absorbance, $abs_t(\lambda)$ (m^{-1}). The final term calculates the fraction of light that is absorbed over the exposure path length, Δz (m), using the common Beers-Lambert light absorbance formulation. Equation 3.2 follows previous work describing the contribution of each absorbing constituent to the overall absorbance of light (Hu et al., 2002; Stedmon et al., 2007). In general, total absorbance is composed

of the contributions from CDOM, phytoplankton, suspended solids and water. In this modeling study, only the absorbance of CDOM and water were considered but the results are still valid in the larger context when including CDOM as a water quality constituent. A summary of all the equations and terminology in the model is given in the Appendix.

$$Iz_i(\lambda) = Iz_0(\lambda)\frac{abs_i(\lambda)}{abs_t(\lambda)}(1 - e^{[-abs_t(\lambda)\Delta z]}) \tag{3.2}$$

Iz_i is then used in Equation 3.3 where the total amount of $CDOC_i$, that is photodegraded from fraction i (i=1-3) to fraction j (j=1,0 where 0 is NCDOC/DIC), $dCDOC_{i,j}\ dt^{-1}$ (mol C m^{-3} s^{-1}) is the integral over the incident irradiance wavelength range, λ_0 to λ_f, of the product of Iz_i and the apparent quantum yield (AQY) of the transformation from CDOC compound i to CDOC compound j, $AQY_{i,j}$ (mol C mol $Photons^{-1}$), at each λ. This formulation assumes that each CDOC pool captures the mean conditions for each source location and therefore the associated bulk molecular composition of the CDOC in terms of both absorption spectra and photoreactivity.

$$\frac{dCDOC_{i,j}}{dt} = \frac{\int_{\lambda_0}^{\lambda_f} Iz_i(\lambda)AQY_{i,j}(\lambda)d\lambda}{\Delta z} \tag{3.3}$$

Equation 3.3 is primarily based on studies conducted whereby the AQY is the amount of light energy that is converted into chemical changes in CDOM and is measured indirectly using DOC proxies (e.g., changes in microbial respiration or microbial biomass) (Miller et al., 2002; Reader and Miller, 2014) or directly using short lived DOC reactive intermediate compounds (Maizel and Remucal, 2017). For DOM-PD to accurately represent photobleaching, the most important step is estimating the AQYs

using the experimental data available from the Rhode River bench top photochemical degradation experiments.

3.3.2 Xenon arc photobleaching experiments

The AQY spectra for CDOC transformations were estimated based on changes in absorption spectra during laboratory exposures of CDOM samples from the GCREW and the Rhode River water column. The exposures used a special polychromatic incubator, the "photoinhibitron", similar to setups previously used for photochemistry and phytoplankton photosynthesis exposures (Kieber et al., 2014; Smyth et al., 2012). Briefly, irradiance from a 2.5 kW Xenon lamp is reflected off a front-surface mirror and directed vertically upward through various long-pass cutoff filters and then into sample aliquots (8 mL) in quartz and fused-silica cuvettes. There were six spectral treatments configured using WG280, WG295, WG305, WG320, WG335 (Schott technologies) and LG350 (SpectraPhysics) long-pass filters with five or six samples exposed to each treatment (average irradiances in Table 1), giving a total of 34 exposures in each experiment. The cuvettes were housed in slots (aluminum tubes) fitted into aluminum blocks machined to have a large internal chamber through which coolant was circulated around the slots to maintain temperature (20°C). All metal surfaces near the cuvette were anodized black to eliminate reflection so that exposure was limited to collimated irradiance from the lamp. Spectral exposure in each slot was measured using a custom-built fiber-optic spectroradiometer (Neale and Fritz, 2012). Exposures were conducted with surface water taken at low tide in a tidal creek draining the GCREW (Jul. 29, Aug. 12, and Aug. 20, 2015) and a point in the middle of the Rhode River estuary (dock of the Smithsonian Environmental Research Center, Aug. 17, 2015). Samples were filtered immediately

after collection sequentially through 0.7 glass fiber filters followed by 0.2 μm pore size nuclepore filters (Whatman) and distributed into cuvettes. Half of the cuvettes were exposed for 12 h, the rest for 24 h. A slot with blocked light served as a dark control. Unexposed sample was kept at 4 °C during the experiment. CDOM absorption in all exposed samples and controls was measured within 1 or 2 days after exposure (stored at 4°C until measured) using previously reported methods (Tzortziou et al. 2008; Logozzo, 2017).

3.3.3 Parameter and initial condition estimates

Spectral AQY parameters (both magnitude and slope) for each pathway in the DOM-PD model were estimated by iterative minimization of the summed squared differences between observed and predicted absorbance spectra. Computations were carried out in MATLAB R2017a using the function, *minimize.m*, version 1.7.0 written by Rody P. S. Oldenhuis, which is, in turn, based on the MATLAB functions *fminsearch* and *fminlbfgs*. Parameter values were iteratively incremented using the Nelder-Mead simplex algorithm. Parameters were constrained to be positive, and AQYs at 284 nm to be < 83 mmol C mol photons^{-1}. Convergence was considered when the step size in both the parameter vector norm and cost function was < 10^{-4}. Uncertainty in parameters was estimated using a "jack-knife" technique: The minimization was re-run *n* times deleting in sequence each one of the samples and using the reduced sample set to give a perturbed parameter set θ_i. The standard error (StdError) was then estimated using Equation 3.4 where *n* is the sample size and $\hat{\theta}$ is the mean of the *n* perturbed parameter sets.

$$StdError(\theta) = [\frac{(n-1)}{n}\sum(\theta_i - \hat{\theta})^2]^{\frac{1}{2}} \quad (3.4)$$

The initial CDOC concentration was estimated by assuming that the initial total $abs_t(\lambda)$ for each incubation can be represented as a linear composite of all three $a^*cdoc_i(\lambda)$. The coefficients of the linear model that minimized sum squared differences between observed and estimated spectra were set as the initial CDOC concentrations for each pool. The coefficients were estimated using the MATLAB function *lsqnonneg* with the constraint that all $CDOC_i \geq 0$. Initial conditions and full incubation information can be found in Table 2 and Table 3. For all GCREW low tide samples (all which were included in the initial definition of $CDOC_3$ [see section 2.2]), the best fit, as expected, was obtained using only $CDOC_3$. For the marsh high tide and estuarine samples, a mixture of all three CDOC classes gave the best fit.

Based on the representation of $CDOC_3$ and $CDOC_2$ by either the marsh low tide or the Rhode River initial condition estimate, each incubation set was used to define the AQYs originating from $CDOC_3$ (marsh low tide) or $CDOC_2$ (Rhode River) using the results from the Xenon lamp exposures. This implicitly assumes that the Rhode River incubations are representative of the estuarine mid-molecular weight end member, while the marsh low tide incubations are representative of the HMW marsh derived end member. This is a logical assumption given that each pool is optically defined based on data collected from either the same place at a different time ($CDOC_3$, GCREW) or a similar estuarine environment ($CDOC_2$; Chesapeake Bay). $CDOC_1$ is modeled as a combination of the breakdown of both $CDOC_3$ and $CDOC_2$ and therefore the removal of $CDOC_1$ to non-colored DOC or DIC was derived as the average $AQY_{1,0}$ from all the incubations combined.

To estimate the final treatment absorbance spectra, the sample initial $CDOC_i$ values in each model formulation were time-stepped (Δt=1 min) through the incubation period using the specific exposure conditions of each treatment. After the treatment period (12 or 24 h) was complete, the final $CDOC_i$ values were used to predict the absorbance spectra for that treatment and sum squared differences between the predicted and observed spectra were calculated. The cost function for each iteration was the grand sum squared differences for all treatment and sample spectra (34 each for the GCREW low tide and Rhode River estuary fits, 102 for the combined data set).

3.3.4 Model parameter testing with an independent PD incubation data set

In order to further assess the robustness and utility of the DOM-PD model, an independent test data set of photochemical degradation experiments from the Rhode River ecosystem across seasons (Logozzo, 2017) was simulated. Detailed methods were previously reported on incubation set up and chemical analysis for these experiments (Logozzo, 2017). Briefly, this set of PD incubations were forced with 17.9 W m^{-2} from a UV-blue wavelength emitting fluorescent lamp (Figure 3.3) over 7-10 day time periods across multiple seasons and locations. In this configuration, daily absorbed light energy was similar to the daily, depth-integrated absorbance in the Rhode River for a clear day in June (Logozzo, 2017). The four SERC Dock samples used for the test data set had an average SR of 1.195, which is very close to the average SR of the data set (1.186) used to generate the $CDOC_2$ specific absorption spectra based on measurements collected during the 2011 NASA GEOCAPE (Geostationary for Coastal and Air Pollution Events) cruise in the Chesapeake Bay (July 2011). Each of the 15 incubations were independently simulated using the AQYs derived from the Xenon lamp exposures. The fit of the model

to the independent test set was assessed using multiple model skill metrics (Stow et al., 2009) comparing observed vs. predicted final CDOM absorbance at 300 nm (a300 m^{-1}) to measure model performance for each test incubation. In addition, CDOM absorbance spectra were measured at daily intervals for two of the incubations, which provided a qualitative comparison with the modeled kinetics.

3.4 Results and Discussion

3.4.1 Derivation of colored dissolved organic carbon (CDOC) specific absorption spectra

CDOM absorption spectra and DOC concentration data collected from the GCREW Creek, MD, USA in the summer of 2015 and 2016 were used to parameterize the allochthonous, marsh derived $CDOC_3$ pool. Analytical methods that were used for determining CDOM absorption spectra and DOC concentration have been previously reported (Tzortziou et al., 2008; Logozzo, 2017). To estimate the marsh $CDOC_3$ concentration, the CDOM absorbance at 355 nm (a355, m^{-1}) was ordinary least squares regressed against measured DOC concentration across five 24 hour periods in July and August, 2015 and June, July, and August, 2016 (n=113; Table 4) (Figure 3.4a). The y-intercept of each individual regression, when a_{355} is equivalent to zero, was defined as the background non-colored DOC (NCDOC) for each sampling period (Table 4). The NCDOC was subtracted from the total DOC at each time point to yield the CDOC. This method implies that for this study any DOC that absorbs light only at wavelengths less than 355 nm is non-colored. Hereinafter, NCDOC refers to DOC that only absorbs light into the UV-B range. 355 nm was used as the cutoff to be consistent with the measurements of a355 and DOC concentration in the two NASA data sets used below. If

300 nm was used instead as the cutoff for the $CDOC_3$ pool, the estimated $CDOC_3$ would increase by 7.8%, on average, which would decrease the specific absorption by a similar proportion. This in turn would cause the AQYs to increase because there is less light being absorbed per unit carbon with the same amount of CDOC transformation. This implies that with the $CDOC_3$ specific absorption estimated using 355 nm as the cutoff the AQYs are relatively conservative.

Conditions that best represented the time points when marsh derived DOC was at its highest relative concentration were only included in the $CDOC_3$ specific absorption spectra. To do this, the SRs for each time point were sorted into quartiles and the SRs for each time period that were in the lowest quartile (i.e., most marsh-like) were identified (n=28). At these time points, the CDOM absorption spectra were divided by each associated CDOC concentration estimate to yield 28 individual CDOC specific absorption spectra. These spectra were then averaged to yield the $CDOC_3$ specific absorption spectra that were used to parameterize DOM-PD (Figure 3.2).

The other two CDOC classes were defined using National Aeronautics and Space Administration (NASA) cruise data (CLiVEC cruise in the mid-Atlantic and GEOCAPE in Chesapeake Bay) that were downloaded using the NASA SeaBASS data hub (Werdell et al., 2003) and a processing script that extracted and sorted the data into a table. Information on the NASA DOC and CDOM measurement methods has been summarized previously (Mannino et al., 2008). Water samples collected in mid Chesapeake Bay defined the estuarine $CDOC_2$ (Figure 3.1a-c), while samples collected on the Mid-Atlantic continental shelf defined the coastal ocean $CDOC_1$ end member (Figure 3.1d-f).

DOC concentration at each station was averaged to get an average station DOC concentration for use in the CDOC estimating procedure.

$CDOC_1$ and $CDOC_2$ concentration was estimated for each location using a similar procedure as above (Figure 3.4b,c). The data from the GEOCAPE cruise ($CDOC_2$; n=61) had a calculated background of 119.3 μM NCDOC (Table 4). For the CLIVEC cruise ($CDOC_1$; n=398), a background NCDOC concentration of 50 μM was used instead of the regressed value of 72. The linear regression was much less robust than the wetland and estuarine data set (Figure 3.4c) and if the regressed intercept was used, then there were values that ended up with an unreasonably high $a^*cdoc(\lambda)$ which skewed the mean to be greater than that at the wetland. Open ocean DOC has virtually zero absorbance at wavelengths longer than 355 nm (Helms et al., 2008), defined for this study as the cutoff wavelength for CDOM, and a background of 50 μM is a good approximation of the average concentration of open ocean DOC. Differences in the y-intercept were trivial depending if 280 or 355 nm was used as the cutoff, ranging from 70-72 μM C, and the linear relationships always had a R^2 value < 0.09.

3.4.2 Xenon Arc Photobleaching Experiments

Irradiance exposures of samples in the photoinhibitron with the different cutoff filters varied from 0 to 13 W m^{-2} UVB (280-320 nm), 44 to 107 W m^{-2} UVA (320-400 nm) and 239 to 473 W m^{-2} of PAR (Table 1). Depending on the duration of exposure and filter type, the absorbed photons ranged from 0.8 to 31 moles, which resulted in a decrease in a300 from negligible to almost 70%. Relative photobleaching has an approximately linear relationship with absorbed photons (Figure 3.5). The slope of this relationship was steeper for the high tide and Rhode River samples compared to low tide

samples. In other words, it took fewer absorbed photons to produce a given percent photobleaching of high tide/Rhode River CDOM compared low tide CDOM. Another general metric of photobleaching is absolute photoreactivity, estimated as the average change in absorption over the range 280-500 nm divided by the total absorbed energy (expressed as m MJ^{-1}). This was 2.0 m MJ^{-1} for a representative low tide sample, which is comparable to that reported for the GCREW CDOM photobleaching by solar irradiance (Tzortziou et al., 2008). Even though relative photobleaching was strong, absolute photoreactivity was low for the high tide (1.3) and Rhode River (0.8) samples, comparable to the low photoreactivity samples in similar exposures of lake CDOM (Osburn et al., 2001). These contrasting results are due to the much lower average absorbance in the high tide and Rhode River samples compared to low tide.

For both relative photobleaching and absolute photoreactivity, the response of high tide and Rhode River CDOM samples are similar. This indicates that the marsh high tide samples have a high content of estuarine-like DOM. At high tide and in the estuary, the average molecular weight, absorptivity and DOC concentration is less (Tzortziou et al., 2008), coinciding with the predicted decrease in absolute photoreactivity. Changes in photoreactivity appear to be driven by changes in source DOM, which was previously correlated with molecular weight (Helms et al., 2008; Tzortziou et al., 2008), and thus corresponds well with the conceptual model used in designing DOM-PD. The relationship of source material and photoreactivity as it relates to molecular weight and absorption spectra characteristics has also been observed across an estuarine gradient (Helms et al., 2008) and in DOM samples from different environments (Maizel and Remucal, 2017). Therefore, the model formulation presented

here appears to be a robust approximation of CDOM photodegradation in an estuarine environment where photochemistry is important in DOM transformations.

3.4.3 AQY magnitude and slope Parameter estimation

The best-fit parameter sets of the DOM-PD for the two locations resulted in consistent predictions over all treatments and exposure periods (Figure 3.6). The mean percent error between predicted and observed absorbance at 300 nm was 6-7%. Prediction was unbiased for both 12- and 24-hour exposures, suggesting that simple, first-order kinetics are justified for the exposure range encompassed by these experiments. Fitted parameters for selected AQY spectra are given in Table 5. Jack-knife estimates of the standard errors suggested that the slopes are tightly constrained by the fits, but AQY at 284 are less tightly constrained. The AQY for the conversion to NCDOC/DIC, which are substantially lower than the other AQY, have a high degree of uncertainty (relative to their magnitude) (Table 5). The $CDOC_3$ and $CDOC_1$ pools are largely driving the conversion of total CDOC to NCDOC/DIC, although the standard error range is larger than the predicted AQY. The full spectral plots of each AQY are in Figure 3.7. Figure 3.7 also shows an updated model conceptualization with the magnitude of each arrow scaled to the AQYs.

The AQYs estimated here can be compared to measured values from other experimental designs whereby the AQY is directly measured or inferred from the production of intermediate compounds. First, a comparison of the predicted rate of NCDOC/DIC creation ($AQY_{i,0}$) can be directly compared to measurements of CO and CO_2 AQYs derived experimentally (Powers and Miller, 2015). Qualitatively, maximal $AQY_{i,0}$ ($AQY_{3,0}$+$AQY_{1,0}$, 1.77±0.97 mols C mol photons^{-1}) falls within the same order of

magnitude of a large range of reported values for CO_2 AQYs in coastal (Powers and Miller, 2015) and river/estuarine waters (Aarnos et al., 2018). The slope estimated from DOM-PD (-0.0206±0.0015 nm^{-1}) is relatively shallow, but there is substantial variability in slopes of DIC AQY (Aarnos et al., 2018; Powers and Miller, 2015). Recently reported DIC AQYs at 330 nm measured from the St. Lawrence River estuary range from 0.116 at the mouth to 0.231 mmol C $(mol\ photons)^{-1}$ at the head, and up to 0.335 mmol C $(mol\ photons)^{-1}$ in the Mississippi river (Aarnos et al., 2018). The total $AQY_{i,0}$ at 330 nm derived using DOM-PD of 0.410 mmol C $(mol\ photons)^{-1}$, the majority of which is occurring from the $CDOC_1$ pool, would be larger than the measured values but not unreasonable considering marsh derived DOC is extremely fresh and photoreactive and in the large river systems there would be previous exposure during river transport.

If light exposure time in DOM-PD is considered as a proxy for environmental transport away from the HMW source and an increase in salinity along an estuary gradient, without supplementation from other marsh/HMW sources the photoproduction of NCDOC/DIC would decrease rapidly with increasing salinity. This is not due to a lack of photoreactivity in LMW compounds, but due to the decreasing concentration. This suggests that a lack of relationship between DIC photoproduction and salinity (Powers and Miller, 2015) indicates the presence of autochthonous sources of HMW photoreactive compounds in estuarine and coastal ocean systems along a salinity gradient, or additional inputs from fringing wetlands or runoff. DIC photoproduction should decrease as a parcel of water moves offshore and the HMW compounds are removed relatively quickly, which is seen along the St. Lawrence River (Aarnos et al., 2018).

Comparing the colored AQY pathways ($AQY_{3,1}$ and $AQY_{2,1}$) to measured quantities is difficult because of the abstraction made to parameterize DOM-PD; real world comparisons don't exist because $CDOC_{3\text{-}1}$ represents many thousands of compounds across a large environmental gradient. It is reasonable that estuarine, lower molecular weight (greater SR and less specific absorption) CDOC would have a larger AQY relative to HMW, marsh derived compounds. Recently reported laboratory experiments show that the rate of triplet DOM formation during irradiation increases with decreasing molecular weight when using model DOC mixtures that represent high molecular weight allocthonous sources and lower molecular weight autochthonous sources (Maizel and Remucal, 2017). This phenomenon is attributed to photochemical quenching in compounds with HMW (and high aromaticity) allowing much of the absorbed light energy to dissipate rather than transferring the energy into chemical reactions at molecular sites that are more vulnerable to photoreactions. The emergent AQYs of our model are consistent with these findings if $CDOC_3$ and $CDOC_2$ pools are considered as proxies for size-fractionated samples of allochthonous ($CDOC_3$) and autochthonous ($CDOC_2$) DOM.

3.4.4 Model evaluation with an independent photobleaching data set

An independent evaluation of DOM-PD and the associated parameters derived from the Xenon lamp incubations was conducted using fifteen individual photodegradation experiments (Figure 3.8). In all experiments, initial and final a300 values were measured (Figure 3.8a), in addition to two samples (one for marsh-derived and one for estuarine DOM) where daily time series data were measured (Figure 3.8b). Model-data comparison of final a300 shows a robust and tight fit, indicating that for the

Rhode River, across seasons and locations (including far from the marsh near the main stem of Chesapeake Bay), the model performed well in capturing the removal of CDOM absorbance. The model efficiency (MEF) has a value of 0.94, indicating that DOM-PD has very high predictive capacity (a value of 0.0 would indicate the model has no better predictive capacity vs. the mean, a value of 1.0 is a perfect fit) (Stow et al., 2009). The mean percent error of -3.66% indicates a strong overall fit to the data, with a slight over photobleaching bias primarily at marsh low tide samples taken in the summer when CDOM absorption and DOC concentrations at the marsh creek tend to be greatest. Time series of a300 removal of summer time marsh high and low tide water also indicate a slight over-bleaching bias although DOM-PD captured the general trend in the change in a300 over time (Figure 3.8b).

Time series of each CDOC class for average estuary (Figure 3.8c) and marsh low tide (Figure 3.8d) conditions over the seven day numerical incubation show how each sample location differs in terms of the relative change of each pool over time. The loss of absorption in both samples was due to transformations of carbon from the higher molecular weight pools into $CDOC_1$. The maximal rate of change for each CDOC pool and the total CDOC (sum of all three pools) can be estimated by taking the temporal derivate, $dCDOC\ dt^{-1}$, over the course of the incubations. The average estuarine incubations (Figure 3.9a) show some loss of CDOC to NCDOC/DIC (0.091 μmol C L^{-1} hr^{-1}) while the average marsh low tide incubation (Figure 3.9b) lost 0.20 μmol C L^{-1} hr^{-1} at maximum photobleaching. For comparison, St. Lawrence River estuary freshwater and coastal ocean end members have a measured DIC photoproduction rate of 0.582 ± 0.121 and 0.065 ± 0.121 μmol C L^{-1} hr^{-1}. Over the course of the average-condition estuary and

marsh low tide incubations (Figure 3.8c-d), 13.49 (11.4%) and 26.98 (9.56%) μmol C L^{-1} was lost to NCDOC/DIC, respectively. For the average estuary condition, maximal DOC loss to NCDOC/DIC occurred at 139.9 hrs (5.8 days) into the incubation, while for the marsh low tide sample it occurred at 168 hrs (7 days). The maximal production in the marsh low tide sample occurred at 190 hrs (7.9 days) when the model run time was increased to one year to see the long-term degradation of CDOC into NCDOC/DIC (recall that daily absorbed photons in the incubation were configured to be similar to that occurring in the Rhode River). The marsh low tide DOC had a half life of 36.2 days, and after one year only 0.035% of the DOC remained. DOM-PD suggests that it is not the initial marsh derived compounds that are directly producing the most DIC/NCDOC, but the product of the initial photobleaching reaction, $CDOC_1$, that contributes most to the net loss of CDOC. There is less DIC/NCDOC being produced in the estuary not because of less photoreactivity, but because there is less total concentration of CDOC, in addition to less light absorption per unit $CDOC_1$.

Photochemical degradation can drive changes in microbial availability of DOC across inland water ecosystems. Incorporating this important DOC cycling phenomena into a modeling framework is of particular interest. Although biological reactivity is not specified in DOM-PD presented here, if the breakdown of $CDOC_3$ and $CDOC_2$ to $CDOC_1$ is considered as the production of a more biologically available end member the model predicted rates can be compared to measured rates of biologically labile photoproduct (BLP) formation from laboratory incubations (Reader and Miller, 2014). The maximal rate of $CDOC_1$ production in DOM-PD was 1.54 and 3.73 μmol C L^{-1} hr^{-1}, and over the entire incubations 62.40 and 226.2 μM C of $CDOC_1$ was produced for the

average estuary and marsh low tide incubations, respectively. The simultaneous production and destruction of BLPs has been proposed as a potential explanatory pathway for difficult to interpret patterns of BLP formation observed in similar marsh-estuary ecosystems (Reader and Miller, 2014). In DOM-PD, the destruction of CDOC is only represented as a loss to NCDOC/DIC. The net destruction of the $CDOC_1$ pool does occur, but only after nearly all of the $CDOC_2$, and $CDOC_3$ was exhausted. Maximum net loss of $CDOC_1$ occurred at 12.5 and 15.8 days for the average estuarine and marsh low tide incubations, respectively. This suggests that as a parcel of water moves away from a marsh DOM source, net loss of microbially labile DOC can occur and photochemical degradation can decrease microbial production via loss of labile DOC. The full carbon cycle model contains NCDOC as a state variable and the pathway from $CDOC_{1,2}$ to more biologically refractory pools of NCDOC does exist. The reason more pathways are not currently included in DOM-PD is the lack of data to constrain highly non-linear processes. In its current state, DOM-PD does a satisfactory job of recreating the experimental data available while reasonably coinciding with observations from various coastal ecosystems throughout the globe (Aarnos et al., 2018).

The uncertainty around the model parameters was assessed by running the model for the average estuary and marsh low tide test incubation conditions using the upper and lower values of the jackknife standard errors for each parameter (Table 5). AQYs that would be less than zero when the standard error is subtracted from the best-fit AQY were set to zero as a negative AQY is not physically possible. In addition, the specific absorption spectra were also varied by a factor of 2. The total CDOC concentration at the end of the incubation was largely insensitive to parameter variations, with the greatest

difference in total DOC concentration of 22.4 μM C occurring between the lower AQY and upper AQY range in the average marsh condition (Table 6). All other test parameter sets exhibit a very narrow range of final total CDOC concentrations in both the marsh and the estuary average conditions. The standard deviations of final concentrations were 8.83 and 16.94 μM C (8.46% and 6.64% of baseline total CDOC) for the average estuary and marsh conditions, respectively, for all the test parameter sets. The final total a300 was also relatively insensitive to variations in the AQY slope and magnitude with a standard deviation of 1.62 and 3.81 (m^{-1}). The distribution of the CDOC concentrations among the three classes is changed slightly, with more $CDOC_3$ remaining in the low AQY test runs at the end of the incubations.

Altering the specific absorption spectra magnitude has a much more significant effect than the other parameters on the final CDOC distribution but even more so on the total a300. Increasing the specific absorption by a factor of 2 increased the final a300 by 3.09 and 7.44 (m^{-1}) in the estuary and marsh conditions, while decreasing the specific absorption by a factor of two led to a decline in final a300 by 1.84 and 3.95 (m^{-1}), respectively. Increasing specific absorption increases total photochemical reactivity and thus decreases the high molecular weight, more absorbing CDOC pools. However, because the specific absorption spectra are used directly to calculate total absorbance as the product of CDOC, the final total absorption increases substantially even though there are less of the more absorbing pools. For example, in the marsh low tide incubation there was 14.48 μM C less $CDOC_3$ due to more photons being absorbed per unit carbon thus leading to more photochemical degradation, but absorption increased to 18.91 (m^{-1}). This highlights the importance of having a robust data set to parameterize the specific

absorption spectra for a given environment; full absorption spectra and DOC concentration are needed to properly parameterize DOM-PD, and in general to characterize the non-colored and colored DOC pools.

3.5 Conclusions

DOM-PD was able to reasonably estimate the AQY magnitude and slope using a training data set from highly controlled photochemical degradation experiments. Maximal apparent quantum yields range from $3.22 \times 10^{-8} \pm 1.75$ to 56.05 ± 21.5 (mmol C mol photons^{-1}), with non-colored DOM/ inorganic carbon production outpaced by inter-molecular organic carbon transformations. The model was applied to an independent test incubation data set whereby experimental results of photobleaching of spectral absorbance at 300 nm were recreated with a Wilmott model skill of 0.98 and mean percent error of -3.66%. The production of the low molecular weight photodegraded end member ranged from 0.59 to 4.86 μmol C L^{-1} hr^{-1}. The half-life of the marsh derived $CDOC_3$ was 36.2 days with only 0.035% of the total CDOC remaining after 1 year. The high model skill, relative flexibility, and robustness of the model parameterization indicates DOM-PD has reasonable ability to simulate photodegradation across coastal ecosystems. The most important parameter is the CDOC specific absorption spectrum, which can be estimated using observational data from the representative ecosystem.

The successful development, parameterization and application of DOM-PD shows that a first order approximation of photochemical degradation kinetics is possible, and that the dominant transformation pathways to consider are those between separate pools of DOC rather than the production of DIC/NCDOC. The production of DIC is of course important, especially as more marsh derived DOC is degraded and transported through

the estuary. The application of DOM-PD to other systems where parameterization data for $a^*cdom(\lambda)$ are available will allow further model development and validation. The modeling framework described here can now be fully incorporated in bio-optical models to simulate not only the effects of CDOM absorption on light attenuation, but also the resulting effects on spectrally dependent optical properties and carbon transformation. Furthermore, implementation of this novel mechanistic photochemical model into a larger carbon cycle modeling framework in ecosystems where photochemistry has an important control on the distribution and fate of DOC is now possible. Accurately representing changes in CDOM absorption magnitude and spectral shape due to photochemistry will lead to better representation of the role CDOM plays in underwater light attenuation in optically complex coastal waters and quantification of fluxes and fate of DOC in coastal and open ocean environments.

3.6 Acknowledgments

I would like to acknowledge the National Aeronautics and Space Administration SeaBASS data hub for the open access research cruise database that was used to generate model parameters, to Andrew Peresta and other members of the Global Change Research Wetland group at the Smithsonian Environmental Research Center for assistance in acquiring field data, and Laura Logozzo for access to and help with using her Masters Thesis (City University of New York, 2017) incubation data. I would also like to acknowledge my collaborators on this research project including Maria Tzortziou, Fang Cao and Patrick J. Neale for conducting the photobleaching experiments used to parameterize the model, and Raleigh R. Hood. Data used to generate the model parameterization and the model formulations in the form of MATLAB scripts are available from the corresponding author upon request. This research was supported by NASA Grant NNX14AP06G and a fellowship awarded to JBC from Horn Point Laboratory.

3.7 Appendix

$$Iz_i(\lambda) = Iz_0(\lambda)\frac{abs_i(\lambda)}{abs_t(\lambda)}\left(1 - e^{[-abs_t(\lambda)\Delta z]}\right) \quad (1)$$

$$abs_i(\lambda) = CDOC_i\ a^* cdoc_i(\lambda) \quad (2)$$

$$abs_t(\lambda) = abs_w(\lambda) + \sum_{i=1}^{3} abs_i(\lambda) \quad (3)$$

$$\frac{dCDOC_{i,j}}{dt} = \frac{\int_{\lambda_0}^{\lambda_f} Iz_i(\lambda)AQY_{i,j}(\lambda)d\lambda}{\Delta z} \quad (4)$$

$$\frac{dCDOC_1}{dt} = \frac{dCDOC_{3,1}}{dt} + \frac{dCDOC_{2,1}}{dt} - \frac{dCDOC_{1,0}}{dt} \quad (5)$$

$$\frac{dCDOC_2}{dt} = -\frac{dCDOC_{2,1}}{dt} - \frac{dCDOC_{2,0}}{dt} \quad (6)$$

$$\frac{dCDOC_3}{dt} = -\frac{dCDOC_{3,1}}{dt} - \frac{dCDOC_{3,0}}{dt} \quad (7)$$

$$\frac{dNCDOC}{dt} = \frac{dCDOC_{1,0}}{dt} + \frac{dCDOC_{2,0}}{dt} + \frac{dCDOC_{3,0}}{dt} \quad (8)$$

Variable/ Parameter	Description	Value	Units
$Iz_i(\lambda)$	Photon flux absorbed by $CDOC_i$ (1-3) at wavelength λ	calculated	mols photons m^{-2} s^{-1} nm^{-1}
$Iz_0(\lambda)$	Surface (above) total photon flux at wavelength λ	calculated	mols photons m^{-2} s^{-1} nm^{-1}
$abs_i(\lambda)$	Absorption coefficient of $CDOC_i$ (1-3) at wavelength λ	calculated	m^{-1}
$abs_w(\lambda)$	Absorption coefficient of water at wavelength λ	calculated	m^{-1}
$abs_t(\lambda)$	Total absorption coefficient at wavelength λ	calculated	m^{-1}
Δz	Exposure pathlength	0.04	m
$a^*cdoc(\lambda)_i$	Specific absorption of $CDOC_i$ (1-3) at wavelength λ	Figure 3.2	m^2 mols C^{-1}
$CDOC_i$	Concentration of $CDOC_i$ (1-3)	calculated	mols C m^{-3}
$dCDOC_{i,j}\, dt^{-1}$	Transformation rate of $CDOC_i$ (1-3) to DOC_j (0-3 with 0 being to non colored DOC/DIC	calculated	mols C m^{-3} s^{-1}
$AQY_{i,j}(\lambda)$	Apparent quantum yield of $CDOC_i$ (1-3) to DOC_j (both colored and non-colored, 1-3)	Figure 3.7	mol C mols $photons^{-1}$
$dCDOC_1\, dt^{-1}$	Total rate of change of colored DOC_1	calculated	mols C m^{-3} s^{-1}
$dCDOC_{3,1}\, dt^{-}_{1}$	Transformation rate of colored DOC_3 to DOC_1	calculated	mols C m^{-3} s^{-1}
$dCDOC_{2,1}\, dt^{-}_{1}$	Transformation rate of colored DOC_2 to DOC_1	calculated	mols C m^{-3} s^{-1}
$dCDOC_{1,0}\, dt^{-}_{1}$	Transformation rate of colored DOC_2 to non-colored DOC and DIC	calculated	mols C m^{-3} s^{-1}
$dCDOC_2\, dt^{-1}$	Total rate of change of colored DOC_2	calculated	mols C m^{-3} s^{-1}
$dCDOC_{2,0}\, dt^{-}_{1}$	Transformation rate of colored DOC_2 to non-colored DOC and DIC	calculated	mols C m^{-3} s^{-1}
$dCDOC_3\, dt^{-1}$	Total rate of change of colored DOC_3	calculated	mols C m^{-3} s^{-1}
$dCDOC_{3,0}\, dt^{-}_{1}$	Transformation rate of colored DOC_3 to non-colored DOC and DIC	calculated	mols C m^{-3} s^{-1}
$dNCDOC\, dt^{-}$	Total rate of change of non-colored DOC/ DIC	calculated	mols C m^{-3} s^{-1}

Figures Chapter 3

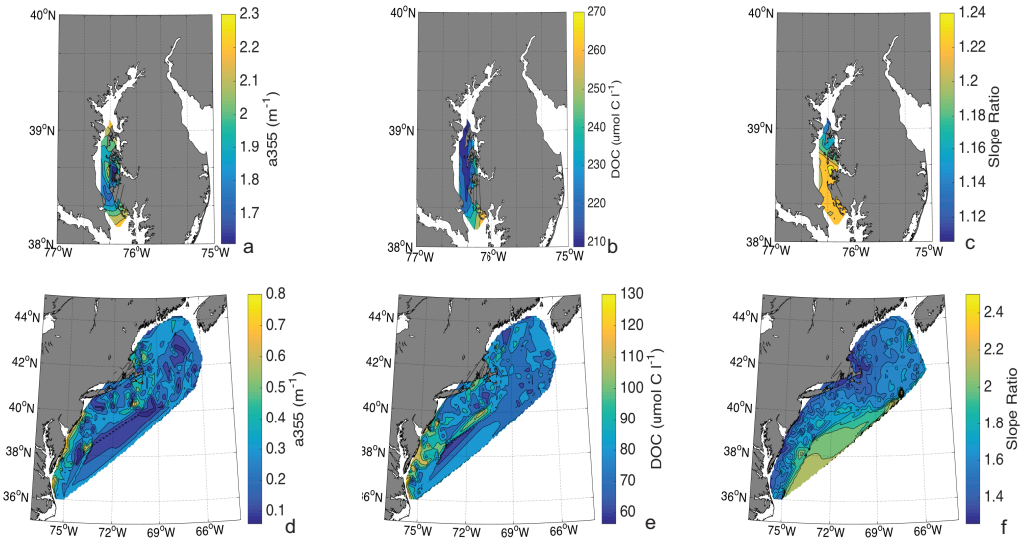

Figure 3.1 Chesapeake Bay (a-c) and mid-Atlantic Bight (d-f) absorption at 355 nm (a355), dissolved organic carbon concentration (DOC), and spectral absorption slope ratio (SR) used to parameterize the specific absorption for colored DOC_2 and colored DOC_3. SR is the ratio between the slope of the absorption spectra in the 275-295 nm region and the 350-400 nm region.

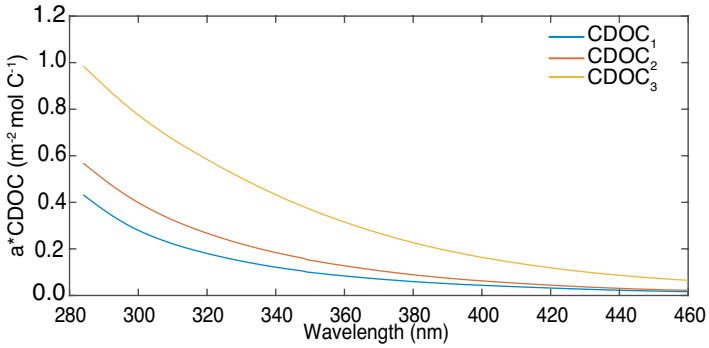

Figure 3.2 Colored dissolved organic carbon (CDOC) specific absorption spectra for the three photoreactivity classes in DOM-PD.

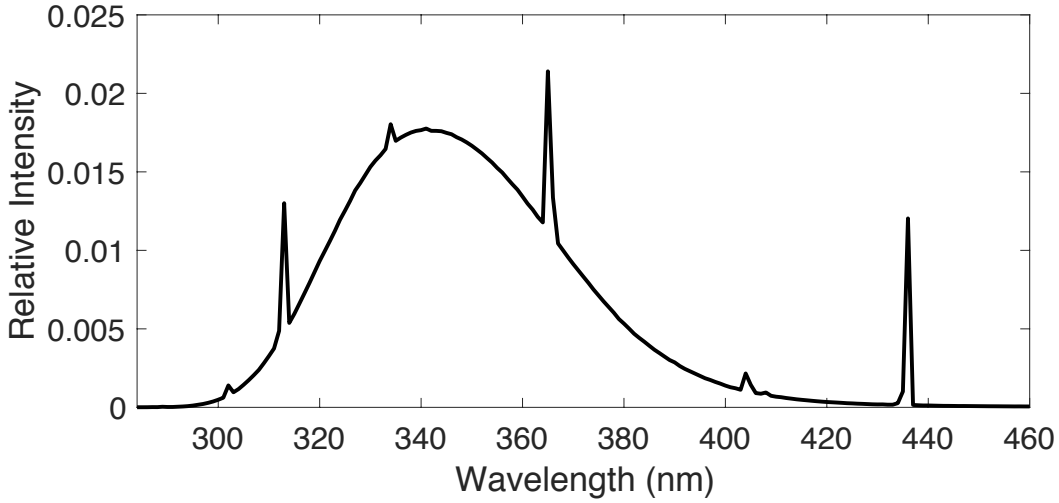

Figure 3.3 Spectral distribution of the irradiance used to force the numerical model of the test data set. The total irradiance used was 17.9 W m^{-2}

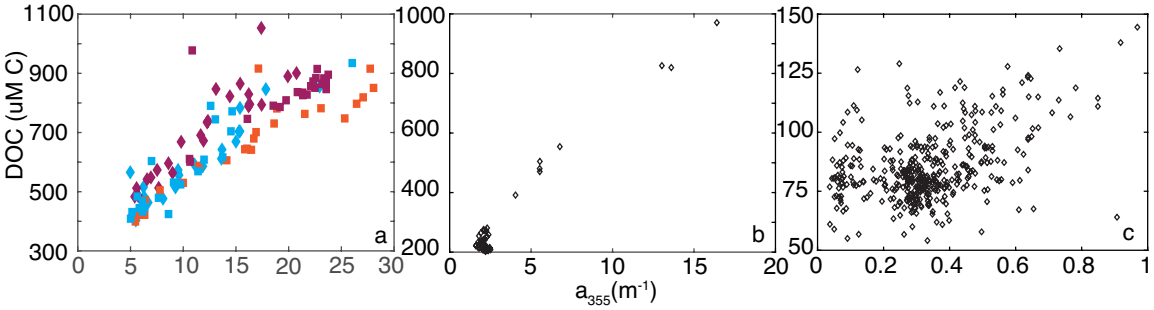

Figure 3.4 Dissolved organic carbon (DOC) as a function of absorbance at 355nm (a355) for (a) the GCREW marsh creek derived samples used to generate the colored DOC_3 specific absorption spectra (diamonds=2015, squares =2016, orange=June, blue=July, magenta=August.),(b) the mid-Chesapeake Bay NASA GEOCAPE cruise data used to generate the colored DOC_2 specific absorption spectra, and (c) the mid-Atlantic coastal ocean NASA CLiVEC cruise data used to generate the colored DOC_1 specific absorption spectra. Information on each data set can be found in Table 3.4.

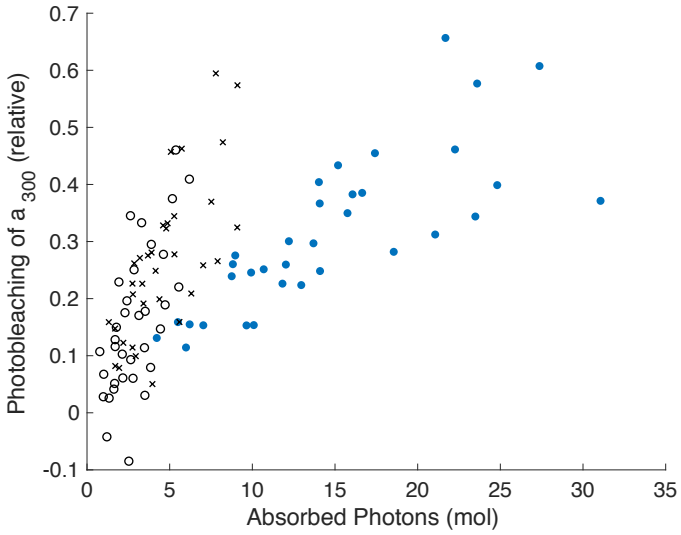

Figure 3.5 Photobleaching of absorbance (a300) after filtered Xenon lamp exposure for filtrate from the marsh low tide sample (filled circles), marsh high tide samples, (x's) and Rhode River estuary sample (circles) as a function of total absorbed energy during the exposure. Variation in exposure and photobleaching results from the use of six long-pass cutoff filters and exposure durations of 12 and 24 h.

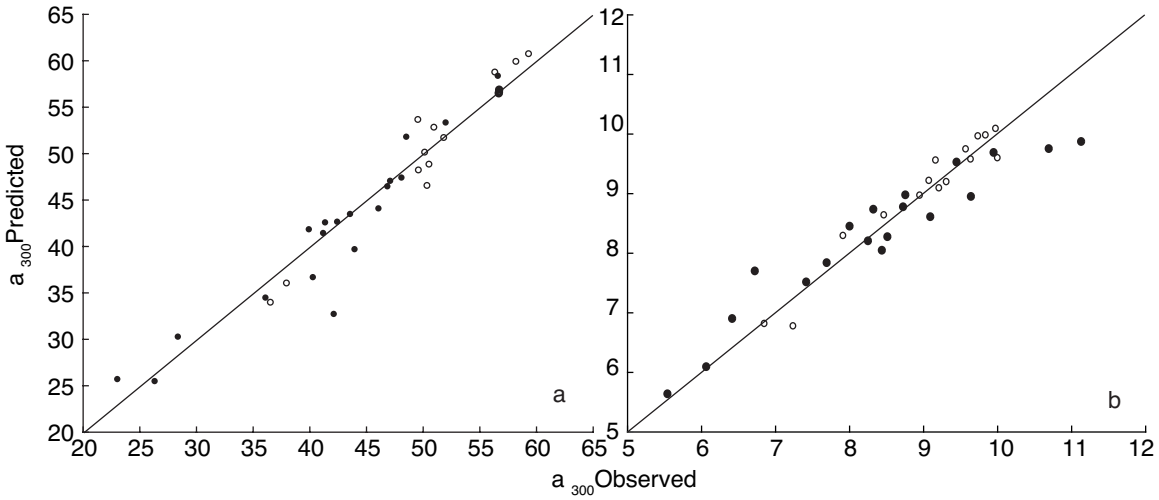

Figure 3.6 Predicted vs observed a300 (m^{-1}) for DOM-PD model fits to the (a) marsh low tide data and (b) Rhode River estuary samples. Open symbols are for 12 hour exposures, filled symbols 24 hour exposures to Xenon irradiance through the various long-pass filters (Table 3.2). The marsh low tide samples were used to estimate $AQY_{3,j}$ and the Rhode River estuary samples were used to estimate $AQY_{2,j}$.

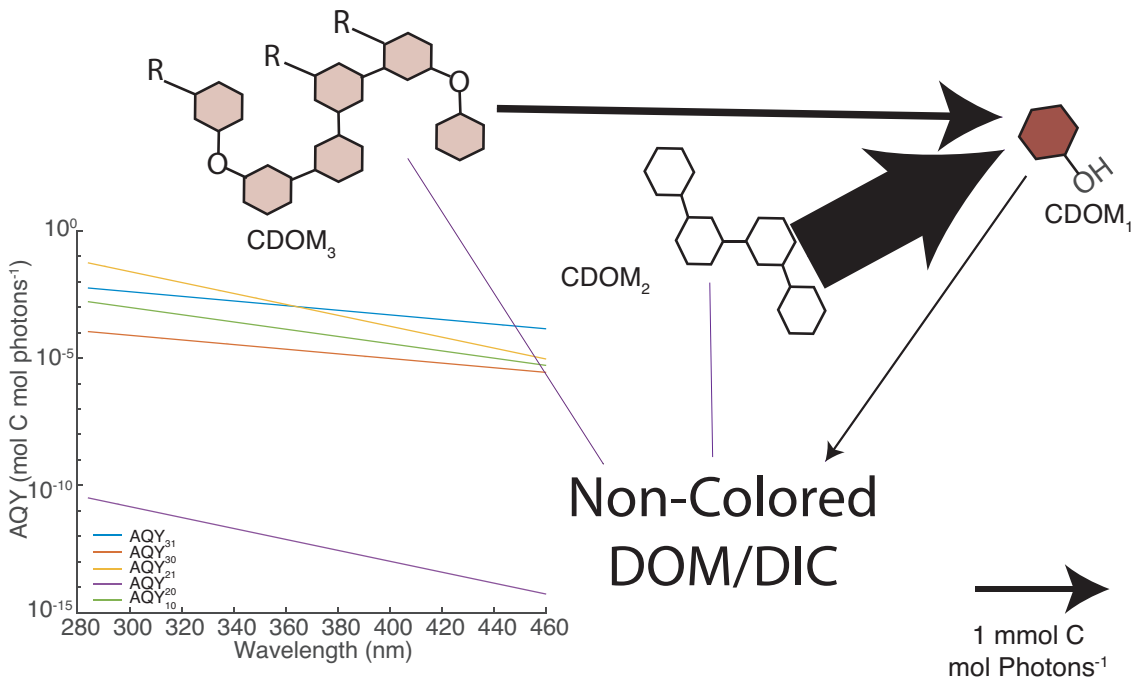

Figure 3.7 The spectrally explicit apparent quantum yields (AQY) estimated from the Xenon lamp solar exposures for each pathway and a photochemical degradation conceptual diagram with the shading of each dissolved organic matter (DOM) pool representative of the fraction of the total absorbance in each pool after the seven day incubation experiments for an average marsh low tide condition. The width of the arrows are scaled to the magnitude of the apparent quantum yield (AQY) for each pathway (see scale key in lower right corner). There is no arrow from $CDOM_2$ to non-colored DOM/DIC because the AQY for that pathway is virtually 0.

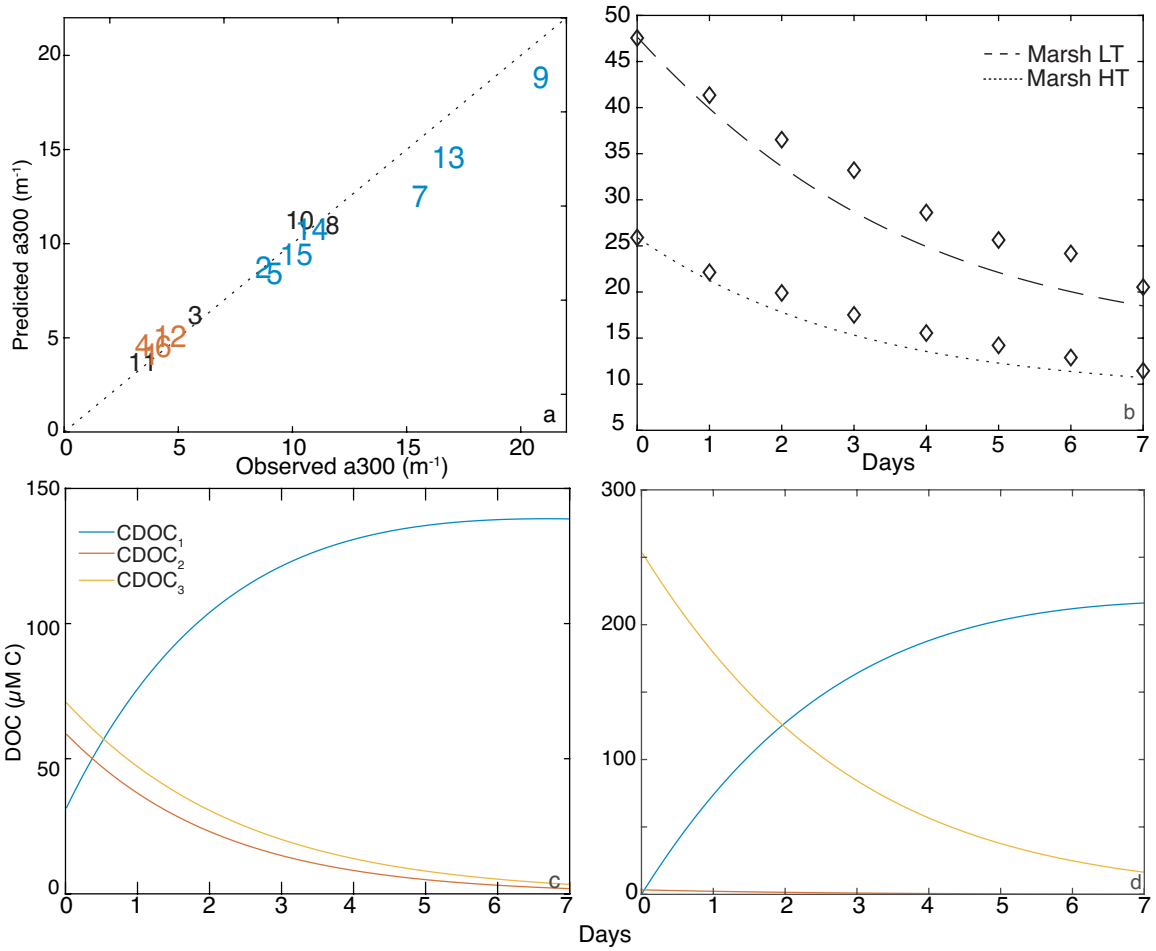

Figure 3.8 (a) Seven day final predicted and observed absorbance at 300 nm (a300, m^{-1}) for all 15 Rhode River incubations in the test data set, with the numbers corresponding to the incubation data in Table 3.3. Blue numbers indicate marsh low tide incubations and orange numbers dock (estuary) water incubations. (b) Predicted (dashed lines) and observed (diamonds) colored dissolved organic carbon (CDOC) absorbance at 300 nm (a300) for marsh low tide (LT) and marsh high tide (HT) samples from incubations 8 and 9. Time series of modeled CDOC concentration beginning with the (c) average dock initial concentration and (d) average marsh low tide initial concentration.

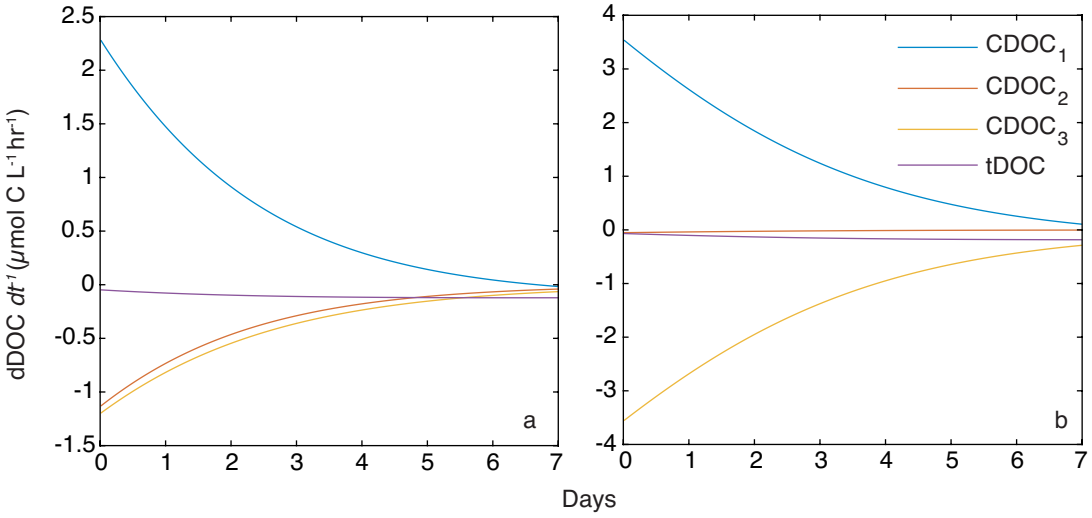

Figure 3.9 Rate of change of colored dissolved organic carbon (CDOC; dDOC dt^{-1}, µmol C L^{-1} hr^{-1}) over the course of the (a) average estuary incubation and (b) the average marsh low tide incubation. The total DOC (tDOC) is the sum of each pool and the negative rate of change is the loss of CDOC to non-colored DOC and dissolved inorganic carbon.

Tables Chapter 3

Table 3.1 Average irradiances (W m^{-2}) used for photobleaching experiments with Xenon lamp exposures for each filter type

Filter	UVB	UVA	PAR
WG280	4.08	68.3	343.1
WG295	13.2	106.7	394.6
WG305	4.11	43.6	238.5
WG320	0.98	48.2	263.0
WG335	0.01	102.4	472.6
LG350	0.01	55.2	408.3

Table 3.2 Initial colored dissolved organic carbon concentration (CDOC; μM C) for each photoreactivity class for the Xenon Lamp exposures

Identification	Initial $CDOC_1$ [a]	Initial $CDOC_2$	Initial $CDOC_3$	a300[b]	Date Sampled
Rhode River[c]	0	178.33	N/A	10.25	Aug. 17, 2015
GCREW HT[d]	42.29	117.61	81.71	17.64	Jul. 30,2015
GCREW HT	0.00	167.14	115.81	22.55	Aug. 13, 2015
GCREW HT	62.77	34.07	61.90	11.49	Aug. 21,2015
GCREW LT[e]	0.00	0.00	598.09	66.91	Jul. 29, 2015
GCREW LT	0.00	0.00	642.69	71.67	Aug. 12, 2015
GCREW LT	29.93	0.00	308.33	35.30	20-Aug-15

a. $CDOC_{1\text{-}3}$ were estimated using a multiple linear regression of the observed absorbance spectra as a function of the CDOC concentration and the a^*cdoc_i detailed in the methods section of the main text. For the Rhode River sample, $CDOC_3$ was assumed to be 0.
b. Initial colored dissolved organic matter absorbance at 300 nm (a300; m^{-1})
c. Sample collected at the SERC Dock in the Rhode River, MD, USA (38.8856 N, -76.5419 E)
d. Sample collected at high tide at the GCREW Marsh, Rhode River, MD, USA (38.8749 N, -76.5465 E)
e. Sample collected at low tide at the GCREW Marsh, Rhode River, MD, USA (38.8749 N, -76.5465 E)

Table 3.3 Initial colored dissolved organic carbon estimates for DOM-PD test data set

Identification	Duration (Days)	Initial[a] $CDOC_1$	Initial $CDOC_2$	Initial $CDOC_3$	a300 [b]	Date Sampled
1. SERC Dock[c]	7	0.00	99.06	3.33	6.06	Jan. 13, 2016
2. GCREW LT[d]	7	0.00	46.22	164.61	21.22	Jan. 14, 2016
3. Lower MC[e]	9	47.58	86.56	27.30	9.97	Apr. 5, 2016
4. SERC Dock	10	83.25	13.93	21.18	6.54	Apr. 22, 2016
5. GCREW LT	10	22.15	62.49	122.73	18.33	Apr. 22, 2016
6. SERC Dock	8	46.20	50.07	18.98	6.89	May 5, 2016
7. GCREW LT	8	0.00	0.00	291.98	32.95	May 5, 2016
8. GCREW HT[f]	7	1.49	73.35	193.52	26.10	Jun. 10, 2016
9. GCREW LT	7	0.00	0.00	426.31	48.10	Jun. 10, 2016
10. Upper MC[g]	7	0.00	214.97	72.59	20.43	Jun. 28, 2016
11. RR Mouth[h]	7	62.20	0.00	32.31	6.15	Jun. 28, 2016
12. SERC Dock	7	28.76	92.65	7.24	7.29	Jul. 21, 2016
13. GCREW LT	7	46.66	0.00	299.10	35.63	Jul. 21, 2016
14. GCREW LT	7	0.00	53.58	204.75	26.18	Oct. 19, 2016
15. GCREW LT	7	0.00	0.00	223.18	25.18	Jan. 5, 2017
16. Dock Avg.[i]	N/A	39.58	63.92	14.42	5.84	N/A
17. Marsh Avg.[j]	N/A	11.50	23.17	247.50	11.76	N/A

a. Initial colored dissolved organic carbon (CDOC; μM C) estimates for each of the 15 test incubations derived from Logozzo (2017).
b. Initial colored dissolved organic matter absorbance at 300 nm (a300; m^{-1})
c. Sample collected at the SERC Dock in the Rhode River, MD, USA (38.8856 N, -76.5419 E)
d. Sample collected low tide at the GCREW Marsh, Rhode River, MD, USA (38.8749 N, -76.5465 E)
e. Sample collected lower Muddy Creek, Rhode River, MD, USA (38.8775 N, -76.5527 E)
f. Sample collected high tide at the GCREW Marsh, Rhode River, MD, USA (38.8749 N, -76.5465 E)
g. Sample collected upper Muddy Creek, Rhode River, MD, USA (38.8843 N, -76.5576 E)
h. Sample collected at the Rhode River Mouth, MD, USA (38.8605 N,-76.4931 W)
i. Average for all SERC Dock samples
j. Average for all GCREW LT samples

Table 3.4 Average total dissolved organic carbon and derived non-colored dissolved organic carbon for data sets to derive NCDOC

Date	total DOC[a]	NCDOC[b]	% NCDOC[c]	SR[d]	a_{300} (m^{-1})[e]	n[f]
Jul. 2015[g]	616.3	319.5	51.83	0.870	39.34	21
Aug. 2015[g]	705.8	332.9	47.16	0.887	40.56	24
Jun. 2016[g]	658.6	342.4	51.99	0.822	57.21	24
Jul. 2016[g]	571.5	301.9	52.82	0.908	36.00	20
Aug. 2016[g]	831.9	583.9	70.18	0.804	49.32	24
GEOCAPE[h]	279.3	119.34	42.73	1.183	5.94	61
CLiVEC[i]	85.1	50	58.75	1.595	1.17	398

a. Total dissolved organic carbon (total DOC) in μM.
b. Non-colored DOC (NCDOC) in μM derived as the intercept of the regression of total DOC for each data set as a function of absorbance at 355 nm (a355 m^{-1})
c. Percent of total DOC that is NCDOC
d. Spectral absorption slope ratio (SR) for the samples used to define the specific absorption spectra. SR is calculated as ratio of the exponential slope of the 275-295 nm range and 350-400 nm range of the absorption spectra (Helms et al., 2008)
e. Absorption at 300 nm (a_{300}) for the samples used to define the specific absorption spectra
f. Number of samples (n)
g. Samples taken at the GCREW Marsh creek in the Rhode River, MD, USA over 24 hour period
h. Samples collected by the NASA GEOCAPE research project in Chesapeake Bay, MD, USA
i. Samples collected by the NASA CLiVEC research project in the mid-Atlantic bight, East Coast, USA

Table 3.5 Apparent quantum yield parameter estimates derived from the Xenon Arc photobleaching experimental setup

Parameter	Source	AQY(284)[a]	Slope[b] (nm^{-1})
AQY_{31}	Marsh LT	5.74±0.69	-0.021±0.0014
AQY_{30}	Marsh LT	0.111±0.154	-0.021±0.0014
AQY_{21}	Rhode River	56.05±21.5	-0.0495±0.0101
AQY_{20}	Rhode River	$3.22x10^{-8}$±1.75	-0.0495±0.0101
AQY_{10}	Rhode River	1.66±0.82	-0.0328±0.0065

a. Apparent quantum yield (AQY; mmol C mol photons^{-1}). Each pathway is represented by the subcript (e.g. AQY_{31} is the transformation of $CDOC_3$ to $CDOC_1$)

b. AQY spectral slope estimates (nm^{-1})

Table 3.6 Results of sensitivity analysis of the DOM-PD for initial parameters representative of dissolved organic matter in the Rhode River estuary and that exported from associated tidal marshes

Estuary[a]	$CDOC_1$	$CDOC_2$	$CDOC_3$	$a300_1$	$a300_2$	$a300_3$	Total a300	Total CDOC
Base[b]	101.98	1.81	0.64	4.11	0.10	0.07	4.28	104.4
Upper AQY[c]	93.68	0.34	0.40	3.77	0.02	0.04	3.84	94.43
Lower AQY[c]	109.3	0.46	0.98	4.40	0.03	0.11	4.54	110.7
Upper Slope[d]	98.22	0.25	0.50	3.96	0.01	0.06	4.03	98.98
Lower[d] Slope	101.57	6.05	0.80	4.09	0.35	0.09	4.53	108.4
2x a*CDOC[e]	91.37	0.07	0.04	7.35	0.01	0.01	7.37	91.37
0.5x a*CDOC[e]	98.56	10.26	2.93	1.99	0.29	0.16	2.44	111.8

Marsh	$CDOC_1$	$CDOC_2$	$CDOC_3$	$a300_1$	$a300_2$	$a300_3$	Total a300	Total CDOC
Base	237.7	1.10	16.35	9.58	0.06	1.83	11.47	255.2
Upper AQY	226.2	0.25	10.60	9.11	0.01	1.18	10.31	237.0
Lower AQY	246.2	0.36	24.44	9.92	0.02	2.73	12.67	271.0
Upper Slope	232.8	0.19	13.06	9.38	0.01	1.46	10.85	246.1
Lower Slope	238.5	3.14	20.07	9.61	0.18	2.24	12.03	261.7
2x a*CDOC	229.4	0.10	1.87	18.48	0.01	0.42	18.91	231.4
0.5x a*CDOC	207.2	4.44	57.69	4.17	0.13	3.22	7.52	269.3

a. Modeled average estuary (upper) and marsh low tide (lower) final colored dissolved organic carbon (CDOC) and absorbance at 300 nm (a300; m^{-1}) for each CDOC pool and the total a300 and CDOC (sum of each state variable) for upper and lower bounds of the model derived parameters
b. Baseline model run
c. Upper and and lower apparent quantum yield (AQY) estimates (Table 5).
d. Upper and lower AQY spectral slope estimates (Table 5)
e. 2 times and 0.5 times the CDOC specific absorption (a*CDOC; m^2 mol C^{-1})

Wind Driven Dissolved Organic Matter Dynamics in a Chesapeake Bay Tidal Marsh-Estuary System

4.1 Abstract

Controls on organic matter cycling across the tidal wetland-estuary interface have proved elusive, but high-resolution observations coupled with process-based modeling can be a powerful methodology to address shortcomings in either methodology alone. In this study, detailed observations and three-dimensional hydrodynamic modeling are used to examine biogeochemical exchanges in the marsh-estuary system of the Rhode River, MD, USA. Analysis of observations near the marsh in 2015 reveals a strong relationship between marsh creek salinity and dissolved organic matter fluorescence (*fDOM*), with wind velocity indirectly driving large amplitude variation of both salinity and *fDOM* at certain times of the year. Three dimensional model results from the Finite Volume Community Ocean Model implemented for the wetland system with a new marsh grass drag module are consistent with observations, simulating sub-tidal variability of marsh creek salinity. The model results exhibit an interaction between wind driven variation in surface elevation and flow velocity at the marsh creek, with northerly winds driving increased freshwater signal and discharge out of the modeled wetland during precipitation events. Wind setup of a water surface elevation gradient axially along the estuary drives the modeled local sub-tidal flow and thus salinity variability. On sub-tidal time scales (>36 hours, < 1 week) wind is important in mediating dissolved organic matter releases from the Kirkpatrick Marsh into the Rhode River.

4.2 Introduction

Wetlands can be important buffers for coastal flooding and storms (Haddad et al., 2016) and they provide habitat and nursery grounds for many species of animals that have cultural and economic significance, including birds, fish, mammals and invertebrates. In addition to more tangible ecosystem services, the generally high productivity of tidal wetlands makes them dynamic carbon fixers and transformers of organic material, playing a potentially substantial role in the coastal carbon cycle. In the face of rising seas and warming coastal oceans, interest in marsh biogeochemistry and the ecosystem services and carbon cycling associated with them has been increasing.

Numerous studies have quantified the fluxes of materials between tidal wetlands and adjacent estuaries on varying time scales (e.g., Teal, 1962; Nixon, 1980; Dame et al., 1991; Childers 1993; Tzortziou et al., 2008). Brackish and salt marshes have high rates of primary production, generally being net carbon sinks from the atmosphere (Chmura et al., 2003; Bridgham et al., 2006), while also contributing a large source of dissolved inorganic carbon and dissolved organic matter (DIC and DOM) to the coastal ocean (Wang and Cai, 2004; Herrmann et al., 2014). A recent estimate of a tidal wetland organic carbon flux of 1.2-2.5 Tg C $year^{-1}$ to the eastern coastal waters of the United States indicate tidal wetlands play an important role in the coastal carbon cycle (Herrmann et al., 2014).

In addition, marsh carbon fixation and processing have widespread implications for net ecosystem production of the east coast of North America and in particular Chesapeake Bay (Herrmann et al., 2014). Wetlands make up 1 % of the total watershed in the mid-Atlantic Bight, but contribute up to 40% of the total organic carbon export into

estuarine and coastal waters (Herrmann et al., 2014). Marsh-estuary dissolved organic matter (DOM) fluxes have been studied extensively for over 30 years, with most studies showing that coastal marshes are strong sources of dissolved organic carbon and nitrogen to adjacent waters (e.g. Dame et al., 1986; Childers 1993; Tzortziou et al., 2008). However, generalizations about the magnitude of these fluxes and the factors that drive their spatiotemporal variability have proven elusive.

Wetland inundation regimes and water flux exert substantial control over many biogeochemical processes in marsh-estuary systems (Fagherazzi et al., 2013). Factors that influence marsh water intrusion on temporal scales longer than tidal cycles can have potentially important implications in microtidal environments such as Chesapeake Bay. In Chesapeake Bay, variations in freshwater discharge (Schubel and Pritchard, 1986) and wind speed (e.g. Blumberg and Goodrich, 1990; Scully et al., 2005) can both have a strong influence on the residual flow patterns of the Bay. Wind also affects flushing, residence time and salinity variability in shallow water estuaries (Geyer, 1997). It is therefore not surprising that wind forcing also impacts biogeochemical fluxes associated with marsh ecosystems. For example, Childers et al. (1993) reported that salt marshes in coastal Georgia have varying inorganic nutrient flux responses associated with changes in wind direction and wave height at exposed marsh sites, and that more exposed marshes have higher amounts of potentially wind driven DOM exchange. Sub-tidal inundation variation in tidal wetlands has also been linked to wind forcing (Dame et al., 1986; Childers 1993; Bockelmann et al., 2002), but sub-tidal flow variability has yet to be quantitatively linked to DOM transport across the wetland-estuary interface. Implementing high resolution monitoring programs that can capture transient wind and

storm events associated with marsh-estuary fluxes is challenging, partly due to high human resource and material costs in addition to high spatial and temporal heterogeneity associated with intertidal wetlands (Jordan et al., 1991). The advent of in-situ optical sensors that can measure various water column properties including *fDOM* have made high-frequency observations much more attainable. Furthermore, modeling combined with the in-situ sensing technology can offer insights into the spatiotemporal variability of marsh-estuary coupled water flow with high resolution over a wide range of scales.

Biogeochemical degradation, physical transport and mixing, and photochemical transformations all contribute to the distribution of DOM in estuarine waters. The highly variable tidal signal inherently influences the biogeochemical processes that occur as wetland DOM is advected between the wetland and estuary. This study addresses the processes of physical mixing and transport to examine the influence they have on the observed temporal patterns of DOM variability at a wetland creek. Specifically, a combination of observations and modeling are used to investigate how wind influences the outflow of DOM from the Kirkpatrick Marsh into the Rhode River in Chesapeake Bay, USA. First, an instrument deployment at the marsh creek is used to provide insight into the temporal variability of salinity and *fDOM*. Insight gained from the instrument deployment is then used to inform numerical experiments utilizing a Rhode River implementation of the Finite Volume Community Ocean Model (RhodeFVCOM). Specifically, RhodeFVCOM is used to examine how wind velocity influences the temporal and spatial salinity and flow variability. These experiments reveal that wind forcing affects inundation timing and extent and significantly alters marsh creek flow velocity, with northerly winds enhancing marsh water efflux. The results of this

numerical study, in conjunction with the observational data set, demonstrate that wind largely controls water advection and inundation in the marsh and sub-tidal hydrological variability, and thus controls marsh-estuary DOM exchange.

4.3 Methods

4.3.1 Site description and observations

The Rhode River, MD, USA is a shallow water tributary located on the western shore of Chesapeake Bay just south of Annapolis, MD (Figure 4.1a & b). The Kirkpatrick Marsh is a fully developed mesohaline (0-14 psu) marsh that is located near the head of the Rhode River at 38° 52' 30" N, 76° 32' 50" W (Figure 4.1c). The bathymetry in the Rhode River slopes from a depth of approximately 0.3 m at the marsh edge to 4 m at the mouth of the river.

The largest input of freshwater into the estuary is from Muddy Creek (Figure 4.1c), with a maximum instantaneous discharge of 15 m^3 s^{-1} and a median daily discharge of 0.13 m^3 s^{-1} in the modeled year 2005 (Breitburg et al., 2008). Marsh plant community density in the Kirkpatrick Marsh ranges from 200 to 1000 plants m^{-2} with substantial inter-annual variability (Rasse et al., 2005). *Schoenoplectus americanus* makes up a significant portion of the plant community and average high marsh plant diameter at an adjacent marsh measured 3.75 mm (Ikegami et al., 2006). Among other species commonly found in brackish marshes, there are stands of *Spartina patens* in areas with higher elevation (Jordan and Correll, 1991). The portion of the Kirkpatrick Marsh under study is mainly flushed by a tidal creek outfitted with a flow-through flume that is the

main conduit linking ~3 hectares of marsh area to the Rhode River (Jordan and Correll, 1991).

A multiparameter EXO2 6-port water quality sonde (Yellow Springs Instruments, YSI) was deployed at the Kirkpatrick Marsh creek starting in November 2014 and sampling nearly continuously through 2015. Measurements included salinity, temperature, *chl a* fluorescence, dissolved oxygen, DOM fluorescence (*fDOM*) and pH at 15-minute intervals 0.25 meters above the marsh creek sediment. A similarly configured instrument was operated at the Smithsonian Environmental Research Center (SERC) dock (38° 53' 8" N, 76° 32' 30" W) which is about 1 km downstream of the marsh in the Rhode River (Figure 4.1c). Both instruments are outfitted with an automatic wiper that cleans the active surface of all probes, allowing for less maintenance and longer deployment times. The probes were regularly inspected for bio-film accumulation and the instrument was cleaned and calibrated before and after each deployment. Deployment periods between calibrations in the summer were around two weeks, longer during cool weather. *fDOM* data have been corrected for the effects of turbidity and temperature dependent variation in quantum yield (Downing et al., 2012).

A SonTek-IQ acoustic doppler velocimetry (ADV) probe was intermittently deployed at the marsh creek flume beginning June 2015 to measure current velocity and depth at 5 cm above the marsh creek sediment surface. The ADV sampled for a 120 second period every 5 minutes, averaging the measured velocity and depth over the sample period. Flow measurements obtained at 15 minute intervals over a 55 day ADV deployment in the summer were used to generate a hypsometric relationship for area inundated for a given tidal stage. The flow data obtained was used to compare the

calculated wetland inundation with the model predicted wetland inundation. In addition, a deployment in November 2015 is used for a comparison between model dynamics and observed velocity at the marsh creek.

4.3.2 Model development and implementation

The Finite Volume Community Ocean Model (FVCOM) (Chen et al., 2003)was implemented for a section of mid Chesapeake Bay including the Rhode River and Kirkpatrick Marsh (Figure 4.1b) to analyze controls on hydrodynamic processes in the marsh and the estuary down-stream. The wetting and drying treatment of intertidal areas available in FVCOM gives an accurate representation of intertidal hydrodynamics in a wetland-estuarine system in the Satilla River, GA (Chen et al., 2008), and was therefore selected for this application.

The model domain includes two main stem EPA Chesapeake Bay Program (CBP) long-term water quality model stations as well as four stations on the east and west shoals of the bay. The northern open boundary of the model domain is near the Chesapeake Bay Bridge, and the southern open boundary is just north of Poplar Island. The near continuous measurements of temperature and salinity at the SERC dock allowed for shallow water model validation (see 4.4.2).

Eight freshwater discharge sites were included in the model domain, four of which are adjacent to the Kirkpatrick Marsh (stars in Figure 4.1c). Measured freshwater discharge from the three V-notch weirs (Breitburg et al., 2008) in the Rhode River watershed was extrapolated to the other five discharge points by normalizing the flow measured at the weir to watershed area. When a flow meter records low or no flow over a long period of time and a sudden increase in discharge occurs, the flow recorders miss the

initial increase in discharge. In order to prevent an over-estimate of flow into the model domain, an algorithm was employed to account for the missed flow when doing a linear temporal interpolation (Jordan, personal communication). When there is a sharp increase in flow after extended low flow periods, the algorithm assumes a constant flow rate until the sharp increase in flow is observed.

A nested model approach is used to force the northern and southern open boundaries with temperature, salinity, and sea surface height (SSH). Time series of SSH at the open boundaries were extracted at hourly intervals from a solution of a larger scale FVCOM simulation developed for this study to drive the RhodeFVCOM tidal forcing. A model solution for daily temperature and salinity was taken at daily intervals from the Chesapeake Bay Regional Ocean Modeling System (ChesROMS) (Xu et al., 2012) grid points closest to the RhodeFVCOM north and south open boundaries. Two- and three-dimensional interpolations were done for SSH, temperature and salinity onto the RhodeFVCOM open boundaries. Lastly, the spatially interpolated temperature and salinity from ChesROMS were linearly interpolated in time from a daily output to the hourly time step and used to force RhodeFVCOM.

The estuarine surface boundary is forced using North American Regional Reanalysis (NARR) model output for the year 2005 (http://rda.ucar.edu/datasets/ds608.0/). Three-hourly NARR data from the NARR grid cell that covers the majority of the RhodeFVCOM domain was applied uniformly over the entire model domain. Wind speed *u* and *v* vector components at 10 meters above the sea surface were used to calculate surface wind stress in the model (Large and Pond, 1981). Temperature at 10 m above sea level, surface pressure (Pa) and relative humidity

(%) at 2 meters above sea level, along with the NARR wind and model calculated sea surface temperature (SST, °C), were used to compute the sensible and latent heat flux in the model internally using the COARE 2.6 algorithm (Fairall et al., 1996). This method allowed a dynamic feedback between the model predicted SST and the heat flux calculation. Net short wave and long wave radiation from NARR was used to close the heat flux calculation internally. A correction factor of 0.5 was applied to the NARR estimated net long-wave radiation flux in order to resolve the temperature in the summer and partially account for systematic over prediction of long wave radiation flux (Kumar and Merwade, 2011).

Model horizontal resolution increases from ~400 m in the main channel portion of Chesapeake Bay to less than 10 m in the marsh area. The high spatial resolution is necessary to attempt to resolve bathymetric features within the marsh. The unstructured mesh contains 8,138 nodes and 14,572 elements. Rhode River bathymetry was input manually into the Surface-Water Modeling System (SMS) mesh generation software package (SMS version 8.0, AQUAVEO) from NOAA chart #12270 (www.charts.noaa.gov) and interpolated to the nodes of the model grid.

FVCOM uses a vertical hybrid terrain following coordinate system commonly referred to as sigma coordinates. In areas with still-water depth less than 3 m, the vertical coordinates form an exponential distribution with decreasing resolution with depth. In areas with depth greater than 3 m, the vertical coordinates change to a parabolic distribution with coarser vertical resolution in the middle of the water column. This is implemented to counteract spurious heating and cooling in the surface layers of the shallow areas of the model, while resolving boundary layer effects in deeper regions.

A marsh plant momentum sink was included in the model (Wang et al., 2014) in order to simulate the drag imposed by marsh grass on the tidal water flowing through the marsh. Following Nepf (1999), the momentum sink calculates the drag imposed by a rigid cylindrical body and subtracts it from the momentum equation solved for each grid cell in the water column. Equation 4.1 (Wang et al., 2014) is used to numerically solve for the drag force on the flow due to the presence of marsh grass in a spatially explicit context, where F^M is the momentum sink due to drag (m s^{-2}), N is the number of plants in the marsh element, C_d is the drag coefficient (dimensionless), A is the cross sectional area of plant stems (Diameter x Height, m^2), V_C is the element volume (m^3) and u is the velocity of the water at the element centroid (m s^{-1}).

$$F^M = \frac{1}{2}\frac{NC_dA}{V_C}\left|\vec{u}\right|\vec{u} \tag{4.1}$$

An average stem number density of 600 plants m^{-2} (Rasse et al., 2005) and a stem diameter of 3.75 mm (Ikegami et al., 2006) was used to calculate a cross sectional area of influence in each cell specified upon model startup as containing marsh plants. Table 4.1 summarizes the marsh plant drag model parameterization.

In FVCOM, a minimum depth (D_{min}) is required to maintain computational logic in the intertidal zone for the wetting and drying scheme (Zheng et al., 2003). The minimum depth is the modeled water elevation where "dry" conditions take place and calculations for temperature and salinity diffusion cease until D_{min} is exceeded. A D_{min} value of 0.05 m was used in this research for model stability purposes.

The boundaries of the marsh areas were extracted from traced paths in Google Earth (GoogleEarth 7.1.5). The mode-split time stepping scheme of FVCOM requires a

small external mode (barotropic) to internal mode (baroclinic) time step ratio when grid resolution is fine and intertidal areas are shallow (See Chen et al., 2013 for intertidal tests and numerical constraints). Therefore, an external time step (DTE) of two seconds and internal time step (DTI) of six seconds were used. The computations were carried out using OpenMPI on an 8 core 2014 Mac Pro, which took approximately two days in wall clock time for 242 model days.

4.3.3 Model numerical experiments

Model parameter optimization tests were carried out to find the best parameter set for predicting salinity and temperature in the Rhode River. The parameter set that produced the best results was used as the control run for the numerical experiments (Table 4.1). The bottom friction (B_{FRIC}) and horizontal diffusion coefficient (HORCON) were the most important parameters affecting salinity and SSH in the Rhode River. Temperature variation was strongly dependent on the surface forcing and the vertical layer distribution in the modeled water column. In order to find out how wind velocity affected the system, 2 model "experiments" with varying atmospheric forcing were carried out in addition to a control run. Observations at the Kirkpatrick Marsh creek in 2015 suggested a non-linear relationship between wind forcing and salinity. To explore this relationship, numerical experiments were set up to test how the model replicated the observed non-linear interactions at different times of the year.

Test B is the baseline model run (the control). Tests SW and NW were set up so that southerly (Test SW) and northerly (Test NW) winds blow for a 48-hour bracket (±24 hours) around storm events. Storm events were defined as an increase in total discharge of 0.25 $m^3 s^{-1}$ into the entire Muddy Creek watershed over a 15-minute time period,

totaling 12 events. Wind climatologies from Baltimore-Washington Airport, MD from 2010 through 2013 reveal that, in general, winds are stronger and from a more northwesterly direction in autumn, winter and spring (Vinnikov, 2015; http://www.atmos.umd.edu/~kostya/NIST/WIND/SURFACE/KBWI_2010_13_WIND_2.pdf). In the summer, winds tend to be of smaller magnitude and the direction switches to having a more pronounced southerly component. The two-day wind bracket in the model was designed to capture any potential lag influences associated with salinity intrusion, flow velocity and wind speed.

The model initial condition was set using output from a previous baseline model run ending March 31, 2005 and run recursively three times for the entire year. The numerical experiments were conducted beginning March 31, 2005 running 242 days through November 30, 2005. The model time period captured the spring freshet in 2005 that peaked in mid-April. Hydrodynamic parameters were adjusted in order to minimize model temperature and salinity solution error at the SERC dock (Table 4.1).

4.3.4 Statistical analysis

Time series comparisons of root mean square error (RMSE) and correlation coefficient (r) characterized model skill for temperature and salinity (Stow et al., 2009). A low frequency pass cutoff filter MATLAB function (*lpfilt;* Sherwood 1989,Version R2014B, The Mathworks Inc.) was used to remove the tidal signal from both the observed (salinity, *fDOM*, depth, wind velocity) and the modeled (salinity, flow velocity and SSH) time series in order to examine the response of the sub-tidal variability to the effect of wind. This algorithm employs a fast Fourier transform (fft) and tapered moving box-car algorithm to filter both modeled and observed time series in the frequency

domain before statistical analysis. Non-stationary time series were detrended by removing the best-fit least-squares regression line of the data from the total data set. Cross covariance analysis of the three observed time series was conducted to assess covariance of *fDOM*, salinity, wind velocity and depth.

Equation 4.2 is used to calculate the area of inundated marsh at the Kirkpatrick Marsh creek where AI is the area inundated of the marsh (m^2), V_F is the flow velocity at the marsh flume ($m\ s^{-1}$), A_F is the cross-sectional area

$$AI=\frac{V_F A_F}{\frac{dZ}{dt}} \tag{4.2}$$

of the marsh flume (m^2), and dZ/dt is the temporal derivative of the tidal height ($m\ s^{-1}$). The hypsometry of a wetland is based on the relationship between flooding or ebbing water flow across a known cross sectional area and marsh tidal inundation. If the discharge through the flume is known, then the area flooded within the marsh can be inferred using Equation 4.2. RhodeFVCOM predicted total, instantaneous area inundated combined with the observed area inundated calculated from the hypsometric relationship allows an indirect but useful comparison of the model and the Kirkpatrick Marsh. For the hypsometry analysis, only flood tides where the change in tidal height, dZ, was greater than 0.01 m were used to eliminate noise associated with low or no flow (Jordan and Correll, 1991).

Augmented Dickey-Fuller tests (ADF) conducted using the R statistical software (version 3.1) library "tseries" (version 0.10-34; Trapletti and Hornick, 2014) function *adftest* were used to assess the stationarity and potential cointegration of the detrended,

low-pass filtered time series of *fDOM*, salinity and observed wind velocity components. *fDOM* and salinity were filtered at a 36 hour cutoff, while wind components were filtered at a 24 hour cutoff to remove diel periodicity. The ADF tests accepted the alternative hypothesis of unit root of 0 of N-S and E-W wind ($p<0.05$) for all time periods except fall E-W wind (Table 4.2). Therefore, analysis between wind and *fDOM* avoided the potential spurious relationship of co-integration among variables that could produce dubious correlations. ADF tests of salinity failed to reject the null hypothesis of non-stationarity in the spring but accepted the alternative of stationarity in the summer and fall. In the analysis, westerly and southerly winds are defined as positive (positive *u* and *v* vector components).

4.4 Results

4.4.1 Observations

Observed wind data from Tolchester Beach, MD (tidesandcurrents.noaa.gov) showed an alternating wind pattern corresponding to the sub-tidal variability of salinity and *fDOM* at the marsh creek in 2015 (Figure 4.2). Covariance of salinity and *fDOM* at the marsh creek appeared to have a seasonal component with strong negative covariance in the spring and fall at a lag centered around 0.5 days following changes in wind direction (Figure 4.3a & 4.3c). Southerly and easterly wind components were anti-correlated with the *fDOM* signal while northerly and westerly wind components were positively correlated with the *fDOM* signal (Table 4.3). *fDOM* lagged changes in the peak N-S wind velocity components by 9-10 hours and the peak E-W wind velocity components by 12-22 hours consistently across the three seasons. Wind velocity and *fDOM* had a greater coefficient of covariance in the spring and fall relative to the summer

for both N-S and E-W wind components. This was likely driven by high wind speeds that were sustained for longer periods in both component directions during spring and fall. The seasonal variability in wind direction and speed is relatively consistent with a wind climatology from Baltimore Washington International Airport, MD which is ~40 km away (Vinnikov, 2015).

In the summer, N-S wind velocity exhibited covariance with *fDOM* (r=0.60) as in spring and fall while E-W winds exhibited less covariance with a longer lag than the other two observation periods (r=0.34). The lower relative importance of the E-W wind component in the summer is likely due to a lack of a strong E-W wind event. The higher positive covariance in the N-W wind direction with *fDOM* appears to be due to the sustained low-speed southerly wind during 14-20 August coinciding with a steadily decreasing trend in *fDOM* signal and an increase in salinity (Figure 4.2b). In addition, a strong wind event coinciding with the largest release of *fDOM* in the time series occurred on August 22. Wind patterns also differed across seasons; in the spring and fall there was oscillatory behavior of component wind vectors with strong northwest winds followed by lower wind magnitude from a generally southerly direction (Figure 4.2a & 4.2c). The magnitude of summer wind was lower, on average, with the aforementioned long period of sustained light southerly winds in mid-August, which also coincided with a steady increase in marsh creek salinity.

Low-pass filtered depth and *fDOM* were consistently correlated, with a strong negative covariance across all seasons (Table 4.3, Figure 4.4a). The high correlation and similar lag between depth and salinity and *fDOM* indicates that the primary control on the flux of water between the marsh and estuary was the SSH at the marsh creek and the

marsh inundation, which was influenced by wind on sub-tidal time scales. As the marsh was flooded (high depth) *fDOM* was low due to the presence of primarily estuarine water at the marsh creek. As the marsh drained and SSH dropped due to sustained northwesterly winds, high-*fDOM* marsh water was released from the wetland into the estuary, evidenced by the consistently strong *fDOM* signal at low water depths (Figure 4.4a). This relationship is also indicated by cross-plots of salinity and *fDOM* (Figure 4.4b) although there is substantial variability across seasons. The lack of a strong relationship between *fDOM* and salinity in the summer is clearly shown by the summer scatter plot of salinity and *fDOM* (Figure 4.4b). There also appeared to be two sources of *fDOM*, particularly in the fall, which is indicated by the branching nature of the fall salinity-*fDOM* relationship. The raw observed SSH and *fDOM* data are shown in Figure 4.5.

In the spring and fall, the salinity and *fDOM* negatively covaried consistently with a lag centered around 0 days, suggesting the variance of both were being driven by the same process (Table 4.3). The observed time series from August, however, exhibited a steadily increasing trend in salinity from approximately August 12 to August 22 followed by a complex pattern of high northwest wind velocity accompanied by an increase in salinity and spike in *fDOM* signal (Figure 4.2b). This indicates the wind was driving the same physical mechanism associated with the *fDOM* signal intensity as observed in spring and fall because the pattern of co-variance between wind and *fDOM* remained consistent. However, the covariance of *fDOM* and salinity was much weaker and had the opposite sign compared to the spring and fall (Figure 4.3b; positive correlation) indicating that water that was released out of the wetland had a higher salinity than the

outlying estuary. The August 21 storm event that was followed by a sharp increase in salinity appeared to be driven by wind forcing rather than an increase in freshwater discharge into the system from precipitation. In summer months during long dry periods, evaporation on the marsh surface can concentrate salinity in the marsh porewater (Correll, 1981). As north winds accelerated around August 22nd, high salinity marsh water that was concentrated due to evaporation over the extended dry period from August 14- 20 appeared to have been released from the marsh creek along with a large pulse of *fDOM*. The *fDOM* signal in summer fluctuated both positively and negatively with salinity with an overall higher magnitude of *fDOM* signal compared to the other seasons (Figure 4.4b). The overall higher magnitude in *fDOM* signal in the summer corresponds with observed seasonally higher DOC concentrations at the marsh creek in the summer and early fall months (Jordan et al., 1991; Tzortziou et al., 2008).

Storm events with both wind and precipitation clearly impacted both *fDOM* and salinity in the marsh creek but it appears that wind velocity mediated freshwater transport and mixing as it entered the marsh-estuary system and determined the strength and direction of the salinity signal variation at the marsh creek. In most cases, large declines in salinity covaried with increases in *fDOM* and occurred independently of local rain events (dots in Figure 4.2). This suggests that overland freshwater runoff potentially had some correlation to *fDOM* influx from the marsh to the estuary, but that wind driven inundation and mixing mediated the response in both the salinity and *fDOM* signal. Only when the winds were in a favorable direction for marsh outflow did the freshwater input show up as a decrease in salinity at the marsh creek.

For the entire EXO2 deployment (March 2015 through November 2015), *fDOM* had a negative covariance with N-S wind, and weak positive covariance with E-W winds (Total, Table 4.3). Depth and *fDOM* were also tightly coupled; wind driven changes in SSH at the marsh creek coincided with changes in *fDOM*. As water elevation drops due to NW winds pushing water out of the Rhode River, marsh water is released from the marsh creek into the estuary. Salinity and *fDOM* also had a strong negative covariance throughout the time series centered at a lag of 1 hour. The strong anti-correlation between *fDOM* and salinity and their variation with wind velocity indicates that both variables are related to wind forcing, primarily from the N-S component direction but secondarily from the E-W direction. The reasons for this are addressed with the hydrodynamic RhodeFVCOM model in the next section.

4.4.2 Baseline model validation

RhodeFVCOM tidal elevation (SSH; deviation from mean sea level) was validated at the node closest to NOAA Tides and Currents Annapolis, MD station (tidesandcurrents.noaa.gov) and the SERC dock. At Annapolis, the high-frequency pass filtered tidal elevation showed strong agreement for the amplitude and period with observations (RMSE = 5.25 cm, r = 0.93). Including the low frequency variation, the model captured the overall patterns of tidal height well, although the model missed some of the variability associated with large storm and wind events (RMSE = 15.31 cm, r = 0.63). The model grid coarseness in the Annapolis area likely contributed to an underestimation of some of the shallow water tidal effects at this location, but Annapolis is the closest NOAA continuous tidal monitoring station to the study site with a known datum and therefore provided the best comparison. Modeled tidal elevation at the SERC

dock exhibited similar variability as measured tidal elevation in both the high-frequency pass (r = 0.85) and unfiltered (r = 0.53) records for the entire modeled time period, adding confidence to the model simulation of shallow water tidally driven circulation in the Rhode River.

The majority of the temperature (RMSE = 1.71 °C, r = 0.98) and salinity variability (RMSE = 1.43, r = 0.88) in observations from the SERC dock was captured for the modeled period (Figure 4.6). The high model skill of the RhodeFVCOM temperature and salinity solution added confidence that shallow water circulation in the Rhode River was simulated well. Two early fall cooling events where the magnitude of cooling was over predicted by the model contributed substantially to the error in the temperature solution. There was no observational data for comparison at the beginning of the model time period due to a lack of measurements taken at the dock. Some of the salinity draw down in the early spring and late fall was not captured with the model (see discussion).

The inundated area of the marsh as a function of flooding tidal stage at the marsh creek (hypsometry; Equation 4.2, following Jordan and Correll, 1991) from the model is compared with data collected at semi-continuous frequency from June-August 2015 in Figure 4.7. The inflection point of both scatter sets indicates the tidal stage at which the flooding water surface reaches the edge of the marsh creek bank. This represents the tidal height at which the marsh platform begins to flood. The inflection points of both modeled and observed hypsometry are similar indicating the model marsh platform elevation was similar to the actual Kirkpatrick Marsh, although the model was ~10 cm less, which is due to the modeled creek depth being slightly shallower. The model predicted more area

inundated, on average, but was of correct magnitude. The slope of the marsh hypsometric curve is steeper in the model, indicating RhodeFVCOM predicted a more rapid flooding of the marsh relative to observations. This happened because the modeled wetland bathymetry had a shallower slope compared to the real wetland. A shallower slope favors a conservative prediction of RhodeFVCOM outflow velocity because it reduces gravity driven flow in the model as the wetland is draining. Conversely, a modeled wetland with a steeper slope than the real marsh would favor an over prediction of the outflow velocity. The step function nature of the modeled inundation curve can be attributed to the finite representation of the slope in the wetland area; each cell at each elevation is flooded instantaneously when D_{min} was exceeded. The entire wetland area was generally only flooded on spring tides.

Velocity comparisons between model elements inside the marsh creek and 60 m adjacent on the marsh platform (dot in Figure 4.1c) when there is greater than 10 cm of water depth at an adjacent model node offers insight into the effect of both bottom friction and marsh grass drag on the flow field. Depth and time averaged median horizontal flow velocity on the marsh platform (1.29 cm s^{-1}) was substantially depressed relative to an element in the marsh creek, (1.74 cm s^{-1}). In addition, runs without the marsh grass drag module resulted in a 3.0 % increase in median horizontal surface velocity and a 9.9% increase in median vertical velocity for the same model element. In a model run without the marsh grass drag model, a similar decrease in horizontal velocity from the marsh creek to a node on the marsh platform was also observed. This indicates that the majority of velocity reduction over the marsh platform appears to be independent of the presence or absence of vegetation and most of the velocity reduction is due to drag

induced by the shallow flow over the marsh platform, in agreement with vegetation removal experiments (Leonard and Croft, 2006). Leonard and Croft (2006) also found a substantial decrease in the vertical velocity component in the marsh interior, consistent with the findings in RhodeFVCOM.

4.4.3 Atmospheric forcing sensitivity experiments

Experimentally altering the wind direction during storm events in the model had a strong effect on the salinity variability at the marsh creek in the spring and early summer (Figure 4.8). A southerly wind (test SW) during storms increased depth averaged salinity by 2.15 psu relative to the northerly storm wind (test NW) for the period of March 31 to July 19. The increased freshwater signal at the marsh creek in test NW was greatest in the early April storm events (Figure 4.8). Low salinity water persisted at the marsh creek for multiple days and up to two weeks following a series of storm events. The response of the salinity signal for the two tests occurred before the peak discharge for both the early April and May 22 events (Figure 4.8). This early salinity response is owed to the wind bracket around storm events in the model forcing. The wind started blowing either southerly (test SW, increased salinity) or northerly (test NW, decreased salinity) 24 hours before the increased discharged. The wind set up the salinity signal before the freshwater discharge, further exhibiting the strong effect that wind had on the salinity at the marsh creek. A change in wind direction can drive a change in salinity independent of a large discharge event.

During the summer the salinity remained generally the same across the three model runs. When storms did occur and the wind patterns were experimentally altered in the late summer and early fall (September-November; not shown) only a small difference

in the salinity for each model run occurred. The wind effect was most pronounced in the spring when marsh creek salinity was lower and freshwater input into the system was highest. The strong salinity variation produced by altering the model wind direction corroborates that wind forcing was driving much of the salinity and anti-correlated *fDOM* variability in the measurements in 2015.

The model results also reveal that altering the wind direction caused changes in the flow velocity at the marsh creek in early spring and summer (March 31- July 19, Figure 4.9a). Flow velocity directed out of the marsh creek was consistently elevated at the onset of northerly storm events in test NW compared to southerly events during storm events in test SW. Moreover, the difference in flow velocity at the creek between test SW and NW occurred consistently with changes in salinity, i.e., increases in flow out of the marsh creek were associated with lower salinity and vice versa.

In the model experiments, changes in the wind velocity also caused changes in estuarine surface elevation in the Rhode River (Figure 4.9b). The difference in surface elevation axially along the estuary during the northerly April storm event was > 1.2 cm km^{-1} from the Kirkpatrick Marsh creek to the opposite side of the Rhode River. These changes in salinity, velocity and surface elevation are consistent with the idea that northerly storm winds simultaneously drive water out of Muddy Creek into the estuary while also substantially pushing water out of the mouth of the river towards main stem Chesapeake Bay, setting up a pressure gradient sloping out of and away from the marsh creek. In contrast, it appears that southerly winds push water into the mouth of the Rhode River from main stem Chesapeake Bay, causing water to accumulate opposite the wetland in the Rhode River, sloping back toward the marsh. It should be noted that two

layer opposing flow was not consistently observed in the Rhode River model simulations and therefore likely does not greatly contribute to the mean flow.

4.4.4 Acoustic Doppler Velocimetry (ADV) observations

Limited observational data from a November 2015 ADV deployment allows a tentative corroboration of the modeled wind driven variability (Figure 4.10). Northwest winds increased flow out of the marsh. Large *fDOM* pulses occurred during low water events. These pulses of *fDOM* are likely due to a combination of local wind driven flow out of the Rhode River as predicted by the model and a drop in overall SSH of Chesapeake Bay, as confirmed by similarly low-pass filtered SSH data collected from Tolchester Beach, MD (not shown; tidesandcurents.noaa.gov). As the northwest winds relax the pressure gradient set up by the wind leads to a "slosh" of water out of the marsh, likely enhancing export. The release of hydrostatic pressure on marsh porewater may also enhance porewater export that is high in CDOM into the tidal creek. The *fDOM* peaks in the observational data (e.g. between 11/14 and 11/16) occurred after the flow reversed out of the marsh creek. Estuarine water inflow initially diluted the high *fDOM* signal at the marsh creek, and upon wind relaxation and flow reversal, as hydrostatic pressure was released *fDOM* was released out of the wetland into the tidal creek. CDOM export during low water events is consistent with previously observed tidal dynamics of Kirkpatrick Marsh CDOM fluxes (Tzortziou et al., 2008).

4.5 Discussion

Past studies have examined the effect that winds can have on marsh erosion and sediment transport (Dame et al., 1986; Stevenson et al., 1985) and compared fluxes of

nutrients under differing measured wind regimes and topographically diverse salt marsh sites (Childers 1993). In general, this study corroborates these past studies and previous qualitative estimates of wind driven marsh tracer flux. Winds have an indirect local effect on the marsh water level, either enhancing or depressing marsh inundation at the onset of storm events and thus affecting marsh-estuary water exchange. In the Rhode River, as NW winds persist, flow out of the marsh is enhanced, primarily due to water being driven out of the mouth of the sub-estuary. The effect of wind on the estuarine pressure gradient explains much of the observed variability in both *fDOM* and salinity at the marsh creek. The response of the Rhode River to N-S wind components is primarily related to the geographic orientation of the estuary. Therefore consideration should be given for a particular wetland to the local response of that wetland to wind forcing.

Quantifying the input of both terrestrial and marsh biogeochemical end members into the estuary has implications for estuarine carbon cycling and productivity. Correll (1981) and Jordan et al. (1991) describe nutrient budgets for the Rhode River and Kirkpatrick Marsh, including freshwater runoff inputs. Correll (1981) notes that neglecting overland freshwater inputs can skew results toward overestimation of marsh biogeochemical transformations. The observations presented here show that wind affects how freshwater runoff from the watershed moves between the terrestrial, intertidal and estuarine areas, having a direct effect on the marsh water and *fDOM* export. The model experimental results corroborate these observations; wind largely determines how fresh and saline water mix at the marsh-estuary interface and likely has similar influence over other conservative and non-conservative tracers.

Observations show that during and following northwest wind events, strong pulses of *fDOM* are seen at the marsh creek. These signals are indicative of highly colored DOM, of which the marsh has been shown to be a source to the adjacent estuary across all seasons (Tzortziou et al., 2008; 2011). Model results show that the wind sets up a pressure gradient due to differences in water surface elevation across the Rhode River. In addition, the enhanced flow out of Muddy Creek during northerly wind events can also be a source of *fDOM* to the estuary and potentially contributes to the signal seen at the marsh creek. The magnitude of the pressure gradient is directly dependent on the direction, duration and velocity of wind events. It appears that, as sustained northwesterly winds slacken, the pressure gradient sloping out of the marsh creek is released and large amplitude spikes in *fDOM* are observed (Fig. 2). Because of the sinuous and changing orientation of the river relative to the winds, northwest winds initially drive water back onto the marsh platform while also pushing water out of the mouth of the Rhode River into Chesapeake Bay, while southeasterly winds appear to have the opposite effect.

Large-scale (Bay-wide) circulation and SSH variability patterns that can contribute to the change in surface elevation at the marsh creek and in the Rhode River aren't captured in the model. Main-stem Chesapeake Bay circulation and SSH can be influenced by wind driven events on both short (< 4 days) and long time scales (Wang, 1979a,b). E-W winds influence SSH across the bay on a time scale of 3-5 days, and N-S winds at a shorter time and space scale (Wang, 1979a,b). This study, however, addresses the local forcing on a small tributary that appears to be important on shorter time scales (0-1 days), which is likely embedded in the larger regional atmospheric-driven SSH

signal. The boundaries of RhodeFVCOM are forced with the model predicted SSH under normal atmospheric conditions. Therefore, in the experiments presented in this paper larger scale circulation effects are not captured. There is potentially a significant non-local effect that enhances marsh water inflow and outflow during storm events in addition to the local forcing on the Rhode River demonstrated here. Additional future numerical manipulations utilizing a larger scale regional model can be used to explore more non-local and regional impacts that wind driven dynamics have on marsh water movements. Nonetheless, modeling results suggest that local wind forcing can cause sub-tidal flow variation between the wetland and estuary.

The optical, high-resolution measurements of *fDOM* from the EXO-2 probe at the marsh creek allowed the exploration of the sub-tidal variability of DOM across tidal, sub-tidal and inter-seasonal time scales. *fDOM* spikes were consistently observed with pulses of lower salinity water, although the summer shows a decoupling between *fDOM* and salinity. The salinity and *fDOM* signals appeared to vary independently of precipitation events. Northerly winds following a sustained southerly wind event can drive large fluxes of *fDOM* out of the marsh, independent of season and precipitation. Winds masked the discharge of freshwater into the Rhode River often accompanying strong southwesterly winds. Furthermore, in the summer when marsh water would be expected to have an elevated salinity compared to the surrounding estuary due to evaporation on the wetland surface (Correll, 1981), a northwesterly wind event was followed by an increase in salinity at the marsh creek co-occurring with a spike in *fDOM*. Elevated salinity in marsh water relative to the surrounding estuary during summer time could explain the positive relationship between *fDOM* and salinity seen on August 22nd. The branching nature of the

fDOM-salinity cross-plots in both the spring and fall (Figure 4.4) offers qualitative evidence of Muddy Creek water interacting with marsh-derived water at the marsh creek. Muddy Creek water would contribute *fDOM* to the estuary. Therefore, the combination of low salinity and high *fDOM* could represent mixing of marsh and Muddy Creek waters during northwesterly wind events accompanied by freshwater discharge. The contribution of each source to the overall signal is unclear, but previous studies have shown large amounts of export of *fDOM* at the marsh creek accompanying low water events (Tzortziou et al., 2008; 2011). The August 22nd event clearly shows that *fDOM* can be exported out of the marsh independent of freshwater input.

RhodeFVCOM captured the shallow water temperature and salinity variability well for the year 2005. The model, however, didn't capture all of the variability, over-predicting the salinity in the late spring and fall. The missed salinity variability is potentially due to unresolved overland flow contributing to the salt balance. The high bank to estuary ratio suggests overland freshwater flow contribution may be important when freshwater input via precipitation is high (Correll, 1981; Jordan and Correll, 1991). Some of the watershed, including areas on the east side adjacent to the marsh, is outside of the measured area and wasn't included as freshwater input into the model domain. Including overland diffuse discharge points into the model may help drive the estuary salinity lower during spring and fall freshwater discharge events. Groundwater discharge likely also contributes to the freshwater input into the Rhode River (Jordan et al., 1991), but is currently not included in RhodeFVCOM.

Water-column temperature is accurately predicted in the shallow water and main channel. Water column and sediment temperature variability has important implications

for future biogeochemical simulations of the marsh-estuary ecosystem. The internally calculated heat flux algorithm used here is crucial to resolving the temperature as opposed to forcing the model with a specified net heat flux from atmospheric models, which is commonly done. The heat flux formulation factors in the balance between net short wave and long wave radiation, with both contributing to the heating and cooling of the surface layer of the model. If either is incorrectly predicted it will lead to inaccurate surface heat flux forcing and inaccurate FVCOM water temperature. NARR consistently over predicts net long wave radiation flux (Kumar and Merwade 2011), and this problem is potentially exacerbated by the likely large amplitude variation in long wave radiation that occurs in land-influenced estuarine NARR grid cells. As discussed above, a correction factor of 0.5 is applied to the NARR predicted net long-wave radiation flux in order to resolve the temperature in the summer.

Modeled flow velocity over the marsh platform was extremely reduced relative to the tidal creek. However, these velocity comparisons between model elements inside and outside of the wetland and model runs with and without plant momentum-drag in the marsh area are sensitive to the choice of the locations that are compared and the statistical approaches that are used to compare them. The microtidal environment in the Rhode River and the irregularity with which the Kirkpatrick Marsh is flooded offers an interesting comparison of the flow field from the marsh creek to the marsh interior, similar to observational studies (e.g. Christiansen et al., 2000; Leonard and Croft, 2006). Marsh water depth is consistently low, exceeding 10 cm in surface elevation only 11% of the time at the selected marsh node used for comparison (Fig.1c). Pairwise (20.7 % velocity reduction) vs unpaired (25.7 % velocity reduction) comparisons of the velocity

time series of flow in the marsh creek versus the marsh interior gave different results, although similar conclusions. Comparing flow in the creek and on the wetland surface for all model time points (n=5808) produces a median velocity reduction of 85.4 % from the creek to the marsh interior. Rather, there is a 25.7 % velocity reduction if instead times when the wetland is flooded to a depth greater than 10 cm (n=656) are compared. Spatial heterogeneity in the marsh platform flow field can produce strongly differing velocity depending on the model output location and frequency. Thus, careful consideration is needed in both observational and modeling comparisons to accurately quantify the relative contribution of surface friction and drag induced by marsh grass stems. Nonetheless, the hydrology in the wetland is reasonably recreated in the model and the drag model in RhodeFVCOM allows future studies to assess how the inclusion of explicit marsh plants in wetland areas affects biogeochemical processes and residence time.

The slope of the modeled hypsometric plot indicates the model overestimates the rate at which the marsh floods relative to observations taken in 2015, which is indicative of a shallower slope in the modeled marsh surface relative to the Kirkpatrick Marsh (Fig. 6). The differences between modeled and calculated curves appear to be due to a modeled depth that is shallower on average, which gives rise to the difference in the inflection point, combined with substantially less variance in the model output which is inherent in a deterministic model. Even though the maximum area inundated predicted by RhodeFVCOM is greater than the calculated area inundated, because the slope of the modeled bathymetry in the wetland is less than observed, the model is potentially underestimating flow velocity out of the wetland creek because there is a weaker hydrostatic pressure gradient for any two points across the wetland surface. The total

volume that passes through the creek during a given tidal cycle would be greater, however, which could lead to an overestimation of wetland discharge. Calculated hypsometry is an estimate of inundation based on the relationship between marsh creek flow and change in tidal stage (Equation 4.2). Inherent in the hypsometric estimation from observations at the marsh creek is the assumption that the marsh region in question is only flooded through the tidal creek, which could potentially lead to an under prediction of the inundated area if there is over-edge sheet flow. The model analysis, however, recorded when every marsh grid cell in the area that was deemed to potentially drain the tidal creek has a surface water elevation > 0.055 m, which is independent of the source of the water in the marsh grid cell. The delineation between modeled wetland areas affected the maximum area inundated because if a larger potential inundation area was used in the model analysis, than it would appear that the model is more flooded relative to the observations on any given tide. In addition, some of the difference between modeled and observed inundation from RhodeFVCOM arises from predicted intermittent sheet flow over the marsh edge onto the platform during flood tides. Over edge marsh flooding in the model appears to be related to wind forcing driving water into the back of the tributary, runoff from Muddy Creek, and spring tides. More work is needed to quantify the variability of marsh platform flooding, including the delineation of each region within the marsh, in order to resolve the differences in modeled and observed inundation progression and rate.

It should be stressed that a particular wetland's response to differential wind forcing will be determined by that wetlands orientation in relation to the dominant wind forcing patterns. The orientation of the Rhode River relative to the mainstem of the bay

was important in this response (Figure 4.11). Indeed, there may be a dynamic relationship between dominant wind patterns for a certain region and the likelihood of a wetland to export large amounts of *fDOM*. Although this study did not look directly at wetland erosion/ deposition, the relationship between those processes and inundation patterns would also likely be influenced by wind similarly to *fDOM* and salinity.

4.6 Conclusion

Modeled marsh-estuary water flow is influenced by sub-tidal variability of wind-driven estuarine water surface elevation in the Rhode River, MD. Observed wind driven *fDOM* variability is consistent across the seasons, showing the influence that atmospheric forcing has on marsh DOM efflux. The wind driven setup of pressure gradients can dominate the tidal signal, exerting a strong control on the water exchange across the marsh-estuary interface. Water flow and inundation ultimately govern the timing and magnitude of biogeochemical exchanges and processes between the marsh and estuary. The modeling exercises allow exploration of how different physical phenomena affect the inundation regime, hypsometry, and marsh water residence time on the marsh platform. By varying wind forcing and modeled vegetation characteristics, in addition to bathymetry, RhodeFVCOM can be used as a tool to study how different factors influence the flow across the marsh-estuary interface. Marsh water residence time has been demonstrated to have strong control over many wetland processes (e.g. Childers et al., 1993; Bockelman et al., 2002); therefore it cannot be ignored in any realistic wetland hydrodynamic modeling application.

Modeling of the Rhode River can capture the local effect of wind and allow a detailed analysis that would otherwise be difficult to empirically measure. Ongoing

studies are utilizing the hydrodynamic modeling results to drive a biogeochemical model to further explore marsh-estuary dissolved organic carbon cycling. As understanding of the physical drivers of marsh water exchange broadens, improved models will help foster predictions for future changes in tidal wetland-estuary carbon cycling. Quantifying the physical controls on marsh DOM processes will help reduce the uncertainty that still exists on the role wetlands play in estuarine and coastal ocean carbon cycling.

4.7 Acknowledgements

I would like to thank Andrew Peresta for deploying and maintaining the EXO2 sonde at the Kirkpatrick Marsh creek and the entire MARSHCYCLE team for many thoughtful discussions. I would also like to thank my collaborators that contributed to the published version of this manuscript in Estuaries and Coasts, Wen Long, Maria Tzortziou, Patrick J. Neale, and Raleigh R. Hood. This research was supported by National Aeronautics and Space Administration grant NNH13ZDA001N-CARBON. Contact B. Clark for model forcing and output and post processing scripts.

Figures Chapter 4

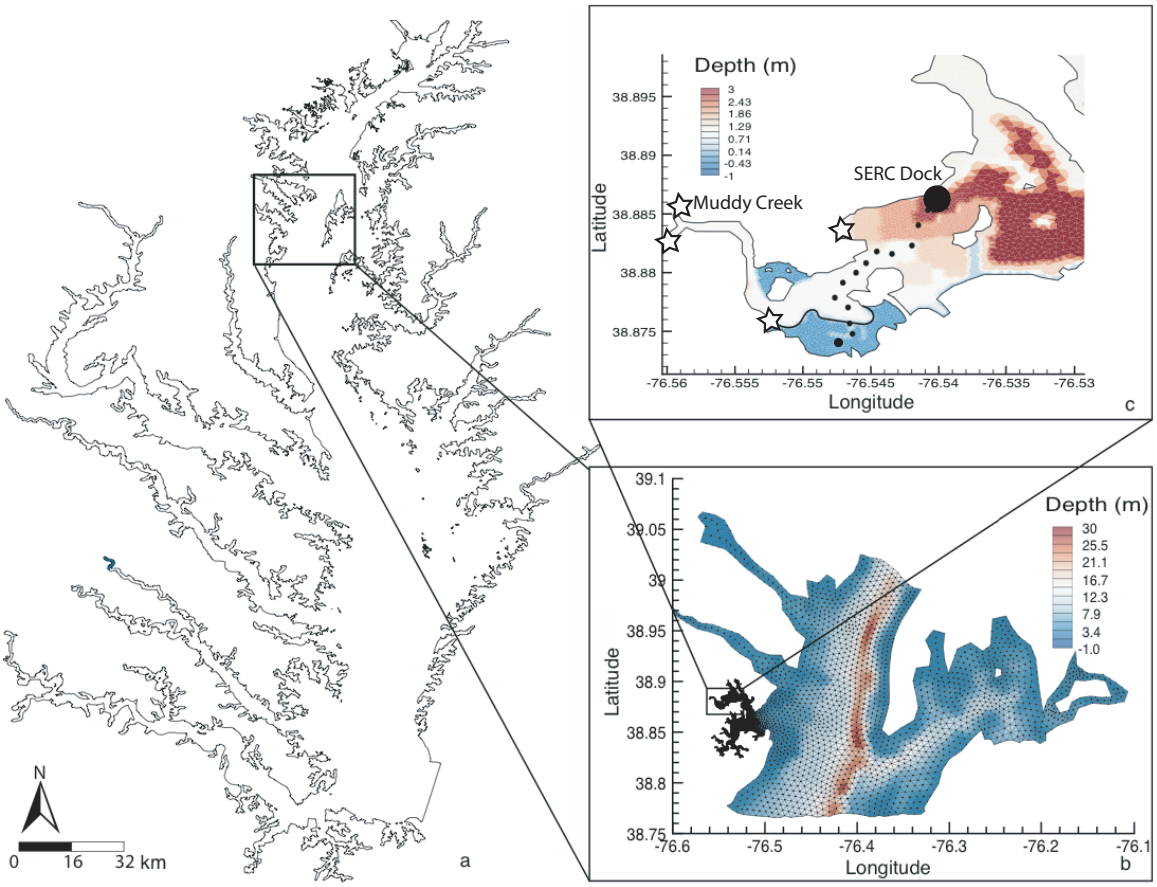

Figure 4.1 (a) Chesapeake Bay with the (b) RhodeFVCOM model domain and (c) the Kirkpatrick Marsh area in the RhodeFVCOM model domain. Stars represent freshwater discharge points and the dot represents the marsh element used in marsh hydrology analysis. The Kirkpatrick Marsh is outlined in (c) and measurements were taken at the marsh creek and SERC, indicated by the arrows.

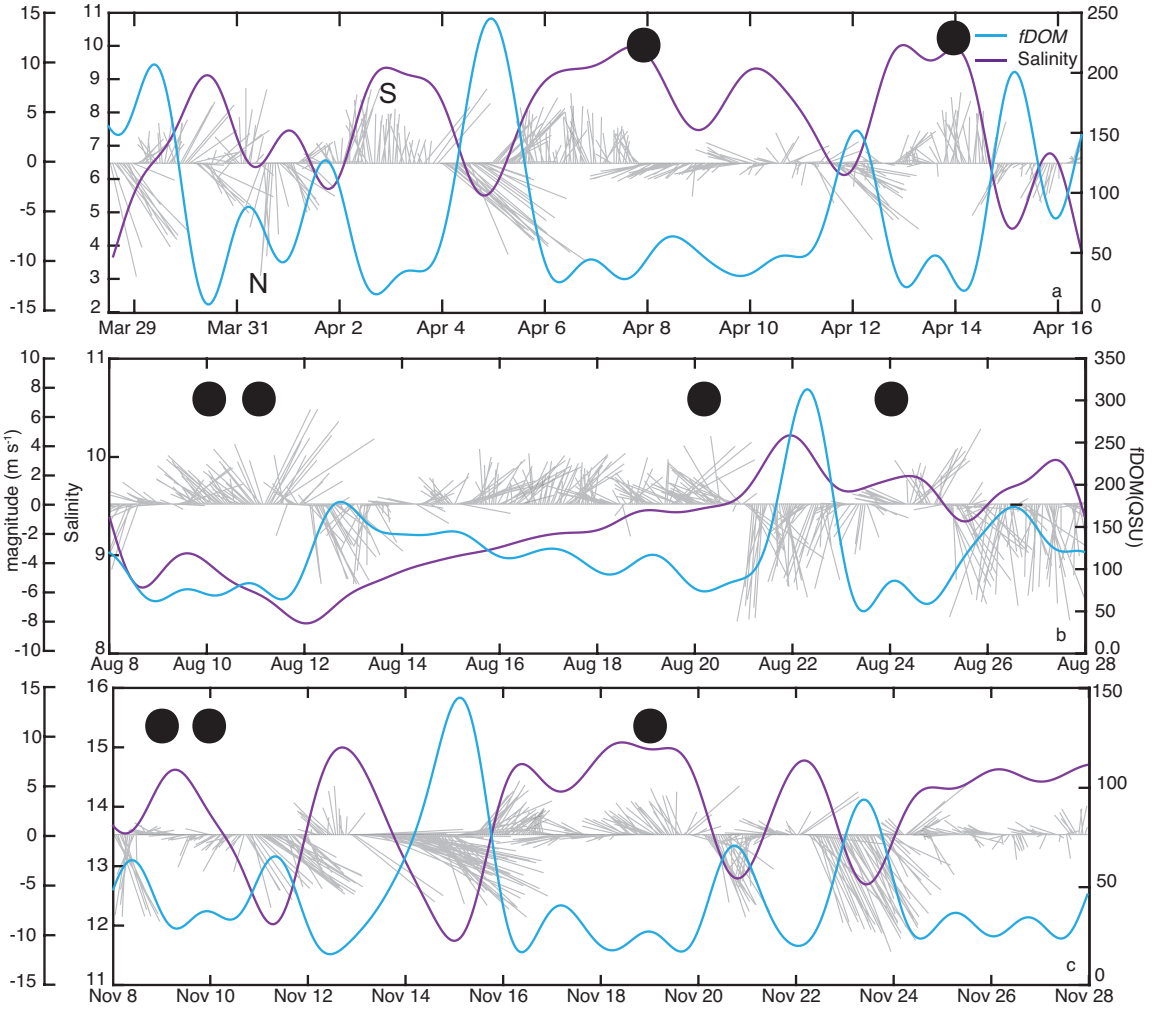

Figure 4.2 Low-pass cutoff filtered (36 hour frequency) salinity and DOM fluorescence (*fDOM)* observed at the Kirkpatrick Marsh creek in (a) spring, (b) summer and (c) fall in 2015. The stick plots are the observed hourly wind speed at Tolchester Beach, MD (NOAA Tides and Currents). Black dots indicate days when greater than 3 mm of rain fell at Annapolis, MD (weatherunderground.com)

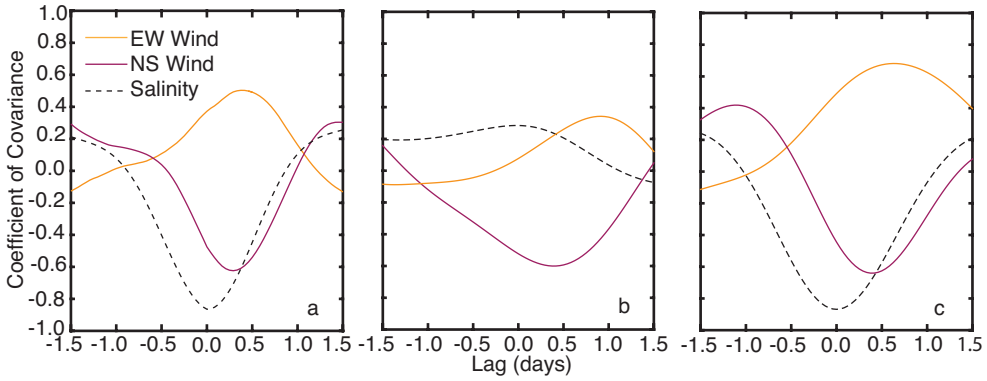

Figure 4.3 Cross covariance of North-South (NS) winds, East-West (EW) winds and salinity with *fDOM* at the Kirkpatrick Marsh creek for the three time periods in Figure 4.2. Southerly wind (*v*) and westerly wind (*u*) are defined as positive. Lags at the maximum absolute covariances are given in Table 3

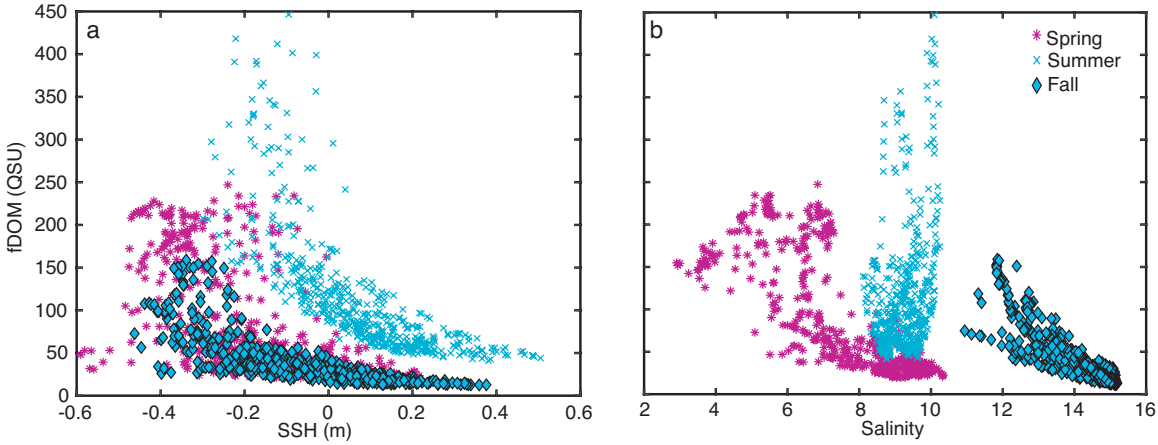

Figure 4.4 *fDOM* versus (a) observed sea surface height (SSH) and (b) salinity at the Kirkpatrick Marsh Creek for the three time series in Figure 4.2.

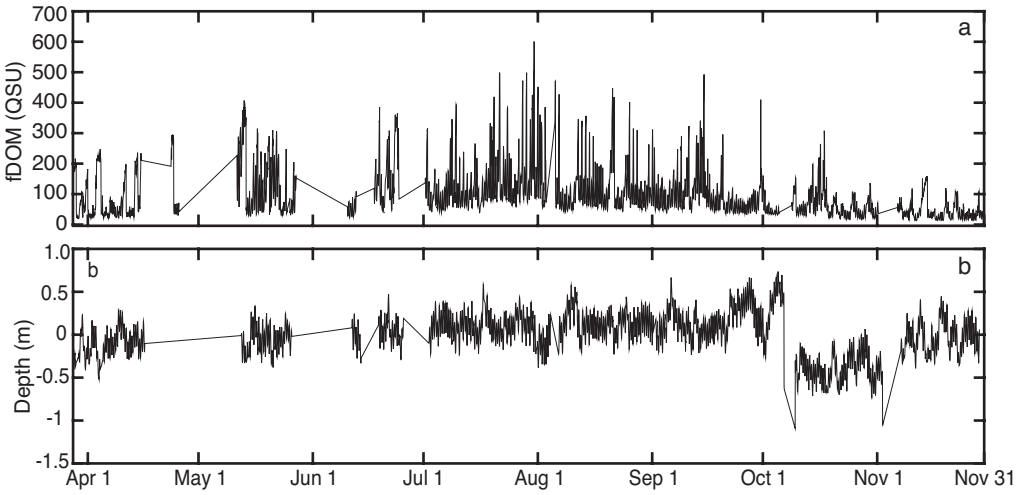

Figure 4.5 (a) Unfiltered *fDOM* and (b) depth for the entire sampling period in 2015. Gaps in the data indicate periods when the EXO-2 Sonde was not deployed.

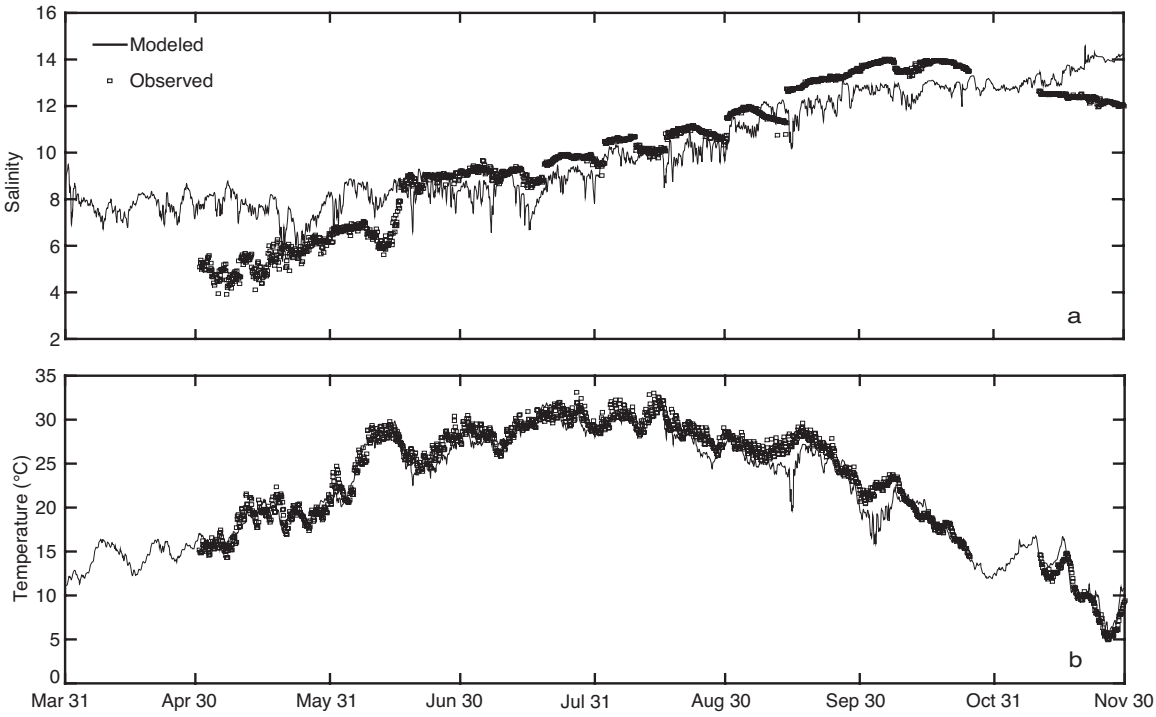

Figure 4.6 Modeled and observed (a) salinity (r = 0.88, RMSE = 1.43) and (b) temperature (r = 0.98, RMSE =1.71 °C) at the SERC dock. Gaps in the observed data are periods when the sonde was removed for maintenance.

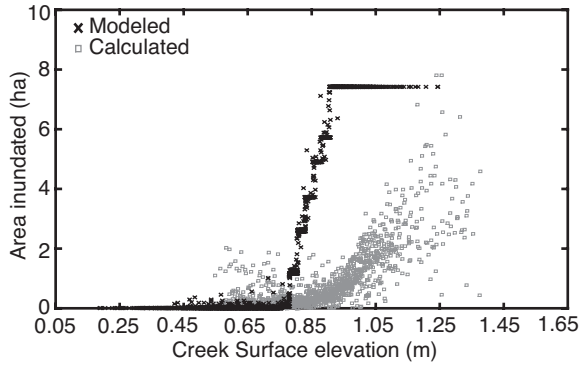

Figure 4.7 A hypsometric curve generated by RhodeFVCOM and calculated inundation area vs. elevation from acoustic Doppler velocimetry (ADV) probe observations at the Kirkpatrick Marsh creek from June – December 2015. Inundation areas were calculated as the flow rate at the marsh creek (m^3 s^{-1}) divided by the rate of tide stage change (m s^{-1}; Eq. 2). The modeled inundated area is the actual area of a sub-section of the marsh that RhodeFVCOM has predicted with a height above D_{min} (0.05 m) at each time step

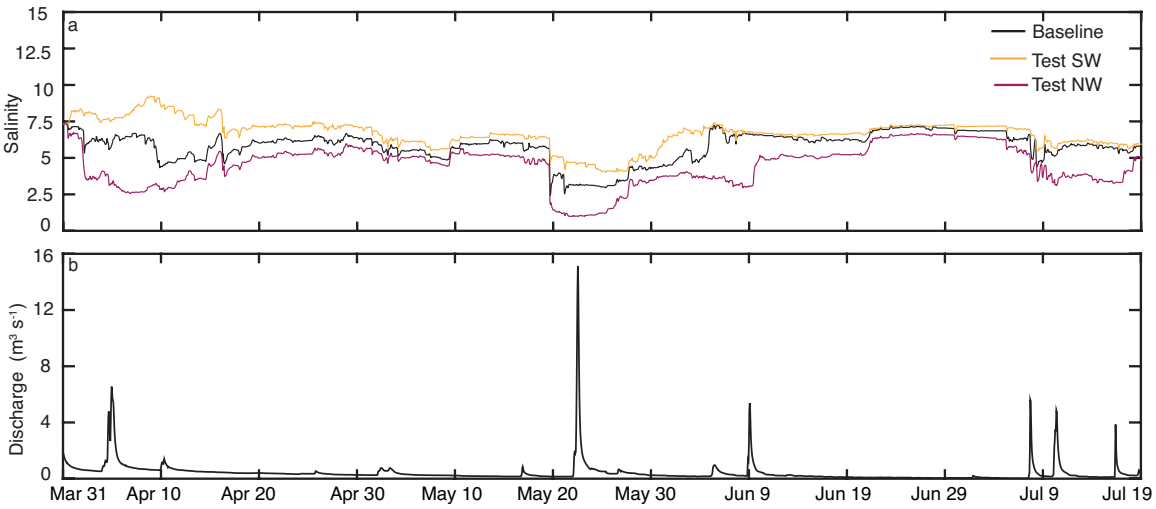

Figure 4.8 (a) Modeled salinity in the Kirkpatrick marsh creek for the three numerical experiments and (b) interpolated river discharge forcing from the Muddy Creek watershed. Test SW is forced with wind from the south during storms, and test NW is forced with wind from the north during storms.

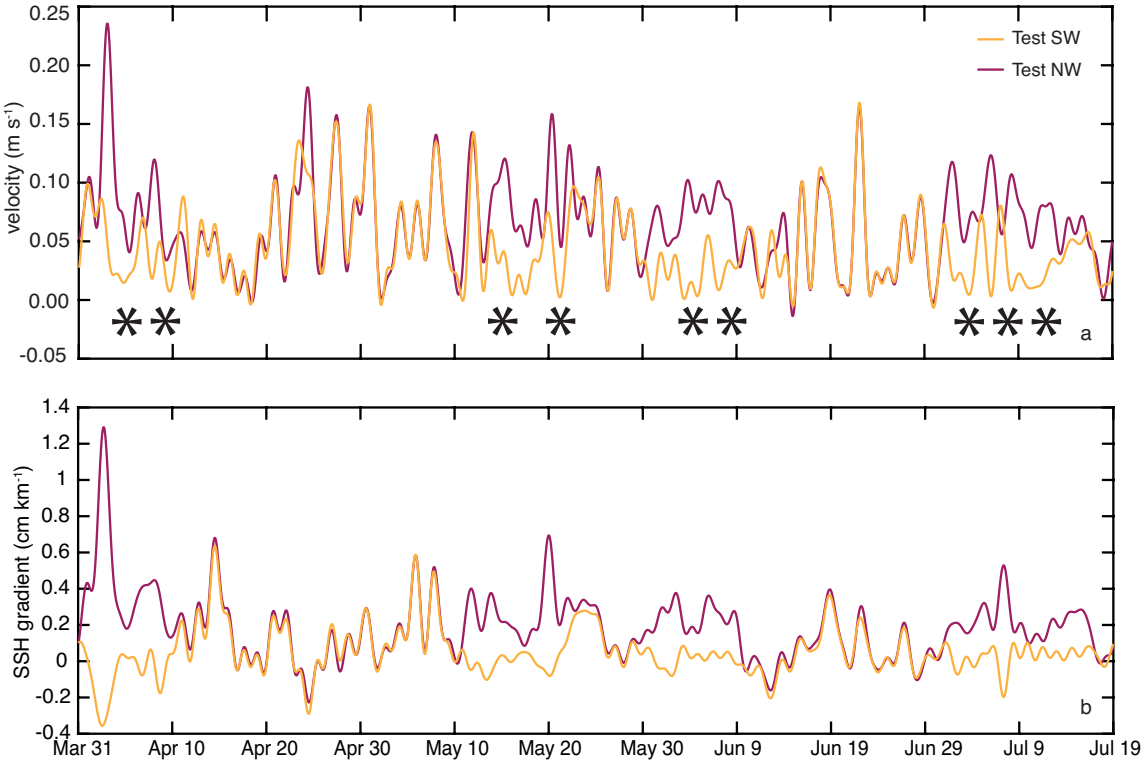

Figure 4.9 (a) Modeled low-pass cutoff filtered (36 hr frequency) marsh creek velocity and (b) sea surface height (SSH) gradient from Kirkpatrick Marsh creek to the opposite side of the Rhode River in spring and early summer. Positive velocity is marsh water efflux and a positive gradient indicates the water surface is sloping away from the marsh towards the mouth of the river. The asterisks indicate when modeled storm winds were applied. Test SW is forced with wind from the south during storms; test NW is forced with wind from the north during storms.

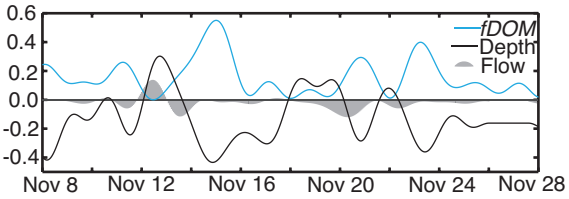

Figure 4.10 Low-pass filtered flow (m^3 s^{-1}), deviation from mean water depth (m), and mean-normalized *fDOM* at the marsh creek. Negative flow is out of the marsh, positive is into the marsh.

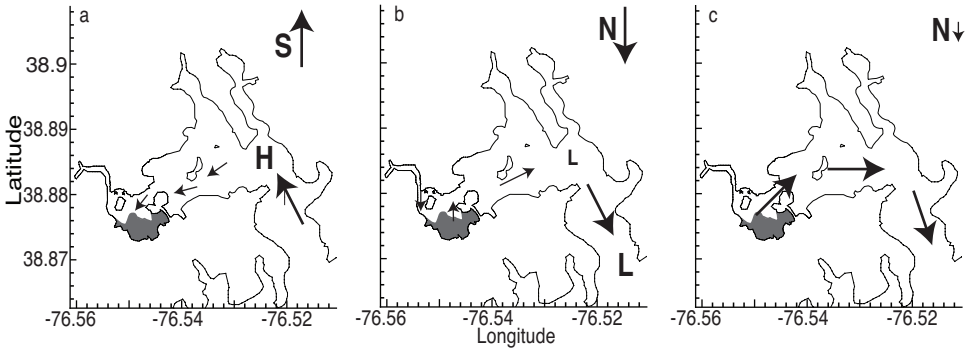

Figure 4.11 Conceptual diagram of the estuarine surface gradient progression during a "typical" wind progression in the Rhode River, MD in the spring and fall. As southerly winds blow a barotropic surface pressure gradient sets up in the back of the Rhode River depicted by the H in (a) that forces water back towards the marsh, depressing flow out of the wetland depicted by the shaded region. As Northwesterly winds progress, local wind driven flow enhances flow out of the creek back towards the marsh, while local wind effects set up a low pressure in the back and mouth of the Rhode River, depicted by the L's (b).

Tables Chapter 4

Table 4.1 Parameters tuned for salinity, temperature and marsh plant drag properties

Parameter	Description	Value
VPRNU	Vertical Prandtl number	1.00
HPRNU	Horizontal Prandtl number	1.00
UMOL	Molecular diffusivity ($m^2 s^{-1}$)	10^{-6}
HORCON	Horizontal diffusion coeff. ($m^2 s^{-1}$)	2.00
B_{FRIC}	Bottom friction	0.002
N	Marsh plant stem density (m^{-2})	600
D	Marsh plant stem diameter (mm)	3.75
C_D	Marsh plant drag coefficient	0.005

Table 4.2 Augmented Dickey-Fuller (ADF) test results and associated p-values for the four variables used in the covariance analysis. If p is less than 0.05, the alternative hypothesis was accepted with 95% confidence of unit root 0 and thus the time series are stationary

Property	Spring ADF, P	Summer	Fall
Salinity	-1.76 , 0.68	-3.99 , <0.01	-3.52, 0.04
fDOM	-3.18, 0.09	-4.83 , <0.01	-2.83, 0.23
NS Wind	-4.09 , 0.02	-3.79, 0.02	-3.74, 0.02
EW Wind	-3.64, 0.03	-5.74, <0.01	-2.83, 0.23

Table 4.3 Lag (hours) at minimum or maximum absolute covariance and the associated coefficient of covariance of observed *fDOM* and wind, salinity and depth for the three observational periods shown in Fig. 2 and for the entire observational record (Total). A complete depth record was not available to coincide with the other measurements.

Property	Spring lag, r	Summer	Fall	Total
NS Wind	10, -0.74	10, -0.64	10, -0.66	9, -0.37
EW Wind	12, 0.66	22, 0.31	16, 0.69	18, 0.36
Salinity	1, -0.81	245 -0.20	0, -0.87	3, -0.55
Depth	1, -0.66	2 -0.76	1, -0.75	-2, -0.09

A comprehensive estuarine organic carbon budget and the importance of tidal marshes in estuarine biogeochemistry

5.1 Abstract

Complicated biogeochemical cycling and differential organic matter reactivity makes quantifying the relative contribution of a given source of organic carbon to the standing stock within an estuary difficult. Here, a new model of tidal wetland-estuary organic carbon cycling is presented for the Rhode River, MD, a well studied tributary of the Chesapeake Bay, USA for April 1-November 30, 2005. The modeling system was used to produce a comprehensive organic carbon budget with unprecedented detail. Tidal wetlands and watershed inputs account for 22.9% of the input of dissolved organic carbon (DOC) into the tributary, with 61.8% coming from phytoplankton production. 95.7% of the particulate organic carbon (POC) within the tributary originated from algal production and subsequent mortality, with 19.86 tons of POC exported from the Rhode River to the mainstem. Overall 87.75 tons of DOC is exported to the mainstem, which accounts for 34.4% of the total allochthonous and autochthonous inputs to the tributary. Removing the wetland at the head of the tributary decreased export of DOC to the mainstem by 20.5%. Furthermore, by removing the marsh, total nitrogen in the tributary decreased, while dissolved oxygen increased. A geographic relationship derived from the Rhode River modeling system indicates that tidal wetlands may contribute 13.4% of the

total DOC stock of Chesapeake Bay. The modeling framework described here can be used across estuarine systems, and provides a new methodology for quantifying the role of tidal wetlands in estuarine biogeochemistry.

5.2 Introduction

Tidal marshes and the estuaries in which they reside are inextricably linked, with biogeochemical processes influencing each sub-ecosystem as tidal water exchanges during flood and ebb. Nixon (1980) showed the nuance through which tidal marshes must be viewed, with the important biogeochemical controls requiring careful consideration within each system. Differences among marsh-estuary ecosystems can be due to plant community (Boschker et al., 1999), salinity regime (Weston et al., 2014), and hydrology (Wolff et al., 1979; Dame, 1995), with all facets convolved to make tidal marsh-estuary organic matter and nutrient cycling difficult to quantify, extrapolate, and generalize across ecosystems. Nonetheless, the important role of tidal wetlands in regional and global carbon cycling is apparent, with estimates of organic carbon export on the same order of magnitude as riverine export (Cai, 2011), and the wetlands of North America fixing as much carbon as the entire continental shelf (Najjar et al., 2018).

Emerging from the research is the clear role tidal brackish and salt marshes play in the carbon cycle within the estuary they reside. Tidal marshes tend to export large quantities of dissolved organic carbon (DOC) (Cai, 2011; Herrmann et al., 2014) much of which is optically complex (Medeiros et al., 2015; Osburn et al., 2015; Tzortziou et al., 2008), with high molecular weight (Helms et al., 2008; Tzortziou et al., 2008), and initially resistant to microbial degradation (Moran et al., 2000; Vähätalo and Wetzel, 2008). In addition, particulate organic carbon (POC) is also exchanged with the estuary, with small-tide, stable marsh systems trapping water column derived inorganic sediment and POC (Jordan, 1991; Kirwan and Megonigal, 2013), and large-tide, ebb dominated marshes exporting marsh derived POC (Dame et al., 1986; Ganju et al., 2013; Ganju et

al., 2015). Substantial variability in the direction and magnitude of POC flux makes generalization difficult (Childers et al., 2002; Najjar et al., 2018), further exhibiting the necessity to develop tools to estimate carbon fluxes in addition to expanding the frequency in space and time over which fluxes are quantified.

Dissolved organic nitrogen (DON) can also be imported or exported from marshes (Dame et al., 1991; Jordan, 1991; Jordan et al., 1983; Wolaver et al., 1983). Marsh-estuary nitrogen exchange is complicated, with plant uptake of inorganic nitrogen, remineralization of DON to NH_4^+, nitrification of NH_4^+, and denitrification of NO_3^-, all influencing the observed exchanges of nitrogen species between marshes and estuaries. These competing processes of uptake and release by both marsh plants and sediment likely lead to the large variance in nitrogen flux direction and magnitude that has been observed (e.g. Dame et al., 1986; Dame et al., 1991; Jordan, 1991; Nixon, 1980; Wolaver et al., 1983).

Across systems, estimates of organic carbon exchange between tidal marshes and the adjacent estuarine waters span multiple orders of magnitude. Herrmann et al. (2014) compiled estimates of United States East Coast salt marsh total organic carbon (TOC) fluxes, that ranged from 48 g C m^{-2} yr^{-1} in the Rhode River, MD (Jordan, 1991), to 456 g C m^{-2} yr^{-1} in North Inlet, SC (Dame, 1995; Herrmann et al., 2014). In the US South Atlantic Bight, tidal marshes are estimated to contribute 1100 g C m^{-2} yr^{-1} to the adjacent bodies of water (Cai, 2011). The most recent comprehensive study of wetland-estuary-coastal ocean carbon cycling in North America found that 64 ± 11% of the carbon fixed by wetland plants is exported to estuaries, while 36 ± 11% is buried in wetland sediment (Najjar et al., 2018). Tidal wetlands are estimated to contribute 33 ± 8% to the organic

carbon input in estuarine systems (Najjar et al., 2018), with the potential for wetland derived DOC to be transported to the coastal and, eventually, open ocean.

Clearly, the wide range in flux estimates across ecosystems, methodologies, and assumptions make extrapolation from one system to regional or global budgets potentially problematic. Based on their relative areal extent, tidal marshes play an outsized role in estuarine elemental cycling (Najjar et al., 2018). But how tidal marshes influence estuarine biogeochemistry, both directly through carbon export and indirectly through biogeochemical cycle alteration, is unclear.

The total amount of marsh-derived DOC that reaches the coastal ocean is unclear, especially because autochthonously produced DOC within estuarine and coastal waters has yet to be quantified on a large scale. Nonetheless, the total amount of carbon moving between coastal systems has been estimated using observational data, although some fluxes still have uncertainty on the order of 100% (Windham-Meyers, 2018), and the original source of the carbon that makes it to the ocean is difficult to quantify. Marsh and riverine derived DOC and estuarine/marine derived DOC can have different biological reactivity and can persist in the environment on different time scales.

To provide an accurate estimate of the exchange of organic matter (both C and N) between marshes, estuaries, and the coastal ocean, tools must be developed that can be utilized across these systems. One such useful tool that is relatively inexpensive and can be reasonably implemented where data availability is sufficient is a numerical model. Numerical models have been utilized to simulate estuarine biogeochemistry and food webs for decades (e.g. Cerco and Noel, 2004; Feng et al., 2015; Xu and Hood, 2006), but only recently have formulations been developed that can simulate organic carbon

transport and transformation processes that are specific to tidal marshes and include, for example, sediment DOC dynamics (Clark et al., 2017) and photochemical degradation of colored DOC.

In this paper a new coupled marsh-estuary hydrodynamic-biogeochemical model is described, hereinafter RhodeFVCOM-ICM. RhodeFVCOM-ICM was developed and implemented in the Rhode River, MD, USA, a well-characterized sub-estuary of Chesapeake Bay. The model allows exploration of the role tidal marshes play in estuary carbon and nitrogen cycling by simulating physical and biogeochemical processes at an unprecedented resolution and scale. Using the model, a comprehensive organic carbon budget for a well-studied tributary of the Chesapeake Bay is presented. The important role of marsh derived DOM and its subsequent transformation during estuarine transit are assessed.

5.3 Methods

5.3.1 The hydrodynamic model and study site

The physical transport of water, salinity and temperature in ICM are driven by the hydrodynamic model, FVCOM (Chen et al., 2003; Kim & Khangaonkar, 2012). FVCOM utilizes a terrain following unstructured grid, making it ideally suited for complex coastal bathymetry. In addition, the wetting and drying treatment within FVCOM makes it well suited for applications in the intertidal range (Chen et al., 2008). Our implementation of FVCOM utilizes 10 sigma layers in the vertical domain, with 14572 elements and 8138 nodes in a mesohaline segment of the main channel of Chesapeake Bay, MD, USA (Figure 5.1a).

The model domain encompasses the study site of the Rhode River, MD, USA where ~21 ha of marsh resides near the head of the small estuary (Figure 5.1c). The main river input in the model is from Muddy Creek, with flows peaking at > 9.0 m^3 s^{-1} during large discharge events. The marsh and estuary is a very well studied system, with researchers from the Smithsonian Environmental Research Center characterizing both the wetland chemistry (https://serc.si.edu/gcrew/nitrogendata) and the water column primary production and nutrient chemistry (Jordan, 1991; Jordan et al., 1991). In addition, multiple studies have characterized the spatial distribution of CDOM and DOC in the water column of the Rhode River (Tzortziou et al., 2008; Tzortziou et al., 2011), and also estimated nutrient and organic matter fluxes at the marsh-estuary interface (Jordan et al., 1983).

5.3.2 The organic carbon cycle model

The U.S. Army Corps of Engineers Integrated Compartment Model (CE-QUAL-ICM; hereinafter ICM) is a well studied and widely applied organic carbon and nutrient cycling model designed for Chesapeake Bay (Cerco and Cole, 1993). ICM has been developed and implemented primarily for quantifying oxygen dynamics in Chesapeake Bay, MD, USA, and has been shown to have good skill at reproducing nutrient cycling variability (Cerco & Noel 2017) and phytoplankton growth (Cerco & Noel 2004). Included here are Appendices in the Supporting Information (SI) that detail all the formulations related to reaction kinetics for each of the ICM water column biogeochemical constituents, including organic carbon, organic nitrogen, inorganic nitrogen, underwater light, phytoplankton and dissolved oxygen. Citations for each parameter are given where available or appropriate in the Appendices.

ICM is offline coupled to FVCOM (Kim and Khangaonkar, 2012), meaning the physical variables relating to water advection and diffusion, and temperature and salinity are first calculated independently of the biogeochemistry. Once a satisfactory hydrodynamic model solution is attained, the solution is stored and then used to drive the biogeochemical kinetic formulations within ICM. This method increases model efficiency by allowing the user to run ICM at a longer time step than the short (6 seconds) required for FVCOM, in addition to decreasing the total number of calculations required at each time step. The FVCOM hydrodynamic model took ~13 hours while the ICM took ~ 6.5 hours to run a 242 day simulation on an Intel® Xeon® E5-2690 24 core server using Intel® Parallel Studio XE 2017 MPI Library.

5.3.3 New components in ICM related to dissolved organic carbon

Marsh derived sediment dissolved organic matter

ICM has been coupled to the sediment flux model SFM (Brady et al., 2013; Di Toro and Fitzpatrick, 1993; Testa et al., 2013), and SFM has also been updated to include DOM (SedDOM-SFM; Clark et al., 2017). As SedDOM-SFM has been detailed in these previous publications, here only the newly introduced model components, namely how the model is loaded with DOM in the marsh, are discussed. There is substantial seasonality in marsh DOM pore water concentration and fluxes (Clark et al., 2018; Schiebel et al., 2018). The model is loaded using a temperature dependent DOC exudation rate that depends on the below ground biomass specified at model startup. The spatial distribution of marsh plant biomass is specified in an input file and remains constant in time but DOM release from the marsh is regulated by temperature from a

basal rate of 0.03 g DOC g biomass^{-1} d^{-1} to simulate seasonality (Appendix I). This provides a relatively simple way to control the loading of DOM into marsh sediments, without having to simulate the complex processes that contribute to it such as physico-chemical reactions in marsh sediment (Qualls and Richardson, 2003) and marsh plant growth and senescence (Schiebel et al., 2018). In addition, a temperature dependent marsh plant uptake of NH_4^+ based on the below ground biomass is included for the potential uptake by marsh plants of inorganic nitrogen (Appendix I) (Bradley and Morris, 1991).

DOM is fractionated as it is loaded into the marsh sediment to resolve the differences in marsh derived DOM reactivity and light absorption, relative to other DOM sources. There are six pools total, divided by biological reactivity (labile, semilabile, refractory) and photoreactivity (colored or non-colored). 80% of the DOM is specified as colored DOC (CDOC) that undergoes interactions with the underwater light field once it enters the water column. 20% is specified as non-colored DOC (NCDOC). DON is similarly fractionated into the model but is scaled with a DOC:DON ratio of 10 g DOC:1 g DON. The coefficients and parameterizations related to marsh DOM loading and marsh sediment characteristics can be found in Appendix I. Sediment DOM is included as a state variable defined at all model locations but the external DOM input is only specified in the marsh locations of the model. It should be noted that the marsh area itself does not contain a dynamic plant community and the associated biogeochemical affects. This was done for simplicity and including a dynamic marsh growth model was beyond the scope of the research questions that are addressed in this paper. However, the variable uptake of

NH_4^+ was accounted for with a first order approximation. Plans exist to couple a dynamic marsh plant m5odel to this modeling system in the future.

Water column DOC formulations and kinetics

Previous versions of ICM included one pool of DOC that was classified based on reactivity by a first order remineralization rate. This updated and enhanced version of the model has split those two classes into three biological reactivity (G) classes (following Keller and Hood, 2011; Westrich and Berner, 1984), and now includes both colored and non-colored dissolved organic matter (CDOx, NCDOx; x stands for C, and N) for a total of six new DOM pools. CDOM absorbs light and an explicit photochemical degradation model transforms that absorbed light energy into chemical reactions. The increased model complexity allows greater flexibility in parameterization, in addition to a more aligned coupling with SedDOM-SFM that also has six classes of DOM. In this section, equations are shown for DOC, while differences are highlighted where appropriate for dissolved organic nitrogen (DON); dissolved organic phosphorus, though included in ICM, is ignored in this research and in the current implementation phosphorus is not included as a limiting nutrient. A model schematic is shown in Figure 5.2 and the detailed formulations are found in Appendix IV.

$$\frac{dDOC_1}{dt} = ADOC_a\, f_{cda1} - kDOC_1\theta_{mnl_1}DOC_1 + (LPOC_{hdr} + RPOC_{hdr})\, f_{hdrc1} - DENIT_c DOC_1 - DDOC_1 + pdDOC_1 \quad (5.1)$$

$$\frac{dDOC_2}{dt} = ADOC_a\, f_{cda2} - kDOC_2\theta_{mnl_2}DOC_2 + (LPOC_{hdr} + RPOC_{hdr})\, f_{hdrc2} - DDOC_2 + pdDOC_2 \quad (5.2)$$

$$\frac{dDOC_3}{dt} = ADOC_a\, f_{cda3} - kDOC_3\theta_{mnl_3}DOC_3 + (LPOC_{hdr} + RPOC_{hdr})\, f_{hdrc3} - K_{COAG}DOC_3 + DDOC_3 + pdDOC_3 \quad (5.3)$$

Equation 5.1 is the mass balance formulation for labile DOC_1. The change in DOC_1 over time $dDOC_1\ dt^{-1}$ (g C m^{-3} d^{-1}) is equal to the first term which represents the formation of algal derived DOC from planktonic algae group a, $ADOC_a$, (g C m^{-3} d^{-1}; see Appendix II for details on phytoplankton growth) fractionated into the DOC_1 pool via fractionation coefficient f_{cda1} (dimensionless) minus the second term which represents the remineralization of DOC_1 via implicit microbial remineralization rate, $kDOC_1$ (d^{-1}) regulated by temperature coefficient θ_{mnl1} (dimensionless). The third term represents the production of DOC_1 by the hydrolysis of labile and refractory particulate organic carbon pools, $LPOC_{hdr}$ and $RPOC_{hdr}$ (g C m^{-3} d^{-1}) fractionated to DOC_1 by hydrolysis fractionation coefficient f_{hdrc1}. The fourth term represents the loss of DOC_1 due to denitrification by rate $DENIT_C$ (d^{-1}) if anoxic conditions exist (see Appendix IV for details). The fifth term represents the rate of change from diffusion across the sediment water interface of DOC, $DDOC_1$ (g C m^{-3} d^{-1}) and the sixth term represents the photochemical degradation of DOC between the photoreactive colored DOC pools (see Clark et al., 2017 for details of the sediment DOC model and Appendix III for details of photochemical degradation model). Diffusion across the sediment water interface can act

as either a source or a sink of DOC but only occurs in the bottom layer of the water column. The detailed formulations for each term can be found in Appendix IV. The first three terms are analogous for all six DOC classes with the fractionation coefficients partitioning the DOC among each pool and the rates being different depending on reactivity. Semi-labile DOC_2 is detailed in Equation 5.2, with the only difference from DOC_1 being no loss occurs via denitrification. Refractory DOC_3 (Equation 5.3) undergoes the same reactions as DOC_2 with the additional potential loss of DOC_3 via coagulation to refractory POC by a salinity dependent coagulation rate K_{COAG} (d^{-1}). In the baseline parameterization, K_{COAG} is equal to 0.0. Appendix V details the formulations for DON where DON is treated very similarly to DOC but is scaled by a C:N ratio where appropriate.

There are three main ways through which DOM is loaded into the estuary: the first is through stream loading from the watershed; the second is from marsh plant exudation and diffusion across the marsh sediment-water column interface during tidal inundation; and the third is through autochthonous algal production, with both DOM exudation and an implicit zooplankton sloppy feeding contributing to the DOC pool. In this version of ICM, two algal groups are used to represent spring and summer time planktonic algae communities. All parameters and equations for algal primary production, nutrient uptake, and DOM production follow Cerco and Noel (2004; 2017) except where otherwise noted in Appendix II.

Lastly, a new photochemical degradation model has been implemented to mechanistically represent the reactions that occur in aquatic systems between colored DOC and light. Upon reactions with light, the colored DOC pools are broken down into

colored pools with less specific absorption and a greater spectral slope (e.g., lower molecular weight; Helms et al., 2008) while some fraction is also completely photobleached. The set of equations and parameters used to calculate $pdDOC_i$ can be found in Appendix III.

Updated underwater light attenuation model: extension into the Ultra-Violet (UV) range

CDOM absorbs light across the UV-Visible spectrum with an exponentially increasing absorption spectra with decreasing wavelength. In order to account for the large amount of light energy that is absorbed by CDOM at short wavelengths and photochemical reactions driven by the light energy, the previous optical model coded into ICM was modified to include UV wavelengths. The previous model used a combination of an optical transfer model to predict the scattering of light in water, in addition to empirically derived functions to calculate the attenuation of light due to algae (chl *a*), total suspended solids (TSS), and CDOM (Gallegos et al., 2006). The attenuation coefficient calculated at every depth in the model was then used to integrate over the visible spectrum to get a total photon flux in the photosynthetically active radiation (PAR) region of the spectrum. This model was inadequate, however, for CDOM because changes in absorption related to the quality of CDOM was not included (e.g., an increasing spectral absorption slope with increased light exposure), and there was no representation of the transmission and attenuation of UV light in the water column. Modifications were made to the spectral light attenuation model to account for the composition of CDOM and its effect on the spectral attenuation of light, in addition to the attenuation of light in the UV range by the other water column constituents. The

modifications were done following Rose et al. (2018) to incorporate specific absorption spectra for TSS and chl *a*, and specific scattering of TSS that extends from the visible range into the UV spectra. Instead of utilizing the previously derived empirical functions (Gallegos et al., 2006), the model now uses the product of the total concentration of each constituent (g m^{-3}) and its specific absorption spectra (m^2 g^{-1} nm^{-1}) to calculate the spectral absorption (m^{-1} nm^{-1}) of each constituent at all of the 417 wavelengths from 284 to 700 nm. The individual absorption spectra are then used to calculate the diffuse attenuation coefficient (kd; m^{-1}) and thus the attenuation of light in the water column. Appendix III details the equations utilized in the light model, and the specific absorption spectra utilized to calculate each water quality constituent are shown in Figure 5.3.

5.3.4 Biogeochemical model forcing

Inputs from the Rhode River watershed

The main watershed input to the Rhode River estuary enters from Muddy Creek. The watershed is extremely well characterized in terms of its biochemical constituents making specification of the forcing relatively simple. However, some assumptions related to organic matter partitioning were necessary. Long term monitoring of the watershed and the estuary allow for detailed forcing for nutrients and algal biomass, and the collection and sample processing has been detailed elsewhere (Jordan et al., 1991). All samples used to extrapolate out to the entire model area were collected at the headwaters of Muddy Creek (Figure 5.1c). Land use was assumed to not be a significant factor across sub-watershed in nutrient dynamics, but was factored in for DOM forcing and partitioning. Discharge is scaled by watershed area while concentration was assumed to be that of Muddy Creek, therefore the loads entering the watershed at each location only

change due to variations in discharge. Algal biomass (g C m^{-3}) was calculated using observed chl *a* concentrations at the head of Muddy Creek and a fixed Carbon to chl *a* ratio of 50 mg C (mg chl *a*)$^{-1}$ and partitioned evenly between the two algal groups in ICM (see Gallegos et al., 2010 for station location and chemical analysis).

NH_4^+ and $NO_{3,}^-$ were measured in the headwaters and were applied to the model directly from observations. Inorganic suspended sediment was estimated as the difference between total suspended solids, algae and particulate organic carbon. DOC and POC were measured as chemical oxygen demand and converted to carbon units by a factor of 2.9 (Oxygen:Carbon, Patrick J. Neale, personal communication). A linear regression method was used to model POM C:N ratio as a function of percent forest in the watershed using data from Lu et al. (2014). Land cover data in the Rhode River watershed was taken from Breitburg et al. (2008). The regression for the C:N ratio from the small streams in Virginia from Lu et al. (2014) is shown in Figure 5.4. 20% of POM from Virginia streams was composed of labile long-chain fatty acids, therefore stream POM was partitioned as 20% labile and 80% refractory (Lu et al., 2014).

The C:N ratio calculated for POM for each sub-watershed was also applied to DOC in the model forcing to calculate DON. Watershed derived DOM (both C and N) was partitioned into the three reactivity classes following Lu et al. (2013) who found that 16.3% of all DOC across watersheds was biologically labile and significant differences didn't occur across varying land use. The remaining 85.7% of the DOC was further partitioned into 30% semilabile and 70% refractory. Importantly, the three reactivity classes were also partitioned into the colored or non-colored (e.g., photoreactive or non-photoreactive) classes to complete the river forcing input. Similar to the C:N ratio, this

was done using a simple least-squares linear regression model of the percent of the DOM pool that is CDOM as function of forest cover. The fraction of CDOM was found to be significantly related to land use type and was modeled as the product of 0.6 and the fraction of forest minus 0.0274 (Lu et al., 2013).

Open Boundary forcing

The RhodeFVCOM-ICM model domain has a northern open boundary located near the Chesapeake Bay Bridge and a southern open boundary that spans across the main-stem of Chesapeake Bay just north of Poplar Island (Figure 5.1). The physical forcing at the boundaries was specified using a Chesapeake Bay implementation of the Regional Ocean Modeling System (ROMS; Xu et al., 2012). For the biogeochemical model forcing, Chesapeake Bay Program (CBP) Water Quality Database (http://data.chesapeakebay.net/WaterQuality) data was used to generate the necessary forcing variables. The CBP stations closest to the model boundaries were extracted for all variables that could either indirectly or directly be used for forcing the model. These data were interpolated in both time and space to the model grids at the open boundaries. NH_4^+, NO_3^-, and total suspended solids (TSS) were used directly to force the model. Chl *a* was converted to the algae 1 (spring) and algae 2 (summer) biomass by splitting the total chl *a* concentration into each group evenly and converting to carbon biomass using a C:Chl *a* ratio of 50:1 (g C g chl a^{-1}).

The remaining state variables were inferred or calculated from the available data as follows: DOC at the open boundary was converted from measured DON assuming Redfield stoichiometry (5.68 g C g N^{-1}) and fractionated into the three reactivity classes

following Keller and Hood (2011) (40 % DOM_1, 59 % DOM_2 and 1.0 % DOM_3). POC was similarly converted from measured PON (difference between measured total organic nitrogen and DON) using the Redfield ratio.

The northern boundary was interpolated from CBP stations CB3.3W, C, and E linearly in time, depth and space to the northern boundary at a daily interval and across the X-Y horizontal and Z vertical domain using the MATLAB function *griddatan*. Each time point was first interpolated to the model layers linearly, extrapolating to points outside the measured depth using a nearest neighbor scheme. Next, a linear interpolation was done in time at each station and each depth to a daily frequency. Finally, a two dimensional interpolation was conducted in space to each model boundary node using a nearest neighbor extrapolation to points that resided beyond stations CB3.3W and CB3.3E. The southern boundary was interpolated in depth and time using a similar scheme to the northern boundary, although 6 stations (CB4.2 W,C,E and CB4.3 W,C,E) were used because the southern boundary was located in between each set of stations.

Surface meteorological forcing

The model was forced at the surface with short wave radiation and wind speed from the North American Regional Reanalysis weather product with spatially constant, time varying values for the modeled time period. The physics for FVCOM are responsive to all surface forcing and ICM utilizes the water column FVCOM-predicted temperature, salinity and velocity fields. The biogeochemical portion of ICM uses wind speed to calculate air-water oxygen transfer and solar radiation to calculate underwater light penetration and attenuation. NARR 3-hourly wind speed was averaged for each day (8

time points per day) to get the daily averaged wind speed over the model domain. The daily averaged NARR short wave radiation product was applied to RhodeFVCOM by scaling it by a factor of 0.43 to remove the infrared portion of the short wave radiation product. The total UV-Visible surface irradiance is then broken down by wavelength into UV-Visible spectra (284-700 nm) by the solar spectral distribution of light (Figure 5.5). ICM calculates the incident irradiance internally utilizing an empirical function that solves for the declination of the sun and length of day based on latitude and the time of the year.

5.3.5 Model validation statistical analysis

Comparison statistics were used to analyze the degree of success of the model at recreating the variability of CBP-measured biogeochemical constituents. Coefficient of variance (r), root mean square error (RMSE), Willmott Skill (WMS), Mean Percent Error (MPE), Reliability Index (RI) and Model Efficiency (MEF) (Stow et al., 2009) were calculated at stations XGE3275 and WT8.2 in the Rhode River (Figure 5.1c) and at stations CB4.1W, C and E which reside near the middle of the main-stem of the model domain (Figure 5.1b). The comparison was made by finding the closest model points in time and depth to each CBP observation, providing the most rigorous and strict model comparison available. Each statistical measure is reported for complete transparency as some model statistics capture phenomena and patterns better than others (Stow et al., 2009). The model was optimized to achieve the best distribution of DOC (and secondarily DON) in the Rhode River at stations XGE3275 and WT8.2 while attempting to maintain relatively high model skill in nutrient, oxygen and chl *a* solutions.

5.3.6 Dissolved organic carbon model scenarios

Four model scenarios were run to examine the influence of marsh derived DOM on the distribution and flux of organic matter throughout the Rhode River. First, marsh DOM production and plant uptake of NH_4^+ was left on in the baseline, full ecosystem scenario (+M). Second, the marsh plant biomass was reduced to zero, removing the input of DOM and uptake of NH_4^+ by the marsh from the model domain (-M). The physical effects and topographic characteristics of the marsh were unchanged. To further understand the role that photochemical degradation and coagulation of DOC_3 played in the total DOC budget in the Rhode River, runs with photochemical degradation off (-PD) and the basal coagulation rate increased from 0.0 to 0.01 d^{-1} (+CG) were also conducted. Budgets for each of these scenarios in the Rhode River were calculated by integrating in time and space all of the sources and sinks for each DOC class grouped by reactivity. A similar process was conducted for total DON, inorganic nitrogen and POC for each model test. The overall budget for the +M scenario is presented for both the Rhode River and the entire model domain for April 1st, 2005 through November 30th, 2005. The balance after integrating and summing all of the source and sink terms was assumed to be the flux across the boundary of the region where the budget was calculated

Initially, due to computational constraints and the challenge of processing output with dozens of variables across the entire model domain at every depth, the model results were output at a period of 0.75 days. Subsequent analysis showed the long sampling frequency biased the outputs to miss fine scale tidal variation and substantially over predict the accumulation of DOC in the tributary while under predicting the export of DOC to the mainstem. This is unsurprising as the Rhode River and Kirkpatrick Marsh are

largely governed by tidal exchange, and by sampling at a longer frequency the only the roughly average condition was captured. A substantial effort was made to give RhodeFVCOM-ICM the computational tools, namely the output for all variables in NetCDF format, to post-process and calculate budget terms at an hourly frequency for the entire model domain. When working in a system where tidal dynamics are potentially important, the effects of aliasing tides due to the model sampling period must be considered to avoid inaccurate estimates of flux terms.

5.4 Results and Discussion

5.4.1 Model Validation

The model parameters were tuned to achieve the best fit to observed DOC data at two CBP water quality monitoring stations in the Rhode River. The model was also adjusted to qualitatively agree with observed DOC concentrations and CDOM absorbance at 440 nm (a440) along a transect. The two main parameters that were adjusted to achieve the best fit to time series (Figure 5.6) and transect (Figure 5.7) data were the DOM remineralization rates, $kDOC_i$, and the loading term into the marsh sediment porewater, $ExRate_0$. The high model skill (Table 5.1) for DOC and DON gives confidence in the model test-scenarios used to determine a budget of sources and sinks of DOC and DON for the Rhode River.

There was a strong correlation between modeled and observed DOC in the Rhode River throughout the year, with the model capturing the observed seasonal trend, exhibiting little bias, and also capturing much of the short term variability in DOC concentration (Figure 5.6). Statistical analyses of DOC comparisons (Table 5.1) confirm the remarkably high skill of RhodeFVCOM-ICM in modeling DOC concentration in time

at these two stations. Each gray transect line in Figure 5.7 displays a model predicted transect of DOC concentration extracted at hourly intervals in July of 2005 on all ebb tides when the water surface elevation is dropping, while the observational data (diamonds) were averaged between three transects collected during ebb tides when the spatial gradient in each component is likely the greatest; two in summer 2006 (Tzortziou et al., 2011) and one in July 2016. Although there was substantial variability in the model solutions at any given point along the transect, the model captures the spatial gradient in DOC and a440 away from the marsh into the estuary quite well. A DON model-data comparison for station WT8.2 can be found in Figure 5.8a & b.

Modeled temperature (WMS of 0.96 and 0.98) and salinity (WMS of 0.78 and 0.83) time series correspond well with observations in the Rhode River, indicative of the models ability to simulate the hydrodynamic variability and freshwater discharge balance into the estuary. The relatively high skill of salinity indicates that transport and mixing within the Rhode River was reasonably simulated, and achieving an accurate temperature solution is key to simulating the biogeochemical reactivity rates with first-order accuracy. Dissolved oxygen (DO) concentration achieved a WMS of 0.61 and 0.57 and coefficient of variance (r) of 0.41 and 0.49 for both stations in the Rhode River (Figure 5.8c & d). Seasonal oxygen variability was well captured, but the high degree of temporal variability caused some model-data comparisons to be slightly mismatched that led to some of the error. Nonetheless, the oxygen field throughout the model was well captured, on average.

Statistics for all other model-observational comparisons where observational data was collected in the main stem of Chesapeake Bay are supplied in Table 5.2. Chl *a* was

predicted with relatively good accuracy in the mainstem of Chesapeake Bay, but the model under predicted concentrations > 80 mg chl *a* m^{-3} in the Rhode River during peak biomass in the late summer (Table 5.1; Figure 5.8e & f). The mean condition is well captured, however, with an MPE of 2.00 and -10.49% for the two stations in the Rhode River. The underestimation of chl *a* during summer can be attributed to the fact that the model lacks the ability to simulate bloom forming species that lead to high algal biomass (Gallegos et al., 1997). NH_4^+ and NO_3^- also show general agreement with the observations in the mainstem of the bay (Table 5.2) while NO_3^- in the Rhode River is generally under predicted in the spring, although values rapidly decline to zero in the early summer and remain low for both the model and observations (Figure 5.8g & h and Figure S4i & j). The quick decline of NO_3^- is owed to the fast uptake by phytoplankton due to primary production and high uptake into the sediment via denitrification as temperatures warm and oxygen demand increases. A similar pattern is observed in the CBP data, although RhodeFVCOM-ICM predicted a more rapid drawdown of NO_3^-. Predicted and observed NH_4^+ shows good agreement in the warm months in the Rhode River and model statistics show a good fit, in general (Table 5.1). As in all biogeochemical models, there are inherent tradeoffs among the skill of model variables when optimizing the solution to the observed data; skill in some variables is sacrificed to achieve the highest skill possible in others.

POC is generally under predicted in the Rhode River (Figure 5.8k & l) with a mean percent error of 27.4 and 44.5% for the two stations. The under prediction of POC is likely due to three factors. First, as previously stated, phytoplankton concentration is generally under predicted and phytoplankton biomass makes up a substantial portion of

the POC standing stock in RhodeFVCOM-ICM. Second, even though there is a formulation to account for the impact of sediment resuspension on light attenuation via the mobilization of ISS (Appendix VIII), this resuspension does not include the sediment POC pool. Not including the POC pool in the resuspension formulation was done for simplicity and to maintain organic carbon mass conservation, but in shallow systems this is likely a large source to the water column. Finally, POC was not measured by the CBP and therefore was estimated from measured particulate organic nitrogen (PON) using the Redfield ratio of 5.67 g C g N^{-1}. If in reality the C:N ratio of the POC in the Rhode River was less than Redfield, the estimated observed POC concentration used for the comparison would be greater than the true value.

Shallow water modeling is particularly challenging, especially when attempting to cross multiple ecosystem types (marsh - shallow estuary - deep estuary) and capture the seasonal and spatial variability in each biogeochemical constituent in each sub-ecosystem. There is an inherent tradeoff between shallow vs. deep systems, with shallow systems being heavily influenced by the benthos (Soetaert and Middelburg, 2009). Physical processes differ in well-mixed shallow systems such as the Rhode River vs. the seasonally stratified mainstem of Chesapeake Bay (Pritchard, 1952). However, in general RhodeFVCOM-ICM broadly captures the observed patterns, especially in relation to DOC and DON in both shallow and deep observational stations. Oxygen is consistently modeled well throughout both shallow and deep areas and in particular in the Rhode River. Sediment oxygen demand accounts for a large portion of the oxygen drawdown in the water column in the shallow areas and is highly sensitive to the POM sinking velocity.

Moving forward, if cross-ecosystem modeling is to progress, fundamental processes that differ substantially between shallow vs. deep estuaries need to be considered. In particular, sediment-water column coupling that explicitly includes more processes such as sediment resuspension (Moriarty et al., 2017) and the subsequent response of biogeochemical cycling to resuspended sediment in the water column should be explored. Reactions of organic matter transformation between particulate and dissolved phases, and vice-versa, should also be considered especially with relation to salinity dependence (He et al., 2016). Potentially expanding or re-parameterizing phytoplankton to represent shallow tributary vs. deep phytoplankton communities may also need to be considered to capture the bloom dynamics in the observational data. Lastly, the plant community within an ecosystem should be represented if more nuance is required to capture the direct interaction between the marsh and the water column during tidal inundation. The contribution of plant senescence in temperate regions to the total annual flux of organic carbon may be significant and currently cannot be captured with RhodeFVCOM-ICM.

5.4.2 Organic carbon flux between the marsh and the estuary.

The DOC flux from the marsh was seasonally variable (Figure 5.9a), increasing through the spring, peaking in late summer and subsequently declining in fall. The flux was also highly variable in time with values ranging from 30.6 to 3158 mg C m^{-2} d^{-1}. The average areal flux from the marsh sediment into the water column is 580.1 mg C m^{-2} d^{-1} (211.7 g C m^{-2} yr^{-1}), which is quite high relative to the previous estimates of 48 g C m^{-2} yr^{-1} (Jordan, 1991) and 32 g C m^{-2} yr^{-1} (Tzortziou et al., 2008). Over the entire 242-day model time period 29.47 tons of DOC effluxed from the marsh sediment into the water

column during inundation. The total POC settling flux (Figure 5.9b) into the marsh of 89.7 mg C m^{-2} d^{-1} (32.7 g C m^{-2} yr^{-1}, 4.56 tons over 242 days) was 84.5% less than the quantity of DOC that is being exported; the marsh traps particulate carbon derived from the estuary (and potentially the watershed) while exporting large quantities of DOC to the Rhode River. The daily flux estimates of DOC and POC, respectively, were determined by dividing the total integrated flux of 29.47 and 4.56 tons C by the model time period of 242 days. The annual estimate was made by taking the daily values of 580.1 and 89.7 mg C m^{-2} d^{-1} and multiplying by 365 days.

The discrepancy between the RhodeFVCOM-ICM predicted flux and what has been measured at the marsh creek could potentially be attributed to multiple factors. First, the area sampled in the two previous observational studies from the Kirkpatrick Marsh (~3 ha) was much smaller than the entire marsh area (21.0 ha) included in RhodeFVCOM-ICM. Second, the observations were collected by measuring DOC and POC concentration and flow coming out of a single creek draining the marsh, whereas the model is directly integrating all of the DOC and POC that crosses the sediment-water interface from the marsh into/out of the tidal waters. Assuming minimal processing of the water column DOC on the marsh surface due to relatively short marsh platform residence times, this would lead the model to be only slightly biased upwards relative to observations. Perhaps the most important difference between the observed and modeled DOC and POC flux estimates is that the observations do not include large weather driven events (e.g., storms and high/low water inundation events that have been shown to drive large variations in concentration and flow) that are captured in their entirety by RhodeFVCOM-ICM. This conclusion is supported by a recent estimate using high

temporal resolution measured fluorescent DOM as a proxy for DOC and water flow that yielded an annual DOC flux of 173.6 g C m^{-2} yr^{-1} out of the marsh creek (Menendez et al., unpublished data). The model predicted net total organic carbon flux of 179.0 g C m^{-2} yr^{-1} is consistent with a synthesis of East Coast estuaries that found that the average annual lateral net (DOC - POC) organic carbon flux between wetlands and estuaries was 185±71 g C m^{-2} yr^{-1} (Herrmann et al., 2014). Lastly, it should be noted that net ecosystem exchange (total uptake of atmospheric CO_2 into the marsh) measured at the Kirkpatrick marsh averaged 1900 g C m^{-2} yr^{-1} over a 19 year time series (Erickson et al., 2013), allowing for ample transfer of carbon fixed by the plants into both sedimentation, DIC lateral export, and the 211.7 g C m^{-2} yr^{-1} of predicted lateral DOC export.

5.4.3 Rhode river organic carbon budget analysis

Baseline DOC budget in the Rhode River

Figure 5.10 shows the DOC budget for the Rhode River estuary from April 1 to November 30, 2005, with the region for the budget depicted in Figure 1c (the entire Rhode River). Each DOC reactivity class has been partitioned to examine differences in source-sink dynamics in each pool, while the total DOC budget (sum of three lability classes) for the Rhode River is presented as the blue bars. All positive values represent a source to the estuary, while negative values indicate a sink from the estuary. The gross DOC production (GDP) is the summation of all DOC sources to the estuary, including the marsh and the watershed. The export to the mainstem is estimated by taking the difference between all sources, sinks and the accumulation of DOC throughout the model time period, **Δ**DOC. Algal derived DOC was the largest source of DOC_1 (67.0% of GDP, 63.05 tons) and DOC_2 (63.3%, 86.70 tons), while only comprising 12.9% of the GDP of

DOC_3 (7.88 tons). Algal derived DOC contributed 157.6 tons of total DOC (61.8%) to the Rhode River, the largest source of DOC to the estuary by a substantial margin. The algal derived DOC includes both direct exudation (10% of primary production, Baines and Pace 1991) and algal death (20% of implicit algal mortality).

The Kirkpatrick Marsh and the Rhode River watershed combined added 22.9% of the total DOC to the Rhode River. 29.06 tons of DOC (11.4%) entered from the watershed, the majority of which was delivered during the spring when discharge was greatest. 16.3% of the riverine DOC is DOC_1, 25.1% is DOC_2 and 58.8% is DOC_3. The Kirkpatrick Marsh contributed 29.47 tons (11.6%) of total DOC, the majority of which was colored and photoreactive (80% of DOC input to marsh sediments is colored). 88.1% (25.98 tons) of the total DOC from the marsh sediments was DOC_3, while 6.96% and 4.90% was DOC_2 and DOC_1, respectively.

Sub-tidal estuarine sediment was a large source of DOC_2 (23.0%, 31.51 tons) and DOC_3 (15.3%, 9.33 tons) while acting as a sink of estuarine DOC_1 (18.7%, 17.55 tons). Over the entire model deployment period, the total net flux of DOC was 23.29 tons from the sediment, making up 9.13% of the GDP in the Rhode River. Although the total DOC flux was the fourth largest source (out of five), the sediment was differentially altering the composition of the DOC pool in the water column, taking up the most reactive compounds into the sediment while releasing less reactive compounds into the water column. The behavior of the model sediment coincides with a previous idealized modeling study looking at main channel Chesapeake Bay sediment (Clark et al., 2017).

The largest sink term of DOC in the Rhode River water column was heterotrophic remineralization. 170.1 tons (66.7%) of the GDP was lost due to remineralization, 69.2%,

73.3% and 7.48% of $DOC_{1\text{-}3}$, respectively. The reason that relatively more DOC_2 is lost to remineralization than the more reactive DOC_1 is the uptake of DOC_1 into the sediment and the greater overall production of DOC_2 from phytoplankton. The direct photo-remineralization of DOC was very small (0.07% of GDP) but the photochemically mediated transformation of DOC between pools was dynamic and substantial. 26.6% (16.27 tons) of the DOC_3 input was lost due to photochemical degradation with the vast majority being shunted to $CDOC_1$, and only 0.26% of DOC_3 being directly photomineralized to DIC. 19.36 tons (20.6%) of the DOC_1 GDP was from photochemical degradation of $CDOC_3$ and $CDOC_2$ indicating the importance of including this pathway in the modeling framework. The degradation of CDOC with lower biological reactivity into the more biological labile pool increased the total remineralization of DOC into inorganic carbon. Photochemistry-driven changes in the biological reactivity of DOC have been observed across systems (Reader and Miller, 2014; Moran et al., 2000; Vähätalo and Wetzel, 2008), and was one of the primary concepts used to formulate the photochemical degradation model utilized here. DOC_2 plays a smaller role in the photochemical degradation pathways, with 2.29% of DOC_2 production being photodegraded.

The Rhode River was a net source of DOC to the mainstem, although the relative biological reactivity of the DOC varied considerably in magnitude. The net total DOC flux out of the Rhode River was 87.75 tons of C, which was 34.4% of the GDP within the tributary. All three reactivity classes of DOC were exported out of the tributary at varying percentages of the total GDP depending on the biological reactivity. 12.0% and 25.2% of DOC_1 and DOC_2 GDP was exported from the Rhode River to the mainstem. The largest

contribution to the total flux was from the DOC_3 pool with 41.9 tons of C, comprising 68.6% of the total DOC_3 inputs and 47.8% of the total DOC export to the mainstem. The export of more refractory DOC components from tidal marshes and watersheds is a well-described phenomenon (Lu et al., 2013; Moran et al., 2000; Osburn et al., 2015; Tzortziou et al., 2008). The variable composition of the total DOC being exported is attributed to the varying sources of DOC to the tributary. This is further explored in section 3.4 where the model scenarios are analyzed.

If the entire model domain including the mainstem of Chesapeake Bay is decomposed into a budget similarly to the Rhode River, the role of each process on a larger scale in a predominantly estuarine system can be analyzed. Unsurprisingly, the relatively tiny Kirkpatrick Marsh contributed 0.03% to the total DOC budget in the mainstem, with 0.34% of the DOC_3 originating from the marsh. The largest sources were estuarine sediment (25.6%, 25351 tons), algal derived DOC (48.4%, 47951 tons) and the hydrolysis of POC to DOC (26.0%, 25720 tons) leading to an export out of the model domain of 15360 tons of DOC (15.5%). The vast majority (84.1%) of total DOC was remineralized in the model domain. Measurements of sediment DOC and DON fluxes in the deep mainstem of Chesapeake Bay have shown a relatively minor role in the overall sediment-water column carbon (both organic and inorganic) budget with DOC efflux ~10% that of CO_2 production via heterotrophic remineralization (Burdige and Homstead, 1994). The model results here suggest a larger impact of sediment DOC efflux on the organic carbon budget. This is likely due to the inclusion of the shallow flanks within the model domain where the contribution of sedimentary fluxes of solutes play a much larger role in water column biogeochemistry (Soetaert and Middelburg, 2009).

Baseline POC Budget in the Rhode River

The POC budget must also be analyzed to provide a full organic carbon production analysis of the Rhode River. It should be noted, however, that POC in the Rhode River is under predicted, while in the mainstem it tends to be over predicted (Figure 5.8k & l). The Rhode River was a source of POC to the mainstem of Chesapeake Bay, with 19.86 tons C (4.92% of gross POC production) being exported from the tributary. Only 1.13% (4.56 tons) of the POC produced within the estuary was trapped in the marsh. Phytoplankton accounted for 95.7 % of the total POC production in the Rhode River, with the remaining 4.3% originating from the Rhode River watershed. 60% of the algal predation mortality is partitioned to POC, 20% of which is labile and 80% of which is refractory (Appendix V). Only 3.87% of the POC is lost via the hydrolytic pathway to DOC.

Net ecosystem production in the Rhode River

Net ecosystem production (NEP) for the Rhode River can be defined as the net total organic carbon that is produced within the estuary. This is following a comprehensive analysis of NEP for the east coast of North America whereby each region's carbon budgets were estimated using representative ecosystems and mass balance budget analysis (Herrmann et al., 2014; Najjar et al., 2018). NEP is defined here as the sum of all the organic carbon budget terms across the interfaces of the Rhode River water column (watershed, wetland, subtidal sediment and tributary mouth) with sinks being positive and sources being negative. NEP is a measure of the trophic status of a

given ecosystem. If NEP is negative, that ecosystem is a net source of carbon dioxide to the atmosphere; the remineralization of organic carbon is larger than the production of organic carbon (net heterotrophic). If NEP is positive, the ecosystem is a net sink of carbon dioxide (net autotrophic). Estuaries, in general, tend to be net heterotrophic due to the large amount of allochthonous input of organic carbon from rivers and wetlands. Chesapeake Bay is an exception, with a net neutral NEP due to the high amount of algal production and long residence time. Trophic status is also linked to the size of the estuary, with large estuaries tending towards autotrophy (Nidzieko, 2018).

The large contribution of organic carbon from algal production drives the Rhode River to be net autotrophic with an NEP of 377.2 tons of C yr^{-1} (89.5 g C m^{-2} yr^{-1}). If the Rhode River trophic status was estimated using the relationship between estuary size and NEP developed by Nidzieko (2018), the Rhode River should be net heterotrophic, although substantial variability exists among ecosystems. The Rhode River is a eutrophic estuary (Gallegos et al., 2010) with relatively high algal biomass and primary production, indicating gross primary production outpaced remineralization even with 22.9% of the DOC entering from the watershed and tidal wetland.

5.4.4 Model scenarios and associated ecosystem impacts

Marsh export of dissolved organic carbon

Completely removing the marsh (-M scenario), rendering the marsh area as an intertidal mudflat with the same initial properties as the subtidal sediments, had large impacts on the organic carbon cycling within the estuary (Figure 5.11). The removal of marsh DOC input decreased export of DOC out of the Rhode River to the mainstem by 20.5% (17.98 tons C). This was dominated by the reduction in the export of DOC_3 by

17.94 tons. DOC_2 export was reduced by 0.74 tons, which was mostly offset by a slight increase in DOC_1 export of 0.70 tons C. The small increase in DOC_1 is likely due to downstream ecosystem impacts of removing the marsh (e.g., on primary production) that can affect the DOC pool. The difference in each budget term for both DOC and POC between the +M and -M scenario shows that the marsh has impacts throughout the organic matter system (Figure 5.11)

A reduction in DOC concentration occurred across all pools by the removal of the marsh input into the Rhode River. This difference in total concentration extended well away from the Kirkpatrick Marsh into the estuary. The average concentration gradient can show differences across lability with and without the marsh (Figure 5.12). Unsurprisingly, there were strong spatial fluctuations in the DOC concentration gradient (dDOC dx^{-1}; g C m^{-3} km^{-1}) for each reactivity class in the +M and -M scenarios (Figure 5.12). dDOC dx^{-1} was calculated by dividing the difference between DOC concentration between successive model node points by the distance between successive points along an extended transect (Figure 5.12a). A positive gradient indicates the concentration decreases away from the marsh. The strong gradient was mostly driven by $CDOC_3$ and $NCDOC_3$ with $CDOC_1$ contributing modestly.

The difference between the DOC gradient between the +M and -M scenarios extended all the way out to the main stem at the end of the transect. The largest difference between the scenarios was near the marsh, with relatively small gradients in the -M scenario compared to large gradients in the +M scenario. Overall the difference decreased from 2.31 g C m^{-3} km^{-1} adjacent to the marsh to < 0.5 g C m^{-3} km^{-1} over ~2 km from the marsh past station XGE3275. The median total DOC concentration gradient difference

was 0.21 g C m^{-3} km^{-1}, with the marsh derived $CDOC_3$ comprising the majority of the total DOC pool. Differences in concentration for most of the DOC pools attenuated past 2 km from marsh, but $CDOC_3$ differences persisted all the way to the mainstem. The largely marsh derived $CDOC_3$ pool accounted for the majority of the difference in the total DOC concentration gradient into the mainstem of the bay (Figure 5.12e). The gradients for $NCDOC_2$ and $NCDOC_1$ slope back towards the marsh in both scenarios, indicative of the primarily phytoplankton source. The large fluctuations in both the direction and magnitude of the gradients in both scenarios in the marsh and the mainstem show the inherent patchiness in the DOC field.

The budget terms outlined above are heterogeneous, with each source contributing a different composition and reactivity of DOC; although the Kirkpatrick Marsh contributed 11.6% to the GDP within the estuary, that does not necessarily mean that the marsh contributed a similar fraction to the total standing DOC stock. This is because of differences in the reactivity of the DOC entering from each source, with watershed and marsh inputs less biologically available than algal produced DOC, on average. For example, in the –M scenario the flux between the Rhode River and the mainstem decreased by 20.5% even though the marsh only made up 11.6% of the GDP. By taking the difference between DOC concentration in the +M and -M scenario and integrating the average concentration field over the volume of the estuary, the net contribution of marsh derived DOC to the total estuarine DOC stock can be estimated. The median total integrated DOC stock over the 242 day model period in +M for the Rhode River was 28.37 tons C and in the -M was 22.51 tons, a difference of 5.86 tons C (20.7% of the median total DOC stock is attributed to the marsh). When the estuarine

DOC stock was greatest (43.64 tons) on Sep. 9th, the difference between scenarios was 13.69 tons C, with marsh export supporting 31.4% of the total DOC stock in the Rhode River.

Ecosystem impacts of the tidal marsh

Removing the marsh also affected other aspects of the estuarine ecosystem including DON, inorganic nitrogen, phytoplankton, and light. First, the presence of the marsh *increased* the total nitrogen in the Rhode River for NH_4^+, NO_3^- and DON. This curious outcome is mostly due to the relatively high flux of NH_4^+ out of the marsh into the Rhode River, in addition to the marsh loading of DON. The marsh derived DON (input at a DOC:DON ratio of 10 g C: 1 g N) increased total DON in the water column which drove an increase in remineralization to NH_4^+ (Figure 5.13a,c). The increase in remineralization of DON (348.9 kg N) and a higher input of NH_4^+ from the marsh sediment (398.5 kg N), led to an increase in average NH_4^+ concentration adjacent to the marsh (Figure 5.14a). The increase in NH_4^+ concentration was also a primary driver of enhanced nitrification of NH_4^+ to NO_3^- (Figure 5.13a,b), which increased the concentration of NO_3^- downstream from the marsh (Figure 5.14b).

Marsh derived organic matter also drives an increase in oxygen demand in the water column via remineralization of DOC. Average minimum dissolved oxygen (DO) concentration throughout the Rhode River increased by 16.7 % from 3.47 to 4.05 g O_2 m^{-3} from the +M to the –M scenario. The total time spent below the critical oxygen threshold of 2.0 g O_2 m^{-3} (e.g. hypoxia) can be an important metric related to water quality and habitat suitability. If each point in the Rhode River is analyzed for how often

it experienced DO < 2.0 g O_2 m^{-3}, the impact of the marsh on oxygen in the water column can be assessed. On average across the Rhode River, removing the marsh decreased the average amount of time that the bottom water of each node spent below 2.0 g O_2 m^{-3} from 137.6 to 24.5 hours. The low oxygen water was mostly confined to locations adjacent to the marsh, although deeper regions away from the marsh area also experienced hypoxia. In total, 20.0 % of the sub-tidal region of the Rhode River experienced hypoxia at some point in the +M scenario. These estimates may change if the marsh plant community was dynamically modeled as marsh primary production would increase water column oxygen during inundation. However, observations show that as water enters the Kirkpatrick Marsh, it becomes depleted in oxygen when the water is over the marsh surface due to heterotrophic oxygen demand (Nelson et al., 2017). The oxygen demand in the tidal marsh sediment due to organic matter breakdown was captured with the current model formulation.

Lastly, the removal of the marsh drove changes in the phytoplankton growth in the water column and increased the amount of light penetrating into the water column. Removing the marsh caused significant changes in average phytoplankton growth, depending on the location within the Rhode River (Figure 5.14c). In RhodeFVCOM-ICM, phytoplankton growth is limited by light or nitrogen, with the relative degree of limitation depending on which is less in supply relative to its demand (Appendix II). Adjacent to the marsh where light was more limiting, the net primary production (NPP) was substantially less when the marsh was included. Moving away from the marsh, NPP was greater in the +M scenario due to a relief from nitrogen limitation because of a greater total amount of NO_3^- (as the product of nitrification) in the water column (Figure

5.14a,b). Adjacent to the marsh where CDOM concentration was high and nutrients are relatively replete because of the watershed inputs, the phytoplankton tended to be light limited. Nutrient limitation is stronger in the –M scenario away from the marsh because there is less nitrogen available for phytoplankton being transported down tributary, regardless of the presence of the marsh. Moving further towards the mainstem, the –M scenario had greater NPP, especially in deeper areas. The nitrogen concentration difference between scenarios was near zero, but the difference in underwater light persists throughout the tributary, therefore NPP increases in the –M because of a slight relief of light limitation. The increase in PAR in the –M scenario occurred throughout the tributary with a relatively constant difference in the two first 2-3 kilometers away from the marsh (Figure 5.14d). The shift in NPP across time and space concurrent with shifts in light and nitrogen availability suggests that phytoplankton are dynamically limited by light and nutrients, with light limitation more important adjacent to the marsh.

Photochemical degradation in the water column

The no photodegradation (-PD) run revealed the influence that photodegradation has on the overall distribution, cycling and export of DOC in the Rhode River. Under the -PD scenario, the export to the mainstem of total DOC increased by 9.78% from 87.75 to 96.34 tons. DOC_3 export increased by 37.7% from 41.90 to 57.98 tons, further exhibiting the strong influence that photochemical degradation has on breaking down this fraction of DOC into the lower molecular weight, more biolabile pool. Surprisingly, removing photochemical reactions in the water column also affected the magnitude of the net DOC flux across the estuarine sediment-water interface. The flux of DOC_1 into the sediment

was reduced by 17.0% from 17.55 to 14.57 tons, which is due to less DOC_1 being created in the water column via photochemical degradation. Turning off the photochemical production of DOC_1 from $CDOC_3$ and $CDOC_2$ reduced the average water column DOC_1 concentration by 13.3%.

Secondary effects also occurred due to removing the impact of photochemical degradation in the water column. First, average mid water column Rhode River PAR, which is directly calculated at each depth in the model, decreased by 1.78%. The increased amount of CDOC that remains in the water column in the –PD scenario increased light attenuation throughout the estuary. The decline in PAR decreased average Rhode River algal net primary production (NPP) by 1.17%, which reduced the algal derived DOC input by a modest 2.20 tons. Remineralization of DOC declined by 4.52% (7.68 tons) in the -PD scenario which is not only due to the reduction in photochemical production of DOC_1 but the small reduction in algal derived DOC which is more labile in general.

Coagulation of refractory DOC in the water column

The potential impact of the flocculation and/or coagulation of the allocthonous, high molecular weight DOC_3 on the spatial distribution and total budget of DOC in the water column is considered here because this term was set to zero in all of the runs that have been examined thus far. When a salinity dependent coagulation term was included (+CG) as a sink for DOC_3 in the water column, the flux of DOC from the mouth of the Rhode River was reduced from 87.75 to 61.43 tons C. Although the coagulation term was included initially in the DOM formulations for ICM (Kim and Khangaonkar, 2012) it

appears to have been removed in the most recent implementation of the CBP Water Quality Model (Cerco and Noel, 2017). The actual physico-chemical process of DOC coagulation and flocculation is uncertain, however, and due to its potentially large impact on the organic carbon cycle was not included in the baseline scenario. In addition, DOC that is marsh or estuarine derived, and thus native to the elevated salinity conditions typical of an estuary, will likely be stable in the dissolved form. In contrast, river derived DOM that comes from a freshwater environment rapidly aggregates to POM at low (1-2) salinity levels (Sholkovitz, 1976) due to a lack of stability in the increased ionic concentration of saline water (He et al., 2016). The aggregation or coagulation process was not included in the +M control run because the RhodeFVCOM-ICM marsh pore water has the same salinity as the overlying water column. Therefore, it follows that the DOM contained in the pore water of the marsh, at estuarine salinity levels, is stable at those ionic concentrations.

When modeling a freshwater wetland at the head of an estuary using the marsh-estuary carbon cycle model described here, coagulation processes affecting high molecular weight terrestrial derived DOM may need to be included. Models simulating POM-DOM exchange have been proposed with differing complexity (He et al., 2016). The approach used in the +CG scenario is relatively simple and can be found in Appendix IV. Factors such as shear stress, particle size, and Brownian motion are neglected in the FVCOM-ICM-PD formulation. In general, more research needs to be done on DOM-POM exchange of marsh derived organic matter across salinity gradients, as these processes can be important transformational pathways in an estuarine environment. For instance, DOM that transforms to POM will enter a grazing food web

rather than the heterotrophic microbial pathway, potentially increasing trophic energy transfer and enhancing food web retention. DOM that transforms to POM will also potentially settle out of the water column, while DOM that remains in the water column will tend to be exported to adjacent water bodies.

5.4.5 Scaling up: Developing a model derived relationship for estimating the impact of a given marsh on an estuary

In a seminal review, Nixon (1980) examined the potential reasons for why certain marshes exhibit vastly differing behavior in terms of nutrients and organic matter fluxes. The takeaway is that marshes are extremely complicated and many aspects of biogeochemistry and hydrology (Fagherazzi et al., 2013) can determine the fluxes of a given solute or particulate between a marsh and its adjacent water body. Some easily measured geographical metrics, such as marsh area and open water area that can clearly affect the influence of a given marsh in an estuary have been used as a way to look across systems, ignoring hydrological, biogeochemical and ecological differences (Nixon, 1980). Nixon (1980) found that patterns relating geographic variability to estuarine productivity were indeterminate. An updated synthesis reached similar conclusions (Childers et al., 2002), and the vast differences in marsh organic carbon lateral export supports these claims (Herrmann et al., 2014). At some level, though, the spatial characteristics of a given marsh-estuary ecosystem must manifest themselves in how organic matter is cycled between each sub-system.

A geographical metric that can capture the influence a particular wetland will have on the organic carbon budget in the estuary within which it resides is the ratio of estuarine volume (EV) to marsh area (MA). As the total volume of water under influence

from a particular marsh decreases, the importance of the marsh to the estuarine biogeochemistry will increase. For the Rhode River tributary described in the budget, this ratio is 35.85 (m). That is, for every 35.85 m^3 of water there is 1.0 m^2 of marsh. By selectively removing estuary water from the budget calculation at the segments in Figure 1c, the amount of DOC that is contributed to the total estuary budget from the marsh can be modeled as a function of EV:MA. Physically measuring the total contribution of a wetland to the carbon budget for differing volumes of the same estuary is difficult if not impossible. If an empirical relationship between the fractional DOC contribution and EV:MA can be established using RhodeFVCOM-ICM, then generalizations can begin to be developed about the geography of a given ecosystem and the role that a wetland can potentially play in the water column carbon budget. This will allow commonly available geospatial information (e.g., National Wetlands Inventory) to be used to estimate a given wetlands contribution to estuarine carbon cycling, assuming other contributing factors such as primary production within the estuary are similar.

In order to make a prediction of the contribution of marsh derived DOC to the estuarine DOC budget across scales, a logarithmic generalized linear model (GLM) predicting the % of GDP that is derived from marshes as a function of EV:MA was built using the MATLAB function *fitglm* (Figure 5.15). To the largest section of the Rhode River, the marsh contributed 11.6% of the GDP; this increased to 49.2% for the smallest estuarine segment directly adjacent to the marsh. At an estuary volume of 6.814×10^{10} m^3 (www.chesapeakebay.net/discover/facts) and a total tidal marsh area of 1.142×10^9 m^2 (www.chesapeakebay.net/state/wetlands) the entire Chesapeake Bay has an EV:MA of 59.6. The GLM derived from the Rhode River as depicted in Figure 5.15 predicts that

2.95% of the GDP of Chesapeake Bay is derived from tidal wetlands.

A similar relationship can be derived to estimate the total contribution of wetland derived DOC to the DOC stock within the Rhode River, and extrapolated out to Chesapeake Bay (Figure 5.15). To do this, the % marsh contribution to the stock is defined using Equation 5.4. The % contribution is equal to the difference in total DOC mass (tDOC g C) in the estuary in the +M and -M scenario divided by the total mass in the +M scenario. The marsh contributed between 20.7 and 35.3% to the total DOC stock moving from the largest to smallest sections in the Rhode River, on average. Extrapolating, the GLM indicates that tidal marshes could contribute 13.4% to the total DOC stock within Chesapeake Bay.

$$\%\ Contribution\ = \left(\frac{(tDOC_{+M} - tDOC_{-M})}{tDOC_{+M}}\right) x\ 100 \qquad (5.4)$$

The log-linear model for the EV:MA vs. % contribution of the marsh to the total DOC stock has a shallower slope and a smaller intercept relative to the GDP curve (Figure 5.15). The hypothetical upper bound of the marsh contribution to either relationship would be 100% if there were no other sources within an estuary. For the Rhode River, the relationship reaches an upper bound of < 50% for both quantities due to the inclusion of the watershed input adjacent to the marsh for the smallest polygon used in the model fit, in addition to algal production near the marsh. The larger contribution of marsh derived DOC to the estuarine stock relative to the GDP as EV:MA increases is indicative of the variable reactivity of marsh derived vs. estuarine derived DOC. Although it makes up progressively less of the gross DOC input as estuarine volume increases, the longer persistence of marsh derived DOC relative to algal sources (the primary source within the estuary) leads an uncoupling of the tDOC stock and the marsh

contribution to the GDP within the estuary. Relatively to its contribution to the GDP, the marsh contributes substantially more to the standing DOC stock.

The application of the geographical relationship derived from the Rhode River to the entire Chesapeake Bay assumes that the Rhode River is representative of all wetlands in Chesapeake Bay. The high amount of algal primary production and DOC production exhibited in the Rhode River makes the above models not necessarily applicable to estuarine ecosystems that are more oligotrophic. As estuarine water column primary production decreases, the importance of a given tidal marsh to its adjacent estuary will tend to increase. Moving forward, it would be useful to establish these kinds of models for certain classes of estuarine ecosystems to reduce error when scaling from sampled "representative" marshes to regional and global budgets. Whether wetlands can be grouped by trophic status, land-use characteristics, tidal variability, or geographic location, perhaps this approach can be used as a tool to establish the model-derived statistical relationships for many ecosystems. Furthermore, as computational power continues to improve, the ability to represent all of the tidal marsh area for a large ecosystem such as Chesapeake Bay will greatly advance our understanding of the role that tidal marshes can play on regional and global scales. Deriving the EV:MA % contribution relationship for an entire system, like Chesapeake Bay, would allow for a robust quantitative assessment of the role marshes play in supporting estuarine productivity, heterotrophic microbial food webs, and the export of DOC to the continental shelf.

5.5 Summary

Tidal marshes are important components of estuarine and coastal ecosystems. The

export of organic carbon is an important and large portion of the coastal carbon cycle. The modeling system developed here, RhodeFVCOM-ICM, is a useful tool that can quantitatively describe both the flux of organic carbon between ecosystems and the different processes that contribute to the total concentration and budget within an estuary. Below are the key findings of this research.

1. The tidal marsh accounted for 20.7% of the median DOC stock in the Rhode River and 20.5% of the export of DOC from the tributary to the mainstem of Chesapeake Bay.
2. 22.9% of DOC within the Rhode River entered from allochthonous sources (tidal marsh and watershed) with estuarine phytoplankton production the largest source of DOC (and POC) to the estuary. The Rhode River was net autotrophic with a net ecosystem production of 89.5 g C m^{-2} yr^{-1}.
3. The tidal marsh increased total nitrogen within the estuary via increased export of DON and NH_4^+ from the tidal marsh sediment.
4. Applying the relationship in the DOC budget from the Rhode River modeled as a function of estuarine water volume and total marsh area to the entire Chesapeake Bay estimates that 13.4% of the total DOC stock in Chesapeake Bay is from tidal wetlands.

5.6 Acknowledgements

I would like to acknowledge my collaborators who worked with me in developing this paper, Wen Long and Raleigh R. Hood. I would also like to acknowledge the Chesapeake

Bay Program for providing ample data for model forcing and validation, Patrick J. Neale and Thomas Jordan (Smithsonian Environmental Research Center) for watershed and estuarine water quality data and assistance in model forcing development, Maria Tzortziou for helpful comments in development of RhodeFVCOM-ICM, Alana Menendez for insight into the measured DOC flux at the marsh creek, and Tecplot Inc for the data visualization software. Lastly, I acknowledge the National Aeronautics and Space Administration for funding (Grant # NNH13ZDA001N-CARBON) and the Horn Point Laboratory Graduate Research Fellowship for support for this research. . The FVCOM model code can be found at http://fvcom.smast.umassd.edu/. The FVCOM and ICM-DOM-PD source code and forcing, in addition to post-processing MATLAB scripts and data to generate the results, can be found in the online repository at https://github.com/bclark805/ICM-DOM-PD.

5.7 Appendices

Appendix I

Equations governing marsh dissolved organic matter (DOM; both Carbon and Nitrogen) loading

These functions were tuned to get appropriate DOC loading in the 3-D model domain and match observed gradients of DOC away from the marsh into the estuary

$$ExRate = ExRate_0 \theta_m{}^{(T-T_m)}$$

$$JMDOM = M_{mrs}\, f_{mrs} ExRate$$

$$MP_{NH4} = Vm_{NH4} M_{mrs} f_{mrs} \theta^{(T-T_m)} \left(\frac{SedNH_4^+}{K_{sedNH4} + SedNH_4^+} \right)$$

Variable/ Parameter	Description	Value	Units
ExRate	Plant DOM exudation rate	calculated	g DOC g biomass^{-1} d^{-1}
$ExRate_0$	Basal exudation rate	0.03	g DOC g biomass^{-1} d^{-1}
θ_m	Temperature control coefficient for marsh DOM exudation	1.15	dimensionless
T	Sediment temperature	calculated	°C
T_m	Reference temperature for marsh DOM exudation	20	°C
M_{mrs}	Below ground biomass	100	g m^{-2}
f_{mrs}	Fraction of marsh at node	1.0	dimensionless
JMDOM	Flux of marsh derived DOM into marsh sediment	calculated	g DOM m^{-2} d^{-1}
MP_{NH4}	Marsh Plant NH_4^+ uptake	calculated	mg N m^{-2} d^{-1}
Vm_{NH4}	Maximum marsh plant NH_4^+ rate[a]	1.344	mg N g^{-1}d^{-1}
$SedNH_4^+$	Sediment NH_4^+ concentration[b]	calculated	mg N m^{-3}

K_{sedNH4}	Half Saturation of plant NH_4^+uptake	70.0	mg N m^{-3}

a. Bradley and Morris 1991
b. Testa et al., 2013

Appendix II

Equations governing water column algal production

$$\theta_{a,sub} = e^{[-kt_{a,1}(T-T_{a,ref})^2]}$$

$$\theta_{a,sup} = e^{[-kt_{a,2}(T_{a,ref}-T)^2]}$$

$$\theta_b = e^{[-kt_b(T-T_b)]}$$

$$\theta_{pr} = e^{[-kt_{pr}(T-T_{pr})]}$$

$$PP_a = PM_a\,\theta_a$$

$$BM_a = BMR_a\,\theta_b$$

$$PR_a = BPR_a\,B_a^2\,\theta_{pr}$$

$$PN_a = NH_4^+\left[\frac{{NO_3}^-}{(kh_{n,a}+{NH_4}^+)(kh_{n,a}+{NO_3}^-)}+\frac{kh_{n,a}}{({NH_4}^++{NO_3}^-)(kh_{n,a}+{NO_3}^-)}\right]$$

$$NL_a = \frac{NO_3 - PN_a({NO_3}^- + {NH_4}^+)}{kh_{n,a} + 2{NH_4}^+ + {NO_3}^- - PN_a({NO_3}^- + {NH_4}^+)}$$

$$Ik_a = \frac{PP_a}{\alpha_a}$$

$$FI_a = \frac{Iavg}{Ik_a^2 + Iavg^2}$$

$$P_a = \frac{PP_a\,min[FI_a, NL_a]}{CChl_a}$$

$$NetP_a = [P_a(1 - PRSP_a) - BM_a]B_a$$

$$WB_a = \frac{WS_a\,B_a^{z-1} - WS_a\,B_a^Z}{\Delta z}$$

$$\frac{dB_a}{dt} = NetP_a - PR_a + WB_a$$

Variable/ Parameter	Description	Value	Units
$\theta_{a,sub}$	Sub optimal temperature control on algal production	calculated	dimensionless
$kt_{a,1}$	Sub-optimal temperature coefficient for algae 1 and algae 2 production[a]	0.0018, 0.0035	$°C^{-2}$
$T_{a,ref}$	Reference temperature for algal production[a]	16.0, 35.0	°C
T	Water Column Temperature	calculated	°C
$\theta_{a,sup}$	Super- optimal temperature control on algal production	calculated	dimensionless
$kt_{a,2}$	Super-optimal temperature coefficient for algae 1 and algae 2 production[a]	0.006, 0.00	$°C^{-2}$
θ_b	Temperature control on algal metabolism	calculated	dimensionless
kt_b	Algal basal metabolic temperature coefficient[a]	0.032	$°C^{-1}$
T_b	Reference temperature for algal metabolism[a]	20	°C
θ_{pr}	Temperature control on algal predation	calculated	dimensionless
kt_{pr}	Algal predation temperature coefficient[b]	0.032	$°C^{-1}$
T_{pr}	Reference temperature for algal predation[b]	20	°C
PP_a	Algal photosynthetic rate before nutrient limitation	calculated	g C g chl a^{-1} d^{-1}
PM_a	Maximum photosynthetic rate[a]	300, 350	g C g chl a^{-1} d^{-1}
BM_a	Algal metabolic rate	calculated	d^{-1}
BMR_a	Basal algal metabolic rate[a]	0.01,0.02	d^{-1}
PR_a	Algal predation rate	calculated	g C m^{-3} d^{-1}

BPR_a	Basal algal predation rate[c,d] (see below)	1.5	$m^3\ g\ C^{-1}\ d^{-1}$
B_a	Algal biomass	calculated	$g\ C\ m^{-3}\ d^{-1}$
PN_a	Algal preference for NH_4^+	calculated	dimensionless
NH_4^+	Ammonium Concentration	calculated	$g\ N\ m^{-3}$
$kh_{n,a}$	Half saturation of inorganic nitrogen uptake by algae[a]	0.025,0.025	$g\ N\ m^{-3}$
NO_3^-	Nitrate + Nitrite concentration	calculated	$g\ N\ m^{-3}$
NL_a	Algal nitrogen limitation	calculated	dimensionless
Ik_a	Intersection of P vs I curve	calculated	mols photons $m^{-2}\ d^{-1}$
α_a	Slope of P vs I curve[a]	8.0, 8.0	g C g chl a^{-1} (mols photons $m^{-2})^{-1}$
FI_a	Light Limitation coefficient	calculated	dimensionless
I_{avg}	Photosynthetically active radiation	calculated	mols Photons m^{-2}
P_a	Realized photosynthetic rate	calculated	d^{-1}
$CChl_a$	Carbon to chl *a* ratio[b]	50, 50	g C g chl a^{-1}
$NetP_a$	Net primary production	calculated	$g\ C\ m^{-3}\ d^{-1}$
$PRSP_a$	Algal respiration[a]	0.25	dimensionless
WB_a	Algal sinking	calculated	$g\ C\ m^{-3}\ d^{-1}$
WS_a	Algal sinking velocity[a]	0.1, 0.1	$m\ d^{-1}$
B_a^{z-1}	Algal biomass in layer above	calculated	$g\ C\ m^{-3}$
B_a^{z-1}	Algal biomass in current layer	calculated	$g\ C\ m^{-3}$
$\boldsymbol{\Delta}z$	Layer thickness	calculated	m
$dB_a\ dt^{-1}$	Change in algal biomass over time	calculated	$g\ C\ m^{-3}\ d^{-1}$

The predation rate (BPR_a) was increased relative to Cerco and Noel (2017) because chl *a* was too high relative to observations in the main stem of the bay. The justification for

this is based on a mathematical argument using measured zooplankton clearance rates. Specifically, Richman et al. (1977) found that calanoid copepods have a filtration rate of ~200 uL ind^{-1} hr^{-1} and copepods are a dominant member of the zooplankton grazing community throughout the year in Chesapeake Bay (Kimmel et al., 2006). To convert to a volumetric clearance rate per biomass of zooplankton, the mean zooplankton biomass per individual must be estimated. This was calculated as 3.21 ug C ind^{-1} which is the mean of the four years of data tabulated in Kimmel et al. (2006; Table 3) for Chesapeake Bay zooplankton. To find the volumetric clearance rate for a given biomass of zooplankton (m^3 g C^{-1} d^{-1}), take the individual filtration rate and divide it by the individual biomass (below).

$$BPR_a = \frac{0.2ml}{ind\ hr}\ x \frac{ind}{3.21\ ug\ C\ ind}\ x\ \frac{1x10^6 \mu g\ C}{g\ C}\ x\ \frac{1\ m^3}{1x10^6 ml}\ x\ \frac{24\ hr}{day}$$
$$= 1.50\ m^3\ (g\ C\ d)^{-1}$$

a. Cerco and Noel 2004
b. Cerco and Noel 2017
c. Richman et al., 1977
d. Kimmel et al., 2006

Appendix III

Photochemical degradation model (Chapter 3)

Methods: Full optical modeling equations and parameterization

$$Iz_i(\lambda) = Iz_0(\lambda)\frac{abs_i(\lambda)}{abs_t(\lambda)}(1 - e^{[-abs_t(\lambda)\Delta z]})$$

$$abs_i(\lambda) = CDOC_i\ a^* cdoc_i(\lambda)$$

$$abs_t(\lambda) = abs_w(\lambda) + \sum_{i=1}^{3} abs_i(\lambda)$$

$$pdDOC_{i,j} = \frac{\int_{\lambda_0}^{\lambda_f} Iz_i(\lambda) AQY_{i,j}(\lambda) d\lambda}{\Delta z}$$

$$pdCDOC_1 = pdCDOC_{3,1} + pdCDOC_{2,1} - pdCDOC_{1,0} - pdCDOC_{1,N}$$

$$pdCDOC_2 = -pdCDOC_{2,1} - pdCDOC_{2,0} - pdCDOC_{2,N}$$

$$pdCDOC_3 = -pdCDOC_{3,1} - pdCDOC_{3,0} - pdCDOC_{3,N}$$

$$pdNCDOC_1 = pdCDOC_{1,N}\ f_{pdc11} + pdCDOC_{2,N}\ f_{pdc21} + pdCDOC_{3,N}\ f_{pdc31}$$

$$pdNCDOC_2 = pdCDOC_{1,N}\, f_{pdc12} + pdCDOC_{2,N}\, f_{pdc22} + pdCDOC_{3,N}\, f_{pdc32}$$

$$pdNCDOC_3 = pdCDOC_{1,N}\, f_{pdc13} + pdCDOC_{2,N}\, f_{pdc23} + pdCDOC_{3,N}\, f_{pdc33}$$

Variable/ Parameter	Description	Value	Units
$Iz_i(\lambda)$	Photon flux absorbed by $CDOC_i$ (1-3) at wavelength λ (284-460 nm)	calculated	mols photons m^{-2} d^{-1} nm^{-1}
$Iz_0(\lambda)$	Surface (above) total photon flux at wavelength λ	calculated	mols photons m^{-2} d^{-1} nm^{-1}
$abs_i(\lambda)$	Absorption coefficient of $CDOC_i$ (1-3) at wavelength λ	calculated	m^{-1}
$abs_w(\lambda)$	Absorption coefficient of water at wavelength λ	calculated	m^{-1}
$abs_t(\lambda)$	Total absorption coefficient at wavelength λ	calculated	m^{-1}
Δz	Exposure pathlength	0.04	m
$a^*cdoc(\lambda)_i$	Specific absorption of $CDOC_i$ (1-3) at wavelength λ	Figure 5.3a	m^2 g C^{-1}
$CDOC_i$	Concentration of $CDOC_i$ (1-3)	calculated	g C m^{-3}
$pdDOC_{i,j}$	Flux of $CDOC_i$ (1-3) to DOC_j (1-3; either colored or non-colored)	calculated	g C m^{-3} d^{-1}
$AQY_{i,j}(\lambda)$	Apparent quantum yield of $CDOC_i$ (1-3) to DOC_j (both colored and non-colored, 1-3)[a]	calculated	g C mols photons^{-1}
$pdCDOC_1$	Total photodegradation flux of colored DOC_1	calculated	g C m^{-3} d^{-1}
$pdCDOC_{3,1}$	Photodegradation flux of colored DOC_3 to DOC_1	calculated	g C m^{-3} d^{-1}
$pdCDOC_{2,1}$	Photodegradation flux of colored DOC_2 to DOC_1	calculated	g C m^{-3} d^{-1}
$pdCDOC_{1,0}$	Photoremineralization flux of colored DOC_2 to DIC	calculated	g C m^{-3} d^{-1}
$pdCDOC_{1,N}$	Photobleaching flux of colored DOC_2 to non-colored DOC	calculated	g C m^{-3} d^{-1}
$pdCDOC_2$	Total photodegradation flux of colored DOC_2	calculated	g C m^{-3} d^{-1}
$pdCDOC_{2,0}$	Photomineralization flux of colored DOC_2 to DIC	calculated	g C m^{-3} d^{-1}
$pdCDOC_{2,N}$	Photobleaching flux of colored DOC_2 to non-colored DOC	calculated	g C m^{-3} d^{-1}
$pdCDOC_3$	Total photodegradation flux of colored DOC_3	calculated	g C m^{-3} d^{-1}

$pdCDOC_{3,0}$	Photobleaching/photomineralization flux of colored DOC_3 to non-colored DOC and DIC	calculated	g C m^{-3} d^{-1}
$pdCDOC_{3,N}$	Photobleaching flux of colored DOC_3 to non-colored DOC	calculated	g C m^{-3} d^{-1}
$pdNCDOC_1$	Total photodegradation flux to non-colored DOC_1	calculated	g C m^{-3} d^{-1}
f_{pdc11}	Fraction of colored DOC_1 photobleaching flux to non-colored DOC_1[a]	0.5	dimensionless
f_{pdc21}	Fraction of colored DOC_2 photobleaching flux to non-colored DOC_1[a]	0.5	dimensionless
f_{pdc31}	Fraction of colored DOC_3 photobleaching flux to non-colored DOC_1[a]	0.5	dimensionless
$pdNCDOC_2$	Total photodegradation flux to non-colored DOC_2	calculated	g C m^{-3} d^{-1}
f_{pdc12}	Fraction of colored DOC_1 photobleaching flux to non-colored DOC_2[a]	0.25	dimensionless
f_{pdc22}	Fraction of colored DOC_2 photobleaching flux to non-colored DOC_2[a]	0.25	dimensionless
f_{pdc32}	Fraction of colored DOC_3 photobleaching flux to non-colored DOC_2[a]	0.25	dimensionless
$pdNCDOC_3$	Total photodegradation flux to non-colored DOC_3	calculated	g C m^{-3} d^{-1}
f_{pdc13}	Fraction of colored DOC_1 photobleaching flux to non-colored DOC_3[a]	0.25	dimensionless
f_{pdc23}	Fraction of colored DOC_2 photobleaching flux to non-colored DOC_3[a]	0.25	dimensionless
f_{pdc33}	Fraction of colored DOC_3 photobleaching flux to non-colored DOC_3[a]	0.25	dimensionless

a. Chapter 3
b. Vahatalo and Wetzel, 2008;

Upon solar exposure, most CDOC is moved to the labile and semi-labile fractions to enhance microbial breakdown of exposed DOC. Vahatalo and Wetzel (2008) found that upon solar exposure, ~50-75% of DOC was remineralized over 400 day incubations.

Appendix III

Other equations of light attenuation model

$$AB_{chl}(\lambda) = \phi_{chl}(\lambda)\, B_a CChl_a{}^{-1}$$

$$AB_{tss}(\lambda) = \varphi_{tss}(\lambda)\, TSS$$

$$SCAT_{\beta}(\lambda) = \beta_{tss}(\lambda)\, TSS$$

$$AB_{cdom}(\lambda) = \sum_{i=1}^{3} abs_i(\lambda)$$

$$AB_{total}(\lambda) = AB_{water}(\lambda) + AB_{cdom}(\lambda) + AB_{chl}(\lambda) + AB_{tss}(\lambda)$$

$$Kd(\lambda) = \frac{\sqrt{AB_{total}(\lambda)^2 + G_{\mu_0} AB_{total}(\lambda) SCAT_{\beta}(\lambda)}}{\mu_0}$$

$$Iz(\lambda) = Iz_0(\lambda) e^{[kd(\lambda)\Delta z]}$$

$$Iavg = \int_{400}^{700} Iz(\lambda)$$

Variable/ Parameter	Description	Value	Units
$AB_{chl}(\lambda)$	Absorption due to chl *a*	calculated	m^{-1}
$\phi_{chl}(\lambda)$	Specific absorption due to chl *a*[a]	Figure 5.3b	m^2 g chl^{-1}
$AB_{tss}(\lambda)$	Absorption due to total suspended solids	calculated	m^{-1}
$\varphi_{tss}(\lambda)$	Specific absorption due to TSS[a]	Figure 5.3b	m^2 g TSS^{-1}
$SCAT_{\beta}(\lambda)$	Scattering of light due to TSS	calculated	m^{-1}
$\beta_{tss}(\lambda)$	Specific scattering of light due to TSS[a]	Figure 5.3b	m^2 g TSS^{-1}
$AB_{cdom}(\lambda)$	Absorption due to CDOM	calculated	m^{-1}
$abs_i(\lambda)$	Absorption of $CDOM_i$ (1-3)	calculated	m^{-1}
$AB_{total}(\lambda)$	Total absorption	calculated	m^{-1}
$AB_{water}(\lambda)$	Absorption due to water[a]	Figure 5.3b	m^{-1}
$Kd(\lambda)$	Diffuse attenuation coefficient at wavelength λ[b]	calculated	m^{-1}

$G_{\mu 0}$	Scaled scattering of light to attenuation and depth[b,c]	calculated	dimensionless
μ_0	Incident angle of light due to time of day and refraction	calculated	dimensionless
Iz(λ)	Photon flux at wavelength λ after attenuation	calculated	mols photons m^{-2} d^{-1}
Iavg	Photosynthetically active radiation	calculated	mols photons m^{-2} d^{-1}

a. Rose et al., 2018
b. Gallegos et al., 1990
c. Kirk 1994

Appendix IV
Equations governing dissolved and particulate organic carbon (DOC & POC) dynamics

$$CPC_a = (P_a\ PRSP_a + BM_a)\ B_a$$

$$LPOC_a = f_{clpa}\ CPC_a\ +\ f_{clppr} PR_a$$

$$RPOC_a = f_{crpa}\ CPC_a\ +\ f_{crppr}\ PR_a$$

$$\theta_{hdr} = e^{[-kt_{hdr}(T-T_{hdr})]}$$

$$LPOC_{hdr} = K_{lpoc}\ \theta_{hdr}\ LPOC$$

$$RPOC_{hdr} = K_{rpoc}\ \theta_{hdr}\ RPOC$$

$$WS_{poc} = \frac{WS_p\ POC^{z-1} - WS_p\ POC^z}{\Delta z}$$

$$ADOC_a = f_{cda} CPC_a + f_{cdp} PR_a$$

$$\theta_{mnl_i} = \theta_i^{(T-T_{mnl})}$$

$$K_{COAG} = 0.5\ [1 + tanh(S - kh_{coag})]\ k_{coag}$$

$$DENIT_c\ =\ kDOC_1\ \theta_{mnl}\ AANOX\ \left(\frac{kh_{odoc}}{kh_{odoc} + O_2}\right)\left(\frac{{NO_3}^-}{kh_{ndn} + {NO_3}^-}\right)$$

$$DDOC_i = \frac{D}{Z}(DOC_i - DOC_{i,sed})$$

$$\frac{dLPOC}{dt} = LPOC_a - LPOC_{hdr} + WS_{lpoc}$$

$$\frac{dRPOC}{dt} = RPOC_a - RPOC_{hdr} + WS_{rpoc} + K_{COAG}DOC_3$$

$$\frac{dDOC_1}{dt} = ADOC_a\, f_{cda1} - kDOC_1\theta_{mnl_1}DOC_1 + (LPOC_{hdr} + RPOC_{hdr})\, f_{hdrc1} - DENIT_cDOC_1 - DDOC_1 + pdDOC_1$$

$$\frac{dDOC_2}{dt} = ADOC_a\, f_{cda2} - kDOC_2\theta_{mnl_2}DOC_2 + (LPOC_{hdr} + RPOC_{hdr})\, f_{hdrc2} - DDOC_2 + pdDOC_2$$

$$\frac{dDOC_3}{dt} = ADOC_a\, f_{cda3} - kDOC_3\theta_{mnl_3}DOC_3 + (LPOC_{hdr} + RPOC_{hdr})\, f_{hdrc3} - K_{COAG}DOC_3 - DDOC_3 + pdDOC_3$$

Variable/ Parameter	Description	Value	Units
CPC_a	Algal respiration and metabolism	calculated	g C m^{-3} d^{-1}
$LPOC_a$	Algal derived LPOC	calculated	g C m^{-3} d^{-1}
f_{clpa}	Fraction of algal production that is LPOC	0.0	dimensionless
f_{clppr}	Fraction of predation derived organic carbon that is LPOC	0.10	dimensionless
f_{crpa}	Fraction of algal production that is RPOC	0.0	dimensionless
f_{crppr}	Fraction of predation derived organic carbon that is RPOC	0.50	dimensionless
θ_{hdr}	Temperature control of hydrolysis	calculated	dimensionless
kt_{hdr}	Hydrolysis temperature control coefficient[a]	0.069	dimensionless
T_{hdr}	Reference temperature for hydrolysis[a]	20.0	°C

$LPOC_{hdr}$	Hydrolysis of LPOC	calculated	g C m^{-3} d^{-1}
k_{lpoc}	Hydrolysis rate of LPOC[b]	0.03	d^{-1}
LPOC	LPOC concentration	calculated	g C m^{-3}
$RPOC_{hdr}$	Hydrolysis of RPOC	calculated	g C m^{-3} d^{-1}
k_{rpoc}	Hydrolysis rate of RPOC[a]	0.006	d^{-1}
RPOC	RPOC concentration	calculated	g C m^{-3}
WS_{poc}	LPOC or RPOC sinking	calculated	g C m^{-3} d^{-1}
WS_p	POC sinking velocity[a]	0.5	m d^{-1}
POC^{z-1}	POC concentration in layer above	calculated	g C m^{-3}
POC^z	POC concentration in current layer	calculated	g C m^{-3}
$ADOC_a$	Algal derived DOC	calculated	g C m^{-3} d^{-1}
f_{cda}	Algal respiration DOC exudation fraction[c]	0.10	dimensionless
f_{cdp}	Algal predation DOC fraction[d]	0.20	dimensionless
θ_{mnli}	Temperature control on DOC_i (1-3) remineralization	calculated	dimensionless
θ_i	Temperature control coefficient for DOC_i (1-3)	1.10,1.15,1.2	dimensionless
T_{mnl}	Reference temperature for remineralization	20.0	°C
K_{COAG}	Coagulation rate of DOC_3 to RPOC	calculated	d^{-1}
S	Salinity	calculated	PSU
kh_{coag}	Half saturation of salinity for DOM coagulation[a]	2.0	PSU
k_{coag}	Basal DOM coagulation rate[a]	0.0	d^{-1}
$DENIT_c$	Denitrification rate of DOC	calculated	d^{-1}
$kDOC_1$	DOC_1 remineralization rate	0.05	d^{-1}
AANOX	Anoxic remineralization scaling	0.90	dimensionless
kh_{odoc}	Oxygen half saturation for anoxic remineralization	0.1	g O_2 m^{-3}
O_2	Dissolved oxygen concentration	calculated	g O_2 m^{-3}

NO_3^-	Nitrate concentration	calculated	g N m^{-3}
kh_{ndn}	NO_3^- half saturation concentration for denitrification[a]	0.01	g N m^{-3}
$DDOC_i$	Diffusive flux of DOC_i (1-3) between sediment and water column bottom layer	calculated	g C m^{-3} d^{-1}
D	Mass transfer coefficient between sediment and water column[c]	calculated	m d^{-1}
Z	Distance between sediment and bottom layer of water column	calculated	m
$DOC_{i,sed}$	Sediment concentration of DOC_i (1-3)[e]	calculated	g C m^{-3}
dLPOC dt^{-1}	Change in LPOC over time	calculated	g C m^{-3} d^{-1}
dRPOC dt^{-1}	Change in RPOC over time	calculated	g C m^{-3} d^{-1}
DOC_3	DOC_3 (refractory) concentration	calculated	g C m^{-3}
dDOC$_1$ dt^{-1}	Change in DOC_1 over time	calculated	g C m^{-3} d^{-1}
f_{cda1}	Fraction of algal derived DOC that is $CDOC_1$, $NCDOC_1$[f,g]	0.10, 0.30	dimensionless
DOC_1	DOC_1 concentration	calculated	g C m^{-3}
f_{hdrc1}	Fraction of hydrolyzed POC that is $CDOC_1$, $NCDOC_1$[g]	0.15, 0.20	dimensionless
$pdDOC_1$	Photodegradation flux of DOC_1 (either colored or non-colored)	calculated	g C m^{-3} d^{-1}
dDOC$_2$ dt^{-1}	Change in DOC_2 over time	calculated	g C m^{-3} d^{-1}
f_{cda2}	Fraction of algal derived DOC that is $CDOC_2$, $NCDOC_2$[f,g]	0.10, 0.45	dimensionless
$kDOC_2$	DOC_2 remineralization rate	0.035	d^{-1}
DOC_2	DOC_2 concentration	calculated	g C m^{-3} d^{-1}
f_{hdrc2}	Fraction of hydrolyzed POC that is $CDOC_2$, $NCDOC_2$[h]	0.20, 0.40	dimensionless
$pdDOC_2$	Photodegradation flux of DOC_2 (either colored or non-colored)	calculated	g C m^{-3} d^{-1}

f_{cda3}	Fraction of algal derived DOC that is $CDOC_3$, $NCDOC_3$[f,g]	0.05, 0.00	dimensionless
$kDOC_3$	DOC_3 remineralization rate	0.001	d^{-1}
DOC_3	DOC_3 concentration	calculated	g C m^{-3} d^{-1}
f_{hdrc3}	Fraction of hydrolyzed POC that is $CDOC_3$, $NCDOC_3$[h]	0.025, 0.25	dimensionless
$pdDOC_3$	Photodegradation flux of DOC_3 (either colored or non-colored)	calculated	g C m^{-3} d^{-1}

a. Cerco and Noel, 2017
b. Etcheber et al., 2007
c. Baines and Pace 1991
d. Møller, 2007
e. Clark et al., 2017
f. Keller and Hood, 2011
g. Romera-Castillo et al., 2010
h. Kinsey et al., 2018

Romera-Castillo et al. (2010) found that algal exudation produced CDOM that had protein like and marine-humic like characteristics which corresponds more to the DOC_1 and DOC_2 pools. The slow production of refractory CDOM was also included to account for the accumulation of CDOM and DOC in surface waters. Kinsey et al. (2018) found that algal-derived aggregates also produced CDOM with distinct marine humic like characteristics. The majority of the hydrolysed DOM is partitioned into the semi-labile pool due to the aggregation of both LPOM and RPOM before fractionation into DOM, assuming some of the DOM would have less reactivity if derived from RPOM. Lastly, there is a slow production of DOM_3 from hydrolysis to also account for the accumulation of CDOM and DOC in the ocean, and the production of humic like fluorescence of likely recalcitrant nature from algal derived particulates (Kinsey et al., 2018).

Appendix V

Equations governing dissolved and particulate organic nitrogen (DON & PON) dynamics

$$LPON_a = (f_{nlpa}\, CPC_a \; + \; f_{nlppr} PR_a\,)\, ANC_a$$

$$RPON_a = (f_{nrpa}\, CPC_a \; + \; f_{nrppr}\, PR_a)\, ANC_a$$

$$LPON_{hdr} = K_{lpon} \theta_{hdr}\, LPON$$

$$RPON_{hdr} = K_{rpon}\theta_{hdr}\, RPON$$

$$WS_{pon} = \frac{WS_p\, PON^{z-1} - WS_p\, PON^{z}}{\Delta z}$$

$$ADON_a = \left(f_{nda}CPC_a + f_{ndp}PR_a\right)ANC_a$$

$$DENIT_n = DON_1\, \theta_{mnl}\, AANOX \left(\frac{kh_{odoc}}{kh_{odoc} + O_2}\right)\left(\frac{{NO_3}^-}{kh_{ndn} + {NO_3}^-}\right)$$

$$DDON_i = \frac{D}{Z}(DON_i - DON_{i,sed})$$

$$\frac{dLPON}{dt} = LPON_a - LPON_{hdr} + WS_{lpon}$$

$$\frac{dRPON}{dt} = RPON_a - RPON_{hdr} + WS_{rpon} + K_{COAG}DON_3$$

$$\frac{dDON_1}{dt} = ADON_a\, f_{nd_{a,1}} - kDON_1\, \theta_{mnl}\, DON_1 + (LPON_{hdr} + LRPON_{hdr})\, f_{hdrn1} - DENIT_n DON_1 - DDON_1 + pdDOC_1 NC_{pd}$$

$$\frac{dDON_2}{dt} = ADON_a\, f_{nd_{a,2}} - kDON_2\, \theta_{mnl}\, DON_2 + (LPON_{hdr} + LRPON_{hdr})\, f_{hdrn2} - DDON + pdDOC_2 NC_{pd}$$

$$\frac{dDON_3}{dt} = ADON_a\, f_{nd_{a,3}} - kDON_3\, \theta_{mnl}\, DON_3 + (LPON_{hdr} + LRPON_{hdr})\, f_{hdrn3} - K_{COAG}DON_3 + DDON_3 + pdDOC_3 NC_{pd}$$

Variable/ Parameter	Description	Value	Units
$LPON_a$	Algal contribution to labile PON	calculated	g N m^{-3}
f_{fnlpa}	Fraction of algal production that is LPON	0.0	dimensionless
f_{nlppr}	Fraction of algal predation that is LPON	0.1	dimensionless
ANC_a	Algal Nitrogen to Carbon ratio[a]	0.135, 0.175	g N g C^{-1}
$RPON_a$	Algal contribution to refractory PON	calculated	g N m^{-3}

f_{nrpa}	Fraction of algal production that is RPON	0.0	dimensionless
f_{nr}	Fraction of algal production that is RPON	0.5	dimensonless
$LPON_{hdr}$	Hydrolysis of LPON	calculated	g N m^{-3}
K_{lpon}	Hydrolysis rate of LPON[b]	0.03	d^{-1}
$RPON_{hdr}$	Hydrolysis of RPON	calculated	g N m^{-3}
K_{rpon}	Hydrolysis rate of RPON[a]	0.006	d^{-1}
RPON	RPON concentration	calculated	g N m^{-3}
WS_{pon}	LPON or RPON sinking	calculated	g N m^{-3} d^{-1}
WS_p	PON sinking velocity[a]	0.5	m d^{-1}
PON^{z-1}	PON concentration in layer above	calculated	g N m^{-3}
PON^z	PON concentration in current layer	calculated	g N m^{-3}
$ADON_a$	Algal derived DON	calculated	g N m^{-3}
f_{nda}	Algal respiration DON exudation fraction[c,d]	0.10	dimensionless
f_{ndp}	Algal predation DON fraction	0.20	dimensionless
$DENIT_n$	Denitrification rate of DON	calculated	d^{-1}
$kDON_1$	DON_1 remineralization rate	0.05	d^{-1}
$DDON_i$	Diffusive flux of DON between sediment and water column bottom layer	calculated	g N m^{-3} d^{-1}
$DON_{i,sed}$	Sediment concentration of DON_i (1-3)	calculated	g N m^{-3}
dLPON dt^{-1}	Change in LPON over time	calculated	g N m^{-3} d^{-1}
dRPON dt^{-1}	Change in RPON over time	calculated	g N m^{-3} d^{-1}
DON_3	DON_3 concentration	calculated	g N m^{-3}
dDON$_1$ dt^{-1}	Change in DON_1 over time	calculated	g N m^{-3} d^{-1}
f_{nda1}	Fraction of algal derived DON that is $CDON_1$, $NCDON_1$	0.10, 030	dimensionless
DON_1	DON_1 concentration	calculated	g N m^{-3}
f_{hdrn1}	Fraction of hydrolyzed PON that is $CDON_1$, $NCDON_1$	0.15, 0.20	dimensionless

NC_{pd}	Photodegradation N:C ratio for colored DOM	calculated	g N g C^{-1}
$dDON_2\ dt^{-1}$	Change in DON_2 over time	calculated	g N m^{-3} d^{-1}
f_{nda2}	Fraction of algal derived DON that is $CDON_2$, $NCDON_2$	0.1, 0.45	dimensionless
$kDON_2$	DON_2 remineralization rate	0.035	d^{-1}
DON_2	DON_2 concentration	calculated	g N m^{-3} d^{-1}
f_{hdrn2}	Fraction of hydrolyzed POC that is $CDON_2$, $NCDON_2$	0.2, 0.4	dimensionless
f_{nda3}	Fraction of algal derived DOC that is $CDON_3$, $NCDON_3$	0.05, 0.0	dimensionless
$kDON_3$	DON_3 remineralization rate	0.001	d^{-1}
DON_3	DON_3 concentration	calculated	g C m^{-3} d^{-1}
f_{hdrn3}	Fraction of hydrolyzed POC that is $CDON_3$, $NCDON_3$	0.025	dimensionless

a. Cerco and Noel 2017
b. Etcheber et al., 2007
c. Bronk et al., 1994
d. Baines and Pace 1991

Appendix VI

Equations governing dissolved inorganic nitrogen (DIN) dynamics

$$\theta_{nt,sub} = e^{[-kt_{nt,1}(T-T_{nt,ref})^2]}$$

$$\theta_{nt,sup} = e^{[-kt_{nt,2}(T_{nt,ref}-T)^2]}$$

$$NT = \left(\frac{O_2}{kh_{ont} + O_2}\right)\left(\frac{NH_4^+}{kh_{nnt} + NH_4^+}\right)\theta_{nt} NT_m NH_4^+$$

$$NH_4A_a = \left(-PN_a\ P_a\ B_a + f_{nip}PR_a\right)ANC_a$$

$$NO_3A_a = (PN_a - 1)P_aB_aANC_a$$

$$\frac{dNH_4^+}{dt} = NH_4A_a + kDON_i\,\theta_{mnl}\,DON_i - NT + DENIT_nDON_1 + pdDOC_{i,0}\,NC_{pd}$$

$$\frac{dNO_3^-}{dt} = NT - NC_{denit}DENIT_c - NO_3A_a$$

Variable/ Parameter	Description	Value	Units
$\theta_{nt,sub}$	Sub-optimal temperature control on nitrification	calculated	dimensionless
$kt_{nt,1}$	Sub-optimal temperature coefficient on nitrification	0.030	°C^{-2}
$T_{nt,ref}$	Reference temperature for nitrification[a]	35.0	°C
$\theta_{nt,sup}$	Super-optimal temperature control on nitrification	calculated	dimensionless
$kt_{nt,2}$	Super-optimal temperature coefficient on nitrification[a]	0.030	°C^{-2}
NT	NH_4^+ loss from nitrification*	calculated	g N m^{-3} d^{-1}
kh_{ont}	Half saturation of Oxygen control on nitrification[a]	0.10	g O_2 m^{-3}
kh_{nnt}	Half saturation of NH_4^+ on nitrification	0.01	g N m^{-3} d^{-1}
NT_m	Maximum nitrification rate	0.20	d^{-1}
NP_a	Production of NH_4^+ from algal respiration	calculated	g N m^{-3} d^{-1}
NH_4A_a	Algal contribution to NH_4^+	calculated	g N m^{-3}
f_{nip}	Fraction of predation that is NH_4^+	0.10	dimensionless
NO_3A_a	Algal contribution to NO_3^-	calculated	g N m^{-3}
$dNH_4^+\ dt^{-1}$	Change in NH_4^+ over time	calculated	g N m^{-3} d^{-1}
$dNO_3^-\ dt^{-1}$	Change in NO_3^- over time	calculated	g N m^{-3} d^{-1}
NC_{denit}	Nitrogen to Carbon ratio of Denitrification[a]	0.933	g N g C^{-1}

a. Cerco and Noel 2017

*Nitrification formulated updated to include NH_4^+ as a limiting reactant (1st order) rather than using the old 0-order equation. This more accurately reflects the substrate limiting nitrification.

Appendix VII

Equations governing dissolved oxygen dynamics

$$DOR_a = ((1.3 - 0.3PN_a)P_a - (1 - f_{cda})CPC_a)\ A_{ocr}\ B_a$$

$$DOP_a = f_{dop} PR_a A_{ocr}$$

$$\frac{dCOD}{dt} = -\frac{O_2}{kh_{ocod} + O_2} k_{cod} e^{[kt_{cod}(T - T_{cod,ref})]} COD$$

$$R_v = 0.54 + \frac{0.7T}{30} - \frac{0.07S}{35}$$

$$K_{rdo} = \alpha_{rear}(\beta_{rear}\ u_{wind})^{\gamma_{rear}} R_v$$

$$DO_s = 14.5532 + T(0.0054258T - 0.38217) - \frac{S}{1.08655}[0.1665 + T(0.00009796T - 0.005886)]$$

$$DO_{rear} = 86400\left[\frac{K_{rdo}}{\Delta z_{surf}}(DO_s - O_2)\right]$$

$$\frac{dO_2}{dt} = DOR_1 + DOR_2 - DOP_1 - DOP_2 - \sum_{i=1}^{3} kDOC_i \theta_i DOC_i A_{ocr} + \frac{dCOD}{dt} - A_{ont} NT - DO_{rear} - \frac{SOD}{\Delta z_{bot}}$$

Variable/ Parameter	Description	Value	Units
DOR_a	Dissolved Oxygen from primary production and respiration of algae a	calculated	g O_2 m^{-3} d^{-1}
A_{ocr}	Oxygen to carbon ratio for production and respiration	2.667	g O_2 g C^{-1}
DOP_a	Dissolved oxygen loss from predation	calculated	g O_2 m^{-3} d^{-1}
f_{dop}	Fraction of algal predation that is respiration	0.20	dimensionless
dCOD dt^{-1}	Change in Chemical oxygen demand (COD) over time	calculated	g O_2 m^{-3} d^{-1}
kh_{ocod}	Half saturation of O_2 for COD[a]	0.10	g O_2 m^{-3}

k_{cod}	Rate of COD oxidation[a]	20.0	d^{-1}
kt_{cod}	Temperature control of COD oxidation[a]	0.041	$°C^{-1}$
$T_{cod,ref}$	Reference temperature for COD oxidation	23.0	°C
COD	Chemical oxygen demand	calculated	g O^2 m^{-3}
$R\nu$	Ratio of kinematic viscosity of pure water at 20 °C to kinematic viscosity at modeled temperature and salinity	calculated	dimensionless
K_{rdo}	Oxygen reaeration velocity[b]	calculated	m d^{-1}
α_{rear}	Reaeration coefficient 1	0.08	m s^{-1}
β_{rear}	Reaeration coefficient 2	1.0	s m^{-1}
u_{wind}	Surface wind velocity	forced	m s^{-1}
γ_{rear}	Reaeration coefficient 3	1.5	dimensionless
DO_s	Empirical relationship for oxygen saturation at modeled temperature and salinity	calculated	g O_2 m^{-3}
DO_{rear}	Reaeration rate of dissolved oxygen[c,*]	calculated	g O_2 m^{-3} d^{-1}
Δz_{surf}	Surface layer thickness	calculated	m
$dO_2\ dt^{-1}$	Change in dissolved oxygen concentration over time	calculated	g O_2 m^{-3} d^{-1}
A_{ont}	Oxygen to NH_4^+ uptake ratio for nitrification	4.33	g O_2 g N^{-1}
SOD	Sediment oxygen demand[c,**]	calculated	g O_2 m^{-2} d^{-1}
Δz_{bot}	Bottom layer thickness	calculated	m

a. Cerco and Noel 2017
b. Wanninkhof 2014
c. Stumm and Morgan 2012
d. Testa et al., 2013 for details

*Only calculated in surface layer of water column
**Only calculated in bottom layer of water column

Appendix VIII
Inorganic suspended sediment mass balance and resuspension formulations

$$U_* = \frac{\kappa(U^2 + V^2)^{0.5}}{log(\Delta z_{bot} {R_h}^{-1})}$$

$$\tau = \rho {U_*}^2$$

$$\frac{dISS}{dt} = \frac{WS_i\ ISS^{z-1} - WS_i\ ISS^z}{\Delta z} + M_r(\tau - \tau_{crit})$$

Variable/ Parameter	Description	Value	Units
U_*	Boundary layer bottom friction velocity	calculated	m s^{-1}
κ	Von Karman's constant	0.41	dimensionless
U	East-West Velocity in bottom layer	calculated	m s^{-1}
V	North-South Velocity in bottom layer	calculated	m s^{-1}
R_h	Roughness height of bottom sediment	0.002	m
τ	Shear stress in sediment-water column boundary layer	calculated	pa
ρ	Water density[a]	calculated	kg m^{-3}
*d*ISS dt^{-1}	Change in inorganic suspended sediment over time	calculated	g m^{-3} d^{-1}
WS_i	Inorganic suspended sediment sinking velocity	1.5	m d^{-1}
ISS^{z-1}	ISS concentration in layer above	calculated	g m^{-3} d^{-1}
ISS^z	ISS concentration in layer below	calculated	g m^{-3} d^{-1}
M_r	Resuspension mass rate[a]	0.005	g m^{-2} d^{-1}
τ_{crit}	Critical shear stress[a]	0.005	pa

a. Xu and Hood, 2006

The general formula applied here (Law of the Wall) utilizes as simple formulation to calculate resuspension of inorganic sediment. If the critical shear stress (τ_{crit}=0.005 pa) is exceeded, sediment is added back into the water column in the bottom layer at a rate of 0.05 g m^{-2} s^{-1} (Xu and Hood, 2006). The model assumes an inexhaustible sediment supply. The critical shear stress resuspension formula is also applied to POC and PON, applying M_r directly to POC and scaling it by a factor of 10 to PON.

Figures Chapter 5

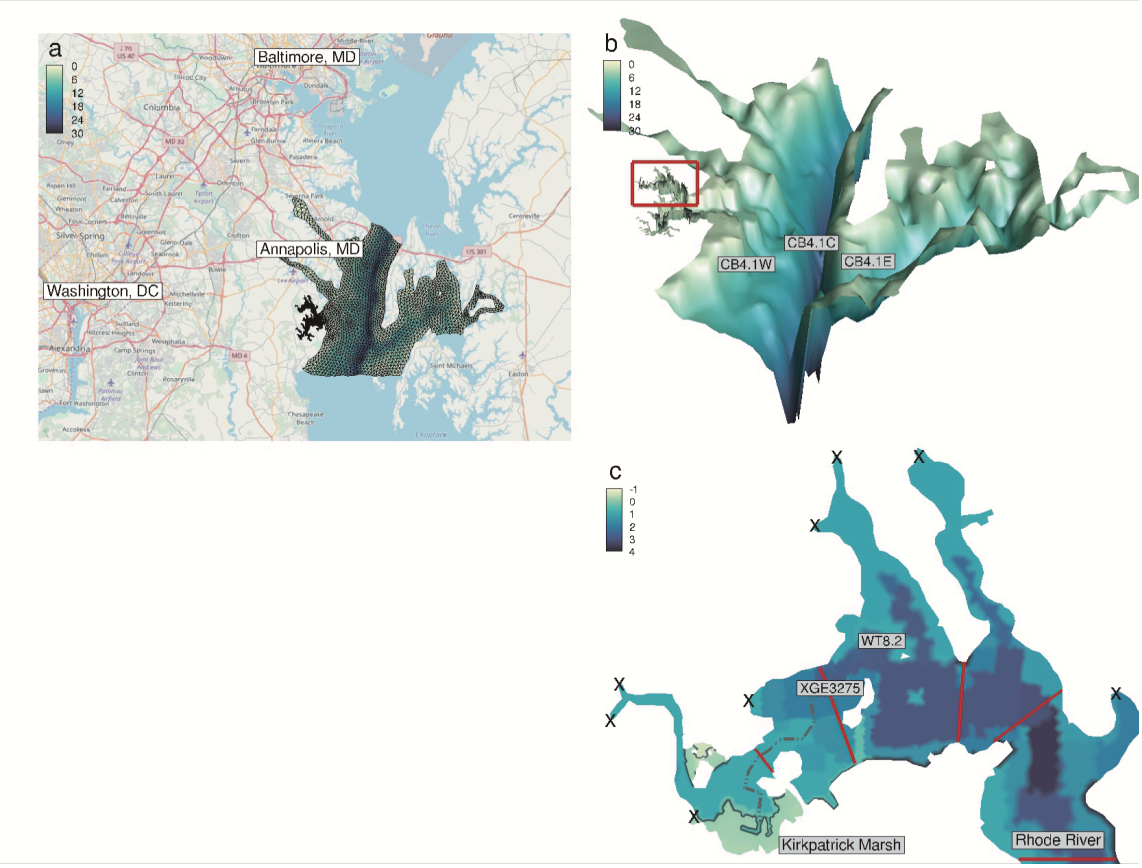

Figure 5.1 (a) RhodeFVM model domain extending from the William Preston Lane Memorial (Chesapeake Bay) Bridge in the north to Poplar Island in the South, (b) 3-dimensional bathymetric rendering of (a) showing three Chesapeake Bay Program (CBP) stations used for model tuning and validation and (c) the Rhode River with the Kirkpatrick Marsh at the head of the tributary and the eight watershed inflows depicted with X's. CBP stations XGE3275 and WT8.2 are shown which were used for modeling tuning and validation. Contours represent model depth. These figures were generated using Tecplot 360.

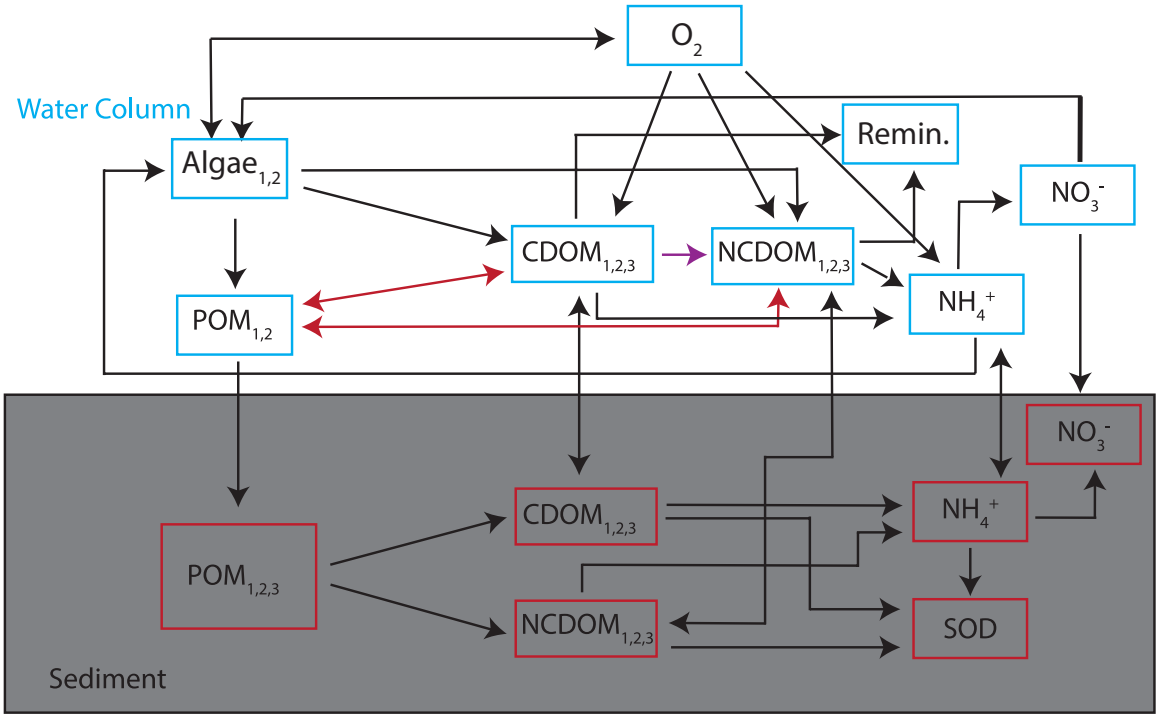

Figure 5.2 Model Conceptual Diagram with an emphasis placed on transformations related to colored and non-colored dissolved organic matter (CDOM and NCDOM; both C and N). The potential coagulation pathway and hydrolytic pathway between DOM and particulate organic matter (POM) is highlighted by a red arrow, and the photochemical reaction pathway is highlighted by a violet arrow. All reaction terms and parameters are defined in the Appendices.

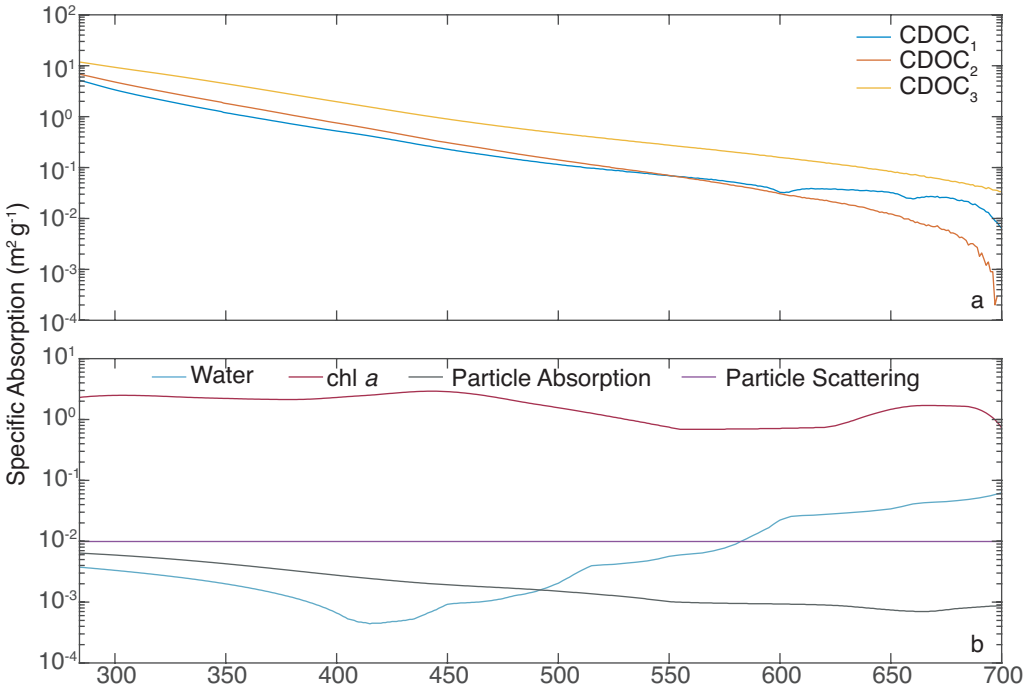

Figure 5.3 Specific absorption spectra for (a) colored dissolved organic carbon (CDOC) 1-3 and (b) water, particles, and chl *a*. Curves in (b) were taken from Rose et al. (2018) and interpolated to the 1 nm interval.

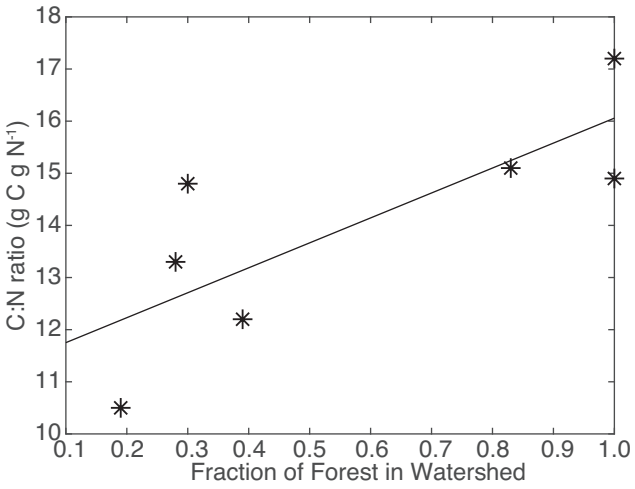

Figure 5.4 Regression of fraction of forest cover with the particulate organic carbon to nitrogen ratio (C:N); Final equation is C:N = 4.78x + 11.27 where x is fraction of the watershed that is forest.

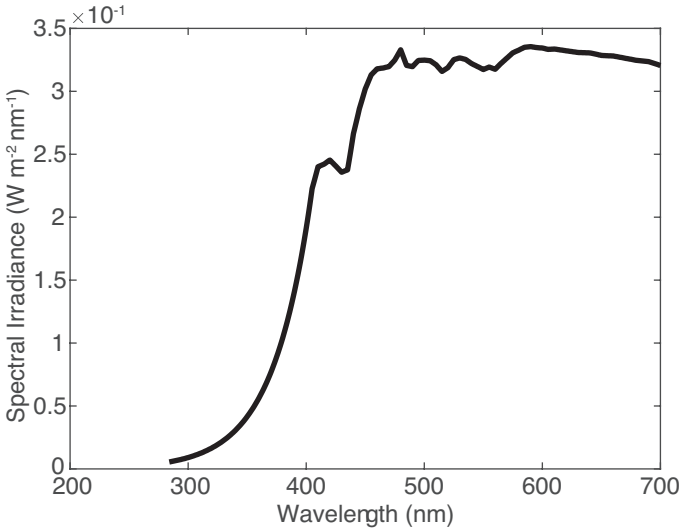

Figure 5.5 The spectral distribution of light at 100 W m^{-2} of incident irradiation.

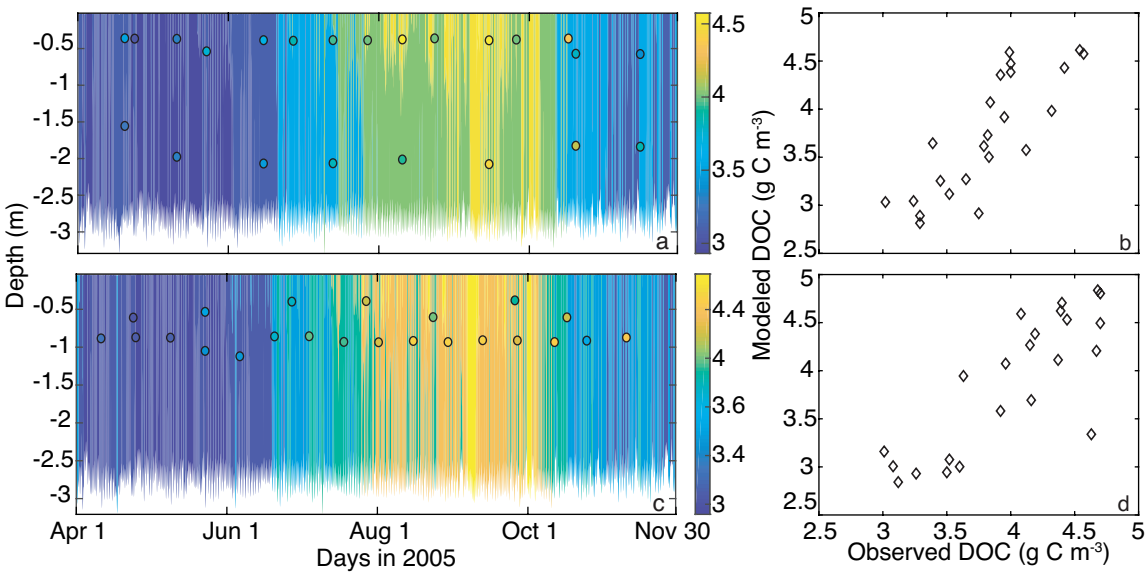

Figure 5.6 Model-observation comparisons for station WT8.2 (a,b) and station XGE3275 (c,d). Contours represent model output for dissolved organic carbon (DOC) in time, while each dot represents an observation.

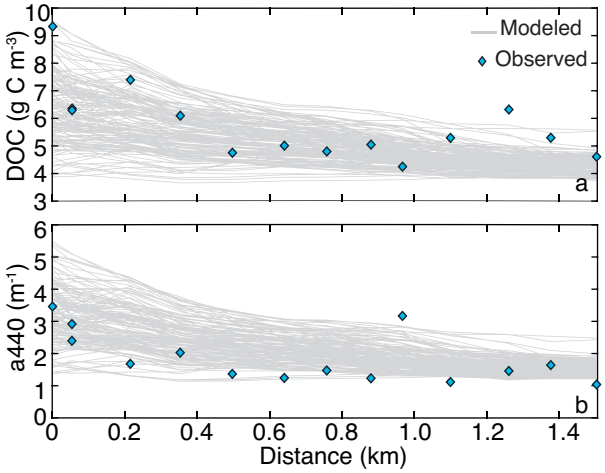

Figure 5.7 Model-observation comparison along the transect in Figure 1c for (a) dissolved organic carbon (DOC) and (b) colored dissolved organic matter (CDOM) absorbance at 440 nm (a440). Observations were collected at various times during ebb tide phase and averaged. The model output is at an hourly interval for July 2005 when the change in tidal elevation, dz dt^{-1}, was less than the median change in tidal elevation for all ebb tides (dz dt^{-1} < -2.16 cm hr^{-1}; n=153). Collection methods and analytical techniques can be found in Tzortziou et al., (2011) and Logozzo (2017). Modeled a440 is the product of the specific absorption of each colored DOC class (1-3) at 440 nm (m^2 g C^{-1}) and colored DOC concentration (g C m^{-3}).

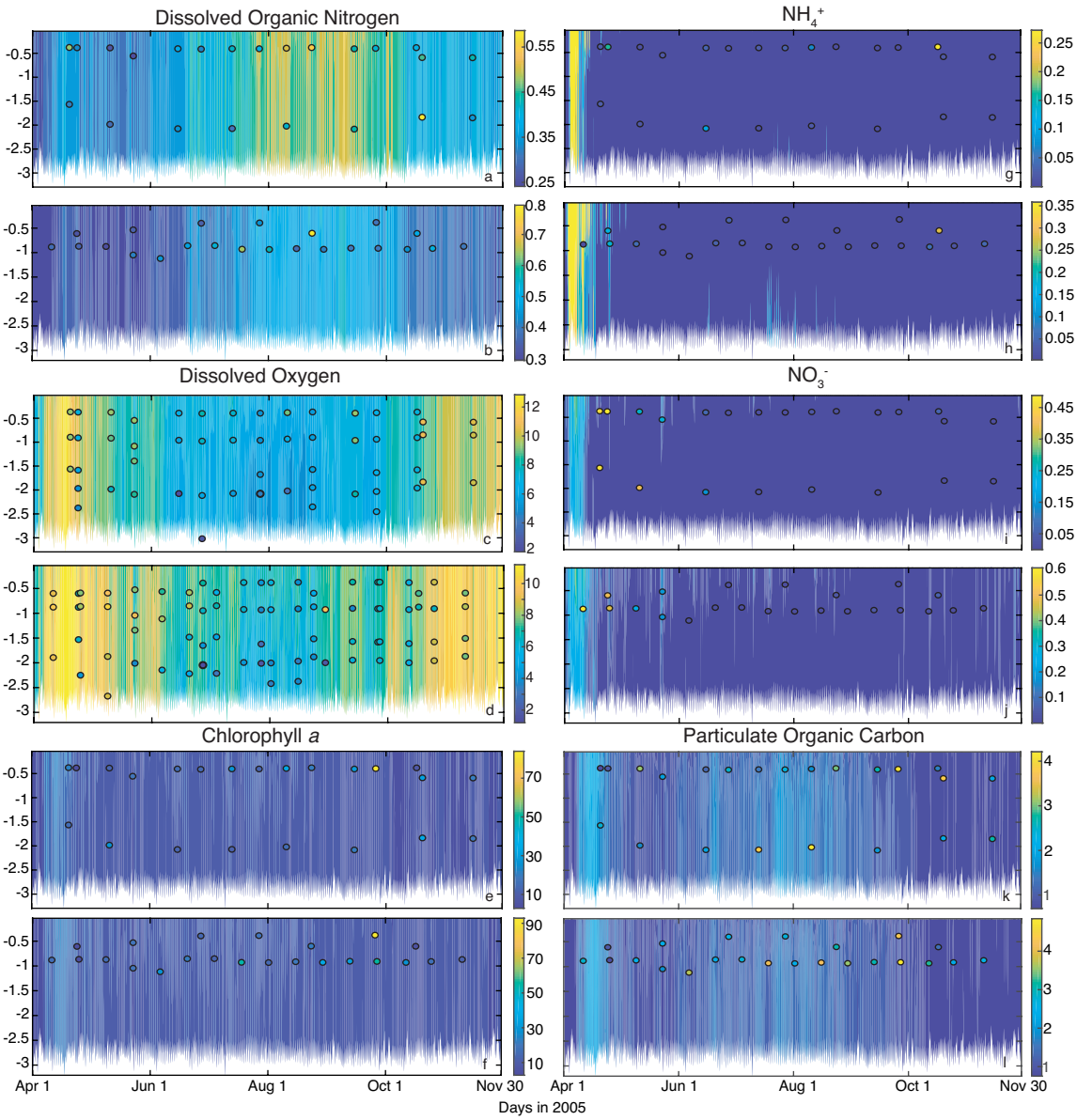

Figure 5.8 Model (contours) and Chesapeake Bay Program observations (circles) for stations WT8.2 (upper) and XGE3275 (lower) for dissolved organic nitrogen (a,b)(g N m^{-3}), dissolved oxygen (c,d) (g O_2 m^{-3}), chlorophyll *a* (e,f)(mg chl *a* m^{-3}), NH_4^+ (g,h)(g N m^{-3}), NO_3^- (i,j)(g N m^{-3}) and particulate organic carbon (POC)(k,i)(g C m^{-3}). Observed POC is estimated from measured values of particulate organic nitrogen and converted to carbon units using a ratio of 5.67 g C g N^{-1}.

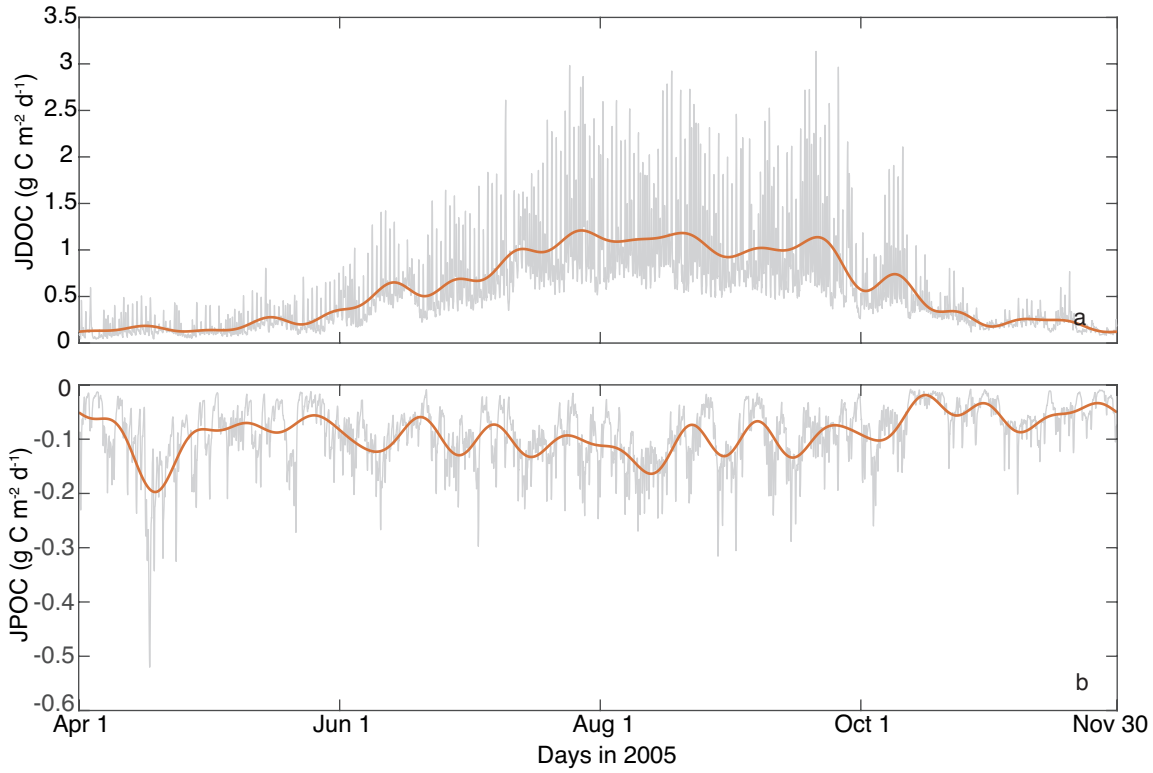

Figure 5.9 Average marsh-estuary (a) dissolved organic carbon flux (JDOC) and particulate organic carbon flux (JPOC). A positive flux is out of the marsh, negative flux into the marsh. The orange line represents the low pass frequency filtered flux using a period of 14 days as the filter cutoff frequency. The grey line is the instantaneous average flux taken at an hourly interval.

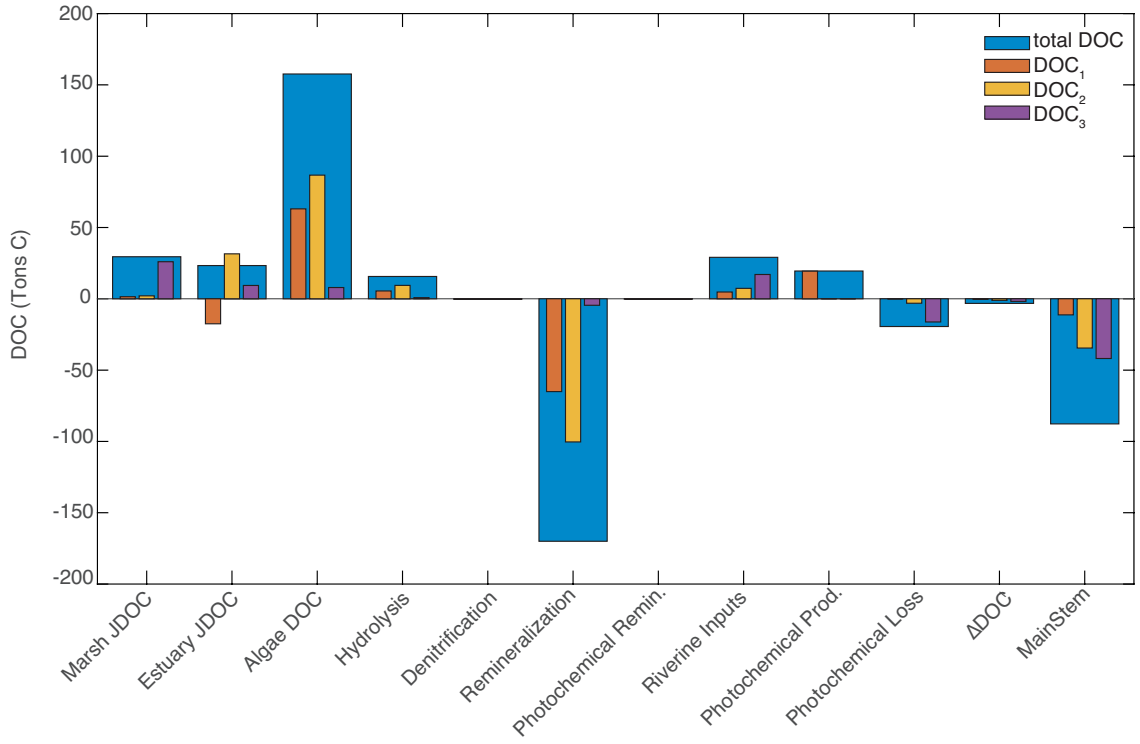

Figure 5.10 The complete dissolved organic carbon (DOC) budget for the Rhode River tributary (Figure 1c). Each bar represents the cumulative DOC sources (positive) or sinks (negative) for DOC over April 1 – November 30, 2005. The total is the sum of the three reactivity classes. From left to right, the terms are defined as the marsh sediment-water column DOC flux (Marsh JDOC), estuarine sediment-water column DOC flux (Estuary JDOC), planktonic algal derived DOC from both exudation and predation (Algae DOC), hydrolysis of particulate organic carbon to DOC, denitrification loss of DOC, heterotrophic remineralization of DOC, abiotic photochemical remineralization of DOC, riverine inputs from the watershed of DOC, photochemical transformation of DOC between colored and non-colored pools and reactivity classes, photochemical loss of DOC (inverse of production), the change in DOC concentration over the model time period (ΔDOC) and the flux between the Rhode River and the main stem of the model domain (MainStem).

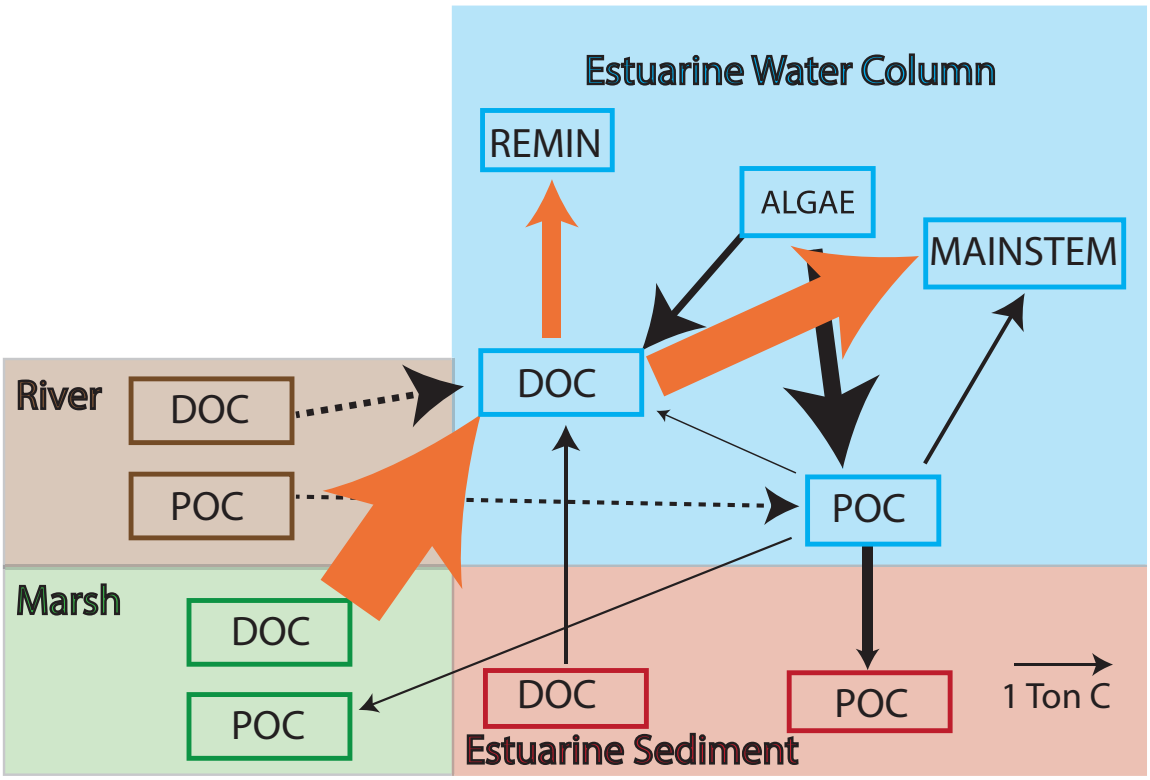

Figure 5.11 Difference network between the model scenarios with (+M) and without (-M) marsh dissolved organic matter (DOM) inputs and NH_4^+ uptake. The dashed lines represent processes that are unchanged, orange arrows represent processes that decreased under the –M scenario, black arrows represent processes that increased under the –M scenario. The width of the arrow represents the total difference between the two scenarios (tons C) over the 242-day model time period.

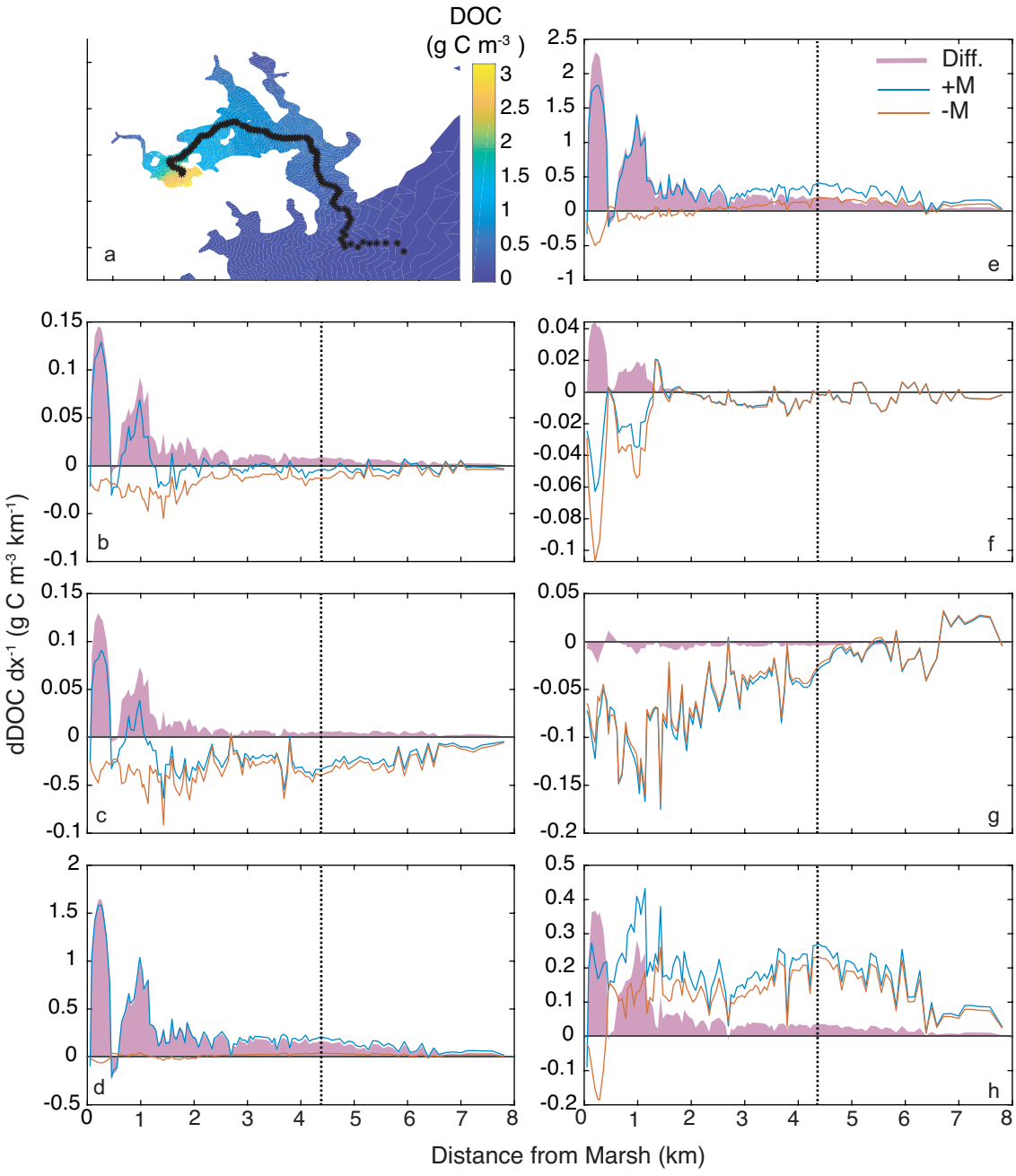

Figure 5.12 (a) The average difference in DOC concentration between the +M and –M scenarios and a transect line (for b-h) used to calculate the concentration gradient in the +M and –M scenarios and the difference (Diff.) between the two for (b) $CDOC_1$, (c) $CDOC_2$, (d) $CDOC_3$, (e) total DOC, (f) $NCDOC_1$, (g) $NCDOC_2$, and (h) $NCDOC_3$. The dashed lines on b-h represent the cutoff for the section of the Rhode River used in the budget analysis.

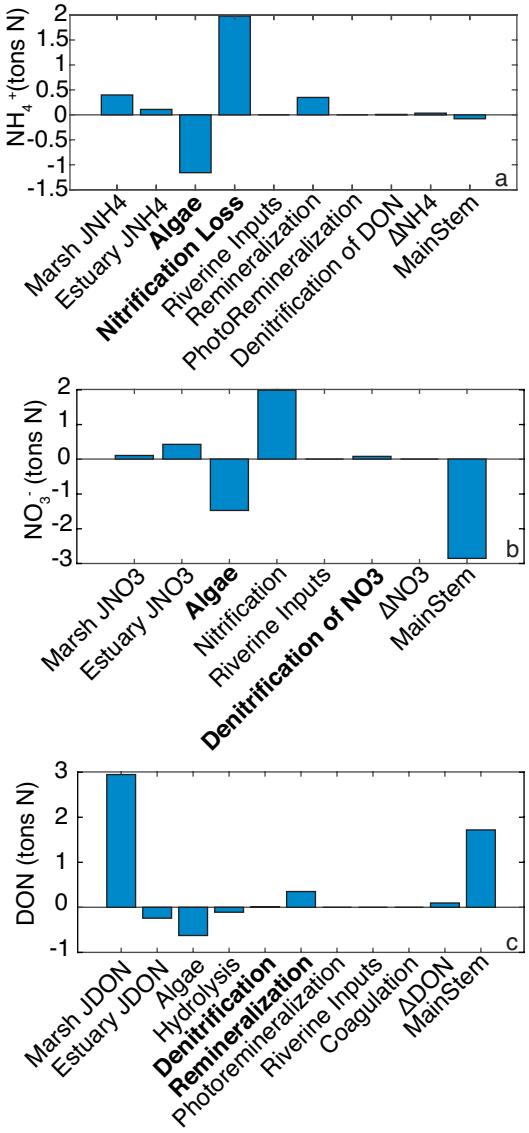

Figure 5.13 Absolute difference in nitrogen budgets for runs with (+M) and without (-M) the marsh for (a) ammonium (NH_4^+), (b) nitrate (NO_3^-) and (c) dissolved organic nitrogen (DON) for the Rhode River integrated from April1st – November 30th, 2005. Terms in regular print are sources while terms in bold are sinks.

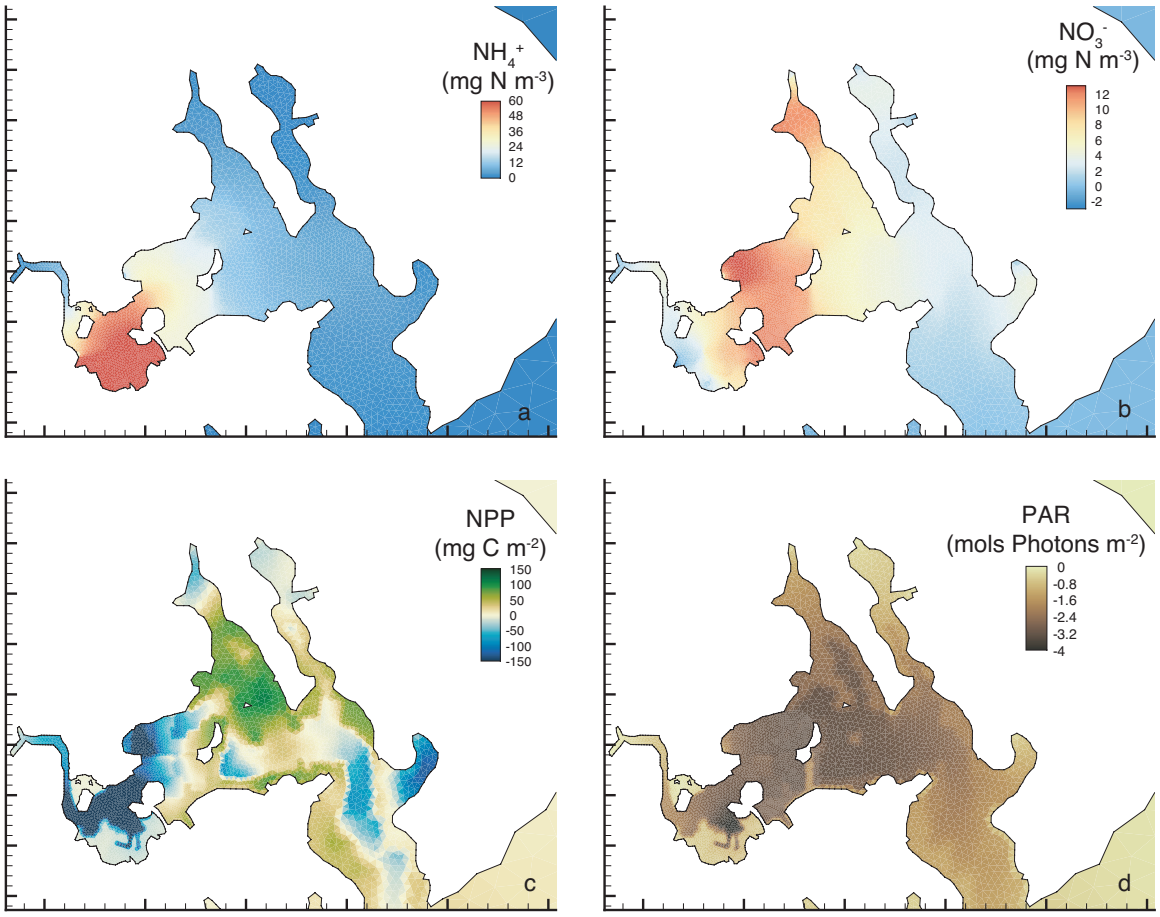

Figure 5.14 The average difference between runs with and without the marsh (+M minus –M) for mid-water column (a) ammonium (NH_4^+), (b) nitrate (NO_3^-), (c) depth integrated net primary production (NPP) and (d) mid-water column photosynthetically active radiation (PAR).

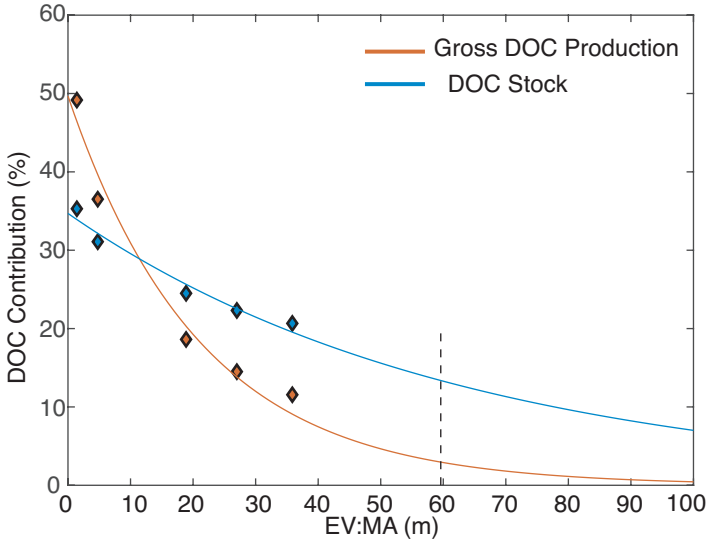

Figure 5.15 Percent dissolved organic carbon (DOC) contribution from the marsh to the gross DOC production and estuarine DOC stock within the Rhode River modeled as a function of the estuary volume to marsh area ratio (EV:MA). The model function was derived using a generalized logarithmic linear model predicted by the five segments from the Rhode River and extrapolated to estimate the marsh DOC contribution based on the EV:MA for the entire Chesapeake Bay (59.6 m, dashed line). Diamonds indicate model-extracted values for each segment. (p value for % GDP = 0.002, p value for stock = 0.001)

Tables Chapter 5

Table 5.1 Model statistics for the two stations in the Rhode River, MD

Station	*WT8.2*						
Variable[a]	**MEF**[b]	**r**[c]	**RMSE**[d]	**MPE**[e]	**WMS**[f]	**RI**[g]	**n**[h]
DOC	0.21	0.82	0.37 (g m^{-3})	2.44	0.86	1.11	23
chl *a*	-0.38	0.23	17.97 (mg m^{-3})	2.00	0.30	2.14	23
DO	-0.25	0.41	2.26 (g m^{-3})	-21.75	0.61	1.40	55
DON	0.08	0.51	0.08 (g m^{-3})	-10.61	0.66	1.22	23
NH_4^+	-0.22	-0.03	0.07 (g m^{-3})	-29.95	0.32	14.23	23
NO_3^-	-0.39	0.13	0.20 (g m^{-3})	71.95	0.45	76.77	23
POC	-1.35	-0.19	1.48 (g m^{-3})	27.36	0.39	2.18	23
Salinity	0.38	0.92	2.56	-34.20	0.78	1.46	55
Temperature	0.85	0.93	2.22 (°C)	-1.11	0.96	1.14	55
Station	*XGE3275*						
DOC	0.43	0.82	0.42 (g m^{-3})	3.33	0.88	1.12	23
chl *a*	-0.40	-0.12	23.11 mg m^{-3})	-10.49	0.35	2.57	23
DO	-0.60	0.49	2.61 (g m^{-3})	-51.54	0.57	1.65	82
DON	-0.02	0.34	0.11 (g m^{-3})	0.38	0.55	1.26	23
NH_4^+	-1.14	0.03	0.10 (g m^{-3})	-763.6	0.33	6.84	23
NO_3^-	0.31	0.71	0.14 (g m^{-3})	-42.44	0.68	246.5	23
POC	-2.46	0.02	1.84 (g m^{-3})	44.54	0.40	2.44	23
Salinity	0.51	0.92	2.18	-26.98	0.83	1.38	82
Temperature	0.91	0.96	1.71 (°C)	-2.20	0.98	1.10	82

a. Observational data collected by the US Environmental Protection Agency Chesapeake Bay Program Water Quality Database for the year 2005. Each comparison is for the closest matching time and depth for the model output and the observational data. Chlorophyll *a* (chl *a*), dissolved organic carbon and nitrogen (DOC and DON), dissolved oxygen (DO), Ammonium (NH_4^+), nitrate (NO_3^-), salinity and temperature were all measured directly, while particulate organic carbon was estimated from particulate organic nitrogen using a C:N ratio of 5.67 (g C : g N).
b. Model efficiency (MEF), values greater than 0.0 are better than the mean at recreating any observation (Loague and Green, 1991; Stow et al., 2009)
c. Coefficient of variance (r), a value of 1 is a perfect match between model and data
d. Root mean square error (RMSE)
e. Mean percent error (MPE), the sign indicates whether the model is less than (positive) or greater than (negative) observations on average
f. Willmott Skill (Willmott, 1981)
g. Reliability Index (RI) indicates the factor by which model data varies from observational (Leggett and Williams, 198l; Stow et al., 2009)
h. Number of observations

Table 5.2 Model statistics for the Main Stem of Chesapeake Bay

Station	*CB4.1C*						
Variable[a]	**MEF**[b]	**r**[c]	**RMSE**[d]	**MPE**[e]	**WMS**[f]	**RI**[g]	**n**[h]
DOC[i]	-0.13	0.30	0.30 (g m^{-3})	-2.26	0.56	1.18	46
chl *a*	0.09	0.36	15.15 (mg m^{-3})	-160.4	0.30	3.22	46
DO	-0.21	0.54	3.64 (g m^{-3})	-706.5	0.67	6.17	130
DON	-1.22	0.27	0.06 (g m^{-3})	-18.15	0.45	1.25	46
NH_4^+	0.43	0.69	0.10 (g m^{-3})	-286.5	0.75	5.98	46
NO_3^-	0.18	0.48	0.21 (g m^{-3})	-343.1	0.62	11.2	46
POC[i]	-0.66	-0.14	1.74 (g m^{-3})	-271.6	0.32	3.66	46
Salinity	-0.17	0.71	3.85	-27.95	0.61	1.38	130
Temperature	0.81	0.97	2.95 (°C)	-13.86	0.96	1.18	130
Station	*CB4.1E*						
DOC[i]	0.13	0.39	0.39 (g m^{-3})	-7.48	0.50	1.23	31
chl *a*	-0.09	-0.05	13.27 mg m^{-3})	-259.6	0.16	3.93	31
DO	-0.75	0.33	4.30 (g m^{-3})	-797.2	0.55	6.52	101
DON	-0.49	0.43	0.07 (g m^{-3})	-23.03	0.51	1.31	31
NH_4^+	-0.13	0.45	0.14 (g m^{-3})	-357.7	0.55	4.26	31
NO_3^-	0.28	0.63	0.21 (g m^{-3})	-427.2	0.64	16.7	31
POC[i]	-1.28	-0.41	1.46 (g m^{-3})	-348.0	0.27	3.87	31
Salinity	-0.67	0.69	4.31	-36.63	0.58	1.45	101
Temperature	0.85	0.97	2.86 (°C)	-11.62	0.97	1.17	101
Station	*CB4.1W*						
DOC[i]	0.03	0.29	0.36 (g m^{-3})	-5.34	0.54	1.22	22
chl *a*	0.03	0.27	10.1 (mg m^{-3})	-73.89	0.43	2.43	22
DO	-0.76	0.34	3.62 (g m^{-3})	-14.87	0.58	1.88	83
DON	-0.66	0.48	0.07 (g m^{-3})	-22.15	0.55	1.29	22
NH_4^+	-0.96	0.29	0.12 (g m^{-3})	-171.5	0.53	5.81	22
NO_3^-	0.19	0.68	0.31 (g m^{-3})	-37.09	0.67	398.5	22
POC[i]	-1.27	-0.37	1.33 (g m^{-3})	-152.5	0.33	2.61	22
Salinity	-3.26	0.85	6.39	-89.39	0.50	1.94	83
Temperature	0.93	0.97	1.92 (°C)	-1.20	0.98	1.11	83

a. Observational data collected by the US Environmental Protection Agency Chesapeake Bay Program Water Quality Database for the year 2005. Each comparison is for the closest matching time and depth for the model output and the observational data. Chlorophyll *a* (chl *a*), dissolved organic carbon and nitrogen (DOC and DON), dissolved oxygen (DO), Ammonium (NH_4^+), nitrate (NO_3^-), salinity and temperature were all measured directly, while particulate

organic carbon was estimated from particulate organic nitrogen using a C:N ratio of 5.67 (g C : g N).

b. Model efficiency (MEF), values greater than 0.0 are better than the mean at recreating any observation (Loague and Green, 1991; Stow et al., 2009)
c. Coefficient of variance (r), a value of 1 is a perfect match between model and data
d. Root mean square error (RMSE)
e. Mean percent error (MPE), the sign indicates whether the model is less than (positive) or greater than (negative) observations on average
f. Willmott Skill (Willmott, 1981)
g. Reliability Index (RI) indicates the factor by which model data varies from observational (Leggett and Williams, 198l; Stow et al., 2009)
h. Number of observations

Conclusion and Future Research Directions

This study offers a detailed look at carbon, and specifically the cycling of organic carbon within an estuarine ecosystem. The first two research chapters focused on developing methods to incorporate specific important processes into a modeling system that were previously unrepresented with any detail, if at all. Next, physical and biogeochemical cycles were identified and quantified for the case-study ecosystem, the Rhode River, MD. The Rhode River is similar to many estuarine systems found in populated watersheds, therefore it is founded to draw some general conclusions from this work. Here, I provide a brief summary of each chapter with some potential future research questions and directions related to each.

Chapter 2 predicted that estuarine sediment organic carbon fluxes are potentially important, especially in shallow estuarine ecosystems such as Chesapeake Bay. Sediment-water column fluxes of DOM are highly variable on seasonal and interannual scales, with substantial variability among stations in both magnitude and flux direction. Semilabile and inert DOM was lost and labile DOM was taken up into the reactive first layer of the sediment, with the net flux out of the sediment a balance of the two processes. The modeling results are striking in that they predict a much larger flux than what has previously been measured, and that the sediment is effectively decreasing the reactivity of the overlying water column DOC. The results from Chapter 2 are potentially testable in a laboratory and *in situ* in an estuarine environment. First, the flux can be measured using an approach that is similar to the widespread measurements of inorganic nitrogen (Boynton and Bailey, 2008; Cowan and Boynton, 1996) and previous

measurements of DOC (Burdige and Homstead, 1994). These flux measurements can be paired with geochemical analysis to characterize the molecular composition of the DOC in the overlying water column and the sediment porewater. Sediment porewater contains DOM with specific optical and molecular characteristics (Burdige et al., 2004; Burdige and Gardner, 1998) and these geochemical measurements can be extended into the water column. In light of the model results, measurements that can confirm the prediction of both flux direction (depending on biological reactivity) and magnitude can then be incorporated into larger regional and potentially global estuarine organic carbon budgets.

Chapter 3 used a new photochemical degradation model paired with laboratory experiments to better understand and predict the transformation of CDOM by the absorption of UV-Visible light. The model predicted rates that are similar to measurements from many different environments, and was successfully parameterized to represent the loss in color (absorption of light) over time. Furthermore, the model could accurately recreate an independent test data set that was not used in the parameterization, indicating its robustness in simulating photochemical degradation in an estuarine environment. Moving forward, DOM-PD can now be used by the scientific community in other systems where observational data exists to parameterize the model. When coupled with an ecosystem model, it offers a powerful tool to more accurately represent the important transformation of DOM by light. The model can also be generalized so that it isn't necessarily limited to the coastal ocean. This could be done by including an open ocean, highly photodegraded CDOC pool. Key to this addition is understanding how photochemical degradation can also *decrease* the biological reactivity of DOM after

exposure, a pathway that is coarsely represented (and unconstrained) in the current modeling framework.

Chapter 4 looked at the physical mechanisms behind the curiosity that *fDOM* observations at a marsh creek were strongly correlated with salinity and in turn wind velocity. A 3-D hydrodynamic model was built for the Rhode River to understand how changes in wind direction can drive changes in salinity at the marsh creek. Because observations of *fDOM* and salinity showed a tight correlation in spring and fall, the modeled salinity variability can be used to infer how the wind velocity would also affect *fDOM*. The model results exhibited an interaction between wind driven variation in surface elevation and flow velocity at the marsh creek, with northerly winds driving increased freshwater signal and discharge out of the modeled wetland during precipitation events. Wind setup of a water surface elevation gradient axially along the estuary drives the modeled local sub-tidal flow and thus salinity variability. On sub-tidal time scales (>36 hours, < 1 week) wind is important in mediating dissolved organic matter releases from the Kirkpatrick Marsh into the Rhode River. To further understand how changes in wind drive changes in flow in tidal marshes, the modeling system should be expanded spatially to incorporate non-local effects such as variations in sea level at the coastal ocean. An FVCOM model already exists that includes Chesapeake and Delaware Bays and the continental shelf, but tidal wetlands are currently unresolved. A top priority moving forward is to include tidal wetlands in this regional model so that physical drivers associated with changes in wind direction (and other weather and climate variables) can be assessed on a larger scale.

Chapter 5 used the research from the first three chapters to build a sophisticated wetland-estuarine carbon cycle model for a representative estuarine ecosystem. The modeling system was used to produce a comprehensive organic carbon budget with unprecedented detail. Tidal wetlands and watershed inputs accounted for ~25% of the input of dissolved organic carbon (DOC) into the tributary, with 61.9% coming from phytoplankton production. 95.7% of the POC within the tributary originated from algal production and subsequent mortality, with 19.93 tons of POC exported from the Rhode River to the mainstem over the warm seasons of 2005. Overall 87.32 tons of DOC was exported to the mainstem, which accounted for 34.2% of the total allochthonous and autochthonous inputs to the tributary. Removing the wetland at the head of the tributary decreased export of DOC to the mainstem by 20.9%. Furthermore, by removing the marsh, total nitrogen in the tributary decreased, while dissolved oxygen increased. A geographic relationship derived from the Rhode River modeling system indicated that tidal wetlands may contribute ~13% of the total DOC stock of Chesapeake Bay. Moving forward, the RhodeFVCOM-ICM system should be updated to contemporary years (2015-2017) where high temporal resolution measurement data exists for multiple biogeochemical variables at the marsh creek. A top priority with the Rhode River model is to understand how variation in tidal forcing on longer time scales (spring-neap variability) drives changes in DOM export. With changes in sea level and shoreline management strategy, the tides of Chesapeake Bay could change significantly (Lee et al., 2017). Thoroughly understanding how complex tidal cycles can govern DOM and solute exchange is important to predict how wetland inundation and carbon export will manifest

in the future. The model coupled with high resolution observations can address these questions.

To advance our understanding of estuarine carbon cycling, the updated ICM-DOM-PD modeling system should be coupled with the regional FVCOM model on the estuary and continental shelf scale (see above) to simulate carbon cycling in wetlands and estuaries on a large scale. A large scale model can be used to better constrain the carbon budget for an important region on the East Coast of the United States. In addition, the inorganic carbon cycle should also be included to quantify the full carbon cycle. Dissolved inorganic carbon and alkalinity modules already exist and can be included in the current iteration of RhodeFVCOM. Furthermore, a dynamic marsh growth and death model could also be included to more realistically represent how a marsh plant community might change over time. This further enhanced modeling system could then be used in longer term studies related to climate change projections to understand how increased atmospheric CO_2 drives changes in marsh plant community and inorganic carbon cycling in the water column. A long term goal is to develop a regional model that includes all relevant inputs and outputs that can be used to make climate change projections for both tidal wetlands and estuaries. This would require substantial human resources and computer infrastructure, but should be a priority over the next decade.

Estuaries are complex ecosystems. Quantifying the cycling of any material, plant, or animal within them is challenging. The importance of estuaries, however, and the role they play at the intersection of the land and the sea, and the intersection of humans and nature, means that understanding them is extremely important. This dissertation has offered a detailed analysis of a specific, relatively small tributary of Chesapeake Bay, and

has produced some general results related to carbon cycling in coastal systems. To advance our understanding of the coastal ocean in a more holistic way, the model developed here should be used in more diverse ecosystems, where data permits. Tidal wetlands have an outsized influence on the total DOC within Chesapeake Bay relative to their contribution to the total DOC inputs. Other more oligotrophic estuaries with a larger amount of marsh relative to estuary will be more heavily influenced by tidal marshes. Developing empirical relationships that can relate not only geographic characteristics but also trophic status and physical forcing (e.g., tidal range) is the next step to scaling up carbon budgets from small representative ecosystems to large areas. Every estuary is different, but with a well parameterized model processes that are difficult to measure can be estimated.

References

Aarnos, H., Gélinas, Y., Kasurinen, V., Gu, Y., Puupponen, V.M. and Vähätalo, A.V., (2018). Photochemical mineralization of terrigenous DOC to dissolved inorganic carbon in ocean. Global Biogeochemical Cycles, 32(2), 250-266

Aarnos, H., Ylöstalo, P. and Vähätalo, A.V., (2012). Seasonal phototransformation of dissolved organic matter to ammonium, dissolved inorganic carbon, and labile substrates supporting bacterial biomass across the Baltic Sea. Journal of Geophysical Research: Biogeosciences, 117(G1)

Adolf, J. E., Yeager, C. L., Miller, W. D., Mallonee, M. E., & Harding, L. W. (2006). Environmental forcing of phytoplankton floral composition, biomass, and primary productivity in Chesapeake Bay, USA. *Estuarine, Coastal and Shelf Science*, *67*(1), 108–122.

Alperin, M. J., Albert, D. B., & Martens, C. S. (1994). Seasonal variations in production and consumption rates of dissolved organic carbon in an organic-rich coastal sediment. *Geochimica et Cosmochimica Acta*, *58*(22), 4909–4930.

Arnosti, C., & Holmer, M. (2003). Carbon cycling in a continental margin sediment: contrasts between organic matter characteristics and remineralization rates and pathways. *Estuarine, Coastal and Shelf Science*, *58*(1), 197–208.

Baines, S. B., & Pace, M. L. (1991). The production of dissolved organic matter by phytoplankton and its importance to bacteria: Patterns across marine and freshwater systems. *Limnology and Oceanography*, *36*(6), 1078–1090.

Bauer, J. E., Cai, W.-J., Raymond, P. A., Bianchi, T. S., Hopkinson, C. S., & Regnier, P. A. G. (2013). The changing carbon cycle of the coastal ocean. *Nature*, *504*(7478), 61–70.

Bélanger, S., Xie, H., Krotkov, N., Larouche, P., Vincent, W. F., & Babin, M. (2006). Photomineralization of terrigenous dissolved organic matter in Arctic coastal waters from 1979 to 2003: Interannual variability and implications of climate change: ARCTIC CDOM PHOTOOXIDATION. *Global Biogeochemical Cycles*, *20*(4). https://doi.org/10.1029/2006GB002708

Benner, R., & Opsahl, S. (2001). Molecular indicators of the sources and transformations of dissolved organic matter in the Mississippi river plume. *Organic Geochemistry*, *32*(4), 597–611.

Blumberg, A. F., & Goodrich, D. M. (1990). Modeling of wind-induced destratification in Chesapeake Bay. *Estuaries*, *13*(3), 236–249.

Bockelmann, A.-C., Bakker, J. P., Neuhaus, R., & Lage, J. (2002). The relation between vegetation zonation , elevation and inundation frequency in a Wadden Sea salt marsh, *Aquatic* Botany, *73*(3), 211–221.

Boschker, H. T. S., de Brouwer, J. F. C., & Cappenberg, T. E. (1999). The contribution of macrophyte-derived organic matter to microbial biomass in salt-marsh sediments: Stable carbon isotope analysis of microbial biomarkers. *Limnology and Oceanography*, *44*(2), 309–319.

Boynton, W.R., & Bailey, E. M. (2008). Sediment Oxygen and Nutrient Exchange Measurements From Chesapeake Bay, Tributary Rivers and Maryland Coastal Bays: Development of a Comprehensive Database and Analysis of Factors Controlling Patters and Magnitude of Sediment-water Exchanges. Solomons, MD: University of Maryland Center for Environmental Science.

Boynton, W. R., & Kemp, W. M. (1985). Nutrient regeneration and oxygen consumption by sediments along an estuarine salinity gradient. *Marine Ecology Progress Series*, *23*, 45–55.

Bradley, P. M., & Morris, J. T. (1991). The influence of salinity on the kinetics of NH_4^+ uptake in Spartina alterniflora. *Oecologia*, *85*(3), 375-380.

Brady, D. C., Testa, J. M., Di Toro, D. M., Boynton, W. R., & Kemp, W. M. (2013). Sediment flux modeling: Calibration and application for coastal systems. *Estuarine, Coastal and Shelf Science*, *117*, 107–124.

Breitburg, D. L., Hines, A. H., Jordan, T. E., McCormick, M. K., Weller, D. E., & Whigham, D. F. (2008). Landscape patterns, nutrient discharges, and biota of the Rhode River estuary and its watershed: Contribution of the Smithsonian Environmental Research Center to the Pilot Integrated Ecosystem Assessment. Retrieved from https://repository.si.edu/bitstream/handle/10088/18018/serc_BreiteburgEtAl2008RhodeRiverIEA.pdf

Bridgham, S. D., Megonigal, J. P., Keller, J. K., Bliss, N. B., & Trettin, C. (2006). The carbon balance of North American wetlands. *Wetlands*, *26*(4), 889–916.

Burdige, D. J., Alperin, M. J., Homstead, J., & Martens, C. S. (1992). The Role of Benthic Fluxes of Dissolved Organic Carbon in Oceanic and Sedimentary Carbon Cycling. *Geophysical Research Letters*, *19*(18), 1851–1854.

Burdige, D. J., & Gardner, K. G. (1998). Molecular weight distribution of dissolved organic carbon in marine sediment pore waters. *Marine Chemistry*, *62*(1), 45–64.

Burdige, D. J., & Homstead, J. (1994). Fluxes of dissolved organic carbon from Chesapeake Bay sediments. *Geochimica et Cosmochimica Acta*, *58*(16), 3407–3424.

Burdige, D. J., Kline, S. W., & Chen, W. (2004). Fluorescent dissolved organic matter in marine sediment pore waters. *Marine Chemistry*, *89*(1), 289–311.

Burdige, D. J., Komada, T., Magen, C., & Chanton, J. P. (2016). Modeling studies of dissolved organic matter cycling in Santa Barbara Basin (CA, USA) sediments. *Geochimica et Cosmochimica Acta*, *195*, 100–119.

Burdige, D. J., & Zheng, S. (1998). The Biogeochemical Cycling of Dissolved Organic Nitrogen in Estuarine Sediments. *Limnology and Oceanography*, *43*(8), 1796–1813.

Butman, D., Raymond, P. A., Butler, K., & Aiken, G. (2012). Relationships between Δ 14 C and the molecular quality of dissolved organic carbon in rivers draining to the coast from the conterminous United States : Δ 14 C OF DOC IN US RIVERS. *Global Biogeochemical Cycles*, *26*(4). https://doi.org/10.1029/2012GB004361

Cai, W.-J. (2011). Estuarine and Coastal Ocean Carbon Paradox: CO2 Sinks or Sites of Terrestrial Carbon Incineration? *Annual Review of Marine Science*, *3*(1), 123–145.

Cao, F., Medeiros, P. M., & Miller, W. L. (2016). Optical characterization of dissolved organic matter in the Amazon River plume and the Adjacent Ocean: Examining the relative role of mixing, photochemistry, and microbial alterations. *Marine Chemistry*, *186*, 178–188.

Carlson, C. A., Ducklow, H. W., & Michaels, A. F. (1994). Annual flux of dissolved organic carbon from the euphotic zone in the northwestern Sargasso Sea. *Nature*, *371*, 405.

Carlson, C. A., Hansell, D. A., Nelson, N. B., Siegel, D. A., Smethie, W. M., Khatiwala, S., … Halewood, E. (2010). Dissolved organic carbon export and subsequent remineralization in the mesopelagic and bathypelagic realms of the North Atlantic basin. *Deep-Sea Research. Part II, Topical Studies in Oceanography*, *57*(16), 1433–1445.

Cerco, C.F. and Cole, T., (1993). Three-dimensional eutrophication model of Chesapeake Bay. Journal of Environmental Engineering, 119(6), 1006-1025.

Cerco, C. F., & Noel, M. R. (2004). Process-based primary production modeling in Chesapeake Bay. *Marine Ecology Progress Series*, *282*, 45–58.

Cerco, C.F. and Noel, M.R., (2013). Twenty-one year simulation of Chesapeake Bay water quality using the CE-QUAL-ICM eutrophication model. JAWRA Journal of the American Water Resources Association, 49(5), 1119-1133.

Cerco, C. F., & Noel, M. R. (2017). The 2017 Chesapeake Bay Water Quality and Sediment Transport Model A Report to the US Environmental Protection Agency Chesapeake Bay Program.

Chen, C., Beardsley, R. C., Cowles, G., Qi, J., Lai, Z., Gao, G., … Others. (2013). *An unstructured grid, finite-volume community ocean model FVCOM user manual, SMAST*. UMASSD Technical Report-13-0701, University of Massachusetts-Dartmouth.

Chen, C., Liu, H., & Beardsley, R. C. (2003). An Unstructured Grid, Finite-Volume, Three-Dimensional, Primitive Equations Ocean Model: Application to Coastal Ocean and Estuaries. *Journal of Atmospheric and Oceanic Technology*, *20*(1), 159–186.

Chen, C., Qi, J., Li, C., Beardsley, R. C., Lin, H., Walker, R., & Gates, K. (2008). Complexity of the flooding/drying process in an estuarine tidal-creek salt-marsh system: An application of FVCOM. *Journal of Geophysical Research*, *113*(C7), C07052.

Childers, D. L., Day, J. W., & Mckellar, H. N. (2002). Twenty more years of marsh and estuarine flux studies: revisiting Nixon (1980). In *Concepts and controversies in tidal marsh ecology* (pp. 391–423). Springer.

Childers, D. L., Cofer-Shabicam S., Nakashima, L., (1993). Spatial and temporal variability in marsh- water column interactions in a southeastern USA salt marsh estuary. *Marine Ecology Progress Series*, *95*(1988), 25–38.

Chmura, G. L., Anisfeld, S. C., Cahoon, D. R., & Lynch, J. C. (2003). Global carbon sequestration in tidal , saline wetland soils, *17*(4). https://doi.org/10.1029/2002GB001917

Christiansen, T., P. L. Wiberg, and T. G. Milligan. (2000). Flow and sediment transport on a tidal salt marsh surface. *Estuarine, Coastal and Shelf Science*, *50*(3) 315-331.

Clark, J. B., Long, W., & Hood, R. R. (2017). Estuarine Sediment Dissolved Organic Matter Dynamics in an Enhanced Sediment Flux Model. *Journal of Geophysical Research: Biogeosciences*, *122*(10), 2669–2682.

Clark, J. B., Long, W., Tzortziou, M., Neale, P. J., & Hood, R. R. (2018). Wind-Driven Dissolved Organic Matter Dynamics in a Chesapeake Bay Tidal Marsh-Estuary System. *Estuaries and Coasts*, *41*(3), 708–723.

Correll, D. L. (1981). Nutrient mass balances for the watershed, headwaters intertidal zone, and basin of the Rhode River Estuary 1. *Limnology and Oceanography*, *26*(6), 1142–1149.

Cowan, J. L. W., & Boynton, W. R. (1996). Sediment-water oxygen and nutrient exchanges along the longitudinal axis of Chesapeake Bay: Seasonal patterns, controlling factors and ecological significance. *Estuaries*, *19*(3), 562–580.

Dame, R., Chrzanowski, T., Bildstein, K., Kjerfve, B., McKellar, H., Nelson, D., … Zingmark, R. (1986). The outwelling hypothesis and North Inlet, South Carolina. *Marine Ecology Progress Series*, *33*(3), 217–229.

Dame, R. F. (1995). The net flux of materials between marsh-estuarine systems and the sea: the Atlantic coast of the United States. *Oceanographic Literature Review*, *9*(42), 735.

Dame, R. F., Spurrier, J. D., Williams, T. M., Kjerfve, B., Zingmark, R. G., Wolaver, T. G., … Vernberg, F. J. (1991). Annual material processing by a salt marsh-estuarine basin in South Carolina, USA. *Marine Ecology Progress Series*, *72*, 153–166.

Del Vecchio, R. and Blough, N.V., (2002). Photobleaching of chromophoric dissolved organic matter in natural waters: kinetics and modeling. Marine Chemistry, 78(4), 231-253.

Di Toro, D. M., & Fitzpatrick, J. J. (1993). *Chesapeake Bay sediment flux model*. HYDROQUAL INC MAHWAH NJ. Retrieved from http://www.dtic.mil/docs/citations/ADA267189

Di Toro, D. M., (2001). *Sediment flux modeling* (Vol. 116). Wiley-Interscience New York.

Downing, B. D., Pellerin, B. A., Bergamaschi, B. A., Saraceno, J. F., & Kraus, T. E. C. (2012). Seeing the light: The effects of particles, dissolved materials, and temperature on in situ measurements of DOM fluorescence in rivers and streams. *Limnology and Oceanography, Methods / ASLO*, *10*(10), 767–775.

Erickson, J. E., Peresta, G., Montovan, K. J., & Drake, B. G. (2013). Direct and indirect effects of elevated atmospheric CO2 on net ecosystem production in a Chesapeake Bay tidal wetland. *Global Change Biology*, *19*(11), 3368–3378.

Fagherazzi, S., Wiberg, P. L., Temmerman, S., Struyf, E., Zhao, Y., & Raymond, P. a. (2013). Fluxes of water, sediments, and biogeochemical compounds in salt marshes. *Ecological Processes*, *2*(1), 3.

Fairall, C. W., Bradley, E. F., Rogers, D. P., Edson, J. B., & Young, G. S. (1996). Bulk parameterization of air-sea fluxes for tropical ocean-global atmosphere coupled-ocean atmosphere response experiment. *Journal of Geophysical Research, C: Oceans*, *101*(C2), 3747–3764.

Feng, Y., Friedrichs, M. A. M., Wilkin, J., Tian, H., Yang, Q., Hofmann, E. E., … Hood, R. R. (2015). Chesapeake Bay nitrogen fluxes derived from a land-estuarine ocean biogeochemical modeling system: Model description, evaluation, and nitrogen budgets. *Journal of Geophysical Research. Biogeosciences*, *120*(8), 1666–1695.

Fichot, C. G., & Benner, R. (2014). The fate of terrigenous dissolved organic carbon in a river-influenced ocean margin. *Global Biogeochemical Cycles*, *28*(3), 300–318.

Forbrich, I., & Giblin, A. E. (2015). Marsh-atmosphere CO2 exchange in a New England salt marsh. *Journal of Geophysical Research: Biogeosciences*, *120*(9), 1825–1838.

Friedrichs, C. T., & Aubrey, D. G. (1988). Non-linear Tidal Distortion in Shallow Well-mixed Estuaries: a Synthesis. *Estuarine, Coastal and Shelf Science*, *27*, 521–545.

Gallegos, C.L., Correll, D.L. and Pierce, J.W., 1990. Modeling spectral diffuse attenuation, absorption, and scattering coefficients in a turbid estuary. Limnology and Oceanography, 35(7), pp.1486-1502.

Gallegos, C. L., Jordan, T. E., & Correll, D. L. (1997). Interannual variability in spring bloom timing and magnitude in the Rhode River, Maryland, USA: observations and modeling. *Marine Ecology Progress Series*, *154*, 27–40.

Gallegos, C. L., Jordan, T. E., & Hedrick, S. S. (2010). Long-term Dynamics of Phytoplankton in the Rhode River, Maryland (USA). *Estuaries and Coasts*, *33*(2), 471–484.

Gallegos, C.L., Lewis, E.A. and Kim, H.C., (2006) Coupling suspended sediment dynamics and light penetration in the upper Chesapeake Bay. Edgewater, MD: Smithsonian Environmental Research Center

Ganju, N. K., Kirwan, M. L., Dickhudt, P. J., Guntenspergen, G. R., Cahoon, D. R., & Kroeger, K. D. (2015). Sediment transport-based metrics of wetland stability: Sediment Metrics of Wetland Stability. *Geophysical Research Letters*, *42*(19), 7992–8000.

Ganju, N. K., Nidzieko, N. J., & Kirwan, M. L. (2013). Inferring tidal wetland stability from channel sediment fluxes: Observations and a conceptual model: INFERRING STABILITY FROM SEDIMENT FLUXES. *Journal of Geophysical Research: Earth Surface*, *118*(4), 2045–2058.

Geyer, W. R. (1997). Influence of Wind on Dynamics and Flushing of Shallow Estuaries. *Estuarine, Coastal and Shelf Science*, *44*(6), 713–722.

Gonsior, M., Luek, J., Schmitt-Kopplin, P., Grebmeier, J. M., & Cooper, L. W. (2017). Optical properties and molecular diversity of dissolved organic matter in the Bering Strait and Chukchi Sea. *Deep-Sea Research. Part II, Topical Studies in Oceanography*, *144*, 104–111.

Haddad, J., Lawler, S., & Ferreira, C. M. (2016). Assessing the relevance of wetlands for storm surge protection : a coupled hydrodynamic and geospatial framework. *Natural Hazards*, *80*(2), 839–861.

Hansen, A. M., Kraus, T. E. C., Pellerin, B. A., Fleck, J. A., Downing, B. D., & Bergamaschi, B. A. (2016). Optical properties of dissolved organic matter (DOM): Effects of biological and photolytic degradation: DOM optical properties following degradation. *Limnology and Oceanography*, *61*(3), 1015–1032.

Hawkes, J. A., Dittmar, T., Patriarca, C., Tranvik, L., & Bergquist, J. (2016). Evaluation of the Orbitrap Mass Spectrometer for the Molecular Fingerprinting Analysis of Natural Dissolved Organic Matter. *Analytical Chemistry*, *88*(15), 7698–7704.

Hedges, J. I., Keil, R. G., & Benner, R. (1997). What happens to terrestrial organic matter in the ocean? *Organic Geochemistry*, *27*(5), 195–212.

Helms, J. R., Stubbins, A., & Ritchie, J. D. (2008). Absorption spectral slopes and slope ratios as indicators of molecular weight, source, and photobleaching of chromophoric dissolved organic matter. *Limnology and Oceanography*, *53*(3), 955-969

Hernes, P. J. (2003). Photochemical and microbial degradation of dissolved lignin phenols: Implications for the fate of terrigenous dissolved organic matter in marine environments. *Journal of Geophysical Research*, *108*(C9), 267.

Herrmann, M., Najjar, R. G., Michael, K. W., Alexander, R. B., Boyer, E. W., Cai, W.-J., … Smith, R. A. (2014). Net ecosystem production and organic carbon balance of U.S. East Coast estuaries: A synthesis approach. *Global Biogeochemical Cycles*, *29*, 96–111.

He, W., Chen, M., Schlautman, M. A., & Hur, J. (2016). Dynamic exchanges between DOM and POM pools in coastal and inland aquatic ecosystems: A review. *The Science of the Total Environment*, *551-552*, 415–428.

Hopkinson, C. S., Vallino, J. J., & Nolin, A. (2002). Decomposition of dissolved organic matter from the continental margin. *Deep-Sea Research. Part II, Topical Studies in Oceanography*, *49*(20), 4461–4478.

Hu, C., Muller-Karger, F. E., & Zepp, R. G. (2002). Absorbance, absorption coefficient, and apparent quantum yield: A comment on common ambiguity in the use of these optical concepts. *Limnology and Oceanography*, *47*(4), 1261–1267.

Ikegami, M., Whigham, D. F., & Werger, M. J. A. (2006). Scirpus olneyi (Cyperaceae) shows phenotypical differentiation in a salt marsh on the east coast of the USA. Retrieved from https://repository.si.edu/bitstream/handle/10088/18325/serc_Ikegami_et_al_2006_1.pdf?sequence=1&isAllowed=y

Jordan, E. (1991). Continuous Exchanges Marshes Automated of Nutrients Sampling of Tidal by Brackish, 527–545.

Jordan, T. E., & Correll, D. L. (1991). Continuous automated sampling of tidal exchanges of nutrients by brackish marshes. *Estuarine, Coastal and Shelf Science*, *32*(6), 527–545.

Jordan, T. E., Correll, D. L., Miklas, J., & Weller, D. E. (1991). Nutrients and chlorophyll at the interface of a watershed and an estuary, *36*, 251–267.

Jordan, T. E., Correll, D. L., & Whigham, D. F. (1983). Nutrient flux in the Rhode River: Tidal exchange of nutrients by brackish marshes. *Estuarine, Coastal and Shelf Science*, *17*(6), 651–667.

Jørgensen, B. B. (1978) A comparison of methods for the quantification of bacterial sulfate reduction in coastal marine sediments. 2. Calculations from mathematical models. *Journal of Geomicrobiology* 1, 29-51

Keller, D. P., & Hood, R. R. (2011). Modeling the seasonal autochthonous sources of dissolved organic carbon and nitrogen in the upper Chesapeake Bay. *Ecological Modelling*, *222*(5), 1139–1162.

Kemp, W. M., Sampou, P. A., Garber, J., Tuttle, J., & Boynton, W. R. (1992). Seasonal depletion of oxygen from bottom waters of Chesapeake Bay: roles of benthic and

planktonic respiration and physical exchange processes. *Marine Ecology Progress Series*, *85*(1/2), 137–152.

Kemp, W. M., Sampou, P., Caffrey, J., Mayer, M., Henriksen, K., & Boynton, W. R. (1990). Ammonium recycling versus denitrification in Chesapeake Bay sediments. *Limnology and Oceanography*, *35*(7), 1545–1563.

Kieber, D. J., G. W. Miller, P. J. Neale, & Mopper, K. (2014). Wavelength and temperature-dependent apparent quantum yields for photochemical formation of hydrogen peroxide in seawater. Environmental Science: Processes & Impacts 16: 777-791.

Kim, T., & Khangaonkar, T. (2012). An offline unstructured biogeochemical model (UBM) for complex estuarine and coastal environments. *Environmental Modelling and Software*, *31*, 47–63.

Kirwan, M. L., & Megonigal, J. P. (2013). Tidal wetland stability in the face of human impacts and sea-level rise. *Nature*, *504*(7478), 53–60.

Komada, T., Burdige, D. J., Crispo, S. M., Druffel, E. R. M., Griffin, S., Johnson, L., & Le, D. (2013). Dissolved organic carbon dynamics in anaerobic sediments of the Santa Monica Basin. *Geochimica et Cosmochimica Acta*, *110*, 253–273.

Komada, T., Burdige, D.J., Li, H.L., Magen, C., Chanton, J.P. and Cada, A.K., (2016). Organic matter cycling across the sulfate-methane transition zone of the Santa Barbara Basin, California Borderland. *Geochimica et Cosmochimica Acta*, *176*, 259-278.

Kumar, S., & Merwade, V. (2011). Evaluation of NARR and CLM3.5 outputs for surface water and energy budgets in the Mississippi River Basin. *Journal of Geophysical Research*, *116*(D8), 2415.

Large, W. G., & Pond, S. (1981). Open Ocean Momentum Flux Measurements in Moderate to Strong Winds. *Journal of Physical Oceanography*, *11*(3), 324–336.

Lee, S. B., Li, M., & Zhang, F. (2017). Impact of sea level rise on tidal range in Chesapeake and Delaware Bays: SEA LEVEL RISE CHANGING TIDES. *Journal of Geophysical Research, C: Oceans*, *122*(5), 3917–3938.

Leonard, L. A., & Croft, A. L. (2006). The effect of standing biomass on flow velocity and turbulence in Spartina alterniflora canopies, *69*, 325–336.

Lignell, R. (1990). Excretion of organic carbon by phytoplankton: its relation to algal biomass, primary productivity and bacterial secondary productivity in the Baltic Sea. *Marine Ecology Progress Series. 68*(1), 85–99.

Logozzo, L. (2017). Marsh-Exported Dissolved Organic Matter Fate in Estuaries: Bioavailability and Photoreactivity. *Masters Thesis*.

Lu, Y. H., Bauer, J. E., Canuel, E. A., & Chambers, R. M. (2014). Effects of land use on sources and ages of inorganic and organic carbon in temperate headwater streams. *Biogeochemistry*. Retrieved from https://link.springer.com/article/10.1007/s10533-014-9965-2

Lu, Y., Bauer, J. E., Canuel, E. A., Yamashita, Y., Chambers, R. M., & Jaffé, R. (2013). Photochemical and microbial alteration of dissolved organic matter in temperate headwater streams associated with different land use: DOM IN STREAMS OF DIFFERENT LAND USE. *Journal of Geophysical Research: Biogeosciences*, *118*(2), 566–580.

Maizel, A.C. and Remucal, C.K., (2017). Molecular composition and photochemical reactivity of size-fractionated dissolved organic matter. Environmental science & technology, 51(4), 2113-2123.

Mannino, A., & Harvey, H. R. (2000). Biochemical composition of particles and dissolved organic matter along an estuarine gradient: Sources and implications for DOM reactivity. *Limnology and Oceanography*, *45*(4), 775–788.

McKay, G., Couch, K. D., Mezyk, S. P., & Rosario-Ortiz, F. L. (2016). Investigation of the Coupled Effects of Molecular Weight and Charge-Transfer Interactions on the Optical and Photochemical Properties of Dissolved Organic Matter. *Environmental Science & Technology*, *50*(15), 8093–8102.

Medeiros, P. M., Seidel, M., Dittmar, T., Whitman, W. B., & Moran, M. A. (2015). Drought-induced variability in dissolved organic matter composition in a marsh-dominated estuary: ESTUARINE DOM COMPOSITION. *Geophysical Research Letters*, *42*(15), 6446–6453.

Medeiros, P. M., Seidel, M., Niggemann, J., Spencer, R. G. M., Hernes, P. J., Yager, P. L., … Hansell, D. A. (2016). A novel molecular approach for tracing terrigenous dissolved organic matter into the deep ocean: Terrigenous DOM in the Ocean. *Global Biogeochemical Cycles*, *30*(5), 689–699.

Miller, W. L., Moran, M. A., Sheldon, W. M., Zepp, R. G., & Opsahl, S. (2002). Determination of apparent quantum yield spectra for the formation of biologically labile photoproducts. *Limnology and Oceanography*, *47*(2), 343–352.

Møller, E. F. (2007). Production of dissolved organic carbon by sloppy feeding in the copepods Acartia tonsa, Centropages typicus, and Temora longicornis. *Limnology and Oceanography*, *52*(1), 79–84.

Moran, M. A., & Hodson, R. E. (1990). Bacterial production on humic and nonhumic components of dissolved organic carbon. *Limnology and Oceanography*, *35*(8), 1744–1756.

Moran, M. A., Sheldon, W. M., Jr., & Zepp, R. G. (2000). Carbon loss and optical property changes during long-term photochemical and biological degradation of estuarine dissolved organic matter. *Limnology and Oceanography*, *45*(6), 1254–1264.

Moriarty, J. M., Harris, C. K., Fennel, K., Friedrichs, M. A. M., Xu, K., & Rabouille, C. (2017). The roles of resuspension, diffusion and biogeochemical processes on oxygen dynamics offshore of the Rhône River, France: a numerical modeling study. *Biogeosciences* , *14*(7), 1919–1946.

Najjar, R. G., Herrmann, M., Alexander, R., Boyer, E. W., Burdige, D. J., Butman, D., ... & Feagin, R. A. (2018). Carbon budget of tidal wetlands, estuaries, and shelf waters of eastern North America. *Global Biogeochemical Cycles*, *32*(3), 389-416.

Neale, Patrick J., and Jennifer J. Fritz. (2002). Experimental exposure of plankton suspensions to polychromatic ultraviolet radiation for determination of spectral weighting functions. *In Ultraviolet Ground-and Space-based Measurements, Models, and Effects*, 4482, 291-297. International Society for Optics and Photonics.

Nelson, N. G., Muñoz-Carpena, R., Neale, P. J., Tzortziou, M., & Megonigal, J. P. (2017). Temporal variability in the importance of hydrologic, biotic, and climatic descriptors of dissolved oxygen dynamics in a shallow tidal-marsh creek. *Water Resources Research*, *53*(8), 7103–7120.

Nepf, H. M. (1999). Drag, turbulence, and diffusion in flow through emergent vegetation. *Water Resources Research*, *35*(2), 479–489.

Nidzieko, N. J. (2018). Allometric scaling of estuarine ecosystem metabolism. *Proceedings of the National Academy of Sciences of the United States of America*, *115*(26), 6733–6738.

Nixon, S. W. (1980). Between coastal marshes and coastal waters—a review of twenty years of speculation and research on the role of salt marshes in estuarine productivity and water chemistry. In *Estuarine and wetland processes* (pp. 437–525). Springer.

Odum, E. P. (2000). Tidal Marshes as Outwelling/Pulsing Systems. In M. P. Weinstein & D. A. Kreeger (Eds.), *Concepts and Controversies in Tidal Marsh Ecology* (pp. 3–7). Dordrecht: Springer Netherlands.

Opsahl, S., & Benner, R. (1997). Distribution and cycling of terrigenous dissolved organic matter in the ocean. *Nature*, *386*, 480.

Osburn, C. L., Mikan, M. P., Etheridge, J. R., Burchell, M. R., & Birgand, F. (2015). Seasonal variation in the quality of dissolved and particulate organic matter exchanged between a salt marsh and its adjacent estuary: SALT MARSH POM AND DOM. *Journal of Geophysical Research: Biogeosciences*, *120*(7), 1430–1449.

Powers, L.C. and Miller, W.L., (2015). Photochemical production of CO and CO 2 in the Northern Gulf of Mexico: Estimates and challenges for quantifying the impact of photochemistry on carbon cycles. Marine Chemistry, 171, 21-35.

Pritchard, D. W. (1952). Salinity distribution and circulation in the Chesapeake Bay estuarine system. *Journal of Marine Research*, *11*(2), 106–123.

Qualls, R. G., & Richardson, C. J. (2003). Factors Controlling Concentration, Export, and Decomposition of Dissolved Organic Nutrients in the Everglades of Florida. *Biogeochemistry*, *62*(2), 197–229.

Rasse, D. P., Peresta, G., & Drake, B. G. (2005). Seventeen years of elevated CO2 exposure in a Chesapeake Bay Wetland: sustained but contrasting responses of plant growth and CO2 uptake. *Global Change Biology*, *11*(3), 369–377.

Raymond, P. A., & Spencer, R. G. M. (2015). Chapter 11 - Riverine DOM. In D. A. Hansell & C. A. Carlson (Eds.), *Biogeochemistry of Marine Dissolved Organic Matter (Second Edition)* (pp. 509–533). Boston: Academic Press.

Reader, H. E., & Miller, W. L. (2014). The efficiency and spectral photon dose dependence of photochemically induced changes to the bioavailability of dissolved organic carbon. *Limnology and Oceanography*, *59*(1), 182–194.

Roden, E. E., Tuttle, J. H., Boynton, W. R., & Kemp, W. M. (1995). Carbon cycling in mesohaline Chesapeake Bay sediments 1: POC deposition rates and mineralization pathways. *Journal of Marine Research*, *53*(5), 779–819.

Romera-Castillo, C., Letscher, R. T., & Hansell, D. A. (2016). New nutrients exert fundamental control on dissolved organic carbon accumulation in the surface Atlantic Ocean. *Proceedings of the National Academy of Sciences of the United States of America*, *113*(38), 10497–10502.

Romera-Castillo, C., Sarmento, H., Álvarez-Salgado, X. A., Gasol, J. M., & Marrasé, C. (2010). Erratum: Production of chromophoric dissolved organic matter by marine phytoplankton. *Limnology and Oceanography*, *55*(3), 1466–1466.

Rose, K. C., Neale, P. J., Tzortziou, M., Gallegos, C. L., & Jordan, T. E. (2018). Patterns of spectral, spatial, and long-term variability in light attenuation in an optically complex sub-estuary. *Limnology and Oceanography*.

Schiebel, H. N., Gardner, G. B., Wang, X., Peri, F., & Chen, R. F. (2018). Seasonal Export of Dissolved Organic Matter from a New England Salt Marsh. *Journal of Coastal Research*, 939–954.

Schubel, J. R., & Pritchard, D. W. (1986). Responses of upper Chesapeake Bay to variations in discharge of the Susquehanna River. *Estuaries*, *9*(4), 236–249.

Scully, M. E. (2010). Wind Modulation of Dissolved Oxygen in Chesapeake Bay, (June 2009), 1164–1175.

Scully, M. E., Friedrichs, C., & Brubaker, J. (2005). Control of estuarine stratification and mixing by wind-induced straining of the estuarine density field. *Estuaries*, *28*(3), 321–326.

Sharpless, C.M. and Blough, N.V., (2014). The importance of charge-transfer interactions in determining chromophoric dissolved organic matter (CDOM) optical and photochemical properties. Environmental Science: Processes & Impacts, 16(4), 654-671

Sholkovitz, E. R. (1976). Flocculation of dissolved organic and inorganic matter during the mixing of river water and seawater. *Geochimica et Cosmochimica Acta*, *40*(7), 831–845.

Smith, E. M., & Benner, R. (2005). Photochemical transformations of riverine dissolved organic matter: effects on estuarine bacterial metabolism and nutrient demand. *Aquatic Microbial Ecology: International Journal*, *40*, 37–50.

Smyth, R. L., C. Sobrino, J. Phillips-Kress, H.-C. Kim, and P. J. Neale. (2012). Phytoplankton photosynthetic response to solar ultraviolet irradiance in the Ross Sea Polynya: Development and evaluation of a time-dependent model with limited repair. *Limnology & Oceanography*. 57, 1602–1618.

Soetaert, K., & Middelburg, J. J. (2009). Modeling eutrophication and oligotrophication of shallow-water marine systems: the importance of sediments under stratified and well-mixed conditions. *Hydrobiologia*, *629*(1), 239–254.

Soetaert, K., Middelburg, J. J., Herman, P. M. J., & Buis, K. (2000). On the coupling of benthic and pelagic biogeochemical models. *Earth-Science Reviews*, *51*(1), 173–201.

Søndergaard, M., & Middelboe, M. (1995). A cross-system analysis of labile dissolved organic carbon. *Marine Ecology Progress Series*, *118*, 283–294.

Spencer, R. G. M., Aiken, G. R., Dornblaser, M. M., Butler, K. D., Holmes, R. M., Fiske, G., … Stubbins, A. (2013). Chromophoric dissolved organic matter export from U.S. rivers: CDOM EXPORT FROM U.S. RIVERS. *Geophysical Research Letters*, *40*(8), 1575–1579.

Spencer, R. G. M., Butler, K. D., & Aiken, G. R. (2012). Dissolved organic carbon and chromophoric dissolved organic matter properties of rivers in the USA: DISSOLVED ORGANIC MATTER IN U.S. RIVERS. *Journal of Geophysical Research*, *117*(G3). https://doi.org/10.1029/2011JG001928

Stedmon, C.A., Markager, S., Tranvik, L., Kronberg, L., Slätis, T. and Martinsen, W., (2007). Photochemical production of ammonium and transformation of dissolved organic matter in the Baltic Sea. Marine Chemistry, 104(3-4), 227-240.

Stevenson, J. C., Kearney, M. S., & Pendleton, E. C. (1985). Sedimentation and erosion in a Chesapeake Bay brackish marsh system. *Marine Geology*, *67*(3), 213–235.

Stow, C. A., Jolliff, J., McGillicuddy, D. J., Jr, Doney, S. C., Allen, J. I., Friedrichs, M. A. M., … Wallhead, P. (2009). Skill Assessment for Coupled Biological/Physical Models of Marine Systems. *Journal of Marine Systems: Journal of the European Association of Marine Sciences and Techniques*, *76*(1-2), 4–15.

Teal, J. M. (1962). Energy Flow in the Salt Marsh Ecosystem of Georgia. *Ecology*, *43*(4), 614–624.

Testa, J. M., Brady, D. C., Di Toro, D. M., Boynton, W. R., Cornwell, J. C., & Kemp, W. M. (2013). Sediment flux modeling: Simulating nitrogen, phosphorus, and silica cycles. *Estuarine, Coastal and Shelf Science*, *131*, 245–263.

Thornton, D. C. O. (2014). Dissolved organic matter (DOM) release by phytoplankton in the contemporary and future ocean. *European Journal of Phycology*, *49*(1), 20–46.

Trapletti, Adrian and Kurt Hornik (2015). tseries: Time Series Analysis and Computational Finance. R package version 0.10-34.

Twardowski, M.S., Boss, E., Sullivan, J.M. and Donaghay, P.L., (2004). Modeling the spectral shape of absorption by chromophoric dissolved organic matter. Marine Chemistry, 89(1), 69-88.

Tzortziou, M., Neale, P. J., Megonigal, J. P., Pow, C. L., & Butterworth, M. (2011). Spatial gradients in dissolved carbon due to tidal marsh outwelling into a Chesapeake Bay estuary. *Marine Ecology Progress Series, 426*, 41–56.

Tzortziou, M., Neale, P. J., Osburn, C. L., Megonigal, J. P., Maie, N., & JaffÉ, R. (2008). Tidal marshes as a source of optically and chemically distinctive colored dissolved organic matter in the Chesapeake Bay. *Limnology and Oceanography*, *53*(1), 148–159.

Tzortziou, M., Osburn, C.L. and Neale, P.J., 2007. Photobleaching of dissolved organic material from a tidal marsh□estuarine system of the Chesapeake Bay. Photochemistry and photobiology, 83(4), pp.782-792.

Vähätalo, A. V., & Wetzel, R. G. (2004). Photochemical and microbial decomposition of chromophoric dissolved organic matter during long (months–years) exposures. *Marine Chemistry*, *89*(1), 313–326.

Vähätalo, A. V., & Wetzel, R. G. (2008). Long-term photochemical and microbial decomposition of wetland-derived dissolved organic matter with alteration of 13C:12C mass ratio. *Limnology and Oceanography*, *53*(4), 1387–1392.

Vlahos, P., Chen, R. F., & Repeta, D. J. (2002). Dissolved organic carbon in the Mid-Atlantic Bight. *Deep-Sea Research. Part II, Topical Studies in Oceanography*, *49*(20), 4369–4385.

Vinnikov, Konstantin. 2015. Baltimore – Washington Airport Wind Climatology. http://www.atmos.umd.edu/~kostya/NIST/WIND/SURFACE/KBWI_2010_10or13_WIND_2.pdf. Accessed March 8, 2017.

Wang, D.-P. (1979a). Subtidal Sea Level Variations in the Chesapeake Bay and Relations to Atmospheric Forcing. *Journal of Physical Oceanography*, *9*(2), 413–421.

Wang, D.-P. (1979b). Wind-Driven Circulation in the Chesapeake Bay, Winter, 1975. *Journal of Physical Oceanography*, *9*(3), 564–572.

Wang, T., Khangaonkar, T., Long, W., & Gill, G. (2014). Marine Science and Engineering Development of a Kelp-Type Structure Module in a Coastal Ocean Model to Assess the Hydrodynamic Impact of Seawater Uranium Extraction Technology, 81–92.

Wang, Z. A., & Cai, W.-J. (2004). Carbon dioxide degassing and inorganic carbon export from a marsh-dominated estuary (the Duplin River): A marsh CO 2 pump, *49*(2), 341–354.

Weston, N. B., & Joye, S. B. (2005). Temperature-driven decoupling of key phases of organic matter degradation in marine sediments. *Proceedings of the National Academy of Sciences of the United States of America*, *102*(47), 17036–17040.

Weston, N. B., Neubauer, S. C., Velinsky, D. J., & Vile, M. A. (2014). Net ecosystem carbon exchange and the greenhouse gas balance of tidal marshes along an estuarine salinity gradient. *Biogeochemistry*, *120*(1), 163–189.

Westrich, J.T. and Berner, R.A., (1984). The role of sedimentary organic matter in bacterial sulfate reduction: The G model tested. *Limnology and oceanography*, *29*(2), 236-249.

Windham-Myers, L., W.-J. Cai, S. R. Alin, A. Andersson, J. Crosswell, K. H. Dunton, J. M. Hernandez-Ayon, M. Herrmann, A. L. Hinson, C. S. Hopkinson, J. Howard, X. Hu, S. H. Knox, K. Kroeger, D. Lagomasino, P. Megonigal, R. G. Najjar, M.-L. Paulsen, D. Peteet, E. Pidgeon, K. V. R. Schäfer, M. Tzortziou, Z. A. Wang, and E. B. Watson. (2018). Chapter 15: Tidal wetlands and estuaries. *Second State of the Carbon Cycle Report (SOCCR2): A Sustained Assessment Report*. https://doi.org/10.7930/SOCCR2.2018.Ch15

Wolaver, T. G., Zieman, J. C., Wetzel, R., & Webb, K. L. (1983). Tidal exchange of nitrogen and phosphorus between a mesohaline vegetated marsh and the surrounding estuary in the lower Chesapeake Bay. *Estuarine, Coastal and Shelf Science*, *16*(3), 321–332.

Wolff, W. J., Van Eeden, M. J., & Lammens, E. (1979). Primary production and import of particulate organic matter on a salt marsh in the Netherlands. *Netherlands Journal of Sea Research*, *13*(2), 242–255.

Xu, J., & Hood, R. R. (2006). Modeling biogeochemical cycles in Chesapeake Bay with a coupled physical–biological model. *Estuarine, Coastal and Shelf Science*, *69*(1), 19–46.

Xu, J., Long, W., Wiggert, J. D., Lanerolle, L. W. J., Brown, C. W., Murtugudde, R., & Hood, R. R. (2012). Climate Forcing and Salinity Variability in Chesapeake Bay, USA. *Estuaries and Coasts*, *35*(1), 237–261.

Zheng, L., Chen, C., & Liu, H. (2003). A modeling study of the Satilla River estuary, Georgia. I: Flooding-drying process and water exchange over the salt marsh-estuary-shelf complex. *Estuaries*, *26*(3), 651–669.